

**CRANFIELD UNIVERSITY**

**LAWRENCE COOK**

**VISUAL INSPECTION RELIABILITY FOR COMPOSITE  
AIRCRAFT STRUCTURES**

**SCHOOL OF APPLIED SCIENCES**

**PhD THESIS**

**Supervisors:**

**Prof. Phil Irving & Dr. Don Harris**

**October 2009**



**CRANFIELD UNIVERSITY**

**SCHOOL OF APPLIED SCIENCES**

**PhD THESIS**

**LAWRENCE COOK**

**VISUAL INSPECTION RELIABILITY FOR COMPOSITE  
AIRCRAFT STRUCTURES**

**Supervisors:**

**Prof. Phil Irving & Dr. Don Harris**

**October 2009**

© Cranfield University 2009. All rights reserved. No part of this publication may be reproduced without the written permission of the copyright owner.



## ***Abstract***

This thesis presents a study of the effects of surface colour, surface finish and dent shape on the visual inspection reliability of 3D surface indentations common in shape to those produced by impact damage to carbon fibre reinforced epoxy laminates.

Falling weight (2.5kg) apparatus was used to produce impact damage to non-painted, non-mesh Hexcel AS4/ 8552 carbon fibre reinforced plastic (CFRP) laminates and painted AS4/ 8552 laminates containing bronze mesh and glass fabric lightning strike protection layers. Ø20 mm and Ø87 mm hemispherical tip impacts to painted 17ply and 33ply laminates at varying energy levels typically produced circular shaped, smoothly contoured, rounded sectional profiles with an absence of surface breaking cracks.

Sectional profiles through coordinate measuring (CMM) data of the impact dents were described using a set of geometric variables. Identifying relationships between impact energy and the geometric variables allowed the typical sectional profile through impact damage dents from Ø20 mm and Ø87 mm hemispherical tips on 17ply and 33ply painted CFRP laminates to be calculated for energies between 5J to 80J.

Calculated sectional profiles typical of impact damage dents to CFRP laminates were reconstructed as simple revolved shapes using 3D computer aided design (CAD) models. The 3D CAD models were computer numerical control (CNC) machined into 3mm Plexiglas panels to produce facsimiles of hemispherical impact damage dents on CFRP laminates.

Facsimile specimen sets of sixteen 600 mm x 600 mm panels were produced in gloss and matt grey, white and blue finishes. Each set contained the same 32 different sized machined dents representing Ø20 mm and Ø87 mm hemispherical tip impact damage to 17ply & 33ply painted CFRP laminate. Each facsimile specimen set was combined with similarly finished unflawed (dent free) panels. 64 panels in each colour/ finish were presented for 5 seconds in a randomised order to a minimum of 15 novice participants in a visual inspection task lasting approximately 25 minutes.

A set of corresponding visual inspection experiments were performed in which physical specimens were replaced by digitally projected actual size photorealistic images of the machining CAD data. Comparisons between the results of the physical and virtual specimen trials revealed differences in detectability for similarly sized dents.

The detection results obtained from visual inspection of physical specimens demonstrated that the detectability of dents similar to those caused by higher (>40J) energy impacts from a Ø87 mm hemispherical tip was less than that of the dents caused by lower energy (<20J) impacts from Ø20 mm tips. However, larger subsurface delamination area was demonstrated by the higher energy Ø87 mm impacts than lower energy Ø20 mm impacts on 150 mm x 100 mm coupons of the same thickness laminate. The results of these experiments imply that detectability of dents caused by larger diameter objects at higher energies cannot be assumed to be greater than that of lower energy impacts from smaller diameter objects.

The detection results demonstrate that detectability by visual inspection cannot be assumed the same for an impact dent on different surface colours and finishes. In general terms, the highest numbers of dents returning >90% detection were observed on grey specimens and the highest number of dents returning 0% detection were observed on matt blue specimens. The difference in detection rates for similarly sized dents on a gloss and matt finish was least on grey coloured specimens and greatest on blue coloured specimens.

## *Acknowledgements*

The author would like to thank the CAA, and everyone at the CAA involved in kindly sponsoring and conscientiously supporting the work conducted for this thesis.

The author would like to extend personal thanks to the following people, and to all the people whom were there to help throughout the work of this thesis:

To Rachel, thank you for your love, understanding and support. Thank you for always being there, for listening, and keeping it all as simple as “dents in planes”. To Lewis, thank you for being such a wonderful, happy child and for providing some of the most rewarding distractions from “dents in planes”. To Dad, thank you for always being encouraging and for taking such keen interest.

To Phil Irving, thank you for being such a patient and approachable supervisor. Thank you for being willing to listen, for always being involved, and for always wanting the best. Throughout my time at Cranfield, I could not have wished for more support and encouragement.

To Don Harris, it seemed you were always able to give just the right input at just the right time. Thank you for providing the encouragement to explore blind alleys, whilst all the time finding time for unique and refreshing humour.

To Ted Blacklay and Hazel Courteney, thank you for your unwavering support throughout the project. Thank you for always being interested in the work, and for helping out wherever you could.

Thank you to Simon Waite and Larry Ilcewicz for providing the opportunity to present this work, and for your kind support in Salt Lake City.

To Jim Hurley & Gary Muir – always a joy to walk in the lab, be brought down to Earth, and be allowed to learn by doing. To Jim, thank you for being a true friend, an inspiring mentor, and for reminding me to keep things short, know your facts

and not waste time with discussions. To Gary, thank you for the friendship, the homely welcome in Bedford, and the fatherly understanding.

To Ben Hopper, thank you for all your help, support and input with the trials, for helping with no end of tedious but invaluable tasks, and above all for being a great friend.

To Anne Boulic, thank you for conducting some of the most painstaking work, for learning so quickly in so little time, and for providing us with such valuable results.

To Trevor Mead & Russell Martin at M&M Patterns and Roy Harris, thank you for your patience, experience and skill. Without your willingness and enthusiasm to take on the unusual, this thesis would not have been possible.

Thank you to all at Cranfield University whom kindly gave up their time to participate in visual inspection trials. Without your help, it would not have been possible to gather the results presented in this thesis.

To the staff at Kings Norton Library, thank you for consistently providing the excellent library services on which much of this thesis has depended.

The help and assistance of the following people and organisations is also gratefully appreciated:

Terry Wynne, (Aero Consultants); Dennis Murphy (DHL Global Logistics); John Gamblin, Derek Miller & Pete Wetherill and Cranfield Aerospace; Paddy Rathbone, Stewart Oates, Sue Richardson, Glenda Metcalf & all the team at Cranfield Students Association; Charles Marshall, Andrew Mills, Tony Scott, Barry Walker and Cranfield University; Giovanni Marengo & Paul Saunders (GKN Aerospace); Gavin Creech (Scott Bader); Lt Cassie Williams & the Repair Management Team (RAF Cottesmore).



For James Thomas Cook...

... January 2010

Page left intentionally blank

## ***Contents***

<b>Abstract</b> .....	<b>I</b>
<b>Acknowledgements</b> .....	<b>III</b>
<b>Notation</b> .....	<b>XII</b>
<b>Chapter 1 – Introduction</b> .....	<b>1</b>
<b>Chapter 2 – Literature search</b> .....	<b>3</b>
2.1 – Composite materials .....	3
2.1.1 – Use of composite materials in modern commercial aircraft .....	5
2.1.2 – Typical composite aircraft structures .....	7
2.1.3 – Impact damage & failure of composite materials .....	9
2.1.4 – Characterisation of impact damage to composite materials .....	11
2.1.5 – Factors affecting impact damage morphology .....	11
2.1.6 – Impact testing of composite materials .....	15
2.1.7 – Impact damage scenarios for composite aircraft structures .....	18
2.1.8 – Damage tolerance of composite aircraft structures .....	19
2.1.9 – Non-Destructive Testing/ Inspection (NDT/ NDI) of composite aircraft structures .....	22
2.2 – Visual Inspection .....	26
2.3 – Visual perception and visual inspection .....	33
2.3.1 – Shadow & Shading .....	33
2.3.2 – Lighting .....	36
2.3.3 – Specular Highlights .....	38
2.3.4 – Specular Reflections .....	39
2.3.5 – Surface Slant and Tilt .....	42
2.3.6 – Surface colour & surface finish .....	44
2.4 – Aircraft paint finishes .....	49
2.5 – Reliability assessment of NDI/ NDT techniques .....	50
2.5.1 – Participants .....	53
2.5.2 – Experimental setup .....	54
2.5.3 – Specimen Characteristics .....	55
2.5.4 – Flaws .....	56
2.5.5 – Specimen numbers .....	58
2.5.6 – Other issues pertaining to specimens & procedures .....	60
2.5.7 – Experimental Variables .....	61
2.5.8 – POD Analysis methods .....	65
2.5.9 – Single variate POD models .....	66
2.5.10 – Multi-variate POD .....	67
2.6 – Overall summary of literature .....	68

<b>Chapter 3 – Experimental Design</b> .....	<b>70</b>
3.1 – Experimental aims & objectives.....	70
3.2 – Examples of impact damage to CFRP laminates.....	70
3.3 – Initial visual inspection trials with virtual specimens.....	71
3.4 – Reproduction of impact dents as facsimile specimens .....	73
3.5 – Visual inspection trials with physical specimens .....	75
3.6 – Second series of trials with virtual specimens .....	76
<b>Chapter 4 – Experimental Methods</b> .....	<b>78</b>
4.1 – Production of fully finished CFRP laminate samples .....	78
4.2 – Ultrasonic C-Scanning.....	79
4.3 - Falling weight impact damage .....	79
4.4 – Measurement of delamination .....	81
4.5 – Measurements of impact damage surface topography.....	81
4.5.1 – Width measurement with Vernier callipers .....	81
4.5.2 – Depth measurements with a depth gauge .....	82
4.5.3 – Depth gauge profiles .....	82
4.5.4 – CMM (Coordinate Measuring Machine) coupon surface digitisation.....	84
4.5.5 – Width measurements from depth gauge & CMM data.....	84
4.5.6 – Metallographic sectioning technique.....	86
4.6 – Reconstruction of surface flaws using geometric lines & arcs.....	86
4.7 – Reproduction of impact flaws as 3D CAD data .....	88
4.8 – Production of virtual facsimile specimens.....	89
4.9 – Production of physical facsimile specimens.....	90
4.9.1 – Application of matt finish to physical specimens.....	91
4.9.2 – CMM checking of physical specimens.....	92
4.9.3 – Gloss measurements of physical specimens .....	93
4.9.4 – Paint thickness measurement of physical specimens.....	93
4.10 – Flaw and specimen characteristics .....	94
4.10.1 – Specimens for virtual trial 1 (series 1).....	94
4.10.2 – Specimens for virtual trial 2 (series 1).....	95
4.10.3 – Specimens for virtual trial 3 (series 1).....	96
4.10.4 – Specimens for virtual trial 4 (series 1).....	97
4.10.5 – Specimens for virtual trial 5 (series 2) and trials with facsimile specimens.....	98
4.11 – Display of virtual specimens to participants.....	105
4.12 – Display of physical facsimile specimens to participants .....	106
4.13 – Participant briefing for visual inspection trials.....	109
4.14 – Experimental task for visual inspection trials participants .....	110
4.15 – Recording participant responses – series 1 virtual specimen trials .....	110

4.16 – Recording participant responses– physical specimen & series 2 virtual specimen trials.....	110
4.17 – Data collection method for visual inspection trials .....	111
4.18 – Participants – Series 1 trials (with virtual specimens).....	113
4.19 – Participants – Series 2 trials (physical & virtual specimens) .....	113
<b>Chapter 5 – Experimental Results.....</b>	<b>114</b>
5.1 – Impact damage to CFRP laminates .....	114
5.1.1 – Basic measurements of impact flaw morphology for fully finished CFRP laminates....	115
5.1.2 – Relationship between flaw and subsurface damage sizes.....	116
5.1.3 – Comparisons between impact damage on painted & unfinished laminates.....	119
5.1.4 – Characterisation of surface flaws from hemi-spherical objects.....	126
5.1.5 – Quantitative measurements of surface flaw topographies .....	128
5.1.6 – Relationships between impact flaw geometry variables.....	129
5.2 – CMM checking of physical facsimile specimens .....	134
5.3 – Gloss measurements of physical facsimile specimens .....	135
5.4 – Results of visual inspection trials with virtual specimens – series 1 .....	136
5.4.1 – Results of trial 1 .....	136
5.4.2 – Results of trials 2 and 3 .....	138
5.4.3 – Results of trial 4 .....	143
5.4.5 – Summary of results from series 1 of virtual trials .....	146
5.5 – Results of visual inspection trials – series 2.....	146
5.5.1 – Results data for series 2 visual inspection trials.....	147
5.5.2 – General Summary of results from series 2 trials .....	156
5.5.3 – Detailed summaries of results from series 2 trials.....	156
<b>Chapter 6 – Discussion.....</b>	<b>162</b>
6.1 – Experimental issues; impact damage.....	164
6.1.1 – Flaw width measurements on impact damaged CFRP coupons.....	164
6.2 – Experimental issues – visual inspection trials .....	165
6.2.1 – Inspection time .....	165
6.2.2 – Use of novice inspectors in visual inspection trials.....	166
6.2.3 – Lighting .....	166
6.2.4 – Design of facsimile specimen flaws .....	167
6.2.5 – Size range of physical trial results.....	169
6.2.6 – significance of participant responses.....	169
6.2.7 – Generic applicability of physical trial results .....	169
6.2.8 – Existing experimental paradigms and protocols.....	171
6.3 – Visual perception cues and visual inspection of impact damage .....	174
6.3.1 – Effects of surface colour & surface finish on modularity of visual perception cues .....	175
6.3.2 – Effect of surface colour & finish on specular reflection cues.....	176

6.3.3 – Effects of flaw shape on visual perception cues .....	177
6.2.4 – Role of head movements in visual perception/ inspection .....	179
6.4 – Implications for aviation safety .....	180
6.4.1 – Lighting for visual inspection tasks on composite structures .....	180
6.4.2 – Implications for designers of composite material structures .....	181
6.4.3 – Implications for aviation personnel .....	183
6.5 – Recommendations to industry & regulatory bodies .....	184
6.5.1 – Damage size assumptions.....	184
6.5.2 - Damage reporting.....	185
6.5.3 – Reporting culture .....	185
6.5.4 – Effects of surface colour, finish & lighting .....	185
6.5.5 – Flaw significance/ perceived severity.....	186
6.5.6 – Reliability assessment protocols.....	186
<b>Chapter 7 – Future Work.....</b>	<b>187</b>
7.1 – Expansion of flaw size range.....	187
7.2 – Experimental protocols/ guidelines .....	187
7.3 – Alternative Visual Inspection Trials Methodology .....	188
7.4 – Paint Patterns.....	191
7.5 – Curved specimen panels.....	191
7.6 – State of knowledge of pilots, maintenance & ground crew personnel .....	192
<b>Chapter 8 – Conclusions.....</b>	<b>193</b>
8.1 – Impact damage to fully finished CFRP laminates .....	193
8.2 – Visual inspection reliability of impact damage dents.....	193
8.3 - Effects of surface finish and colour on visual inspection reliability .....	194
8.4 – Visual inspection reliability for composite aircraft structures.....	195
<b>References .....</b>	<b>196</b>
<b>Appendix A .....</b>	<b>208</b>
CAD system rendering settings for virtual specimens .....	208
Lighting settings.....	208
Materials settings.....	209
<b>Appendix B .....</b>	<b>210</b>
Specimen & Flaw specifications for series 1 visual inspection trials.....	210
Trial 1 specimen/ flaw characteristics .....	210
Trial 2 Specimen/ flaw characteristics .....	211
Trial 3 specimen/ flaw characteristics .....	213
Trial 4 specimen/ flaw characteristics .....	215
<b>Appendix C .....</b>	<b>217</b>
Drawings of specimen panels for series 2 visual inspection trials .....	217

<b>Appendix D .....</b>	<b>225</b>
Examples of impact damage to AS4/8552 CFRP Coupons.....	225
<b>Appendix E .....</b>	<b>256</b>
Hit/Miss results data from Trial 1 .....	256
Hit/Miss results data from Trial 2 .....	257
Hit/Miss results data from Trial 3 .....	258
Hit/Miss results data from Trial 4 .....	259
<b>Appendix F.....</b>	<b>260</b>
POD curve & RIM calculations .....	260
POD curve calculations for Trial 2.....	262
POD curve calculations for Trial 3.....	265
POD curve calculations for Trial 4.....	266
<b>Appendix G .....</b>	<b>270</b>
Hit/Miss data for series 2 visual inspection trials.....	270
Hit/Miss data for trials with virtual grey specimens.....	270
Hit/Miss data for trials with gloss grey specimens.....	271
Hit/Miss data for trials with matt grey specimens.....	272
Hit/Miss data for trials with gloss white specimens .....	273
Hit/Miss data for trials with matt white specimens .....	274
Hit/Miss data for trials with gloss blue specimens .....	275
Hit/Miss data for trials with matt blue specimens .....	276
<b>Appendix H .....</b>	<b>277</b>
Detection plots of results from series 2 visual inspection trials .....	277

## ***Notation***

AC	Advisory Circular
AGARD	Advisory Group for Aerospace Research and Development
AMM	Aircraft Maintenance Manual
BVID	Barely Visible Impact Damage
BSS	Boeing Support Specification
CAA	Civil Aviation Authority (United Kingdom)
CAD	Computer Aided Design
CAI	Compression after Impact
CAP	Civil Aviation Publication (CAA)
CATT	Computer Aided Tap Test
CFRP	Carbon Fibre Reinforced Plastic/ Polymer
CNC	Computer Numerical Control
CMM	Coordinate Measuring Machine
DIN	Deutsches Institut für Normung
DLL	Design Limit Load
DLR	Deutsches Zentrum für Luft und Raumfahrt
DUL	Design Ultimate Load
DVI	Detailed Visual Inspection
EASA	European Aviation safety Agency
EN	European (Technical) Standard
FAA	Federal Aviation Administration (United States of America)
FOD	Foreign Object Damage
GFRP	Glass Fibre Reinforced Plastic/ Polymer
GLARE	Glass Reinforced (Fibre/ Metal Laminate)
GU	Gloss Units
GVI	General Visual Inspection
IGES	International Graphics Exchange Specification
ISO	International Organisation for Standardisation
LSP	Lightning Strike Protection
MAUS	Mobile Automated Ultrasonic Scanner
MIL-HDBK	Military Handbook (United States of America)
MLE	Maximum Likelihood Estimators



MRO	Maintenance Repair and Overhaul
NASA	National Aeronautics and Space Administration
NTSB	National Transportation Safety Board
PMMA	Poly (methyl methacrylate)
POD	Probability of Detection
POFA	Probability of False Alarm
NC	Numerical Control
NDE	Non Destructive Evaluation
NDI	Non Destructive Inspection
NDT	Non Destructive Testing
NVD	Non Visible Damage
RFI	Resin Film Infusion
RIM	Range Interval Method
ROC	Receiver Operating Characteristic
RTM	Resin Transfer Moulding
SAM	Scanning Acoustic Microscopy
SLAM	Scanning Laser Microscopy
SRM	Structural Repair Manual
UD	Unidirectional
US	United States (of America)
USAF	United states Air Force
US DoD	United States Department of Defence
2D	Two Dimensional
3D	Three Dimensional
Ø	Diameter
°	Degrees
°C	Degrees Celsius
exp	Exponential
g	Gram
GPa	Gigapascal
In	Inches
J	Joules
Kg	Kilogram

kN	Kilonewton
ksi	Kilo-pound-force per square inch
log	Logarithm
m	Metre
mm	Millimetre
μm	Micrometre
MHz	Megahertz
MPa	Megapascal
msi	Mega-pound-force per square inch
mph	Miles per hour
ln	Natural logarithm
s	Seconds

## ***Chapter 1 – Introduction***

The aviation industry is familiar with inspection of metallic aircraft structures, and there is a wealth of knowledge and experience amongst trained personnel regarding damage manifestation in metallic structures. Maintenance crew and pilots perform regular checks in order to ensure that aircraft are undamaged. Airport ground handlers are trained to be aware that aircraft are easily damaged, and are instructed to report suspected damage, such as a bag dropped onto an aircraft skin, or a bump from a vehicle. Much of the day-to-day damage to aircraft on the ground, i.e. ramp rash, is caused by impacts from objects.

Most aviation personnel would be capable of identifying a dent or tear in a metallic structure, and reporting it as suspected damage. However, after a heavy impact, a fibre reinforced laminate (composite) structure could appear undamaged if no surface marks or flaws are present. Where flaws are present, they may go unreported due to having similar appearance to small dents on a metallic structure (which ground crew may be inclined not to report, and maintenance crew would not need to repair on a metallic structure). Whilst aviation personnel may be highly experienced at recognising impact damage to a metallic structure, there is concern that maintenance technicians, pilots, and ground crew may be less experienced at recognising impact damage on a composite aircraft structure. This could lead to a situation where damage to composite aircraft structures is not reported due to personnel not recognising damage. Failure to report impact damage, and subsequent non-repair of impact-damaged composite aircraft structures has far greater airworthiness implications for primary structures (such as pressurised fuselage skins) than for secondary structures (such as fairings and non-pressurised skins).

Furthermore, where surface flaws *are* present due to impact damage, personnel must firstly be able to see the flaw, i.e. detect it. For metallic aircraft structures, the relation between probability of detection for cracks and flaws and their size is well established for many non-destructive testing (NDT) techniques, including visual inspection. The size at which cracks can be detected with 90% probability is well specified. In contrast, the reliability of detection of surface flaws in composite structures is not well

established; surface flaws resulting from impact damage may not be detected, meaning significant damage may not be reported.

This study was performed in order to identify the visual appearance of flaws arising from impact to an aircraft structure, and then to determine the relation between detection reliability and the size and shape of surface flaws for visual inspection procedures. The potential influences of surface colour and finish on visual detection reliability were also investigated.

## ***Chapter 2 – Literature search***

### ***2.1 – Composite materials***

Composite materials constitute a combination of two or more materials that are chemically distinct [Kalpakjian 1995]. Based on such a description, the oldest composite materials can be dated back to 4000 B.C. when straw was added to clay for construction of buildings [Kalpakjian 1995]. Today the term ‘composite’ material generally refers to fibre-reinforced plastics (FRP). The first application of reinforced plastics was in 1907, when asbestos fibres were used to reinforce a phenolic resin [Kalpakjian 1995].

Typical modern fibre reinforced plastics (FRP) may contain glass (GFRP), aramid (*Kevlar*) (AFRP), boron, carbon or graphite fibres (CFRP) [Kalpakjian 1995; Bunsell & Renard 2005]. Other materials such as nylon, silicon carbide, silicon nitride, steel, tungsten, molybdenum and polyethylene (*Spectra*) can be used as fibre reinforcements [Kalpakjian 1995; Bunsell & Renard 2005]. Reinforcing fibres have high tensile strength and high elastic modulus, as described in table 2.01. Carbon fibres are less dense (1800 Kg/m<sup>3</sup>) and less costly to produce than boron, making them a common choice for aerospace structures where higher specific strength and specific module are desired [Kalpakjian 1995; Campbell 2004]. The reinforcing fibres themselves are brittle and their strength is effective only in the fibre direction.

<b>Fibre Type</b>	<b>Tensile Strength (ksi/ MPa)</b>	<b>Elastic Modulus (msi / GPa)</b>	<b>Density (Kg/m<sup>3</sup>)</b>	<b>Strain to Failure (%)</b>
Boron	520 / 3600	11 / 380	2600	0.9
Carbon (AS4)	530 / 3700	33 / 228	1800	1.5
Carbon (IM-7)	730 / 5000	41 / 283	1770	1.8
Kevlar (aramid) 49	550 / 3800	19 / 131	1440	2.8
E-Glass	500 / 3400	11 / 76	2490	4.8
S-Glass	650 / 4500	12.6 / 87	2540	5.6
Spectra 1000	450 / 3100	25 / 172	970	0.7

Table 2.01 – Fibre properties, from Campbell 2004, pp 6

The plastic or resin matrix can be produced from a range of materials, although polyester, polyamide, polypropylene, phenolic and epoxy are the most commonly used [Bunsell & Renard 2005]. The service temperature resistance of epoxies is 150°C, their flexural strength can be between 80-140 MPa, and their flexural modulus is typically 3 GPa [Bunsell & Renard 2005]. However, in order to allow safety margins, continuous service temperatures of epoxy composite aircraft structures are limited to 100°C [US DoD 2002, MIL-HDBK-17 & Rouchon 2010]. Thermoplastic resins can have higher toughness, and thus greater resistance to impact damage, than thermoset resins, but their temperature resistance can be as low as 100°C [Kalpakjian 1995]. Polyester resins account for 53% of total matrix material sales, although advanced (i.e. aerospace) applications favour the low shrinkage, high tensile strength (90 MPa vs. 35~80 MPa), higher temperature resistance (150°C vs. 85~125°C) and superior chemical resistance offered by epoxy matrices [Kalpakjian 1995; Bunsell & Renard 2005].

Despite earlier suggestions of the potential for RTM and RFI processes in aerospace applications [Halpin 1994], the autoclave curing process, with manual lay-up of prepreg material continues to be a predominant choice for complex structures in US (and other) aerospace applications [dti 2006].

A high strength carbon fibre reinforced epoxy laminate offers superior specific strength (strength/ density) and specific modulus (strength/ modulus) to traditional materials such as titanium, steel or aluminium, as seen in figure 2.01, hence the popularity of CFRP materials within the aircraft industry.

However, a unidirectional laminate will only have excellent tensile strength and compression strength in the fibre, or ply, direction, i.e. the laminate will exhibit excellent in-plane load performance, but poor out-of-plane performance. To reduce the anisotropy of a fibre-reinforced laminate, and provide strength in multiple directions, the fibres are generally laid up in varying configurations of 0°, 90° and +/- 45° orientations [see Matthews & Rawlings 1994; Campbell 2004; Bunsell & Renard 2005; Rouchon 2010].

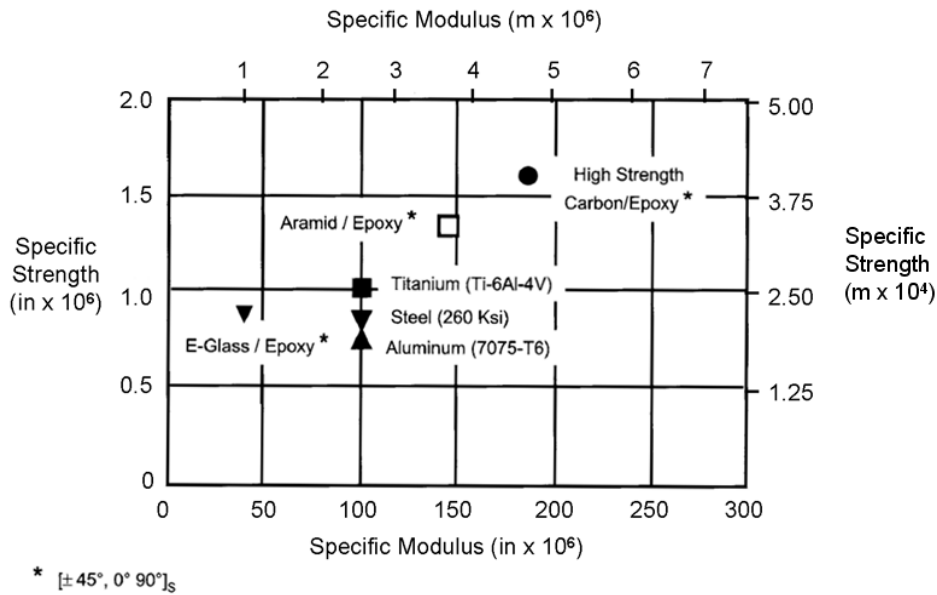


Figure 2.01 – Material strength & modulus, from Campbell 2004, pp 27

### 2.1.1 – Use of composite materials in modern commercial aircraft

Including other uses such as automotive, cycling, boating and consumer products [Campbell 2004; Cuffaro 2006], composite materials have seen increasing use in aviation applications, for both military and commercial aircraft [Kalpakjian 1995]. The 1970s saw fairing panel, spoiler and pylon skin components produced from composite materials enter service on commercial aircraft [Harris & Shuart 2001]. Use of composite materials has grown through the 1970s, 80s & 90s, from structures on the aircraft that had little structural importance (secondary structures), to primary structures such as horizontal & vertical stabilisers and ailerons [Harris & Shuart 2001]. An excellent review of the earlier period of the development of composite materials in aerospace applications is provided by Harris & Shuart, 2001, and a more recent review is given by Rouchon, 2009.

**1980~1990** – The Boeing 757 aircraft entered service in 1983 utilising composite materials for elevator, aileron, spoiler and rudder components, although the structural components of the fuselage, wing and stabilisers remained of metallic construction [Boeing 757-200 2009, Kalpakjian 1995]. In 1985, the Airbus A310 aircraft became the first commercial airliner to utilise composite materials for construction of the vertical stabiliser and rudder structures (primary structures) [Harris & Shuart 2001;

Rouchon 2009]. Airbus ventured further with composites in 1988 with the A320 family aircraft, employing composite materials for control surfaces, vertical and horizontal stabilisers (empennage) [Airbus 2009, Robois 2005; Rouchon 2009]. Much of the composite structures used during this period are of sandwich type construction (see US DoD MIL-HDBK-17 Vol 1 2002, Campbell 2004 for details on sandwich construction), although glass and aramid fibres began to be replaced by carbon or graphite fibres [Kalpakjian 1995, Robois 2005, Rouchon 2010]. The period leading up to the 1990's also saw the introduction of monolithic fibre reinforced composite materials for horizontal and vertical stabiliser structures [Rouchon 2010].

**1990~2000** – The Boeing 777 entered commercial service in 1995 containing 9% of composite materials by weight [Boeing 777 2009; Kalpakjian 1995]. From the same era, the Airbus A330/A340 family also contain around 10~11% composites by weight [Robois 2005]. The 777 and A330/A340 aircraft represent the highest utilisation of carbon-fibre reinforced composite materials on wide-body aircraft currently in *widespread* service. The 777 and A330/A340 aircraft are similar in several respects, and utilise carbon fibre reinforced monolithic and sandwich structures for primary and secondary structures including floor beams, floor panels, fairings, keel beams, spoilers, control surfaces, horizontal stabilisers and vertical stabilisers [Kalpakjian 1995, Robois 2005; Brosius 2007]. However, the fuselage of both aircraft are constructed from a traditional metal frame with a metal skin. Furthermore, whilst empennage structures on the 777 are produced from composite materials, their construction is termed as having a ‘black metal’ approach i.e. the composite panels are attached to composite stringers and ribs as opposed to the use of unitary construction methods [Webborn 2006]. Smaller business type aircraft such as the Beech (Raytheon) Premier and Horizon have employed greater use of unitary composite structures, albeit sandwich type, for their fuselages [Mills 2006].

**2000 ~** – The Airbus A380 entered service in 2007, and contains approximately 25% composites by weight, which is currently the highest ‘in-service’ level of composite materials usage on large commercial aircraft. Sections of the Airbus A380 fuselage are produced from GLARE, a metal/ composite sandwich material [Robois 2005]. Many of the primary structures including the empennage and control surfaces are also produced from carbon and glass fibre reinforced composite materials [Robois 2005].



However, the A380 fleet is operated by only a small number of airlines, and cannot be considered to be in ‘widespread’ service.

Currently, no commercial aircraft in airline service have monolithic carbon fibre reinforced plastic (CFRP) fuselage structures. The next generation of wide-body commercial aircraft will use monolithic carbon fibre reinforced composite laminate structures for the fuselage skins, centre wing boxes and wing skins. The Boeing 787 utilises composite materials in the construction of its fuselage, wings and horizontal & vertical stabilisers [Brosius 2007; Boeing July & November 2008]. Airbus has also designed the A350, a new wide-body aircraft with composite materials used for fuselage and wing construction. However, the main difference between the A350 and the 787 is that the A350 employs a ‘black metal’ approach, utilising the traditional method of fastening fuselage skin panels to a CFRP structural frame [Airbus A350 ‘Fuselage Production’ 2009], whereas the 787 fuselage is constructed from three one-piece barrel sections that are joined together to construct the whole fuselage [Boeing 2007]. The barrel sections of the 787 are produced by placing fibres, pre-impregnated with Toray 3900 series epoxy resin, onto a rotating mandrel before autoclave curing [Boeing 2005; dti 2006; Brosius 2007]. Filament winding and fibre placement onto a rotating mandrel are commonly used methods for the production of cylindrical tubes and pressure vessels [Bunsell & Renard 2005]. Entry into service for the 787 is expected in 2010 [Boeing 787 2009] and the A350 is expected to enter service by 2013 [Airbus January 2009], thus large commercial aircraft containing high percentages of composite structures, including fuselage skins, will soon be commonplace.

### ***2.1.2 – Typical composite aircraft structures***

Both the Boeing 777 and Airbus A330/A340 aircraft use monolithic carbon fibre reinforced epoxy laminates in the construction of their horizontal stabiliser skins [Airbus AMM 2002; Airbus SRM 2003; Ishibashi 2006; dti 2006; Brosius 2007]. The Boeing 777 is understood to use 180°C cure pre-preg materials containing Toray’s T800 [Gros et al. 1998; Toray 2001; Ishibashi 2006; Brosius 2007 ] carbon fibres, and the Airbus A340 is understood to use 180°C cure Hexcel AS4/8552 [Hexcel AS4] carbon fibre pre-preg material [see Airbus SRM 2002]. Hexcel AS4/8552 also

features heavily on the Boeing 787, although in uses such as window frames and engine nacelles [Brosius 2007].

The horizontal stabiliser (see figures 2.02 & 2.03) is open to the elements and subjected to high-speed airflow during flight. The skin structures are painted in order to protect the composite laminate from ultra-violet degradation, weathering and erosion during flight. Composite aircraft structures also need to be protected against the damaging effect of lightning strike [US DoD MIL-HDBK-17 2002], which can be achieved in several ways, including the use of metal meshes and metal tows within fibre lay-ups [Gardiner 2006; Welch 2007].

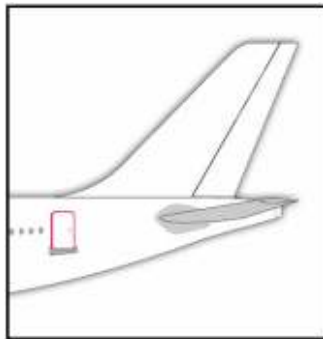


Figure 2.02 – Location of Horizontal Stabiliser  
Courtesy of Airbus



Figure 2.03 – Detail of Horizontal Stabiliser  
Courtesy of Airbus

The horizontal stabiliser of the Airbus A340 aircraft is an excellent example of such a structure [Airbus AMM 2002, Airbus SRM 2003]. A typical cross section through a horizontal stabiliser skin (figure 2.04), such as that on the A340, would consist of a carbon fibre reinforced epoxy laminate (CFRP), with the outside facing surfaces protected against lightning strike by a layer of bronze mesh. Unidirectional carbon fibre/ epoxy pre-preg tape is laid in variations of 0°, 90° & 45° orientations, with thickness varying between 17 and 33 plies.

Between the outermost (outside facing) ply of the CFRP and the bronze mesh, a thin layer of glass fibre fabric is employed to facilitate handling and production operations relating to the bronze mesh [Rouchon 2010]. The outer surface of the skin would normally be painted with primer coats and topcoat.

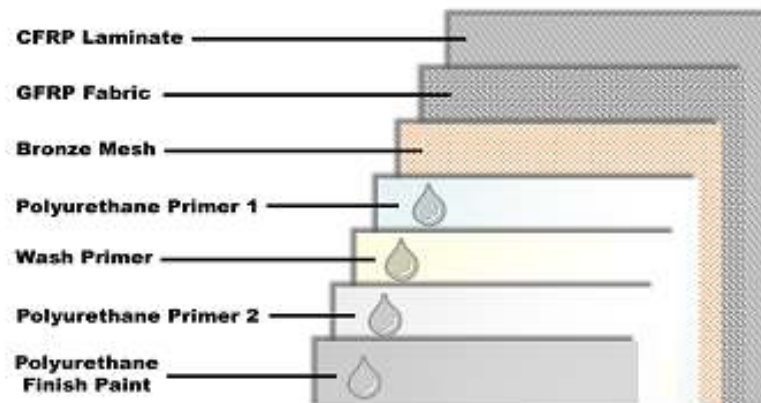


Figure 2.04 – Typical advanced composite aircraft skin structure

When viewing the painted exterior surfaces of an aircraft, one will have few (if any) visual cues as to what materials were used to construct the various structures.

### ***2.1.3 – Impact damage & failure of composite materials***

Aircraft structures may be subjected to excessive loading, environmental damage, and impact damage threats. Such occurrences may lead to structural degradation, which can in turn reduce structural performance [US DoD MIL-HDBK-17 2002].

CFRP laminates are susceptible to matrix cracking and delamination failure due to impact events [Matthews & Rawlings 1994, Campbell 2004]. Dissipation of impact energy into the laminate causes matrix cracking. During impact events, the laminate flexes under the force of the impacting object, causing inter-laminar shear forces, which cause ply separation or delamination [Bunell & Renard 2005]. Failure of the matrix material close to the surface leaves the reinforcing fibres unsupported, which renders them unable to support the transverse force imparted by the impact object, resulting in fibre breakage. Failure and crushing of the upper surface or plies results in a dent like appearance [Shyr & Pan 2003; Aktas et al. 2008]. As seen in figure 2.05 and in specimens presented by Lance & Nettles 1990, Shyr & Pan 2003 and Aktas 2008, impact damage from an object to a CFRP material will manifest itself in the form of subsurface delamination and a three-dimensional (3D) surface indentation [see also Abdallah et al. 2009]. The subsurface delamination and matrix cracking is not visible from the painted side of the laminate. Only the surface flaw is visible on the painted side.

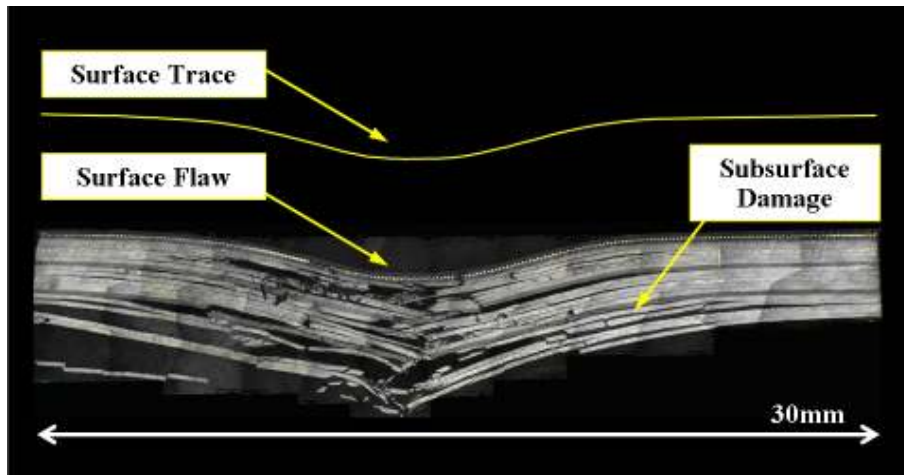


Figure 2.05 – Cross section through 30J, Ø20 mm impact to a bronze mesh incorporated, painted, 17ply AS4/8552 CFRP laminate [from Boulic 2007]

The impact indentations can be relatively small, compared to the delamination size beneath, and may exhibit little visual evidence of damage on the impacted surface [Campbell 2004; Cartié & Irving 2003; Brookes 2004, Shyr & Pan 2003; Aktas et al. 2008]. Delamination widths of between 0 and 60 mm have been observed from Ø4 mm to Ø20 mm indentations (i.e. delamination 3 times greater than indentation width) on a 7 mm laminate [Brookes 2004].

Abrate 1998 and Shyr & Pan 2003 demonstrate that for thick laminates, the propagation path of the cracking in a laminate takes the form of a triangular shape, with the upwards point at the centre of the impact site, as seen in figure 2.05. For thin laminates, the path is inverted [Abrate 1998; Shyr et al. 2003]. Examples published by Aktas illustrate that the planar shape of the delamination area depends on the fibre orientations of the plies, that the delamination is not always circular, and that the delamination extends furthest in the 0° fibre direction [Aktas 2008]. Damaged matrix material is unable support the reinforcing fibres, which subsequently buckle and fail when subjected to compressive loads in the fibre direction. Delamination and matrix cracking due to impact damage reduces the compressive strength of composite materials [Dorey 1989; Papanicolaou & Stavropoulos 1995; Mitrovic et al. 1999; Cartié & Irving 2002; Brookes 2004]. 40 mm of delamination in a 7 mm thick laminate is sufficient to cause a 50% reduction in compression after impact (CAI) strength [Brookes 2004].

### ***2.1.4 – Characterisation of impact damage to composite materials***

Much of the available literature on impact behaviour of composite materials refers to impact damage in terms of its delamination size. Part of the reason is likely to be the correlation between delamination size and CAI strength. Some authors such as Shyr & Pan 2003 and Mitrevski et al. 2006 have presented sectional photographs of impact damage, which provide only qualitative information. Where surface dent morphology is presented quantitatively, such as by Mitrevski et al., authors tend to have used dent depth as the sole metric for describing surface damage, and dent width measurements such as those given by Brookes 2004 are rare. However, recently published literature and conferences have begun to question the use of a single metric such as dent depth to describe impact damage to composite materials [CMH-17 2009, Rouchon 2009].

When observing figure 2.05, one can clearly see that the traced line of the surface indentation, or impact dent, has a complex curved shape. The dent has not only width and depth, but also a sectional profile, which requires further information in order to be fully described. To this effect, Aktas et al. 2008 appear to be the first to have published a realistic diagrammatic sectional representation of impact damage, as seen in figure 2.06, although no quantitative delamination or dent sizes are given in their results.

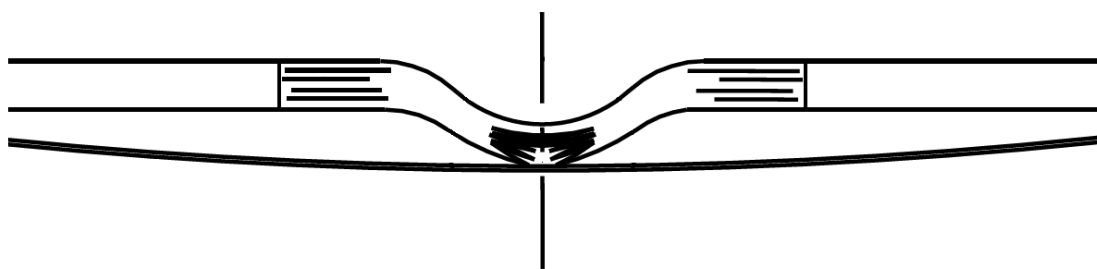


Figure 2.06 - Typical cross sectional profile of impact damage to composite laminate, From Aktas et al. 2008

### ***2.1.5 – Factors affecting impact damage morphology***

Many factors are reported to affect the impact damage extent of composite laminates. However, more relevant to this thesis are factors likely to affect the shape, or morphology of the impact dent.

**Impact force** – Instrumented impact testing of a 32ply [(45/0-45/90)<sub>4</sub>]<sub>s</sub> carbon fibre laminate by Hu et al. 2008 demonstrates predictions and demonstrations of typical force/ time curves during 7.2J impact events. The first laminate appears to fail, or crack, at between 4kN and 5kN. Subsequent laminate, or shear failures continue to occur up to forces of around 6kN, after which flexural failure of the complete specimen occurs. Impacts below a given energy threshold are unable to generate sufficient force in order to initiate first ply cracking and cause detectable damage, or dents, to the laminate. Results from Cartié & Irving, 2004 demonstrate that the energy level required to achieve the threshold force can vary from 5J to 10J depending on the laminate properties. A model is given by Davies & Zhang, whereby the square of the force required to produce matrix cracking in the first ply is “*proportional to the cube of the laminate thickness*” [Davies & Zhang 1995, in Shyr & Pan 2003]. Figure 2.07, illustrates typical damage threshold load/ laminate thickness plots for three resin/ fibre systems, in which it can be seen that higher impact forces are required in order to reach the threshold force at which damage initiation begins.

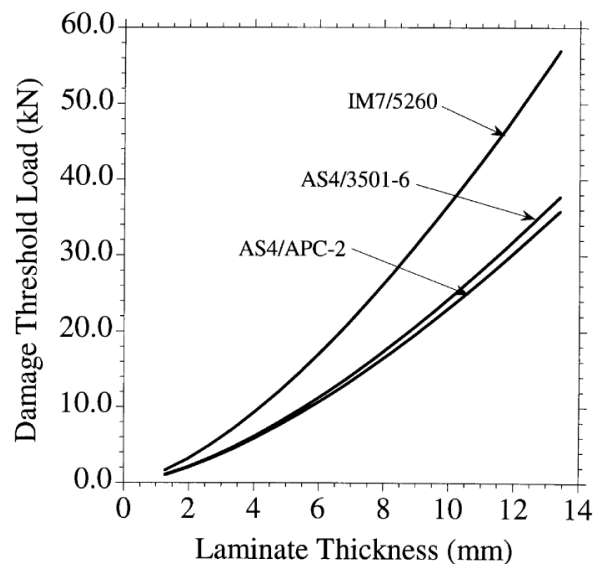


Figure 2.07 – Damage threshold vs. thickness, from Schoeppner & Abrate 2000

**Impact energy** – it is generally accepted that higher impact energies produce larger damage under the same conditions [see Robinson & Davies 1992; Papanicolaou and Stavropoulos 1995; Hounslow 2000; Cartié & Irving 2002]. Given that impact energy

is given by  $\frac{1}{2}mv^2$ , impactor mass and velocity can affect damage size. Additionally, high velocity impacts do not allow sufficient time for the laminate to flex before generating high impact forces capable of breaking and crushing the plies, thus high velocity impacts are more likely to result in penetration than surface dents [Matthews & Rawlings 1994]. However, variations of impactor mass or velocity at the same impact energy have been demonstrated to have no effect on damage size for low velocity impacts [Robinson & Davies 1992]. Davies et al. [1994] demonstrated delamination sizes of 500~900 mm<sup>2</sup> for 10J impacts and 700~1300 mm<sup>2</sup> for 30J impacts (see figure 2.08). Studies by Brookes 2004 and Cartié & Irving 2004 have also demonstrated greater delamination at higher impact energies. Dent depth is also affected by impact energy [Brookes 2004; US DoD MIL-HDBK-17 Vol. 1 2002], and Brookes demonstrated dent depths ranging from below 1 mm to greater than 6 mm across and energy range of 0~60J, with variations in dent depth for the same impact energy depending on the impactor size and the laminate thickness (see figure 2.09).

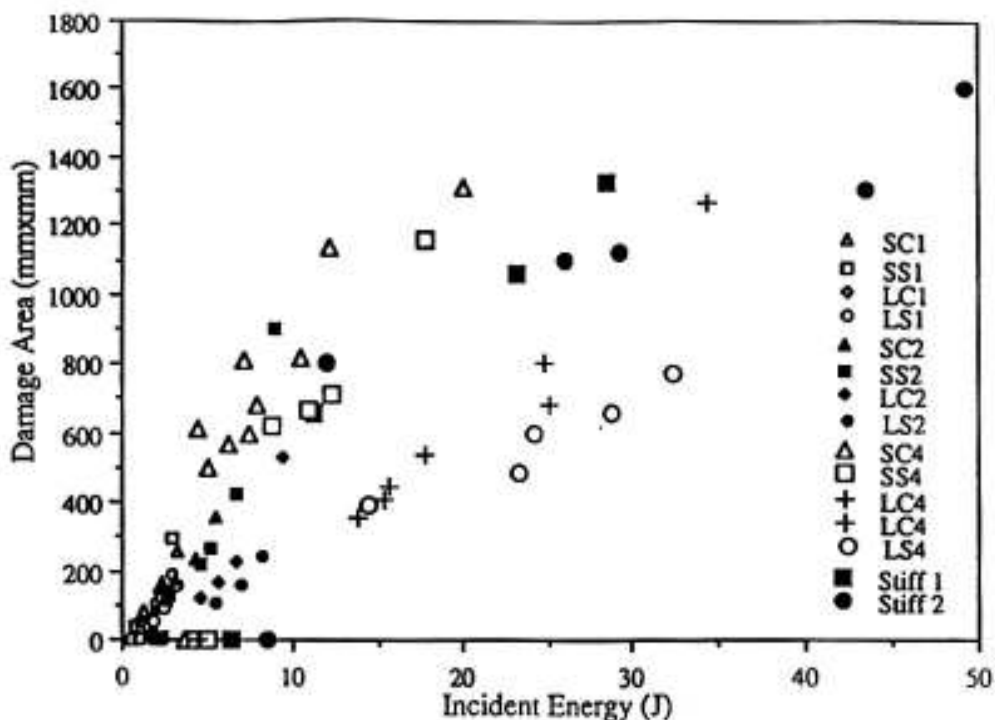


Figure 2.08 – Impact Energy/ Delamination Area plot from Davies et al. 1994

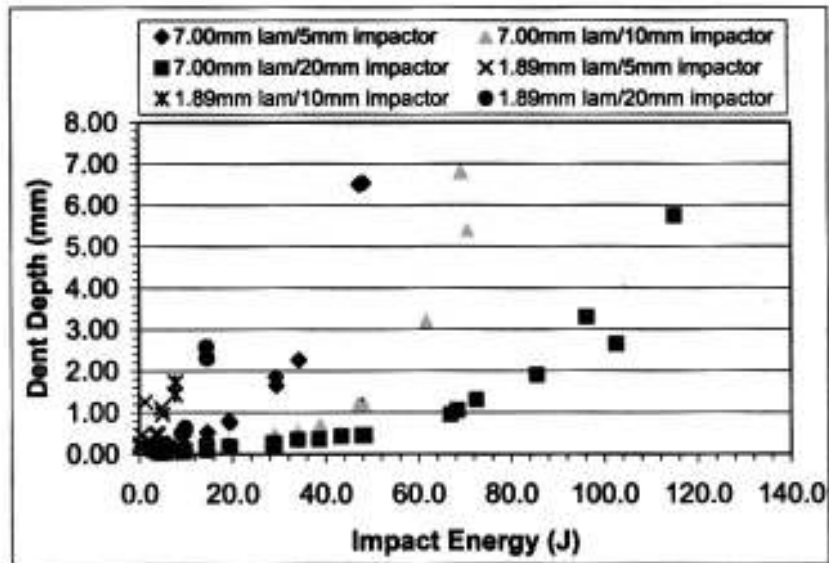


Figure 2.09 – Impact Energy/ Dent Depth plot from Brookes 2004

**Laminate thickness** – it is accepted that thin and thick laminates consisting of the same matrix & reinforcement materials have different responses to impact damage [US DoD MIL-HDBK-17 2002]. Results published in MIL-HDBK-17 demonstrate that the same impact produces delamination three times larger on a 16ply laminate than on a 10ply laminate. A long span, thin laminate (2 mm) flexes under impact load, and is susceptible to flexural and penetration failure. A short span, thick laminate is more susceptible to delamination failure [Robinson & Davies 1992; Matthews & Rawlings 1994]. Aerospace applications generally use thick (15, 30 or 60 ply) laminates [Airbus SRM 2002], and are thus more prone to delamination failures [Matthews & Rawlings 1994; Campbell 2004]. Results from Brookes 2004 show Ø20 mm impacts of over 100J producing dents around 2.5 mm deep on a 7 mm laminate, whereas less than 20J were required for the Ø20 mm impactor to produce the same dent depth on a 1.89 mm laminate. It can therefore be said that thick laminates will exhibit less indentation for the same impact conditions, although the significant delamination damage (that is not visible to the human eye) may exist beneath the indented surface.

**Ply orientations** – altering the ply orientations within a laminate can alter dent depth for the same impact conditions. Using a target dent depth of 1 mm, Lopes et al. 2009 demonstrated that for a  $[+/-45/90/0/45/0_4/-45/0_2]_s$  (baseline) laminate, the impact energy required is 24.4J versus 26.4J for  $[+/-45/0/70/-70/0/15/10/-10/-15/15/-15]_s$  and



[+/-45/80/5/20/-20/10/-80/-10/-5/15-15]<sub>s</sub> (alternative) laminates. At 40J, the impact indentation was reported as 2.6 mm for the baseline laminate and 3.0~3.2 mm for the alternative laminates. Lopes et al. report that for a given energy, the delamination sizes for the alternative laminate, containing 70°-orientated fibres, are smaller than the baseline (45° orientations) laminate, although the delamination sizes for the 80° orientation laminate were larger than baseline.

**Impactor shape** – work by Brookes 2004 and Mitrevski et al. demonstrated that impactor size and shape could alter the size of impact damage. Mitrevski et al. October 2006 studied the delamination induced by differently shaped impactors and the results show that a hemispherical object produced greater (10~15%) delamination than a conical object at the same energy. However, a later study by Mitrevski et al. November 2006 demonstrated that that a conical shape produces impact dents between five and eight times deeper than a hemispherical shape at the same energy. The work of Mitrevski et al. demonstrates that a sharp, pointed object is likely to produce a deeper indentation than a blunt shaped object at the same impact energy.

### ***2.1.6 – Impact testing of composite materials***

Mechanical testing of composite materials, especially for impact damage and compression after impact testing is a well-researched topic. It is apparent from recent conferences on composite materials that academic researchers and manufacturers are attempting to model the impact damage behaviour, crack propagation behaviour and compression after impact behaviour of advanced composite materials [CMH 17 2009]. However, when reading literature that concerns either mechanical testing, design or repair of composite materials, other fundamental issues become apparent.

**Specimen size** – Robinson & Davies 1992 demonstrated that for 6J impact energy, the impact dent produced on a Ø102 mm specimen was around 5 mm larger (wider) than on a Ø337 mm specimen of the same laminate. Although demonstrations of impact testing on structural elements, such as those of Davies et al. 1994, are available, published examples of impact damage available to an academic researcher are generally limited to small-scale test specimens [see Cartié & Irving 2002, Shyr & Pan 2003, Brookes 2004, Mitrevski et al. 2006, Aktas et al. 2008 and Hu et al. 2008]. Whilst such specimens provide basic information regarding impact damage behaviour

& characteristics for composite materials, the results from Robinson & Davies 1992 make it clear that the damage characteristics reported in much of the available literature are only applicable to small size test specimens.

Furthermore, an issue raised by Ilcewicz in 2009 is that publically available, detailed information on mechanical testing of composite materials is generally limited to testing of coupons or structural elements. Figure 2.10 illustrates how the level of information regarding testing of composite materials can be considered as a pyramid. The lower level, performed on small coupons, spans a wide range of published material, and is widely available. Mechanical testing performed on larger structural elements and complete assemblies such as the wing box tests run by NASA in 1996 & 2000 [Raju 2006] is less frequently performed, and although (sometimes) available on request to regulatory bodies such as the FAA, EASA or CAA, the results remain proprietary information and are unavailable in the public domain.

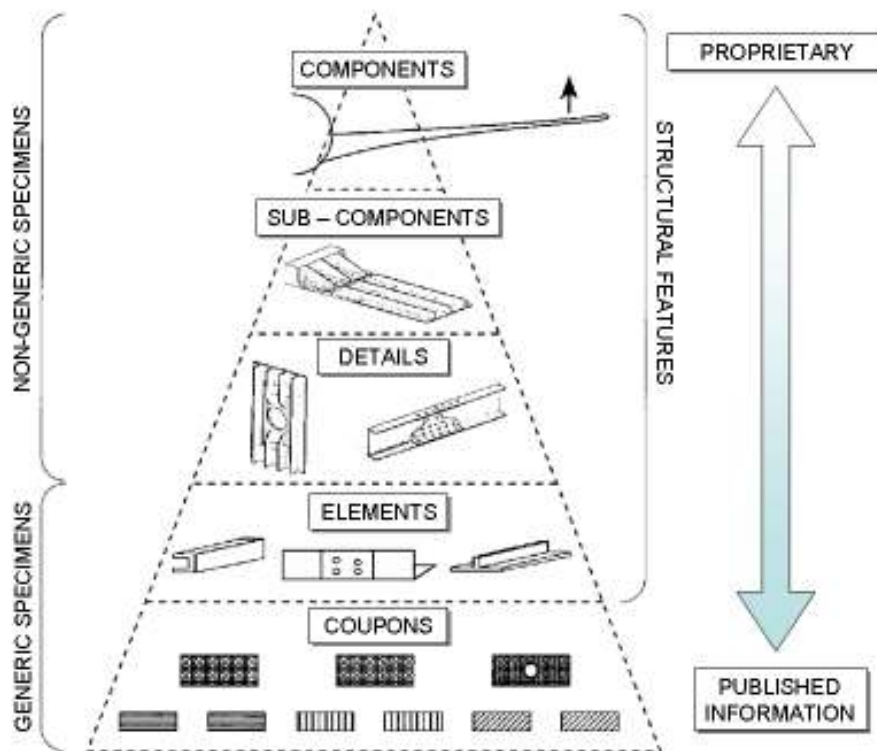


Figure 2.10 – Testing levels for composite materials, from Rouchon 1990, in US DoD MIL-HDBK-17 Vol 1 2002

**Laminate & surface finishes** – published works such as those of Robinson & Davies 1992, Davies et al., Sohn et al. 2000, Cartié & Irving 2002, Shyr & Pan 2003, Brookes 2004 and Mitrevski et al. 2006 and Aktas et al. 2008 all conducted tests on

laminates that were prepared without lightning strike protection or paint finishes. The top layers of such laminates will be visible to the eye, and matrix or fibre cracking (as seen in the work of Robison & Davies, Mitrevski or Aktas) will be clearly visible. Such laminates are not representative of those that an aircraft inspector is likely to encounter on an actual aircraft structure, and differences in appearance of impact damage on finished laminates has already been reported [Gantt 2003]. Furthermore, the phosphor bronze threads (5.5~7.0 Sn, 0.01~0.4 P, Rest Copper to ISO 9044 [Bopp 2006]) used for lightning strike protection are more ductile than carbon fibres laminates. Glass fibres have a strain to failure value of between 4.8% & 5.6% (see table 01), and phosphor bronze can exhibit up to 60% elongation over 50 mm under strain [Kalpakjian 1995 pp. 184, Table 6.6]. The lightning strike protection materials are thus more capable of deforming or stretching under impact load than carbon fibres, which have lower strain to failure values of between 1.5% and 1.8% (see table 01). The higher ductility of the materials used for lightning strike protection means that they are capable of deforming under impact as opposed to cracking, which may result in a different surface appearance to a typical impact on a non-finished laminate.

**Impactor geometry** – specifications for impact test specimens, particularly for compression after impact tests, require the use of hemispherical shaped impactors [Boeing BSS7260 1988, DIN EN 6038 1996]. However, the work of Mitrevski et al. provides a clear indication of the fact that impactor shape can alter the dent morphology of impact damage to composite materials. Aside from Mitrevski et al. Jul & Aug 2006, it is apparent that published material on the impact behaviour of composite materials is limited to impacts from hemispherical objects between Ø10 mm and Ø25 mm in size. Work currently in progress by Kim [see Kim, 2007] and EASA/ DLR [Waite, 2009] aims to move towards using larger impactors such as the Ø320 mm example reported by DLR [Waite, 2009]. The study by Kim aims to demonstrate the damage behaviour full scale composite aircraft structures subjected to vehicle damage, which are represented low velocity (0.447m/s / 1mph), high mass (500kg), blunt edge (127 mm radii) impacts. The results of the work by Kim and DLR, when published, will provide greater understanding of composite material impact-damage behaviour, under realistic damage scenarios on large, full-scale specimens. Given that larger sized impact objects are reported to produce indentations that differ to smaller sized impacts, with subsequent increased likelihood of greater

delamination with reduced indentation size (i.e. little visual evidence of significant damage), work for this thesis should consider impacts that represent the largest recommended object sizes for impact testing of laminates, as opposed to the smallest.

### **2.1.7 – Impact damage scenarios for composite aircraft structures**

Damage to aircraft can occur from a variety of sources. Impact damage is a common occurrence with aircraft structures, and around 80% of damage to composite aircraft structures is caused by impact strike [CAA 2005]. Aircraft can encounter impact damage from a variety of sources, as identified by Kolesnikov and Herbeck and illustrated in figure 2.11 [Kolesnikov & Herbeck 2005].

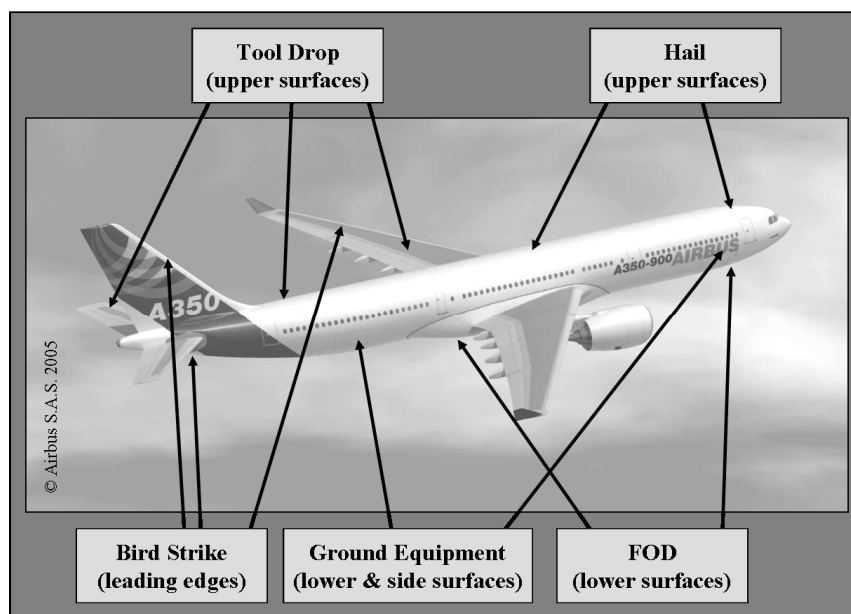


Figure 2.11 – Impact damage scenarios for aircraft in service (based on information from Kolesnikov & Herbeck 2005)

Bird strike, hail damage and foreign object debris (FOD) damage are everyday occurrences in airline operations. Bird strikes to aircraft are often noticed by the flight crew, and reported to maintenance personnel for inspection at a suitable time [Psymouli et al. 2005]. Evidence of a bird strike often presents itself in the form of bird remains. Hailstorms are known events, and once again, inspectors can be notified that an aircraft has been subjected to a hailstorm and may have been damaged [Psymouli 2005]. FOD damage, such as flying stones and tyre shreds, generally occurs in specific areas, such as around undercarriages and engine exhausts. Aircraft inspectors are known to pay particular attention to these areas [Psymouli et al. 2005]. Impacts events such as hail, bird strike and FOD are all *expected* to happen. Impact

damage from ground equipment, whilst the possibility of it occurring is acknowledged, is not *expected* to happen, although it is widely known within the airline industry (as experienced personally by the author) that ground equipment and aircraft are strangely attracted to one another.

To explain the likelihood of damage from ground equipment and aircraft, one only has to view figure 2.12, in which the ground equipment arrangements for servicing of a 787 aircraft are shown. Aircraft are often surrounded by ground handling equipment, all of which in close proximity to the aircraft, and having the potential to collide with the aircraft and cause impact damage.

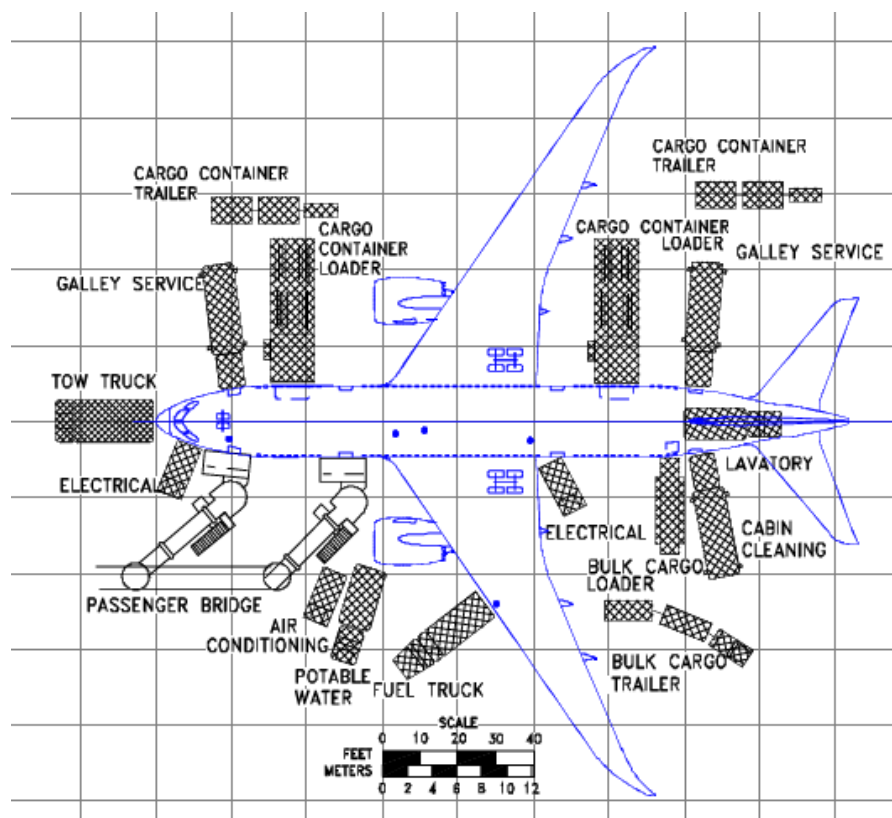
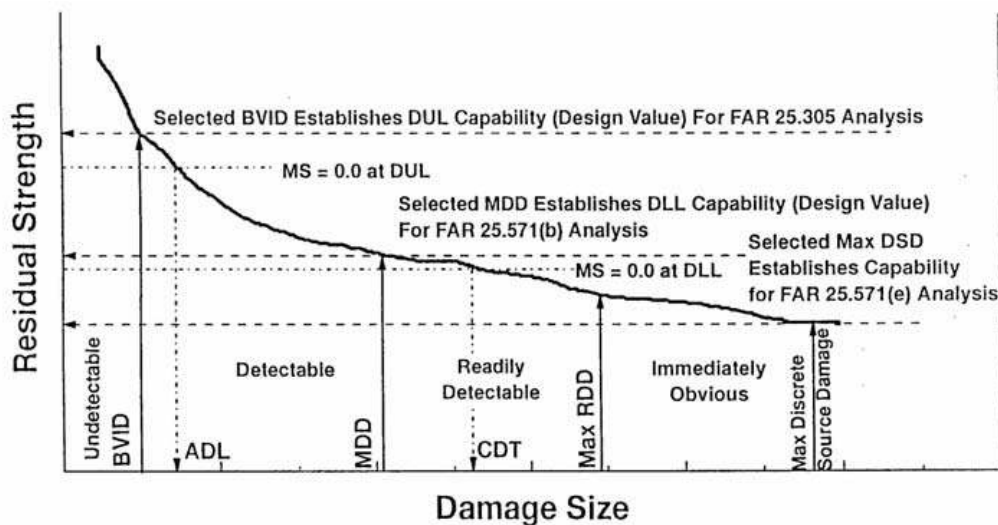


Figure 2.12 - Boeing 787 – Airplane servicing arrangement during typical turnaround [Boeing 787 Airplane Characteristics, September 2007]

### 2.1.8 – *Damage tolerance of composite aircraft structures*

Damage detectability is split into four categories: Undetectable, Detectable, Readily Detectable and Immediately Obvious, as described in figure 2.13 [US DoD MIL-HDBK-17 Vol. 3 2002]. The size of damage that falls just between undetectable and detectable is known as ‘barely visible’. Barely visible impact damage (BVID) is an important concept in the design of composite aircraft structures, as the BVID size is

used to determine design ultimate load (DUL) capability [see US DoD MIL-HDBK-17 2002, Transport Canada AC 500-009]. As previously described, damage to the matrix material will reduce the compressive load performance of a fibre-reinforced laminate. For damage below the detection threshold or BVID size, the structures must demonstrate capability to sustain design ultimate loads in both tension and compression “*without failure or excessive structural deformation*” [EASA 2008] for an indefinite period or until the structure is replaced due to cyclic or time limits [as per EASA CS-25, FAA AC-20-107A & Transport Canada AC 500-009].



- |                                    |                                |
|------------------------------------|--------------------------------|
| BVID: Barely visible impact damage | DLL: Design limit load         |
| DUL: Design ultimate load          | DSD: Discrete source damage    |
| MDD: Maximum design damage         | RDD: Readily detectable damage |
| ADL: Allowable damage limit        | MS: Margin of safety           |
| CDT: Critical damage threshold     |                                |

Figure 2.13 – Damage detection levels, from US DoD MIL-HDBK-17 2002

With regard to published BVID sizes, US regulatory materials such as MIL-HDBK-17 state an energy value of 140J as highest level of impact damage that is likely to occur to a composite aircraft structure before the damage mode progresses from above the barely visible threshold (2.54mm deep) into readily detectable (RDD) damage. [US DoD MIL-HDBK-17 2002; Rouchon 2009]. Data presented in MIL-HDBK-17 (see figure 2.13a) demonstrate that higher energy impacts are required to BVID damage on thicker laminates, and the 140J limit is intended to represent the level of energy required to produce BVID dents on the thickest of laminates. However, the impact energy at which the transition from BVID to RDD actually occurs will depend

on the impact conditions and the laminate thickness and type [see chapter 2.1.5 & MIL-HDBK-17 3F, 7.5.1.1, 7-38].

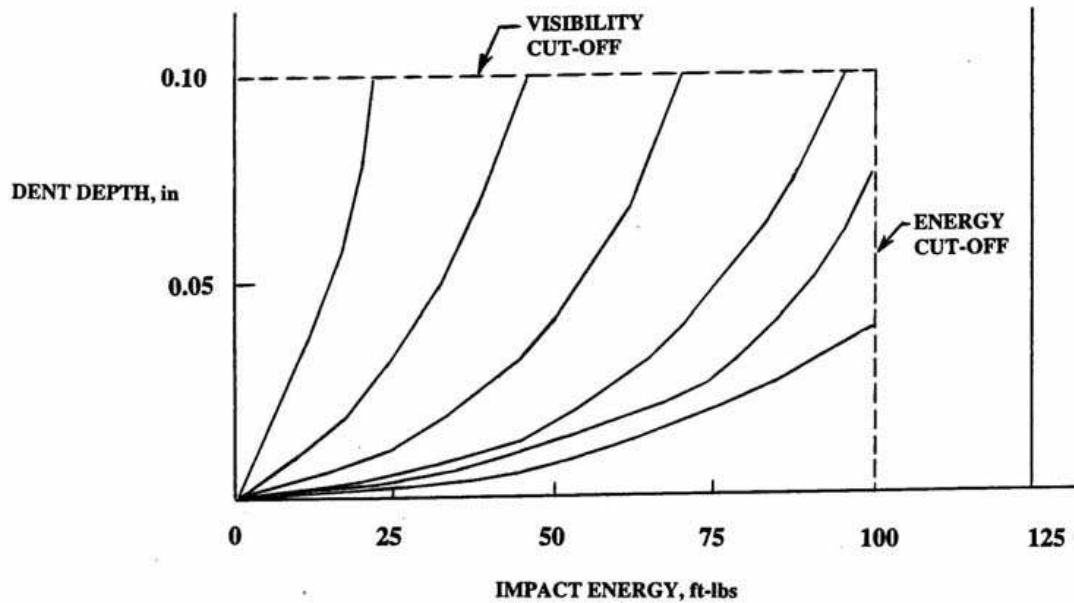


Figure 2.13a – test results demonstrating the higher energies required to produce the same dent depth, from MIL-HDBK-17 3F, 7-38 [US DoD 2002].

European material is generally limited to using a dent depth metric for defining BVID [see Rouchon 2009]. Published values for BVID vary from 2.5 mm deep (USAF), 1.25 mm deep (US Navy), 0.3 mm deep (Aerospatiale) [Forsyth et al. 1998] and 0.254 mm [Boeing 2006, in Rouchon 2009]. In order to set the size of damage tolerance size for a structure, one is required to demonstrate that the chosen damage size can be reliably detected by the chosen inspection procedure [EASA CS-25 2008; US DoD MIL-HDBK-17 2002; FAA AC-200-107A, AC 500-009].

If cyclic loading of the structure causes damage growth, inspection intervals must be set such that damage growth beyond BVID size, and thus past DUL tolerance limits, can be found before design limit load is reached with possible subsequent structural failure [US DoD MIL-HDBK-17 Vol.3 2002; EASA CS-25; FAA AC-20-107A; Transport Canada AC 500-009].

The design philosophy for composite aircraft structures is that they should demonstrate ‘no-growth’ for BVID damage up to DUL [MIL-HDBK-17 Vol. 3, FAA AC-20-107A, EASA CS-25]. Experiments by Krutop 2007 demonstrated that for a

15J impact, a threefold increase in delamination area occurs after 15000 cycles at 75% CAI strength for a 32ply CFRP laminate. However, delamination is not visible during visual inspection. Consider that a 15J impact produces a dent below BVID size. If the visual inspection reliability is based on surface dent visibility, and the dent does not grow along with delamination, the dent visibility will remain below detectability limits whilst the delamination may have grown beyond structural tolerance limits. To compound the visual detectability issue, composite materials are known to exhibit surface relaxation after impact – i.e. dent depth reduces by up to 45% with time and cyclic loading [Komorowski et al. 1993, Donckels et al. 2000]. Furthermore, increased humidity and subsequent absorption of moisture can lead to dent surface relaxation [Rouchon 2010]. Hence, other inspection methods capable of characterising sub-surface damage are available.

### ***2.1.9 – Non-Destructive Testing/ Inspection (NDT/ NDI) of composite aircraft structures***

Several methods of non-destructive testing or inspection techniques are available for detection of damage in composite materials, and a detailed review is given by Harris, B. 2003.

Human visual inspection is widely used for inspection of composite aircraft structures, and there are different levels of visual inspection. A general visual inspection (GVI) is performed within a distance of 1.2m [CAA CAP562 2005]. GVI inspections are non-directed inspections, in which the inspector will inspect all areas of the aircraft structure for signs of damage. A detailed visual inspection (DVI) is performed within 0.3m [CAA CAP562 2005]. The purpose of a DVI is to search a specific area on a structure for signs of damage. There also exists a special detailed inspection (SDI), which may be a visual inspection, in which inspectors are directed to inspect a specific structure for a specific fault or a specific type of damage. Published figures for the capability of visual inspection claim 90% probability of detection (POD), with 95% confidence for dents between 0.3 mm and 0.5 mm deep [Aerospatiale 1991, in Rouchon 2009]. Aerospatiale results cited by Forsythe et al. 1998 claimed 50% POD at 0.3 mm dent depth under ‘close’ visual inspection, i.e. within 0.3m. However, the details of the experiments performed in order to arrive at such values remain unpublished.



Non-destructive inspection (NDI) of composites can also be performed by several other mechanical methods, including tap-testing, computer aided tap testing (CATT), ultrasonic testing (C-scan), shearography, thermography and scanning acoustic microscopy (SAM). The probabilities of detection for each method were investigated by Roach in 2007, and the results are presented in figure 2.14.

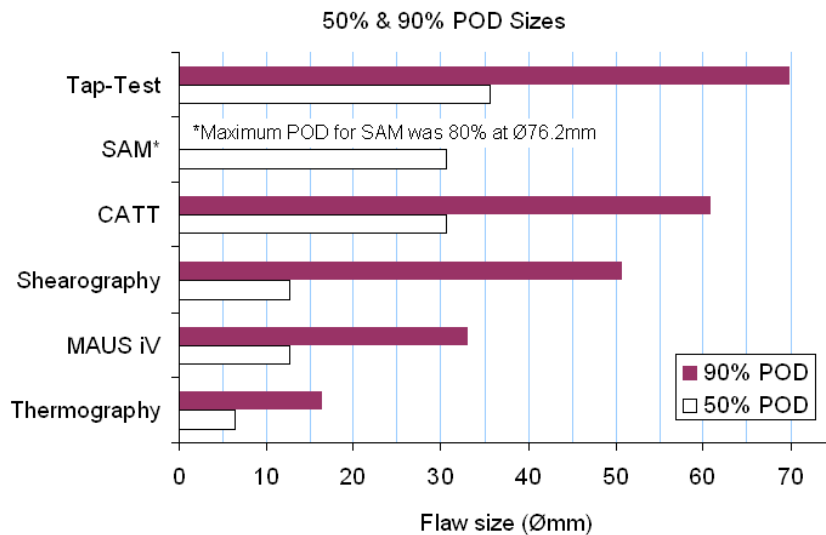


Figure 2.14 – NDT/NDI capabilities, from Roach 2007

NDT methods were also investigated by Gros et al. in 1998, and the results are presented in Figure 2.15. Gros et al. choose to describe minimum size detectable in terms of the impact energy that could be detected, as opposed to a description of the delamination size. Gros et al. did present a plot of surface flaw size (length, mm) vs. impact energy, allowing the minimum detectable impact energy and minimum detectable surface flaw size to be shown together in figure 2.15. The results of Gros et al. demonstrate that visual inspection is highly efficient at detecting small sizes of impact-damage surface flaws. However, it is important to remember that the other methods would be capable of detecting delamination damage regardless of whether a surface flaw is indentation, whereas visual inspection is reliant on the presence of a surface indentation.

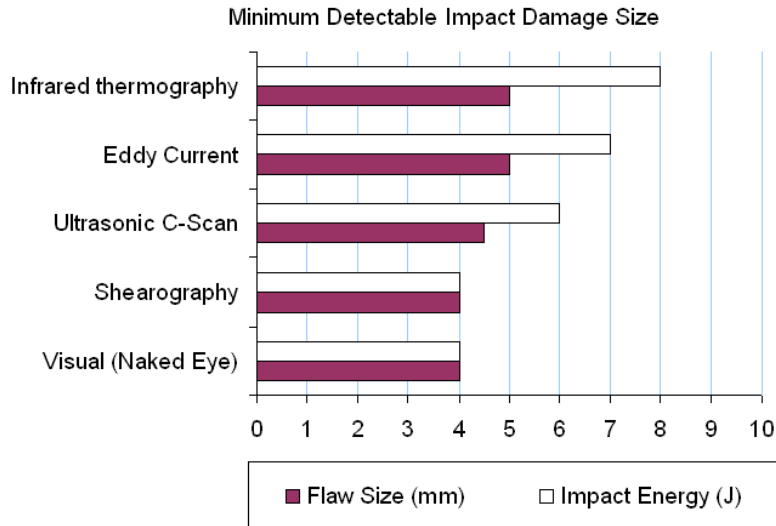


Figure 2.15 – NDT capabilities, from Gros et al. 1998

Tap testing can be used to identify areas of delamination in monolithic structures & areas of disbonded laminate in sandwich structures, is a well-known technique and can be performed using either specialist equipment or a simple round coin. Damaged laminate emits a lower frequency sound than undamaged laminate when tapped [Campbell 2004]. Inspectors are said to be accurate (within ½ inch) at estimating the size of delamination or disbonds using tap testing [RAF 2006]. The capability of tap-testing was demonstrated by Roach in 2007, and based on flaw width, the 50% probability of detection (POD) size was approximately Ø36 mm and the 90% POD size was approximately Ø70 mm. Computer aided tap testing, or CATT, is a development of tap testing, which uses a computer to analyse the frequency of sound produced by the tap, and has been demonstrated to 50% POD for Ø30.5 mm wide flaws and 90% POD for Ø61 mm flaws [Roach 2007]. Other acoustic testing procedures, such as Scanning Laser Acoustic Microscopy (SLAM) and Scanning Acoustic Microscopy (SAM) use ultrasonic waves to detect delamination and matrix cracking [see Gao & Kim 1999]. SAM has been demonstrated to 50% at a flaw size of Ø31 mm and although the system was unable to demonstrate above 80% POD (Ø3in / 76 mm) [Roach 2007].

Ultrasonic (C-Scan) scanning of composite components, using 0.5~50MHz probes is a widely employed means of characterising delamination damage to composite materials, and can determine delamination size to within 0.4~0.7 mm [see Harris, B. 2003]. Traditional C-scan techniques require a liquid coupling between the probe and

the structure being examined. Water immersion is impractical for structures that are inconvenient to remove from an aircraft, an issue that can be mitigated by using gel coupled scanning probes. Mobile ultrasonic equipment such as the Boeing MAUS-V system [Boeing MAUS-V 2009] have been developed, and Roach 2007 demonstrated a capability of 50% POD at a dent width of Ø12.7 mm and 90% POD at Ø33 mm. Recent air-coupled C-Scan equipment designs have been developed, which eliminates the need for a liquid coupling, giving greater freedom of operation [Imielinska et al. 2004].

Double pass retroreflection, or D-Sight, is an optical damage detection system that has been demonstrated as being capable of detecting impact damage between 0.152 mm and 0.256 mm deep on composite materials with between 85% and 100% POD [Forsyth et al. 1998]. The system detects surface flaws as opposed to sub-surface delamination, and requires a specular (glossy) surface, meaning that matt paint finishes must be wetted before inspection can be performed [see Forsyth et al. 1998]. Along similar lines, i.e. using analysis of the visual appearance of the laminate to identify flaws, double-pass retroreflection, moiré interferometry and laser shearography systems are also capable of visualising damage to composite structures [see Harris, B. 2003]. Roach 2007 demonstrated shearography to have 50% POD at a flaw width of Ø13 mm and 90% POD at a flaw width of Ø51 mm.

Thermography or vibrothermography [see Harris 2003] identifies damaged laminate by detection of changes in heat emission from the laminate being tested. Thermography was demonstrated to 50% POD at Ø6.35 mm and 90% POD at Ø16.51 mm [Roach 2007].

Whilst techniques such as tap test, C-Scan, D-Sight, moiré interferometry, thermography and vibrometry are all available for aircraft inspection, and undoubtedly highly effective, they all require the use of specialist equipment, which must be set up and operated by qualified personnel. The aforementioned techniques are all useful for *characterising* damage, but to use them to scan an entire aircraft in order to *detect* damage would be time consuming due to the relatively small working area offered by these techniques. To reduce aircraft downtime, the use of NDI/NDT may be rationalised to inspections of structures suspected of being damaged, or to inspection

of structures as directed by maintenance manuals, service bulletins or airworthiness directives. Visual inspection can be performed relatively quickly over large areas, thus lending itself to scanning larger sections of aircraft structure for suspected areas of damage. The results of Gros et al. show that visual inspection is also capable of detecting small (4 mm/ 4J) impact damage flaws, although minimum the size that can ever be detected, and the size of damage that can be reliably detected are not necessarily one and the same. Once damage is suspected, the other available NDT/NDI techniques can then be implemented. Visual inspection acts as guidance for effective and time-efficient deployment of more detailed NDT/ NDI procedures.

## ***2.2 – Visual Inspection***

Visual inspection accounts for between 80% and 99% of aircraft inspection activities [CAA CAP716 2003], and is the first line of damage detection for composite materials [Armstrong et al. 2005; Psymouli et al. 2005].

Instructions for performing a visual inspection are generally found in proprietary training documents, such as an aircraft maintenance manual [see Airbus A340 SRM; Airbus A340 AMM], or within regulatory guidance material [see CAA CAP716 2003]. The CAA, in Appendix O of CAP 716, cite the FAA’s description of visual inspection as being “*the process of using the eye, alone in conjunction with various aids, as the sensing mechanism from which judgements may be made about the condition of a unit to be inspected*” [CAA CAP716 Appendix O p1.].

The statement “*using the eye alone*” is of key importance. The only ‘equipment’ used in visual inspection is the inspector’s eyes. Reliability of visual inspection cannot be considered in the same manner as other NDT techniques, such as tap testing, C-Scan, Thermography or Inferometry, which require the use of probes and display screens in order to make the flaws visible to the inspector. The effects of procedural deviations such as probe lift off, or failure to use probe guides, as demonstrated by Murgatroyd et al. 1993 are not applicable factors in visual inspection.

Experiments by Spencer, 1996a & Spencer, 1996b indicated that the visual search method of the inspector, i.e. how the inspector’s eye scans for defects, varies from inspector to inspector. The results of Spencer’s study also imply that experience in an

aviation inspection environment and expectation of where to find defects are positively correlated to visual inspection performance. However, Spencer does also report that inspectors using their expectancy to search specific areas tended to look only in the area defects were expected, rather than searching, or scanning the entire structure.

Following on from the work of Spencer in 1996, Asada et al. 1998 published the findings of a study into in-service visual inspection of metallic structures. Asada et al. also found that directed inspections, i.e. inspecting with expectancy to find flaws, resulted in 75% of cracks shorter than 1 inch (25.4 mm) being found compared to less than 50% of cracks less than 1 inch in length being found by undirected inspections. Asada et al. state that for around 90% of the 1054 cracks detected, the inspectors had prior information concerning the crack characteristics, thus highlighting how visual inspection reliability can be improved by inspectors knowing what to look for. The probability-of-detection (POD) curves presented by Asada et al. also indicate that visual inspection reliability is affected by:

- Surface condition – dirty surfaces resulted in lower POD than clean surfaces
- Inspection distance – inspection from greater than 0.5m gave lower POD than inspection from within 0.5m
- Surface finish – for cracks between 0.5 inch (13 mm) and 3.5 inch (90 mm), the POD is lower on unfinished structures than on primer coated or topcoat finished structures

Whilst the results of Spencer and Asada et al. provide valuable information on factors affecting the visual inspection process, (Spencer's experiment also includes inspection of tie clips on wiring looms), the studies were limited to inspection on 'metallic' aircraft. The results of studies of visual inspection performed on sections of composite material aircraft structures have been published [Erhart et al. 2004; Gant 2007].

Erhart et al. 2004 performed a visual inspection experiment using sections of composite structure provided by an airline from an in-service aircraft. The results from Erhart et al. identified that flaws below 0.025 inches (0.64 mm) deep were visible to less than 80% of participants. For flaws below 0.025 inches (0.64 mm) deep,

detections were increased for the specimen illuminated by a lamp, compared to the specimen illuminated only by ambient daylight. However, for flaw sizes greater than 0.035inch (0.89 mm) the effect of illumination on detection performance was less marked. The results show differences of up to 57% between detections on a top surface and a bottom surface. No differences in detection rates were reported for clean or dirty areas. The results of Erhart et al. demonstrate that detection of flaws can be affected by the available lighting, which may depend on the presence of illumination devices or the position of the inspection surface with regard to the available light. Gant, 2007 performed an assessment of visual inspection using GFRP/ foam sandwich structures. The specimens represented wing sections of a Cirrus SR22 aircraft. The specimens were impacted with a hemispherical tipped Ø25.4 mm steel tube, in common with aforementioned impact testing procedures. The damage ranged from 20J to 30J, resulting in flaws between 0.18 mm & 7.54 mm deep and 232 mm<sup>2</sup> & 6087 mm<sup>2</sup> in planar area. The results published by Gant show that greater numbers of detections were obtained from filler painted surfaces than top-coat painted surfaces. This was likely due to surface breaking cracks in the filler paint at the impact site providing greater visual cues as to the presence of impact damage. Similar to the Erhart study, Gant’s results also show more flaws detected on upper wing skins than on lower wing skins, again demonstrating a negative effect on detection rates due to inspection in an under-wing or under-belly scenario. The results obtained by Gant using the upper wing specimens, for all surface finishes are plotted below in figures 2.16 and 2.17:

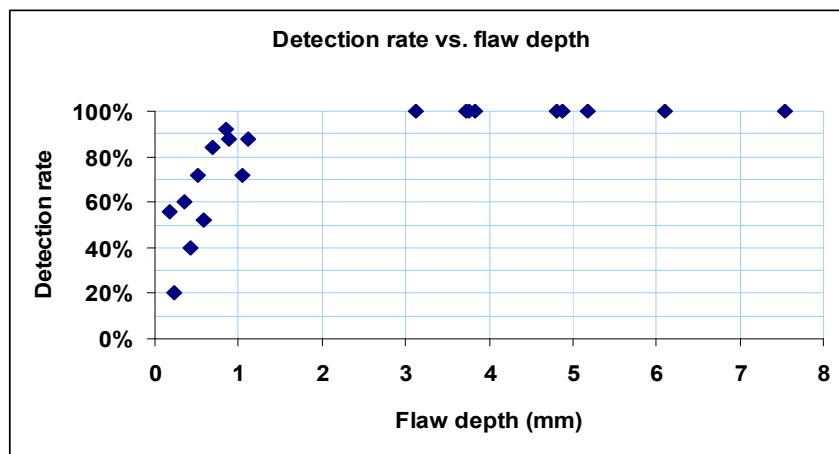


Figure 2.16 – Plot of detection rate vs. flaw depths from Gant 2007

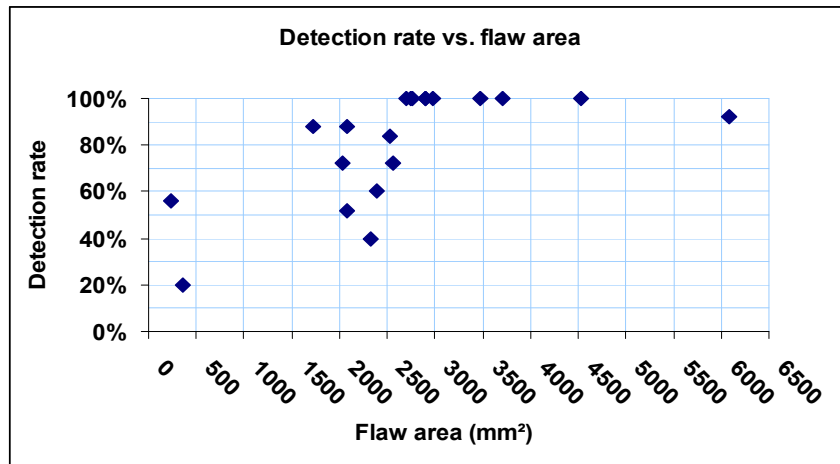


Figure 2.17 – Plot of detection rate vs. flaw areas from Gant 2007

It is important to note that the data presented in figures 2.16 and 2.17 were obtained by Gant from visual inspection of impact damage from several 20J & 30J impacts on laminates with differing ply orientations, stacking sequences, and surface finishes. However, despite the variance in flaw/ specimen characteristics, increases in detection rates accompany increases in flaw depths, with detection rates increasing from ~20% up to 100% for flaw depths below 3 mm. The relationship between flaw area and detection rates is less well defined, and there is considerable variation in the detection rates obtained for flaws of areal size between 1000 mm<sup>2</sup> and 2500 mm<sup>2</sup>. It is also evident that the flaw with the widest areal size (~6000 mm<sup>2</sup>) gave lower detection rates than flaws with lower areal sizes (3000 mm<sup>2</sup>~4500 mm<sup>2</sup>). It is thus clear from the results of Gant that whilst detection rates may increase with increasing flaw depth, the relationship between detection rates and areal size, and hence flaw width, is less distinct.

The works of Erhart et al. and Gant were rudimentary investigations into visual inspection of composite materials. Many of the recommendations concerning specimen numbers, inspection process control and protocols for NDT reliability assessment experiments, which will be presented later, were not implemented by either author. Erhart et al. allowed participants to touch the panels during inspection, meaning that the inspection was no longer a ‘visual’ inspection and had in fact become a ‘tactile’ inspection. The study by Gant used very limited flaw numbers, and a small range of flaw sizes. Furthermore, the flaws were spread across various different laminates and finishes, making it impossible to compare detectability of

similarly sized flaws on different finishes and laminates. However, between them, Erhart et al. and Gant demonstrated that:

- poor luminance levels had a negative effect on detectability of impact damage on composite materials
- some inspectors found a flashlight beneficial whilst others did not
- viewing angle affected detectability
- surface finish affected visual inspection reliability
- impact damage dent detectability increased with increasing dent depth
- detectability did not necessarily increase for larger values of dent width (or dent area)

In 1979, Megaw published a comprehensive list of factors liable to affect the reliability, or accuracy of the visual inspection process, and listed published experiments that had been performed to demonstrate them [Megaw, 1979]. Megaw placed the factors into 4 categories – subject, physical & environmental, task, and organisational factors. From Megaw’s paper, one concludes that a large proportion of the research into visual inspection prior to 1979 was concerned with actually ‘detecting’ flaws or defects. This continues after 1979 with publications on eye movements [Megaw & Richardson 1979], scanning/ search strategies [Megaw & Richardson 1979], task complexity [Gallwey & Drury, 1986] and lighting [Cayless 1983].

Megaw & Richardson 1979 found that there was little correlation between task complexity and inspection time for visual inspection. Eye fixations were found to be shorter for tasks involving inspection of objects that had no defined fixation points, such as large sheets of material. Megaw & Richardson also proposed that peripheral vision is an important aspect of visual inspection of large sheet surfaces. Gallwey & Drury, 1986 found that adding more ‘types’ of fault, or flaw, to a visual inspection task reduced visual search performance. The results obtained from faults placed in set regions and results obtained from faults placed indiscriminately all over the inspection object revealed little effect on visual inspection performance due to flaw location.

Coupled with NTSB findings in 1989 that human factors contributed to a mid-air decompression of an airliner [NTSB/AAR-89/03], aircraft inspection research efforts



of the 1990's shifts towards research on factors that affect the 'human' performing the inspection. In 1989, Drury described the visual inspection task for airframe inspection, splitting it into 7 'tasks'; Initiate, Access, Search, Decision Making, Respond, Repair and Buy-back Inspect [Drury 1989]. Drury classes the act of actually 'searching' the unit, or structure, for defects as the third task within the sequence of events [Drury 1989]. Although he was not the first to break down the inspection task in such a way [see Colquhoun 1964, in Megaw 1979], published works on visual inspection *prior* to Drury's generic task description of visual inspection appear to have concentrated mainly on the visual 'search'.

Research on aircraft inspection reliability conducted after Drury's generic task description in 1989 begins to study the whole process, from being directed to, and gaining access to the task, through to factors affecting judgement on whether a defective structure requires repair or further NDT/ NDI to better determine the structure's condition (as per CAP 716 Appendix O p1.). Drury and Lock studied aircraft inspection reliability in both the United States and the United Kingdom, and studied not only the inspection procedures themselves, but also how the inspectors were trained, inspection personnel/ supervisory relationships and inspection environments [Drury & Lock 1995]. Other examples are works by Murgatroyd et al. and Lock, which, following on from the work of Megaw in 1979 describe how the performance of aircraft inspectors can be reduced by a variety of factors, including poor accessibility, lack of procedural compliance [Murgatroyd et al. 1995], noise and lighting [Lock 1998]. Training and prior knowledge/ experience were identified as factors that affect an inspector's visual search strategy during visual inspection [see Drury 1993], and training was shown to improve visual inspection search strategy by Gramopadhye et al., 1997. In the same study by Gramopadhye, training and feedback were also shown to be beneficial to the 'decision' task that follows the 'search' task [Gramopadhye et al. 1997]. However, the person performing a visual inspection and the person performing further, more detailed NDT/ NDI or repair may not be one and the same [Drury & Lock 1995]. In such instances, the visual inspector may need to request further NDT/NDI or repair by more qualified personnel. It is proven that inspectors can be trained to recognise defects [Gramopadhye et al. 1997], and inspectors may well call out *all* suspected defects for further inspection or repair.

It is important to remember at this point, that if the visual ‘search’ fails to find defects, because the inspector fails to detect them, the visual inspection sequence cannot progress to a ‘decision’. Inspectors cannot be encouraged to recognise, or call out a defect as requiring further NDT or repair if they cannot actually see it in the first place. This helps further explain the difference between works on aircraft inspection published prior to Megaw’s paper and those published after Drury’s 1989 paper. After the 1970s, authors of visual inspection literature switch from assuming that all cracks can be made visible and recommending improvements that will make cracks more visible, to acknowledging that not all cracks will be detected, and recommending how the number of missed cracks can be reduced. This observation is also made by Hagemaiier 1998 & Georgiou 2006 & Georgiou 2007, whom both acknowledge that early experiments (pre 1970) had previously asked the question “*how small a crack can be detected?*” and later experiments (post 1970) ask “*how large a crack can be missed?*” [Hagemaiier 1998; Georgiou 2006 & Georgiou 2007] (Reliability assessments are discussed separately in this chapter).

The distinction between detection and decision is of paramount to this thesis. Signal detection theory (SDT) [see Wickens 2000] is commonly associated with aviation inspection reliability. Many of the publications referred to in previous paragraphs concern factors affecting inspector bias towards calling out flaw ‘signals’ as defects (hit), rejecting detected flaw ‘signals’ as not being defects or simply failing to call out detected ‘signals’ (miss) or incorrectly calling out the presence of ‘signals’ or defects when no flaw is actually present (false call). However, signal detection theory relates to the ‘decision’ step of inspection, i.e. the next step after the eye actually detects a ‘signal’. SDT is particularly relevant to flaws similar in size to surrounding noise items not requiring call outs. In visual inspection for impact damage dents, the decision outcome depends on the inspector’s ability to distinguish detected signals as being from a dent, rather than something similar in appearance such as a paint chip or dirt. Signal detection theory is used to determine whether inspectors are simply calling out every detected signal, whether from dents, paint chips or dirt, as defects, or judging very few of the ‘signals’ to actually be dents, and only calling out some signals as dents. For this thesis, the ability of observers to *detect* dent signals, not their *decision* on whether or not the signal comes from a dent, is under investigation; therefore, signal detection theory shall not be pursued further.

A fundamental issue is apparent in all but the most recent of studies on visual inspection [Psymouli et al. 2005, Erhart et al. 2004; Gant 2007]. Within literature concerning visual inspection in aviation circles, it is apparent that the word ‘defect’ or ‘flaw’ was synonymous with the word ‘crack’, likely due to most of the published work having been performed during an era when the aircraft in service were constructed predominantly from metallic structures. This thesis is concerned with the visual inspection of composite aircraft structures, which, as previously discussed, do not necessarily exhibit surface breaking cracks when impacted. Impact damage to a composite material is three-dimensional in shape, whereas cracks in metallic structures are effectively two-dimensional. Hence, much of the work on actually *detecting* ‘defects’ or ‘flaws’ in aerospace structures using visual inspection is relevant only to the inspection for cracks in metallic structures. The detection of 3D surface flaws is influenced by far more complex visual perception issues.

### ***2.3 – Visual perception and visual inspection***

When observing an object, as in visual inspection, the human eye sees nothing more than patterns of light [Todd 2004]. The patterns of light, or depth cues, produced by 3D objects or surfaces are projected onto the retina within the human eye [Gibson 1950a]. Three-dimensional information about an object is reconstructed from a two-dimensional retinal image [Gibson 1950a; Tsutsui et al. 2005]. Theories on visual perception, and how the human brain develops a three-dimensional representation from two-dimensional images, began to emerge in the 19<sup>th</sup> century (see Gordon 1989 for a review of significant theories), and research on visual perception continues into the 21<sup>st</sup> century [Sakata et al. 2003; Todd 2004; Tsutsui et al. 2005; Wexler & van Boxtel 2005; Kingdom 2008]. Gibson, 1950a & Gibson, 1979 discusses depth cues in great detail, and it is also convenient at this point to quote Kingdom, who advises that patterns of light, or depth cues, can be created by areas of shadow and shading, light sources, reflections of light sources (highlights) or reflections of the surrounding environment (specular reflections) [Kingdom, 2008].

#### ***2.3.1 – Shadow & Shading***

Before continuing, shading must first be distinguished from shadow: “*A shadow results from occlusion of a light source, while shading...results from a change in*

*angle of the surface normal with respect to the direction of illumination*” [Kingdom 2008]. Both, however, are dependent on the lighting conditions.

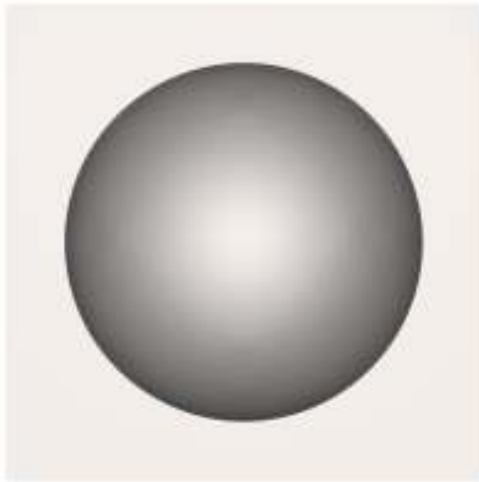


Figure 2.18 – Shading cues

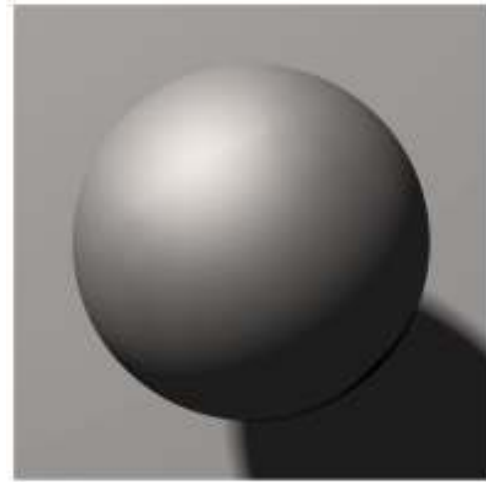


Figure 2.19 – Shading *and* shadow cues

Figure 2.18 illustrates a sphere depicted by shading alone. A point made clear by Gibson [Gibson 1950a] is that the observer of figure 2.18 will be aware that the shape is spherical, but the absence of shadow could lead to a perception of either a convex or a concave spherical shape. Figure 2.19, on the other hand, depicts a shape that exhibits shadow both on its own surface and on the base on which it sits (lower right corner). In both images, the shape provides a circular occlusion, leading us to assume that the shape is spherical [see Gibson 1950a]. In figure 2.19, the sphere blocks out the light passing over it, resulting in a darkened side, and casts a shadow across the ground. Without the shadow cue, one could not be sure that the shape in the image is definitely a sphere sitting on a surface. Both figure 2.18 and 2.19 are of the same scene, the only difference being that in figure 2.18 the lighting is directed directly downwards from the centre of the page, and in figure 2.19 the lighting is directed from 45° above, and 45° to the left side of the object. The effect of lighting direction on shading and shadow cues is thus shown.

Gibson [Gibson 1950a pp. 91-100] points out that in conjunction with contour and silhouette information, the shading on an object’s surface makes it appear “*object-like*”. In the same section, Gibson provides a useful explanation of gradients of shading by stating that where two shaded regions are observed, “*If the transition from light to shade is gradual the shape is a curve; if the transition is sudden, the shape will be a corner*” [Gibson 1950a pp96]. Gradients in shading caused by shadow may also be referred to as ‘penumbra’; “*the partially shaded outer region of the shadow*

*cast by an opaque object*”, whilst “*the fully shaded inner region of a shadow cast by an opaque object*” may be referred to as ‘umbra’ [Oxford Dictionary 2005].

From Gibson’s work, it is clear that shading, penumbra and shadows (umbra) provide both depth information about a scene or object, and provides the eye with information about the actual shape of an object. This is represented to good effect in figure 2.20, which illustrates a set of shapes that exhibit different shading gradients, from which a perception of their shape can be made. The gentle change from light to dark across the sphere is distinguishable as a large diameter sphere, compared to the changes in shading observed along the smaller radius edge running around the top of the hexagon, which take place within a shorter distance.

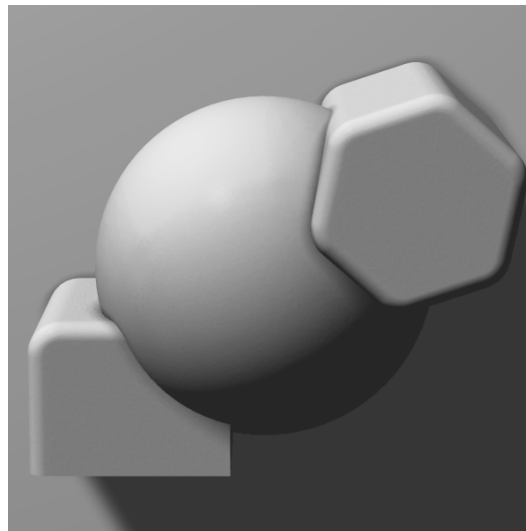


Figure 2.20 – Shading (penumbra) and shadow (umbra) cues from differently shaped objects.

Experiments have shown that humans *can* extract depth information, and perceive depth solely from shading cues [Erens et al 1993; Norman et al. 1995, 2004 & 2006]. However, it is not easy to do so [Erens et al. 1993], and experiments have shown that there is variation in different observer’s judgments of depth when presented with shading cues alone [Norman et al. 2004]. From the texts available, it is clear that whilst shading is a powerful cue to 3D perception, it can only provide limited 3D information.

The shading of an object will change as the direction of the lighting on the object changes [Todd et al 1996]. The human perception of shading can be influenced by lighting direction [Erens et al. 1993], as experimentally determined by Todd et al. in

1996. Thus, an aircraft inspector may perceive a structure differently when it is illuminated from different lighting directions.

### **2.3.2 – Lighting**

Megaw 1979 cites lighting (an environmental factor) as a key factor in visual inspection reliability. Megaw reviewed research on lighting for visual inspection purposes and identified that previous studies tended to concentrate on lighting levels and that whilst works such as Dekoker & Frier 1969 had investigated the qualitative aspects of lighting; further research was required on lighting quality [Megaw 1979].

Reading Dekoker & Frier 1969, Faulkner & Murphy 1973, De Boer 1977 and Cayless & Marsden 1983, one can conclude that the optimum design for visual inspection lighting is task dependent. However, whilst some of the studies investigate the inspection of three-dimensional surface flaws, such as sheet metal flaws [Dekoker & Frier 1969], defects in woven cloths or scratches in plastic sheets [Faulkner & Murphy 1973] none of the works considers the inspection of 3D dents on a surface.

In his 1998 paper, Lloyd refers to another work [Lloyd & He 1998] in which it was determined that defect topography of dents or flaws in painted automobile class-A surfaces can be characterised quite simply by their “*specular highlight area and modulation*”. Drury in 2000 helps define Lloyd’s ‘modulation’ as the contrast between the defect and the background surface [Drury 2000, p50]. Lloyd found that lighting effects that would enhance the visibility of specular highlights and increase defect-background contrast are generally considered as ‘glare’ in other types of visual inspection task, but are actually highly beneficial to visual inspection of surface defects on painted surfaces [Lloyd 1998]. Although he does not give any examples of how to achieve the desired effect, Lloyd recommends that for visual inspection of painted surfaces, the “*illuminance levels should be minimised*” and the lighting environment should be “*rich in light source edges*” [Lloyd 1998]. Given that the task studied by Lloyd is similar in nature to visual inspection of an aircraft structure, particularly fuselage or wing skins, it follows that Lloyd’s recommendations are also valid for inspection of aircraft structures.

The issue of specular highlights and lighting in visual inspection receives further interest in 2002 and again 2006. Brombach et al. 2006 found that whilst specular reflections aid the detection of 3D flaws, the lighting conditions that produce such reflections (directional lighting) can also cause glare, and thus recommended that both diffuse (non-directional lighting) and directional lighting be employed for visual inspection tasks [Brombach et al. 2006]. A significant finding of the study by Brombach et al. is the fact that different lighting conditions suited different surface finishes. Visual inspection of a brushed finish was found to give better results with a directional light source, whereas the same lighting conditions produced glare, and thus a detrimental effect on visual inspection of a vibratory polished finish [Brombach et al. 2006]. The findings of Brombach et al. are undoubtedly beneficial to visual inspection of metallic finishing operations. However, these recommendations are specific to a task that has different requirements to visual inspection of large surfaces for dents. Whilst they may seem contradictory to the findings of Brombach et al., the lighting scenarios suggested by Lloyd 1998 to enhance perception of specular reflections, and changes in them, are thus more likely to aid perception of 3D dents on aircraft wing or fuselage skins.

Aluze et al. 2002 developed a vision system that analysed deformations or distortions in specular reflections and surface contour information obtained from specular highlights in order to identify flaws in perfume bottle tops, which have a highly reflective, or specular, finish. The equipment developed by Aluze et al. used a lighting system consisting of a set of backlit, sliding slats. As the slats slid across each other, a series of illuminated bands were projected onto the inspection specimen. The movement of the slats caused the width of the illuminated bands to change. The use of a moving light source has links to theories of human visual perception and motion parallax, which follow later in this chapter.

The effects of changing lighting direction on the visual perception process, and the increase in shading and shadow cue saliency afforded by directional lighting shining across a surface are demonstrated by Todd et al, 1996. Furthermore, whilst inspection of other subjects may have attempted to avoid such conditions, visual inspection, and detection performance, of 3D defects may benefit from lighting conditions that produce, or enhance the visibility of specular highlights & specular reflections.

### 2.3.3 – *Specular Highlights*

Specular highlights are best described as the regions of high light level intensity [Norman et al. 2004], usually observed on shiny surfaces. Glossy surfaces exhibit small, intense specular highlights, whereas less glossy surfaces exhibit less intense, diffuse highlights [see Norman et al. 2004]. As an example of specular highlights, figure 2.21 illustrates a shape that has been given a matt, diffuse finish and figure 2.22 illustrates the same shape in a glossy, specular finish.

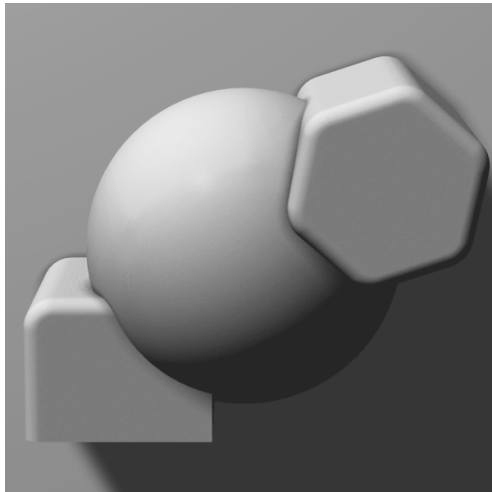


Figure 2.21 – Matt, diffuse finish

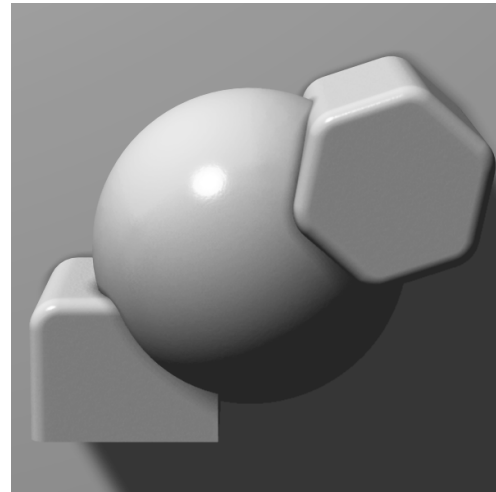


Figure 2.22 – Gloss, specular finish

It will be noted that the shading exhibited by the object in figure 2.21 is the same as that in figure 2.22. However, the presence of specular highlights in figure 2.22 leads to a perception of a shinier surface, and help identify rounded edges, such as those on the edge of the hexagon shape. Specular highlights such as these are understood to be effective, salient cues for the perception of 3D shape [see Norman et al. 2004, Todd 2004 and Kingdom 2008].

The subject of visual perception of specular highlights has received specific scientific interest, notably from Norman and Todd. It is noteworthy that much of their work was published in the late 1990s and researchers continue attempts to develop models of human visual perception for use in machine vision systems. In experiments on shape perception, Norman et al. found that depth discrimination was at its best when the participants were presented with specimens that exhibited specular highlights [Norman et al. 2004], thus re-iterating their importance to visual perception. Todd, in 2004 discusses the deformations in specular highlights that occur as an object is viewed in motion, i.e. due to head movements when viewing. As late as 2004, Todd



feels the need to state that, contrary to wide held belief, the presence of and deformations in specular highlights should not be considered as detrimental glare, but as being beneficial to perception of 3D shape [Todd 2004]. Furthermore, Lloyd has identified, and demonstrated, a positive correlation between the saliency of specular highlights and the area (size) of the highlights [Lloyd 1998].

From the literature available, one is led to conclude that specular highlights are compelling and salient cues for accurate visual perception of 3D shape, although some previous visual inspection researchers may have regarded them as 'glare' and thus recommended the use of lighting that diminishes the saliency of specular highlights, rather than increasing their saliency.

#### ***2.3.4 – Specular Reflections***

Specular reflections are the mirror like reflections observed on the surface of objects, particularly those with shiny or glossy surfaces. Glossy (specular) surfaces reflect light with little distortion, and so produce clear, mirror like reflections of their surrounding environments. Matt (diffuse) surfaces spread the reflections of light from surrounding environment. The clarity of specular reflections is dependent on the surface finish. Clean, glossy surfaces will exhibit specular, almost mirror like reflections, whereas reflections on dusty, satin or matt finish (diffuse) surfaces will vary from faint & blurry to none [Norman et al. 2004].

The use of deformations in specular reflections to identify surface dents was successfully demonstrated in 1981 [Lippincott & Stark 1981]. By using a video system to detect deformations of a projected grid pattern, Lippincott & Stark were able to detect 0.053 mm deep flaws, within 1% of the viewed field on a specular metal surface [Lippincott & Stark 1981]. The use of a grid, or geometrical, pattern in this experiment that is the key factor; both machine and human can easily recognise deformations of a shape with known, and simple geometry such as a grid. The difference being that the machine is limited to using a grid of known dimensions, whereas the human eye can determine shape changes from specular reflections of a far greater range of objects, the size of which may not be known.

In figure 2.23, a highly specular sphere is illustrated in a scene surrounded by a brick wall. The lines of the brick wall appear as specular reflections on the surface of the sphere. A small indentation on the surface of the sphere is visible, and in this region, the mortar lines of the brick wall become distorted. Figure 2.24 illustrates how the sphere would appear without a surface dent, with the brick and mortar lines appearing undistorted. Figure 2.25 illustrates the distortions that take place due to the presence of the surface dent. The altering surface slant and tilt in the dented region causes light to be reflected in different directions, thus distorting the reflections of the mortar lines.

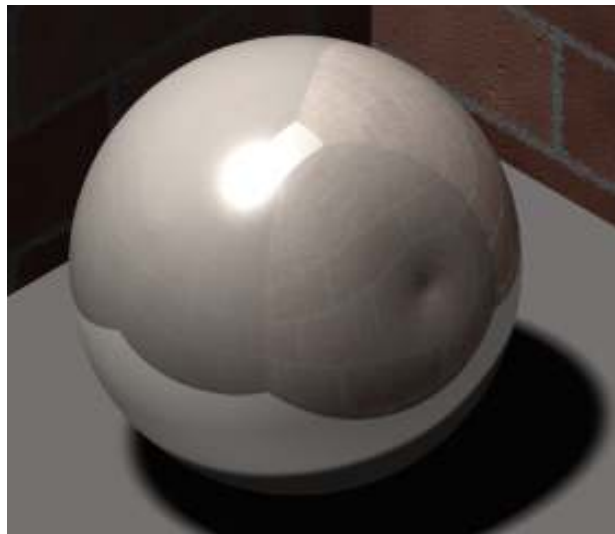


Figure 2.23 – Specular reflections of a brick wall on a spherical object with a dented surface

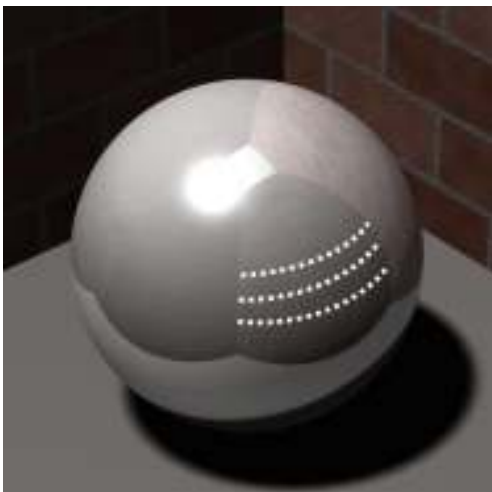


Figure 2.24 – Dent free sphere with undistorted reflections of mortar lines in brick wall

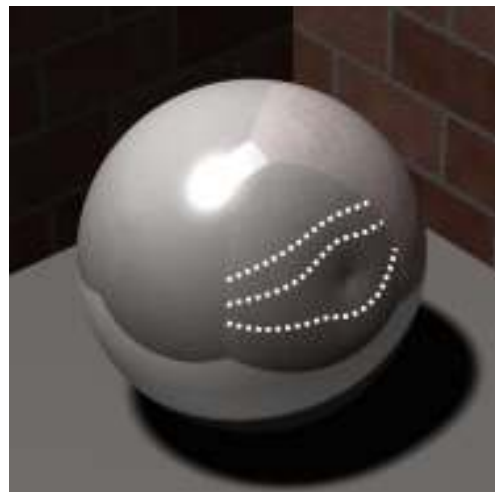


Figure 2.25 – Dented sphere with distorted reflections of mortar lines in brick wall

Humans, when viewing figure 2.23, are able to perceive the deformations in specular reflections as a surface dent because one is aware that the grid shape of the mortar lines has been distorted. However, a human observing figure 2.23 may come to three possible perceptions:

1. The sphere is dented, and the wall is built only from rectangular bricks.
2. The sphere is perfectly spherical and the wall is built from oddly shaped bricks one of which has a deep dimple in it.
3. The sphere is perfectly spherical but has a surface colour pattern that is similar to the surrounding wall but for a small region that looks similar to a dent.

Perception, i.e. deciding what is being seen, is understood to be an active process that builds on previous knowledge and experience, whereas the brain's processing of light information from the eye (i.e. 'seeing' or sight) is a passive sensory process. It is the use of prior knowledge and heuristics, and their weighting during visual perception that allows human to separate specular reflections from object shape and discount option 3 [see Gibson 1950a, 1979, Todd et al. 1996, Kingdom 2008]. Furthermore, most humans are likely to have seen a brick wall, and therefore when presented with specular reflections, and other cues such as shading and shadow, such as those in figure 2.23, will automatically weight against the possibility of option 2, and default to perceiving reflections of a perfect brick wall on a dented sphere. However, if the specular reflections on the sphere were of an unfamiliar, non-geometrical scene or object, or if the observer had never seen a brick wall, the question arises of whether the observer would perceive a dent in the surface or a reflection of strangely shaped object.

Considering an aircraft inspector, it is likely that many of the objects, and possibly parts of the environment in which they work will be geometric in shape. Furthermore, geometric or not, the shape of the objects within an inspectors environment will be familiar to them. A tree, an office block, and an aircraft, for example, are the *shape* of a tree, an office block and an aircraft. Whether an inspector recognises *what* they are, or their names, is of no concern; their *shape* is familiar to the inspector. Therefore, bearing in mind the aforementioned literature of Gibson, Norman, Todd and Kingdom, it can be assumed that distortions in reflections of objects and the

surrounding environment are likely to be perceived as surface shape changes rather than strangely shaped, unfamiliar objects.

The actual saliency, or visibility of distortions to the inspector, i.e. whether the distortions are severe enough to be detected, is another matter. Reading of literature, particularly by Gibson, Norman and Todd leads to the understanding that saliency of specular reflections will depend on the magnitude and rate of change in surface slant and tilt.

### ***2.3.5 – Surface Slant and Tilt***

The effects of surface slant and tilt on visual perception, and their effects on the specular highlights, specular reflections and shading that occur on an objects surface are well researched [See Gibson 1950a, 1950b, & 1979, Norman et al. 2006 & Todd et al. 1996].

Slant is well described by Gibson as the “*angular inclination to the line of regard*” [Gibson 1950b]. When observing objects, surfaces with different slants appear to have different shading and may exhibit different specular reflections to neighbouring surfaces of different slant. Considering a dent on a surface, the slant of the surface in the dented region is different to that of the original, non-dented surface. A dent that one might term as ‘acute’ in shape will exhibit significant changes in slant and the changes in slant will occur across short distances, i.e. have a higher rate of change in slant. However, a less acute dent, or ‘shallow’ dent will be comprised of surfaces that exhibit smaller changes in surface slant, across greater distances, i.e. a smaller rate of change in slant.

Small rates of changes in slant will produce subtle changes in shading (‘soft’ shading gradients), whereas higher rates of change in slant will produce abrupt changes in shading (‘hard’ shading gradients). Subtle changes in shading, or soft gradients, are difficult for humans to perceive (i.e. camouflaged) if they occur across large distances, especially if the surface exhibits other features such as a patterned surface colour [see Kingdom 2008].

Specular reflections are also affected by surface slant, (see Norman et al. 2004. for a detailed description). Subtle changes in surface slant will cause less salient distortions to specular reflections than abrupt changes in surface slant. It thus follows that if a dent in a surface has a smooth, shallow profile, it will produce less salient distortions in specular reflections than an equally sized dent with a less smooth, profile.

The effect of surface slant on specular highlights is complex [Norman et al. 2004], and this section represents an understanding of the available literature with a bearing on visual inspection of aircraft structures. First, consider a small radius on the edge of two perpendicular surfaces, similar in profile to that shown in figure 2.26. Secondly, consider a step between two parallel surfaces, which is joined by a very shallow double curve as illustrated in figure 2.27, placed in the same position and lit from the same light.

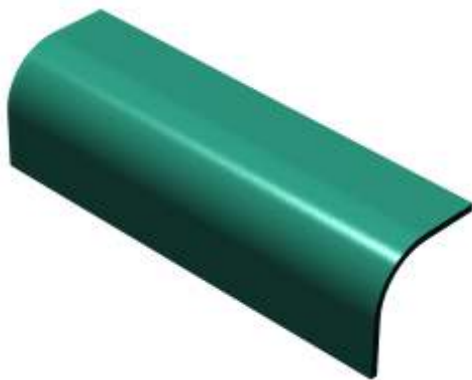


Figure 2.26 – Surfaces oriented in a wide range of slants exhibiting specular highlight

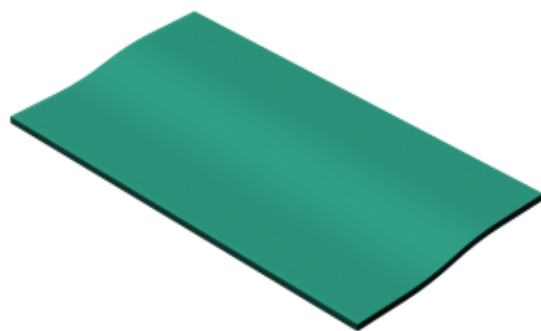


Figure 2.27 – Surfaces oriented through a smaller range of slants failing to exhibit specular highlights

Although the surface of the smaller radius edge may produce a thin specular highlight, the surface covers many slant angles, which allows the surface to reflect light from a wide angular field, i.e. there is a wide angle from which the light source producing the specular highlights could shine. Consider on the other hand, the shallow double curvature shape; under the same lighting conditions, the slant of these surfaces is not conducive to specular highlights being produced. The surfaces of the object in figure 2.27 have not captured a wide enough field of light in order to return or specular highlight to the observer's eye. In view of these considerations, one must bear in mind that whilst larger specular highlights may be more visible to an observer than smaller

ones, specular highlights can only occur if the surface slant is oriented with the observer's line of regard in such a way that it produces a reflection of a light source.

If the shape of a dent in a surface is such that a wider range of slant is present, there exists a greater chance that specular highlights are exhibited from a given viewing angle, which as previously discussed, increases the chance that the shape will be correctly perceived [Norman et al. 2004]. Further to the issue of specular highlights, or lack of, the shape and surface slant(s) of a dent may be such that the saliency of distortions of specular reflections is reduced to a point where an observer is unable to perceive a change in 3D shape. Couple this with the fact that the subtle changes in surface slant may also result in poor shading saliency [see Todd et al 1996], and one is able to see how an observer may have difficulty perceiving the available cues as a surface dent. Thus, a small acute dent, providing greater variations across a wider range of surface slant angles may be more visible than a wider, shallow dent that offers only a small range of slant angles, with very subtle changes in slant.

### ***2.3.6 – Surface colour & surface finish***

The visual perception of colour and research into links between surface colour and surface finish continues to receive scientific interest. It is apparent that the studies by Todd, Norman & co-researchers cited in this thesis have led way to yet more recent publications on the specific issues of surface colour and gloss [Xiao & Brainard 2006 & 2008].

Whilst a matt finish object and a gloss finish object may have the same base, or 'body' colour, the actual colours reflected by a glossy object will vary significantly more than on a matt object [Xiao & Brainard 2006]. Consider two identical shapes, one reproduced in a matt yellow (figure 2.28) and one in a gloss yellow finish (figure 2.29).

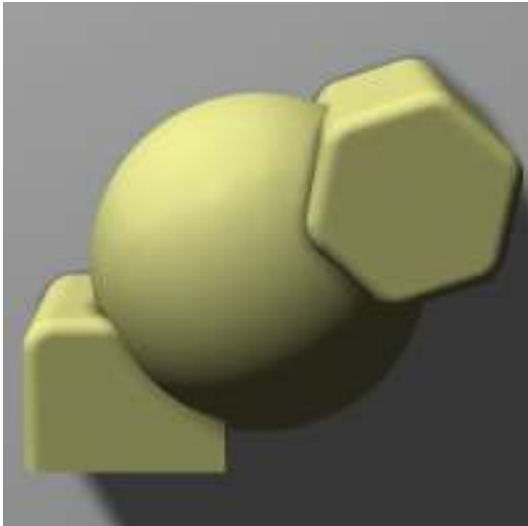


Figure 2.28 – Object with matt yellow finish

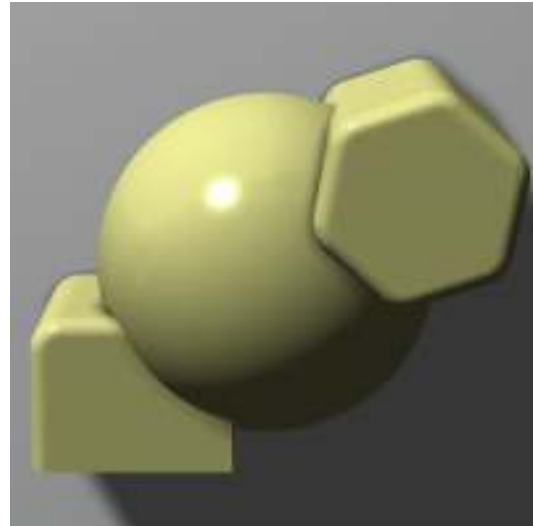


Figure 2.29 – Object with gloss yellow finish

It can be seen that whilst the colours seen on the matt yellow objects vary from dark to grey to light yellow, the presence of specular highlights on the gloss object mean that the colours reflected by the gloss object vary from dark grey to white. Differences in perception of colour due to variations in surface finish have been experimentally demonstrated [Xiao & Brainard 2006 & 2008], and it is likely that the colour of the objects in figures 2.28 and 2.29, although the same, may be perceived a very slightly different. The fact that surface finish affects perceived colour is fundamental to understanding the link between surface colour, surface finish and visual perception of an object's 3D shape. This understanding is further aided by the work of Kingdom in 2008.

Firstly, the effect of surface finish on visual perception can be explained. The shape of the objects in figures 2.28 and 2.29 is clearly and unambiguously perceptible to the observer. The same object has been re-coloured in matt blue and gloss blue, and is presented again in figures 2.30 & 2.31.

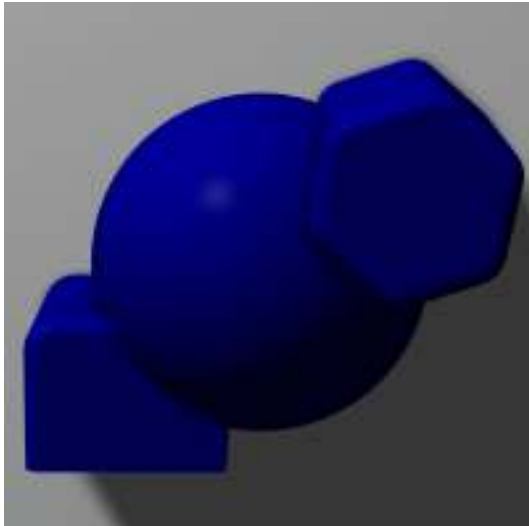


Figure 2.30 – Object with matt blue finish

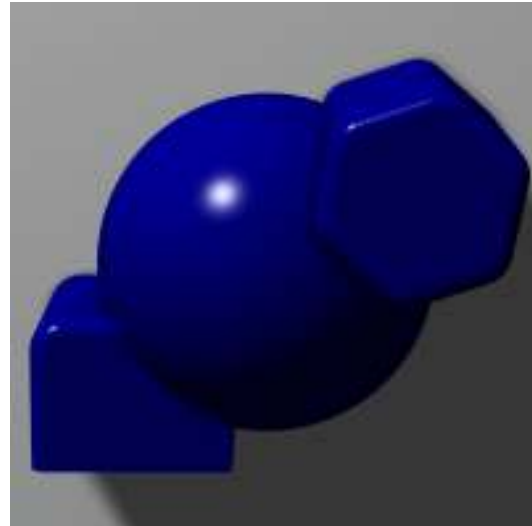


Figure 2.31 – Object with gloss blue finish

In figure 2.30, the shading on the matt blue object has poor modularity with the base colour and it is difficult to distinguish the regions that are darkly shaded from base colour. There exist regions on the sphere that are so dark that it becomes difficult to discern 3D topographical features, i.e. the shape is difficult to perceive. However, the introduction of a gloss finish in figure 2.31 increases the range of colours that are reflected by the objects surfaces [Xiao & Brainard 2006], and introduces the appearance of specular highlights [which enhances perception of shape [Norman et al. 2004]]. The shape of the object in figure 2.31 is thus slightly more perceptible than that in figure 2.30, due to the change in surface finish.

In order to visualise how surface colour and surface finish interact, a series of dented coloured spheres are presented in matt and gloss finishes in different scenes. Consider first the grey sphere in figure 2.32. Perception of the dent on the side of the sphere is facilitated by shading cues and distortions in the specular reflections of the environment. If the same sphere is given a white, glossy finish, as in figure 2.33, the dent still produces salient cues that allow perception of the same dent. However, on the same sphere with a glossy blue finish as shown in figure 2.34, the modularity of the shading cues and the specular reflection cues is poor, resulting in reduced saliency, i.e. the dent is difficult to see. The effect of surface colour on shading and specular reflection saliency is thus demonstrated. Furthermore, it will be noted that the range of colours reflected by the white sphere in figure 2.33 is far greater than the range of colours reflected by the blue sphere.



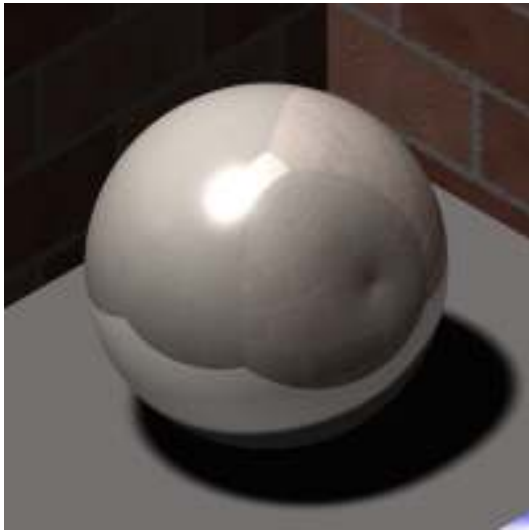


Figure 2.32 – Gloss grey sphere with dent in side

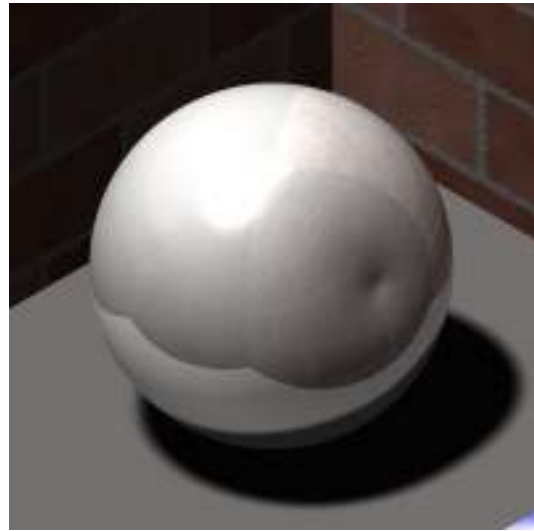


Figure 2.33 – Gloss white sphere with dent in side

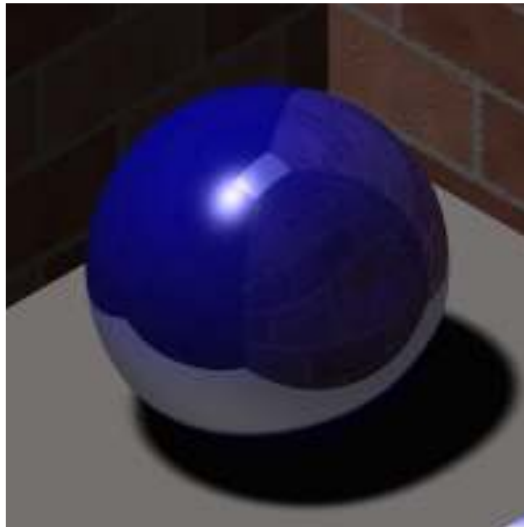


Figure 2.34 – Gloss blue sphere with dent in side

Surface colour can affect the saliency of not only the shading and specular reflection cues, but also the saliency of specular highlights. In figures 2.35 to 2.37, the same grey, white and blue spheres are illustrated, but in a position whereby the dent is at the top of the sphere. In this position, the dent is perceptible on grey sphere due to the small deformations in the specular reflection of the brick wall, and a small area of darker shading. The large specular highlight just below the dent does not affect the saliency of these cues. On the white sphere, however, the specular reflection and the white base colour fuse together, thus eliminating the specular reflection cue and the shading cue. The specular reflections on the blue sphere remain visible at the top of the sphere, and the distortions in the reflection of the brick wall caused by the dented

region are just perceptible. However, whilst the specular highlight on the sphere does not interfere with the cues in the dented region, the shading cue has poor modularity with the base colour and reflected colour, making it imperceptible.

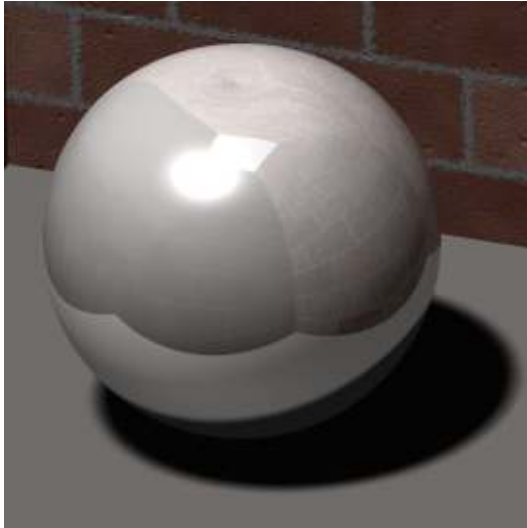


Figure 2.35 – Gloss grey sphere with dent in top

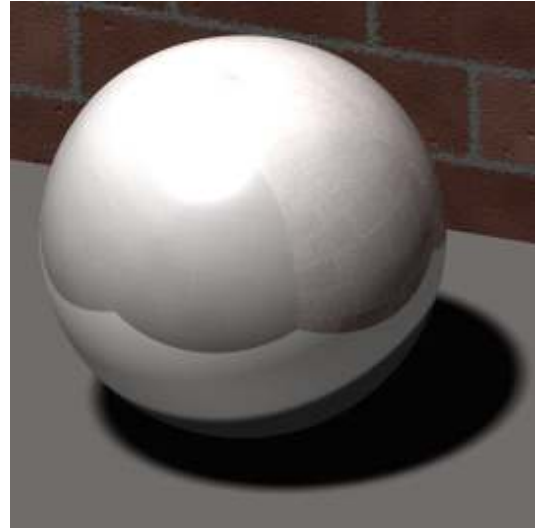


Figure 2.36 – Gloss white sphere with dent in top

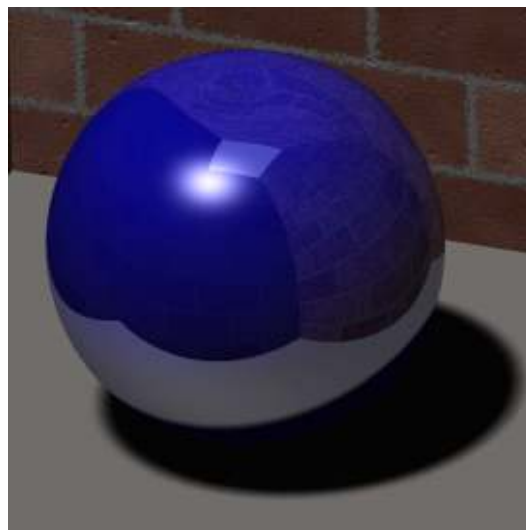


Figure 2.37 – Gloss blue sphere with dent in top

The effects of surface colour and surface gloss combine to affect the visibility of 3D flaws in complex ways. The grey, white and dark blue colours and matt & gloss surface finishes illustrated in this section are commonly found in aviation applications (as seen in figure 2.38). Thus, the visual perceptual issues presented in this section are all likely to be observed during visual inspection of aircraft structures for 3D impact damage dents.

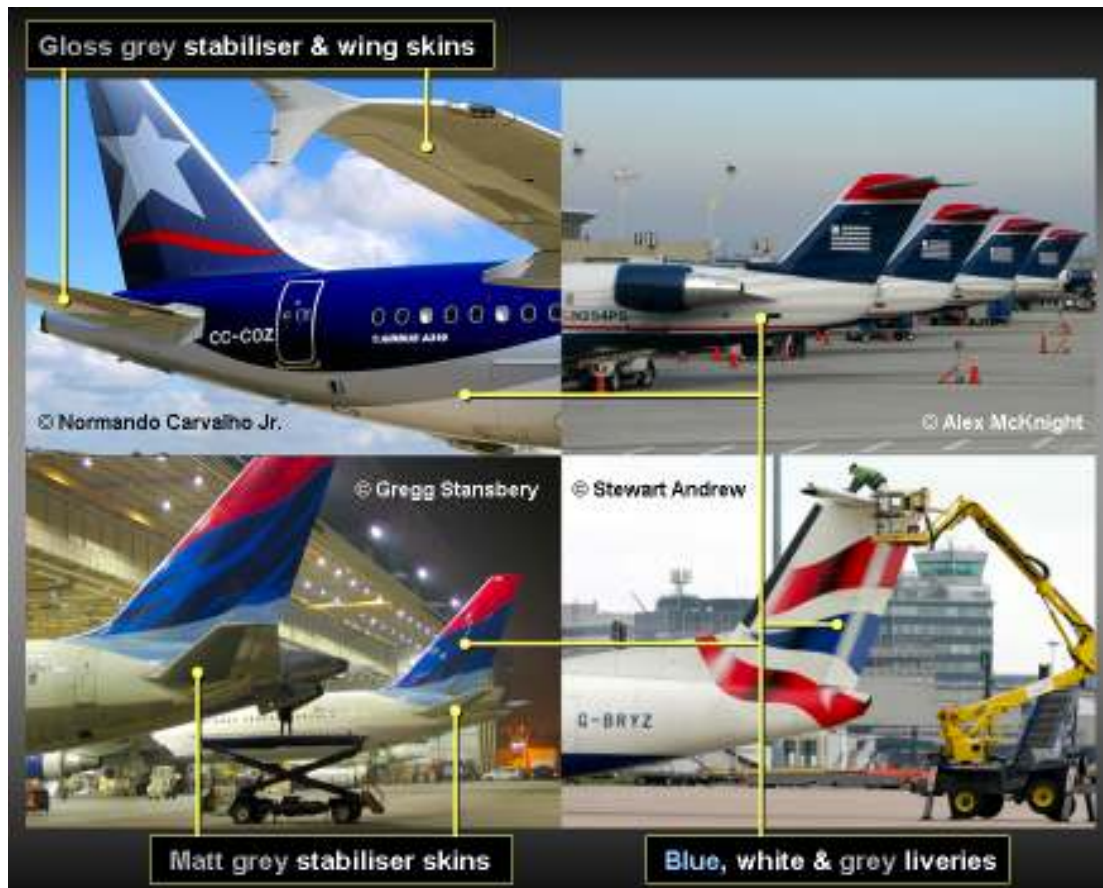


Figure 2.38 – common colours used in airline liveries, from [www.airliners.net](http://www.airliners.net) 2009

## 2.4 – Aircraft paint finishes

The topcoat paints used by airlines to paint liveries are usually applied as a glossy colour coat. Over a period of several months, environmental effects can lead to dulling of the paint surface, resulting in a less glossy surface finish. A piece of black coloured glass would be expected to give the maximum reading of 100 gloss units (GU). Gloss levels for freshly applied aircraft paint usually exceed 90gloss units (GU) [PRC-DeSoto 2003; Akzo Nobel 2006 & 2008]. However, experimental data from Guseva et al. 2003 (see figure 2.39) show a reduction in paint gloss to 60GU after 40 months of service, and a reduction to 40GU after 60 months of service.

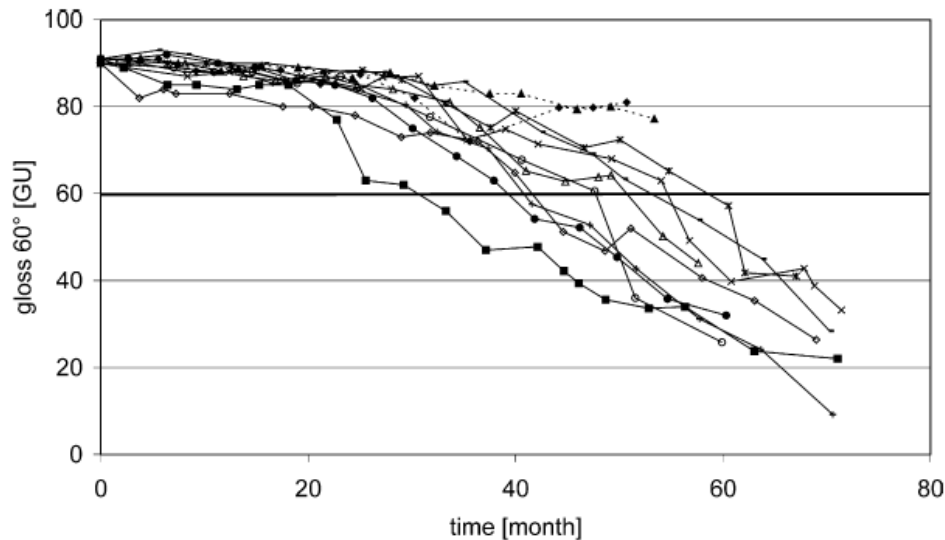


Figure 2.39 – Plot detailing aircraft paint gloss degradation with time, from Guseva et al. 2003

Thus, whilst aircraft may have highly glossy (>90GU) paint finishes for the first 3 years of their lives, older aircraft are likely to have less glossy, semi-gloss (<60GU) paint finishes. In extreme cases, the gloss level may be so low as to be described as matt finish. Dust and dirt may also combine to reduce the glossiness, or specularly of the surface, resulting in a more diffuse surface finish. Given the previously described effects of surface specularly on visual perception, it thus follows that the condition of an aircraft's paint may affect the visibility of 3D surface flaws.

### **2.5 – Reliability assessment of NDI/ NDT techniques**

Reliability assessments provide a quantitative means of determining the detection threshold of a non-destructive testing (NDT) or inspection (NDI) procedure, or probability of detection for flaws of a certain size using said procedure. Reliability assessments typically involve asking participants to inspect specimens containing flaws of known sizes, and identify the presence of said flaws [See Singh 2000; Georgiou 2006 & Georgiou 2007]. As previously mentioned, most reliability assessments are no longer performed to determine the smallest size of defect that can be detected, and since the 1960's and 70's, the has question changed to being 'what is the largest size of defect that will be missed' [Hagemaiier 1998; Georgiou 2007]. The effect of factors that may cause defects to be missed can be quantified by the use of reliability assessments.

An excellent review of NDI reliability research is given by Karta Technologies [Singh 2000], and the capabilities of several aerospace NDT/NDI methods have been quantified and published as a collection of probability of detection (POD) curves [Rummel & Matzkanin 1997]. However, it is important to note that much of the published work studied by Singh, and within the NDE capabilities book concern the inspection of metallic aerospace structures, and the word ‘flaw’ refers exclusively to cracks in metallic structures. In most published NDT/NDI literature, crack length is considered adequate for describing the size of flaws or defects. For inspection of metallic structures, it is thus convenient to give POD as a function of crack length. The use of a single variable to describe flaw or defect size has consequently led to published mathematical methods that model POD solely as a function of a single variable [see Berens & Hovey 1982; Bullock et al. 1994]. The issue of crack width has been acknowledged [Bullock et al. 1994], but in favour of less complex, single variable mathematical models, crack length has remained the single flaw size variable on which POD has been modelled. Current published POD models are thus reliant on the fundamental assumption that a longer crack will always give a higher POD than a shorter one. This assumption is so deep rooted into POD literature that inspection procedures are considered incorrectly designed if POD reduces with increases in flaw size [Georgiou 2007].

As previously described, impact damage to a composite laminate is three dimensional, in shape. The damage does not occur solely in the form of simple surface breaking cracks. Impact damage to composite materials must be characterised by its width, depth and sectional profile in order for its shape and size to be fully described. As previously described, it is feasible that a wider dent will be less visible than a dent with smaller width and equal depth. Currently published POD models cannot simultaneously calculate POD as a function of multiple parameters and cannot accommodate a situation where POD may reduce as the size of a parameter increases. Consequently, published POD models are unsuitable for modelling the reliability of visual inspection for impact damage on composite materials. The issues surrounding POD are presented here in due course.

Of all the available literature, three documents stand out as being the widely accepted, and adopted recommended guidelines for conducting reliability assessments of NDI/

NDT procedures. These are Agard Lecture Series 190 [AGARD 1993], Spencer's Generic Protocol [Spencer et al. 1993] and Department of Defence Handbook 1823 [US DoD 2007]. MIL-HDBK-1823 appears to be a culmination of many works, including Spencer's protocol and AGARD LS190. Unsurprisingly, Spencer and contributors to LS-190 (Annis, Rummel & Vukelich) are acknowledged as having considerable input into the MIL Handbook. As a result, MIL-HDBK-1823, represents the definitive 'how to guide' for reliability assessments.

Within MIL-HDBK-1823, there also exists a grading scheme for reliability assessments, whereby the thoroughness and statistical validity of the experiment is graded against certain criteria and minimum requirements [Appendix I.5, US DOD 2007]. It is evident that the grading criteria were written for NDT and POD of metallic structures, although there are recommendations within that remain valid for reliability assessment of inspection of composite materials. These recommendations, along with those from other documents will be presented in due course.

As can be deduced from published examples [Murgatroyd 1993; Forsyth & Fahr 1998; Georgiou 2007], the three aforementioned guideline documents and the Karta review [Singh 2000], published NDT/NDI reliability assessments follow a generic paradigm, a description of which follows:

- Several participants inspect a series of specimens
- The specimens contain a known range of flaw or defect sizes, in known locations
- The participants use the specified inspection procedure to search for defects
- The participants call out, or mark down the presence of a defect
- The results are recorded in terms of hits, misses and false calls
- The hit/ miss data are analysed as probability of detection (POD) curves and the false call data may be analysed in terms of probability of false alarms (POFA) and may presented as receiver operating characteristic (ROC) curves [see Spencer et al. 1993 & Singh 2000]
- The 90% POD/ 95% confidence size, (the size of flaw that 90% of participants can find 95% of the time), is determined, pending sufficient data/ specimens

The personnel implementing the experiment, be it one or several people, are usually referred to as the ‘moderator’ [Spencer et al. 1993]. The persons performing the inspection may be referred to as ‘inspectors’ [Spencer et al. 1993], although the term implies some form of formal training or qualification. To avoid such confusion, the term ‘inspector’ will be substituted with ‘participant’.

In order to define the experimental plan, issues relating to participants, experimental setup, specimens, flaws and experimental procedures must be addressed.

### ***2.5.1 – Participants***

Participant numbers vary in reliability assessments, often just a handful of participants are used [see Murgatroyd 1993; Spencer 1996, Bruce 1998, Mullis 1998], and there is no specific requirement for the number of participants in a reliability assessment. There are only requirements on the number of successful detections required to demonstrate 90%/ 95% or 90%/ 50% POD/ confidence levels [Hagemaiier 1998]. However, after reviewing previous experiments [Murgatroyd 1993; Spencer 1996; Mullis 1998], it can be considered that 15 individual people is a large number of participants, and can be considered adequate for obtaining representative, and statistically valid results.

Part of the problem in obtaining sufficient participants for NDT/NDE reliability assessments is the reluctance of airlines and MRO facilities to provide inspectors during their duty hours. It should be noted that most published NDT reliability experiments have benefited from the support of military, regulatory or academic establishments such as USAF, NASA, FAA or universities, not commercial airlines [see Lewis 1978; Rummel & Matzkanin 1997; Gramopadhye et al. 1998; Singh 2000 & Erhart et al. 2004].

In order to obtain greater numbers of participants, novice participants without formal training in the inspection task may be used. Studies that utilised novice participants have achieved participant numbers well over 40 [Gallwey & Drury, 1986]. Novice participants can be used instead of trained aircraft inspectors, without significant differences in performance [Gallwey & Drury, 1986; Mullis, 1998]. The condition for doing so being that the experimental procedure is a simulation of the inspection task,

not an inspection of an actual aircraft. This eliminates inspector prior knowledge or expectancy, which can aid inspection reliability [see Spencer 1996], as an experimental variable or factor. Use has been made of novice inspectors or participants in several published NDT/ NDI studies [Forsyth et al. 1998; Mullis 1998; Latorella et al. 1992; Erhart et al. 2004; Vora et al 2002 & Sadasivan 2007].

### ***2.5.2 – Experimental setup***

NDT/NDI reliability experiments seldom use an entire aircraft in the experimental setup, due to cost and logistical considerations [Spencer et al. 1993; Singh 2000]. Experiments commonly represent the section of aircraft structure to which the inspection procedure would normally be applied [Murgatroyd 1993; Spencer et al. 1993; Mullis 1998; Singh 2000; Erhart et al. 2004 & Gant 2007]. Participant buy-in is enhanced by an experimental setup that closely replicates the actual inspection task, and it is recommended that experiments attempt to replicate the environmental conditions, such as lighting, accessibility and noise that would be experienced in the field [Spencer et al. 1993; AGARD 1993; US DOD 2007]. Assessment of an inspection task performed on a difficult to access, poorly lit structure must replicate such conditions [Spencer et al. 1993]. However, NDT/NDI reliability assessments need not be performed exclusively in a hangar or aircraft maintenance facility [Spencer 1998]. The work of Murgatroyd 1993 is an excellent example of how accessibility conditions of an aircraft were replicated by using a raised platform and barriers, without actually needing to perform the experiment high off the ground on an actual aircraft. Murgatroyd's experiment also utilised a specimen support that represented an aircraft fuselage belly and the access issues associated with having to bend or kneel to perform the inspection. Some experiments have asked participants to travel to the experiment, [Murgatroyd 1993; Spencer 1996; Erhart 2004 & Gant 2007] whilst others transported specimens to the participants for inspection at different facilities, as typified by Lewis' renowned 1978 experiment, which is more widely known as the "have cracks, will travel" program [Lewis et al. 1978; Singh 2000]. Transporting an experiment to facilities or participants may help furnish the experiment with greater participant numbers, and indeed Lewis et al. obtained data from approximately 300 inspectors in the four years that their experiment ran. However, this option is unfavourable when wishing to avoid uncontrollable facility-



to-facility variations in lighting or environment, and logistical issues such as damage to specimens during transit [see Spencer et al. 1993; AGARD 1993].

### ***2.5.3 – Specimen Characteristics***

It is convenient to refer to the Karta Technologies review for an excellent review of previous NDT/NDI reliability assessment specimens [Singh 2000]. However, it is important to note that specimens for reliability assessments generally use artificially produced flaws i.e. flaws or cracks produced by machining as opposed to grown by cyclic loading. Previous experiments have also made use of facsimile specimens.

The key advantages offered by using artificially produced flaws are that the specimens all have the same condition, and the flaw locations and sizes can be specified by experimental design. Facsimile specimens are particularly useful when the cost of producing the required specimen numbers and logistical considerations such as weight or production time prohibit the use of original materials [Spencer et al. 1993]. An excellent example of the use of facsimile specimens is the study by Murgatroyd et al. on the influence of various human factors on inspection reliability, in which an electronic tablet provided the facsimile of a row of rivets [Murgatroyd 1993].

When designing specimens, it is recommended that specimens are sized such that they are representative of the original structure [Spencer et al. 1993], and the surface finish & condition of the specimen should be similarly authentic [AGARD 1993; Spencer et al. 1993]. With regard to surface finish, the available recommendations pay reference to metallic finishing operations such as turning, blasting, burnishing or polishing. The term condition usually refers to the condition, i.e. cleanliness of the component during inspection, and is in fact an experimental variable, which must be controlled, as described later in this section.

As previously mentioned, exterior facing composite aircraft structures such as wing, fuselage and empennage skins are painted. The surface finish is ultimately determined by paint finish. Thus, the recommendations for surface finish are best interpreted as meaning that composite specimens should have a surface finish representative of a

painted aircraft structure. Inclusion of details such as panel joints, fasteners or access panels to enhance specimen authenticity [Spencer et al. 1993; AGARD 1993; US DOD 2007] is only required if inspector buy-in and use of their expectancy of damage location is sought.

Flaw locations are also to be authentic to those seen in the field. Flaws that would normally be found on, or originate from component edges or holes, and flaws that would normally break out on surfaces should be replicated in the same manner on the specimens [Spencer et al. 1993; AGARD 1993; US DOD 2007].

#### **2.5.4 – Flaws**

The term ‘flaw’ in a reliability assessment is used to describe intentional defects and can cover a variety of defects such as cracks, disbonds, delamination or dents. For metallic structures, crack and flaw are synonymous. For the purposes of applying the relevant NDT/NDI reliability literature to impact damage on a composite laminate, the term flaw must be considered as the dent produced on the laminate surface by the impacting object.

The flaws used in reliability assessment specimens must be authentic to those seen in the field [Spencer et al. 1993; AGARD 1993; US DOD 2007]. For published assessments, this has meant using cracks that are authentic in size, shape and type to those experienced on service components. For impact damage on a composite laminate, the requirement translates to meaning that the reliability assessment specimens must contain impact damage, or representations of impact damage, that are authentic to the damage an inspector might see on an actual aircraft.

Hovey et al. 1989 suggested a minimum of 30 flaws across a range of sizes covering the 10% to 90% POD range, i.e. region of interest, are sufficient to estimate inspection reliability for a process that results in a hit/miss response. However, if the correct region of interest is unknown, Hovey et al. recommend an extended size range covered by 60 flaws. These recommendations are widely accepted and feature in all protocol guidelines [see Spencer et al. 1993; AGARD 1993; US DOD 2007]. With regard to flaw sizes, one is recommended against using flaw sizes large enough to guarantee 100% detectability and flaws so small they are undetectable [Spencer et al.

1993; AGARD 1993; US DOD 2007]. The contributors to AGARD LS-190 noted that Previous NDI/ NDT reliability assessments have suffered a “*tendency to include too many large flaws*” [AGARD 1993 pp.6]. However, all available reliability assessment literature acknowledges that the sizes likely to produce the required region of interest will be unknown, and therefore the flaw sizes for this region can only be estimated using ‘engineering judgement’ [Hovey et al. 1989]. It is therefore apparent that one must have some idea of the inspection process capabilities in order to set the flaw size range for the specimens.

The recommendations for flaw numbers hold true only for each type of flaw within the experiment [see Spencer et al. 1993; AGARD 1993; US DOD 2007; Georgiou 2007]. For composite materials, if detection of flaws such as impact damage from a rounded object *and* impact damage from a pointed object is to be assessed, the recommendations state that a range of 30 different sizes of flaws for both the rounded *and* the pointed object be used, i.e. 60 flaws in total. If one adopts the more extensive recommendation of 60 flaws per type, the specimens must contain 120 flaws in total. In view of such recommendations, it becomes clear as to why reliability assessments require large numbers of specimens.

Having established that the specimens must contain a minimum of 30 flaws for each type of flaw, one must then distribute the flaws across a range of sizes. The unanimous recommendation is to use an even interval between the logs of the flaw size values [Spencer et al. 1993; AGARD 1993; US DOD 2007]. For metallic structures, the chosen variable has been crack length, so cracks would be distributed across a size range, with even intervals between the log values of the crack lengths. For composite structures, and impact damage dents that require more than one variable to describe their topography (as previously described), one must choose which size variable (width, depth or other) will be used for flaw size distribution.

Once produced, the specimens must be re-characterised in order to ensure that they conform to the original size specifications and are in the correct locations on the specimens [Spencer et al. 1993; AGARD 1993]. If different to the specification, the results must be reported using the sizes and locations of the flaws produced on the specimen as opposed to the specified values.

### ***2.5.5 – Specimen numbers***

Boredom or fatigue due to repetitive tasks has been identified as a human factor likely to cause errors in aircraft inspection, and thus reduced reliability [Rummel 1984 & Dupont 1997 in Hagemaiier 1998]. It is recommended that specimens for reliability assessments also contain unflawed sites [Spencer et al. 1993; AGARD 1993]. This helps introduce the boredom factor to the experiment by requiring the participants to keep searching for flaws, even though their inspections may often result in no flaws being found. Another factor introduced by inspecting unflawed specimens is the propensity of inspectors to make false calls. False call information can signify whether an inspector is being conservative in calling out flaws, or simply calling out flaws even though they are not entirely sure that a flaw is present [see Bullock et al. 1994; Spencer et al. 1993]. Quantification of the probability of false calls or alarms (POFA) is recommended for reliability assessments [Spencer et al. 1993; AGARD 1993; US DOD 2007] although the mathematical models for POFA are limited by the same constraints as those previously mentioned for POD [see Bullock et al. 1994]. In order to follow established experimental paradigms, specimen numbers must therefore allow for the inclusion of unflawed sites.

The decision on specimen numbers will also be driven by flaw density (number of flaws per specimen) considerations. Flaw density can either be set by experimental design, or allowed to mimic the natural flaw densities that would be observed on in-service aircraft, although a mix of the two is also feasible [Spencer et al. 1993]. Where a representative flaw density would result in too large a number of specimens, or too great an inspection time, it is recommended that the specimens contain three unflawed inspection sites for every flawed inspection site [Spencer et al. 1993; AGARD 1993; US DOD 2007]. The 3:1 unflawed/ flawed ratio is one best adopted, in view of the lack of a published flaw density value for impact damage on actual aircraft, i.e. there are no published records of how many ‘dents’ a composite structure on an average aircraft is likely to have sustained during a given period of service.

It is clear, however, that the 3:1 unflawed/ flawed recommendation has only ever been considered with regard to inspection of metallic structures for cracks. The key issue is in the use of the word ‘inspection site’ as opposed to specimen. Consider, for example an assessment of rivet or fastener hole inspection for cracking. An individual hole

could be considered an 'inspection site'. One thus interprets the 3:1 ratio as meaning that the specimen set for the assessment should contain three unflawed holes for every cracked hole. Most published NDT reliability assessments concern inspection of metallic aircraft structures such as fuselage skins or wing spars, and in particular, inspection of rivet or fastener holes and bonded or welded joints. Each row of holes or joints, of which there can be several on any one aircraft, can be considered an 'inspection site', thus the 3:1 unflawed/ flawed ratio can be conveniently adopted. This appears to be the interpretation made by Murgatroyd et al. 1993, whom exceeded the recommendations and used an approximate ratio of 70 unflawed fasteners for every cracked fastener. Furthermore, Murgatroyd et al. presented approximately 7 unflawed rows of fasteners for every row that contained cracks. However, the discrepancy between 'inspection site' and specimen is evident in Bode et al. 2006, in which it is said that NDT reliability data is generally obtained "*from sites containing multiple flaws*". The issue of concern for Bode et al. is whether a 'site' containing multiple flaws has more chance of being detected than one containing a single flaw. In the paper by Bode, it is clear the individual rivet hole is considered a site, rather than a whole row of holes.

Furthermore, there are no published precedents for the implementation of the 3:1 ratio in visual inspection reliability assessments concerning impact damage to composite structures. Whilst the term dent is easily translated into 'flaw', one cannot consider a dent as being 'unflawed' or having 'multiple flaws', i.e. a dent cannot be considered an 'inspection site' and one cannot have three 'unflawed' dents for every 'flawed' dent. Instead, the structure itself, i.e. entire sections of laminate must be considered as flawed or unflawed. It would be unfeasible (financially & logistically), to propose a reliability assessment using four entire wing, fuselage or empennage structures of which only one contained damaged laminate. Instead, the 3:1 ratio is better interpreted by considering structures such as wings, fuselages or stabiliser skins as a collection of individual inspection areas or zones, of which only one zone in every four contains flaws. The individual zones then become discrete 'inspection sites'.

The issue herein is whether one presents individual 'inspection sites' (i.e. single specimens) one at a time to the participants using the 3:1 unflawed/ flawed ratio for complete specimens, or whether one arranges several individual specimens in order to

represent a larger structure such as a stabiliser, a wing skin or a large section of either. Alternatively, and similar to the latter option, one may choose to section a large, single specimen such as a stabiliser or wing skin into individual zones, or ‘inspection sites’, using tape or marked lines. The disadvantage to this method being that the flaw sites cannot be moved at any time during the inspection, meaning that if, for example, a flaw were in a poorly lit location compared to others, one would be unsure whether it was the flaw size or the lighting that affected inspection reliability. Providing all the specimens have the same shape and size, the option of using individual specimens arranged to represent a larger structure would allow one to move the specimens around in order to assess the effect of flaw size and lighting together. If, however, the effects of other factors, aside from those characteristic to the specimen (such as flaw size, flaw shape or surface finish), are to be eliminated, the only option is to present individual specimens for inspection, one at a time, under the same conditions. In this case, the 3:1 recommendation is interpreted such that a single specimen constitutes an ‘inspection site’, and for every specimen in the set that contains intentional damage or flaws, there will be three more containing no intentional damage.

#### ***2.5.6 – Other issues pertaining to specimens & procedures***

In many NDT/NDI reliability assessments, the specimen sets may need to be reused to perform repeat inspections, perhaps under the same conditions to provide demonstration of repeatability or under different conditions to investigate the effect of various factors [see Spencer et al. 1993 or AGARD 1993]. The participants must not become familiar with the specimens used in the reliability experiment [Spencer et al. 1993]. If repeat inspections are performed, the presence of dirt marks, unintentional damage or identification markings may allow participants to recognise a previously inspected specimen, and memorise the position of previously detected flaws, which may lead to artificially high response rates [AGARD 1993]. Careful cleaning and storage of specimens is recommended in order to avoid such occurrences [Spencer et al. 1993; AGARD 1993]. Similarly, any identification numbers used on the specimens must be such that no information as to the flawed/ unflawed status of the specimen can be deduced by the participants [Spencer et al. 1993].

It is recommended that the participants in the reliability assessment be unaware of the results or outcome of their inspections. Allowing participants to learn where they have

made correct calls, or missed flaws would lean to familiarity with the specimens, which in turn rules out the possibility of repeat inspections with the same specimen set. [See Spencer et al. 1993; AGARD 1993]

### ***2.5.7 – Experimental Variables***

Variables within the experiment are either controllable or uncontrollable [Spencer et al. 1993]. Controllable variables are those for which the value or condition is specified by experimental design for each inspection. The value or conditions of uncontrollable variables are adopted at the inspection facility and are not specified in the experimental design [Spencer et al. 1993]. The value or conditions for uncontrollable variables, whilst not specified in the experimental design, should be recorded at the time of inspection in order to allow identification of possible effects on the results [Spencer et al. 1993].

Hovey et al. 1989 proposed a model of the factors, which aside from flaw characteristics, could affect the inspection process. The factors were categorised as human related factors, inspection procedure related factors and equipment related factors. Whilst equipment and procedural factors can be controlled, Hovey et al. imply that the human factors within an experiment will be uncontrollable.

Spencer et al. 1993 assessed the variables likely to affect NDI/ NDT procedures, and in conjunction with similar publications [Megaw 1979; Hovey et al. 1989; AGARD 1993; Hagemaiier 1998 & US DOD 2007] it is possible to place the variables into general categories, which are described forthwith. Each of the variables within the categories should be considered, and methods for either controlling the variables or recording the values/ conditions must be included in the experimental plan and protocols

**Facility characteristics** – Lighting, noise and temperature are all characteristics of the inspection facility. Lighting is likely to vary unless a single facility is used or standardised lighting that travels with the experiment is employed. ‘White noise’ or general background has been demonstrated to have little effect on inspection reliability [Murgatroyd 1993], although unfamiliar loud noises may prove more distracting. Temperature will be entirely facility dependant, and the experimental plan

must consider whether equipment will be required in order to maintain a specified temperature range during inspection. Outdoor inspections will be open to factors such as weather (clouds, rain, cold/ heat) and sunlight, and increased uncontrollability of variables such as lighting and temperature. The experimental plan must consider how environmental, or facility dependent factors such lighting, noise and temperature will be addressed.

**Inspector** – The consensus amongst the NDT/NDE community is that the greatest source of variability in reliability assessments is actually the human performing the inspection [see Hovey et al. 1989; Hagemaiier 1998; Spencer 1998]. Training levels, the date of last training and the level of experience of the task are factors specific to each individual inspector [Hovey et al. 1989]. Age and eyesight are specific to individual inspectors and have been identified as variables that may produce variance, albeit minimal, in inspection reliability [Lewis et al. 1978]. Fatigue has also been demonstrated to affect inspection reliability [Murgatroyd 1993], and therefore the experimental plan must demonstrate how the factors of fatigue, training, age and eyesight will be handled.

**Equipment** – Whilst variables concerning the inspection equipment must be considered in traditional NDI/ NDT reliability experiments, the equipment for human visual inspection is the inspector and their eyes. Thus variables such as probe specifications, display specifications and calibration specifications [Hovey et al. 1989, Spencer et al. 1993, AGARD 1993, US DOD 2007] need not be considered. The only possible ‘equipment’ variable to be considered is the eyesight quality of the participants.

**Part processing** – The condition of the specimens during the reliability assessment is not necessarily the same as the condition in which the component would be found in during service [See AGARD 1993]. The most relevant example to visual inspection of composite structures is cleaning of the inspection area prior to inspection. The experimental plan must consider whether inspectors would always find the component in a clean condition, whether an inspector is expected to clean the component prior to inspection, or whether inspectors perform the inspection on a dirty component.



**Inspection process and procedural variations** – The experimental plan must consider the inspection process and the inspection procedure and identify potential variations. Where the possibility for variation exists, the experimental plan must address how the variation will be avoided, controlled or recorded if uncontrolled. [AGARD 1993; Spencer et al. 1993; US DOD 2007] Foreseeable variations in the visual inspection process include head movements, viewing angle changes and visual scanning techniques.

### **Experimental Protocols**

The design of a reliability assessment experiment must include the production of a set of experimental protocols [AGARD 1993; Spencer et al. 1993; US DOD 2007]. The functions of the protocols are to ensure that:

- The experiment is conducted in a consistent manner
- The data are gathered in a consistent manner
- The participants receive the correct information
- Deviations from the experimental plan are correctly dealt with
- Other parties can perform the same experiment and obtain comparable results

The protocols cover both the actions of the experiment moderator and the participants, and must provide instructions for the following listed items, which are derived from the protocol areas suggested by Spencer et al. 1993:

Operating test equipment – the protocols should provide instructions that ensure the moderators and/ or participants are consistent in their operation of any equipment used during the inspection process.

Briefing the participants – standardised briefing material should be included in the protocols in order to ensure that the moderators give each participant the same briefing containing the same information.

Answering on-the-spot questions – participants may ask questions relating to specimens and the inspection procedure, to which standardised responses, as defined in the protocols, must be given by the moderators in order to avoid biasing the

inspection results. The key issues to avoid are divulging flaw information to the participants and allowing the participants to view documentation that may provide them with links to specimen and flaw characteristics.

**Inspection procedures** – the protocols should specify the correct inspection procedure, and provide guidance to the moderator on how to deal with possible deviations from the specified procedures.

**Interruptions** – provision must be made, and guidance given in the protocols for dealing with foreseeable interruptions such as requiring the toilet, participants requesting help during inspection, unauthorised persons entering the inspection facility and telephone calls.

**Collection of results** – the protocols must ensure that the results are collected in a consistent format, and are correctly labelled or identified by methods such as the use of serial numbers.

## **Results**

It is recommended that inspection results are recorded using permanent media, and then transferred to an electronic database at a more suitable time [Spencer et al. 1993]. Results should be collected in the form of hit/miss data for each flaw, and false call data [Spencer et al. 1993; AGARD 1993; US DOD 2007]. Some inspection procedures may result in a perceived flaw size, such as a flaw seen on a monitor screen or display screen, in which the perceived flaw size must be recorded. However, visual inspection is performed directly on the flaws, and appears as actual size, thus meaning actual and perceived size are the same. Another technique that may be employed is to ask the participants to state how certain they are of their response, i.e. give a percentage of how certain they are of having actually seen a flaw [Spencer et al. 1993].

It is recommended that the experimental results be presented as a description of the experimental design, the individual results from each inspection, and a summary of the test results [AGARD 1993; US DOD 2007]. The results should also identify any failures during the inspections or known anomalies [US DOD 2007]. Once collected,

the recommendations state that the hit/ miss results should be analysed to produce a set of POD curves, and once the POD curve has been determined, it is recommended that the false call data be used to determine POFA and produce received operator characteristic (ROC) curves [Spencer et al. 1993]. The information from ROC curves can be used to adjust the POD curves for varying levels of inspector conservatism.

### ***2.5.8 – POD Analysis methods***

For a review of the POD analysis methods employed by previous reliability assessment experiment, it is convenient to refer to Singh 2000 and Georgiou 2006 & 2007. Probability of detection for NDT/NDI procedures is normally presented as a function of flaw size. It is a widely accepted that POD as a function of flaw size is best modelled using either a ‘log-logistic’ (‘log-odds’) or ‘log-normal’ model [see Bullock et al. 1994 and Georgiou 2007].

In view of the work of Berens & Hovey 1982, ‘log-odds’ became the accepted model for POD of hit/miss data [AGARD-LS190; Spencer et al. 1993]. The ‘log-normal’ model was recommended only for POD of an inspection procedure that resulted in a perceived or apparent flaw size [AGARD-LS190; Spencer et al. 1993]. However, in a comparison between the two models, Fahr et al. 1993 determined that whilst the log-odds model was easy to implement, it gave more conservative POD estimates than the ‘log-normal’ model and therefore recommended the use of the ‘log-normal’ distribution for modelling of hit/miss data. Fahr et al. did acknowledge that the ‘log-normal’ model is mathematically more complex and slower to calculate than the ‘log-odds’ model. Despite their findings in 1993, a later publication in 1998 by Forsyth & Fahr does not make the same distinction and merely presents results that identify differences in the POD curves produced from the same data using the ‘log-odds’ and ‘log-normal’ models. In 1997, Rummel & Matzkanin presented the ‘log-odds’ method for modelling of hit/miss data, combined with maximum likelihood estimates to determine parameters within the model, as earlier proposed by Berens and Hovey. Later publications also recommend the use of the log-odds model for POD from hit/miss data [Georgiou 2007]. The following section will present the log-odds model for POD, and explain its limitations.

### 2.5.9 – Single variate POD models

Berens & Hovey 1982 presented the log-logistic, or log-odds model as being the most suitable distribution for POD as a function of crack length, the formula for which is given below:

$$P_i = \frac{\exp(\alpha + \beta \ln(a_i))}{1 + \exp(\alpha + \beta \ln(a_i))} \quad (1)$$

Where  $P_i$  is the probability of detection of flaw  $i$ ,  $a_i$  is the flaw size and  $\alpha$  &  $\beta$  are constant parameters. In order to find  $\alpha$  &  $\beta$ , the range interval method (RIM) or maximum likelihood estimator (MLE) method can be used. Whilst both RIM and MLE can be used with the log-odds model, only MLE is recommended for use with the ‘log-normal’ model (as presented by Bullock et al. 1994, and in US DoD 2007).

RIM may also be known as regression analysis [see Bullock et al. 1994]. Bullock et al describe RIM to good effect, and to summarise, the range interval method places the flaw sizes into intervals of equal length. Consider the hit/ miss data for cracks of similar lengths, but possibly varying widths. At this point, all crack lengths within a length interval end up being grouped together. For each interval, the probability is calculated as the ratio of detected flaws to total possible flaw detections. A plot using equation (2) is produced, where  $p_i$  is the proportion of flaws detected,  $a_i$  is the flaw size and  $i$  is the interval size (either the mid-point value or endpoint value of the interval).

$$Y_i = \ln\left(\frac{p_i}{1 - p_i}\right), X_i = \ln(a_i) \quad (2)$$

The data points on the graph are fitted with a linear regression line constructed using equation (3).

$$Y = \alpha + \beta X \quad (3)$$

The values of  $\alpha + \beta$  from regression line can then be substituted into equation (1), and the POD curve produced. However, the POD of a given flaw size is in fact an estimation based on the detection data from cracks of similar length but possibly varying widths – the curve is therefore suggesting that for cracks within a length range or interval, the POD will not be affected by crack width

The limitations of POD models can now be illustrated without delving further into the literature surrounding MLE methods, the ‘log-normal’ model [Bullock et al. 1994;, Fahr et al. 1993; US DOD 2007; Georgiou 2007], or statistical treatments for 95% confidence bounds [Berens & Hovey 1982; Spencer et al. 1993]. There are two reasons for not presenting the mathematical details of MLE or 95% confidence bounds. The first being that the MLE is only used to estimate  $\alpha + \beta$ , with equation (1) still used to construct the POD curve. The second reason being that it is adequate to state that, similar to equation (1), the ‘log-normal’ model and the mathematical formulae for the 95% confidence calculations are all based on  $a_i$ , i.e. ‘flaw’ size [see Bullock et al. 1994]. For currently published POD analysis methods, ‘flaw’ size has never needed to be more descriptive than ‘crack length’, and in fact many publications actually refer solely to ‘crack length’ [see Bullock et al. 1994 for an excellent example]. Crack width, i.e. a second variable, is not represented in any of the mathematical formulae – all the currently available models calculate POD as a function of only one variable. The POD model of equation (1) is therefore inherently single variable.

Furthermore, both the ‘log-odds’ and ‘log-normal’ models, due to their logarithmic basis, can only ever produce a positive or negative correlation between POD and flaw size. Whilst different methods can be used to find  $\alpha + \beta$ , the POD functions recommended for analysis of NDT reliability data [Spencer et al. 1993; AGARD-LS190; US DOD 2007], are unable to model an inspection procedure in which flaw detectability may be demonstrated to both increase and decrease with increasing values of a given flaw size variable.

### ***2.5.10 – Multi-variate POD***

Volker et al. published a three dimensional POD surface that was calculated using both the width and depths of the flaws [Volker et al. 2004]. Whilst representing a departure from typical two-dimensional POD curves, it is also noticeable that despite assessing ultrasonic NDT of metallic pipes, Volker et al. refer to pitting corrosion in terms of ‘defect’ width and ‘defect’ depth rather than using the traditional reference to ‘crack length’. The POD data presented by Volker et al. were calculated using Annis’ GLM or generalised linear model [Annis 2008]. However, GLM has the same single-

variate limitation as aforementioned POD methods, and. Volker et al. were only able to produce a multivariate plot because they calculated POD for different defect depths at constant defect widths and POD for different widths at constant depths. The results presented by Volker et al. also demonstrate only positive correlations with flaw size and POD.

Whilst the method employed by Volker et al is technically feasible, it requires vast numbers of flaws in order to estimate POD for a large range of widths and depths, which Volker et al. were able to replicate using a simulated specimens. However, an inspection process that cannot be replicated by simulated or virtual specimens would require actual flaws to be produced. In order for a POD model to be truly multivariate, it must be able to give POD as a function of more than one flaw size parameter, and to date, no such model has been published.

## ***2.6 – Overall summary of literature***

New aircraft designs are set to enter service containing 50% composite materials by weight and utilising monolithic carbon fibre reinforced plastic (CFRP) laminates for fuselage skins. CFRP laminates are particularly susceptible to reduction in compression after impact (CAI) strength due to impact damage, and the environment in which aircraft operate means that impact damage can occur from a multitude of sources. Examples of the surface appearance of impact damage to actual composite aircraft structures remain proprietary information. The available literature concerning impact damage to composite materials has a strong focus on impact testing using hemispherical impactors, usually Ø15 mm, Ø20 mm or Ø25 mm in size, and provides only limited information, due to the lack of metal mesh & paint layers on test specimens. There are no published studies of impact indentation<sup>1</sup> topography for monolithic, fully finished CFRP laminates.

A number of non-destructive testing/ inspection (NDT/ NDI) methods are available for detection and characterisation of impact damage to CFRP laminates. However, despite the availability of advanced NDT/ NDI methods, human visual inspection

---

<sup>1</sup> The term ‘flaw’ is used consistently throughout reliability assessment, NDT/ NDI & POD literature to refer to any form of damage or defect, be it a crack, a dent or delamination. Therefore, to provide consistency with literary terms, when describing the 3D surface topography of impact damage to composite laminates, the terms ‘indentation’ or ‘dent’ will hereafter be substituted by the term ‘flaw’.

remains an efficient method for scanning large areas of structure, and is thus likely to remain first line of damage detection for composite materials. There is, however, a lack of statistically valid information on reliability of visual inspection for impact damage on CRFP aircraft structures in the public domain.

Damage tolerance principles for commercial aircraft can be summarised as requiring that aircraft structures demonstrate continuous airworthiness for damage below barely visible impact damage (BVID) sizes, or inspection procedures be implemented at appropriate intervals to detect damage before it compromises airworthiness. There is little *published* evidence to suggest that the size of impact damage that can be *reliably* detected by visual inspection on an actual CFRP aircraft structure is the same as the BVID sizes that are used to calculate damage tolerance sizes for CFRP aircraft structures. A focal issue for the Civil Aviation Authority (CAA) is whether reliability of visual inspection of composite aircraft structures is adversely affected by the surface colours and surface finishes used on aircraft in airline service.

Reliability studies for NDT processes generally culminate in a set of probability of detection (POD) curves, which quantitatively model the process reliability as a function of a single flaw size variable. Impact damage dents on a composite laminate are 3D in shape, and require multiple variables to describe their topography, all of which may affect their detectability, i.e. POD for 3D flaws is unlikely be accurately modelled solely as a function of a single variable. The term ‘flaw size’ in POD literature has become invariably synonymous with ‘crack length’. The issue of crack width has been conveniently allayed, and a ‘bigger is better’ mindset prevails in NDT & POD literature. Furthermore, widely accepted models for POD, due to their logarithmic basis, cannot model an inspection method whereby detectability increases, then perhaps reduces with an increase in flaw size.

Surface flaw topography, the surface colour, the surface finish of a structure and the available lighting can all affect the saliency of visual perception cues such as shading, specular reflections and specular highlights. Saliency of visual cues is likely to affect the visual detectability of 3D impact damage dents, thus affecting visual inspection reliability for composite aircraft structures. The available literature on visual perception contradicts a ‘bigger is better’ assumption for 3D dent detectability.

## ***Chapter 3 – Experimental Design***

### ***3.1 – Experimental aims & objectives***

The experimental aim was to make measurements of the reliability of visual inspection for impact damage on CFRP aircraft structures. The experimental objectives were to explore the effects of flaw size, surface colour and surface finish on visual inspection reliability.

### ***3.2 – Examples of impact damage to CFRP laminates***

The literature search identified a lack of examples of the visual appearance and surface topography of impact damage to composite aircraft structures. A series of experiments were performed in order to produce examples of different shapes and energies of impact damage on two thicknesses of fully finished and unfinished CFRP laminate. Different shaped tips were used in order to provide information on the impact dent topographies produced by different shapes of striking object. Alongside the traditional Ø20 mm hemispherical impact tip, a larger radii hemispherical tip, a flat cylindrical tip, and a wedge or ‘tool’ shape tip were also used. The experimental methods for the production of the impact dents are reported in chapter 4.3. Ultrasonic C-scans, as described in chapter 4.2 & 4.4 were made of all test coupons in order to characterise the delamination damage.

After observing the dents produced by the impact experiments, it was unclear which flaw characteristic would affect the detectability of such impact dents, i.e. depth, width or other. It was also noted that the circular dents from the hemispherical tips were different in shape to the indentations produced by the other impactor tip shapes. The possible range of impact object shapes likely to be encountered by an aircraft is vast, and a decision was therefore taken to limit further study to impact dents from hemispherical tips similar to those used in standard impact tests on fibre reinforced materials.

A significant issue when describing the impact dents was from hemispherical objects was that neither impact dent depth and dent width could provide a quantitative description of dent shape. Metallographic sectioning methods, as described in chapter



4.5.6 were employed in order to obtain cross sectional views through a selection of impact dents. These sections revealed that the impact dents had a common sectional profile shape, as described in chapter 5.1.4. A geometric model was developed, as described in chapter 4.6 in order to describe this sectional profile in quantitative terms.

In order to quantify the surface topography of the hemispherical impact dents, the values used to construct the geometric model of the dents were derived from touch-trigger probe scans of the actual impact dents, as described in chapters 4.5.5 & 4.6.

Under visual observation, the impact dents from 20 mm tips appeared to produce crisper, more discernable shadows, sharper shading gradients and more discernable highlight distortions than those from the 87 mm tips. After studying available theories of visual perception, it was suggested that the size of the shadow cast by the impact dents might be linked to their detectability. Furthermore, it was suggested that dent detectability might be affected by the “severity” of the flaw shape, i.e. whether the dents were “hard-edged” (sectional profiles with small radii) or “blended edged” (sectional profiles with large radii).

### ***3.3 – Initial visual inspection trials with virtual specimens***

To test the suggestions regarding dent shape and detectability using actual dents on physical specimens would have proven time and cost prohibitive. As a means of quickly testing the above suggestions and providing a means of assessing the possible detectability of different combinations of dent widths and depths without large financial outlay, a series of experiments using projected images of computer produced virtual specimens was devised, as described in chapter 4.11. The series of four virtual trials was performed back-to-back in sequence using a single group of novice participants whom were given adequate briefing as described in chapter 4.13. Inspection time was controlled, as described in chapter 4.11, by means of an automated display sequence. Viewing angle, by nature of the specimens being two-dimensional (as described in chapter 4.10), was controlled although head movements were not controlled. Participant related factors i.e. search/ eye scanning method, eyesight, contrast sensitivity, training/ experience, fatigue level were neither

controlled nor measured. Environmental factors i.e. temperature and noise were uncontrolled and not measured as it was felt that their levels were within reasonable limits hence their effect on detection results would be negligible.

The first virtual specimen trial was designed to assess the detectability of different widths of flaw of the same depth. As described in chapter 4.10, the width and depth of each flaw was controlled, and by replicating the same simulated lighting conditions, the computer rendering of each flaw produced shadows that varied in areal size in direct relation to flaw width. Analysis of the detectability results obtained from this experiment, as described in chapter 5.4, suggested that the shadow cue produced by flaws greater than 6.5 mm wide was sufficient in size for at least 50% of participants to detect.

The second and third virtual specimen trials used specimens containing images of the shadow produced by three widths of flaws of differing depths, chosen as the 50%, 70% and 90% detectable widths from trial 1, as described in chapter 5.4. The shape of the flaws was altered to a hemispherical shape, in order to be more representative of the impact dents seen on CFRP coupons, as opposed to simple cylindrical cut-out shape flaws as used in trial 1.

Trial 2, as described in chapter 4.10 was used to provide preliminary information on how changes in dent depth and resultant changes in shadow cue size might affect dent detectability. The results of the second virtual trial suggested that the shadow cue produced by hemispherical shaped flaws 0.15 mm deep were detectable by at least 50% of participants.

By adding a radius to the edge of the flaws used in trial 2, the specimens in trial 3 (see chapter 4.10) were used to test for discernable differences between the detectability of similarly sized hard-edged and blended-edged flaws. The results of the third trial suggested that a blended edge could reduce the detectability of hemispherical dents for similar depths and widths, although the reduction could not be quantified.

In order to quantify possible differences between detectability of hard-edged and blended-edged dents, a fourth trial was designed in which both hard and blended edge

flaws of the same size were inspected within the same trial. The purpose of trial 4 was to determine whether, for the same participant under the same conditions, a blended edge affected the detectability of dents of the same width and depth. The dents represented in trial 4 varied in both width and depth, as described in chapter 4.10, providing a range of sizes for assessment of the effect of edge blending. The results of trial 4 demonstrated that reductions in dent detectability due to a blended dent profile versus a hard-edged profile could be expected for larger width ( $>15$  mm) flaws at a constant depth.

The first series of virtual trials provided information from which “engineering judgments” were made concerning the possible range of sizes to be replicated in future visual inspection trials for CFRP impact damage dents. The general summary was that a minimum dent width of 5 mm should be used, and that the blended edge observed on actual impact dents had highly significant detectability implications, particularly for wide ( $>15$  mm) and shallow ( $<0.25$  mm) dents, and needed to be authentically replicated in future trial specimens.

An issue of concern following the completion of the virtual trials was whether the detection results obtained from virtual specimens were comparable to inspection of an actual physical specimen.

### ***3.4 – Reproduction of impact dents as facsimile specimens***

The initial series of virtual trials identified that replication of the blended dent shape typical of hemispherical impacts to painted CFRP on test specimens would be essential to obtaining valid visual inspection results. However, facsimile specimens were the only viable option for this study. A method was developed by the author and implemented by M&M patterns of Wavendon, Milton Keynes, whereby circular dents with specified geometries were NC machined & polished into Plexiglas panels in order to produce representations of impact dents to painted CFRP laminate. The NC data for the sectional profile of the machined circular dents was produced as 3D CAD data by revolving a section line that was produced using the same geometric variables as used to describe the impact dents on CFRP laminates. Hence, the same blended edges that were observed on actual dents, and understood to be important to visual

inspection reliability, could be reproduced in the same proportions on facsimile specimens.

Reproducing accurate sectional profiles was a key requirement for the facsimile specimens, in particular retaining the proportions, or relationships between geometry variables so as to accurately represent either an Ø20 mm or Ø87 mm impact to a 17 or 33 ply laminate. Whilst it would have been possible to reproduce CMM data of impact dents described in section 4.2 & 5.1, the controlled factor in producing these dents was impact energy. Flaw sizes and geometries in these sets of dents were not controlled and as a result there was uncontrolled distribution between the values of the geometric variables within the dent shapes. To allow the effects of dent depth and width on flaw detectability to be investigated, it was preferable to distribute the flaw sizes by either width or depth. However, it was unfeasible to attempt to obtain flaw geometry data for specified dent depths or widths due to the difficulty in guaranteeing that falling weight impacts would produce exact dent sizes and shapes, across a specified size range.

As a solution to the problem of obtaining dent geometry data for given dent sizes, the geometry data obtained from CMM data of the examples of actual dents produced by Ø20 mm and Ø87 mm impacts to 17 & 33 ply painted CFRP were plotted, as described in chapter 5.1.6. Using these plots, relationships were derived to interlink impact energy to the geometric variables used to describe dent sectional profiles. For each impact tip and laminate combination, discrete relationships were identified. These relationships facilitated the calculation impact energy and each of the geometric variables required for reconstruction of the sectional profile of a dent, based on a single variable, be it depth, width or impact energy. Thus, for Ø20 & Ø87 mm hemispherical impacts to 17 & 33ply painted CFRP laminates, it became possible to choose a range of dent sizes, and reconstruct the sectional profile of each size of dent.

The sectional profile reconstructions were used to build 3D CAD models representing a range of sizes of impact dents, which were then forwarded to M&M Patterns for NC machining. Matching the values of the geometric variables in the 3D CAD model to those calculated using the relationships from data of actual impact dents ensured the

sectional profiles of the facsimile dents were accurate representations of impact damage to a CFRP laminate.

### ***3.5 – Visual inspection trials with physical specimens***

Having developed a repeatable method for producing representations of impact damage to CFRP laminates, facsimile specimen panels were produced for use in visual inspection trials with physical specimens, as described in chapter 4.9 & 4.10.5.

In order to investigate the effects of colour, it was decided that examples of impact damage should be replicated on three different colours of specimens. Grey, dark blue and white were chosen as colours typical to those seen in aerospace applications. It was also foreseen that the prominence, or saliency of shadow and shading cues for visual perception (and hence detectability of flaws) could differ across these colours due to white being a “light” base colour, grey a “medium” base colour and blue a “dark” base colour. In order to investigate the effect of differences in surface finish on flaw detectability, it was decided that examples of impact damage (flaws) should be replicated on both gloss and matt finishes in each colour.

The experimental method for physical specimen trials, as described in chapter 4.12, was a development of that used for virtual specimen trials. A 20-second interval between each specimen display period was introduced in order to allow panel changeover, although the display time of 5 seconds was retained. A trial duration limit of 20~30 minutes was imposed to avoid participant fatigue, leading to 64 specimens being chosen as a convenient number of specimens that allowed incorporation of a 3:1 unflawed to flawed specimen panel ratio within the time limit. Thus, 16 of the 64 specimen panels contained between one and three of 32 machined impact dent facsimiles. The variation in numbers of dents per panel ensured that participants did not always expect to find a given number of dents on a flawed specimen. The distribution of flaw sizes across the flawed panels was randomised and the flaw locations on each panel were also randomised, as described in 4.12. To reduce the possibility of participants learning where and when flaws might be present, the display sequence of flawed and unflawed specimens was randomised. To further guard against specimen familiarisation for participants undertaking more than one

trial, the randomised specimen display sequence was alternated between forward and reverse.

Novice, paid, participants were used and participant briefing (4.13) included examples of the dents to be detected on the specimen panels. Some of the participants had previously undertaken the first series of trials with virtual specimens. Several participants undertook trials with more than one colour/ finish specimens, although there was no particular sequence due to trials being performed on different days in different weeks, as per facility, personnel and participant availability. Personal data such as gender, age, eyesight ability, colour-blindness, previous experience or current level of fitness/ well being was not recorded. The participants were seated in a chair placed at a marked distance of 1.2 from the screen. Head movements were allowed during the visual inspection task, which meant that some participants would have obtained views of the specimen panels from different visual angles. It was accepted that some advantage may have been gained by this practice, and it was felt that physically constraining participant head movements may have deterred participation. Standing up or reaching forward to touch the specimens was not permitted, as doing so would have altered the mode of inspection from visual to tactile.

The visual inspection trials with physical specimens were performed in a meeting room, with ambient lighting provided by external windows and overhead fluorescent luminaires. Light levels were assumed to be constant and were neither measured nor controlled. Temperature and humidity were not recorded and were not controlled.

The results of the trials with physical specimens are presented in chapter 5.5.1.

### ***3.6 – Second series of trials with virtual specimens***

The first series of trials with virtual specimens proved to be a valuable tool for generating visual detection data on a cost and time efficient scale, with minimal logistical requirements compared to use of physical specimens. However, due to differences in the dent geometries used and variations in the experimental method, a like for like comparison between the virtual and physical specimen data was not possible. A second series of virtual trials was implemented in order to identify

whether detection results obtained with virtual specimens were comparable to those obtained with physical specimens. Grey specimens were used in order to provide comparison with the grey physical specimens. The ability of a grey surface to exhibit both shadow and shine also helped mitigate possible bias due to increased or reduced shadow or highlight cue saliency on lighter or darker colours. The methodology for these trials is described in 4.12. The same display timings and sequences as the physical specimen trials were retained, the only difference between the trials being the lack of physical specimens and the reduction of ambient lighting in order to improve display clarity.

Some of the participants in the second series of virtual trials undertook physical specimen trials, although the exact sequence in which individual participants undertook trials was not recorded. Display brightness was not recorded, although the display size of the images was checked using a ruler in order to ensure they were being displayed at actual 600 mm x 600 mm size.

The detection results from the virtual specimen trials differed to the detection results obtained with physical specimens, suggesting that visual inspection reliability data obtained with virtual specimen was not directly comparable to inspection of physical specimens, although similar detection vs. dent size trends were identified within both sets of results.

## ***Chapter 4 – Experimental Methods***

### ***4.1 – Production of fully finished CFRP laminate samples***

In order to replicate a typical CFRP aircraft structure, laminates were produced at Cranfield University from similar materials to those specified in the Structural Repair Manual for an Airbus A340 horizontal stabiliser skin [Airbus SRM 2003]. The materials were as follows:

- Hexcel AS4/8552 pre-preg Carbon Fibre Epoxy Pre-Preg Carbon Tape (UD)
- Hexcel P0108 - 8552/42%/120 (Pre-Preg Glass Fibre 120 Style, 120g/m<sup>2</sup>, 4H Satin)
- Aeroconsultants Bronze Mesh, 166 threads/in [See Bopp 2006]

Four 750 mm x 1000 mm panels of carbon fibre (CFRP) laminate, two 17ply and two 33ply, were produced at Cranfield University by laying up 300 mm wide Hexcel AS4/8552 pre-preg tape as follows:

17ply - [+45,-45,0,-45,+45,90,-45,+45,0,+45,-45,90,+45,-45,0,-45,+45]

33ply - [+45,-45,0,-45,+45,90,-45,+45,0,+45,-45,0,-45,+45,+45,-45,90,-45,+45,+45,-45,0,-45,+45,0,+45,-45,90,+45,-45,0,-45,+45]

The lay-up was de-bulked every fifth ply. The lay-up for one of the 17ply and one of the 33ply panels included a single layer of glass fabric and a single layer of bronze mesh on one side of the panel before curing. The CFRP lay-up, glass fabric and bronze mesh were co-cured at 180°C according to the manufacturers recommended cure cycle for the 8552 resin [Hexcel 2003]. For the panels containing the lightning strike protection (LSP) layers, the mesh incorporating side of the panels were painted by GKN Aerospace with primer and paint according to Airbus specifications [Airbus Oct 2005, Dec 2005 & Mar 2006]. The completed painted and unpainted panels were cut into 100 mm x 150 mm coupons for impact testing. The coupons were labelled (on the unpainted side for fully finished laminate) with a self-adhesive label, which was numbered with a permanent marker pen. Water immersion ultrasonic C-Scans of each coupon were made in order to identify, and remove from the specimen set, any coupons containing voids within the laminate. Samples of undamaged, painted LSP laminate from a panel of each thickness were prepared using metallographic sectioning methods, and were used to confirm that the ply-lay up sequence was



correct. Figure 4.01 shows a section through the laminate, which is free of significant voids or resin rich areas.

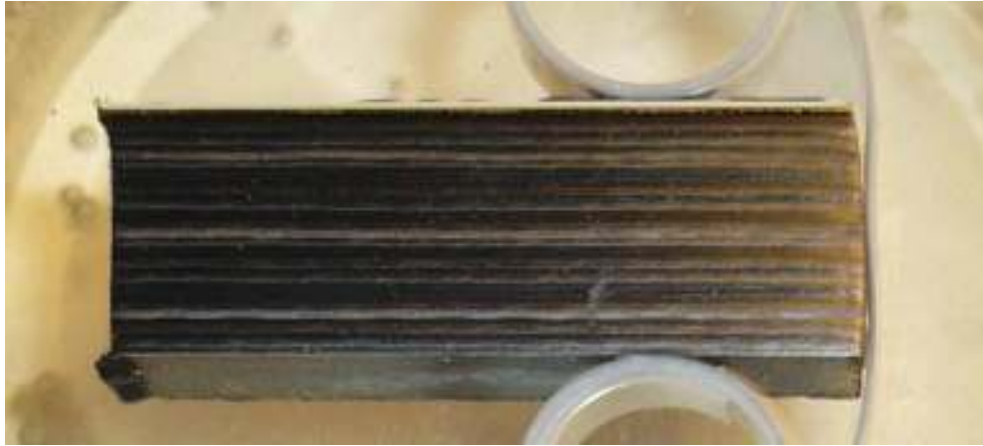


Figure 4.01 – Section through 33ply laminate with painted surface to the top

#### ***4.2 – Ultrasonic C-Scanning***

The equipment used for C-Scans was a Structural Diagnostics Inc. water immersion ultrasonic scan system coupled with an ultrasonic flaw detector [Baugh & Weedon] and a 386 personal computer running Windows 3.11. All scans were made using the SDI SCAN-4 program [Richards Computer Products 1991] with a scanning pitch of 0.25 mm x 0.25 mm thus achieving an acceptable compromise between scan resolution and scan time.

#### ***4.3 - Falling weight impact damage***

A Rosand Type 5 falling weight impact tester with interchangeable tips was used to create impact damage on the coupons. For impact testing, the coupons were placed into an open aperture support fixture conforming to Boeing BSS7260 [Boeing 1988]. The test conditions for each of the coupons are given in table 4.01. The impact energy for each impacted coupon was written onto the coupon identification label.

As detailed in Table 4.01, four different types of stainless steel impact tips were used. The Ø20 mm hemispherical impact tip is typical of that used in published examples of impact damage and CAI testing of composite materials. The Ø87 mm impact tip is a larger variant of the hemispherical shape. The flat cylindrical tip was included in order to provide information on the impact flaws produced by such shapes in comparison to the hemispherical shaped tips. Likewise, the wedge (or tool) shape

impactor was included in order to assess the damage morphology that impacts from items such as tools might cause. As reported by Cartié & Irving, 2002, impact energies below 5J are unlikely to produce subsurface delamination, thus the 5J lower limits of impact energy. Table 4.01 provides details of sample numbers, impact energies and impact tip type for each of the tested coupons.





Impactor Type							
							
Ø20 mm Hemispherical	Ø87 mm Hemispherical	Ø70 mm Flat Cylinder	13 mm x 4 mm Wedge/ Chisel				
Carriage Mass – 2.030kg	Carriage Mass – 2.030kg	Carriage Mass – 2.030kg	Carriage Mass – 2.030kg				
Total Mass – 2.172kg	Total Mass - 2.431kg	Total Mass - 2.960kg	Total Mass - 2.054kg				
<b>17ply LSP &amp; Painted CFRP coupons</b>							
Coupon #	Impact Energy	Coupon #	Impact Energy	Coupon #	Impact Energy	Coupon #	Impact Energy
27	5J	95	5J	36	10J	34	5J
26	10J	94	10J	37	15J	33	10J
25	15J	93	15J	38	20J	32	15J
24	20J	29	20J	40	30J	35	17.5J
23	30J	92	30J	39	40J	31	20J
		30	40J				
		90	50J				
<b>17ply non finished CFRP Coupons</b>							
Coupon #	Impact Energy	Coupon #	Impact Energy	Coupon #	Impact Energy	Coupon #	Impact Energy
U13	5J	U18	5J	U25	10J	U30	5J
U14	10J	U19	10J	U26	15J	U31	10J
U15	15J	U20	15J	U27	20J	U32	15J
U16	20J	U21	20J	U28	30J	U34	17.5J
U17	30J	U22	30J	U29	40J	U35	20J
		U23	40J				
		U24	50J				
<b>33ply LSP &amp; Painted CFRP Coupons</b>							
Coupon #	Impact Energy	Coupon #	Impact Energy	Coupon #	Impact Energy	Coupon #	Impact Energy
2	5J	9	20J	18	10J	14	20J
3	10J	8	30J	19	20J	15	30J
4	15J	10	40J	20	30J	16	40J
5	20J	11	50J	21	40J	17	50J
6	30J	12	60J	1	50J		
7	50J	13	70J	70	60J		
<b>33ply non finished CFRP Coupons</b>							
Coupon #	Impact Energy	Coupon #	Impact Energy	Coupon #	Impact Energy	Coupon #	Impact Energy
U38	5J	U44	20J	U50	10J	U56	20J
U39	10J	U45	30J	U51	20J	U57	30J
U40	15J	U46	40J	U52	30J	U58	40J
U41	20J	U47	50J	U53	40J	U59	50J
U42	30J	U48	60J	U54	50J		
U43	50J	U49	70J	U55	60J		

Table 4.01 – Testing matrix for impact testing of CFRP coupons

#### ***4.4 – Measurement of delamination***

Each coupon was C-Scanned after impact, in order to measure the sub-surface delamination damage at the impact site. Images of the C-Scan data were produced as bitmap format screen captures from the ANALYSIS program [Richards Computer Products 1991]. The bitmap images were fitted with a 10 mm grid using suitable image processing software, and used to measure to the width of the sub-surface damage (delamination) to the nearest 1 mm. By using a square count method, or where possible, an area calculation based on measurements taken from the image, the area of the delamination can be measured. Figure 4.02 illustrates a typical C-Scan image of an impact-damaged coupon.

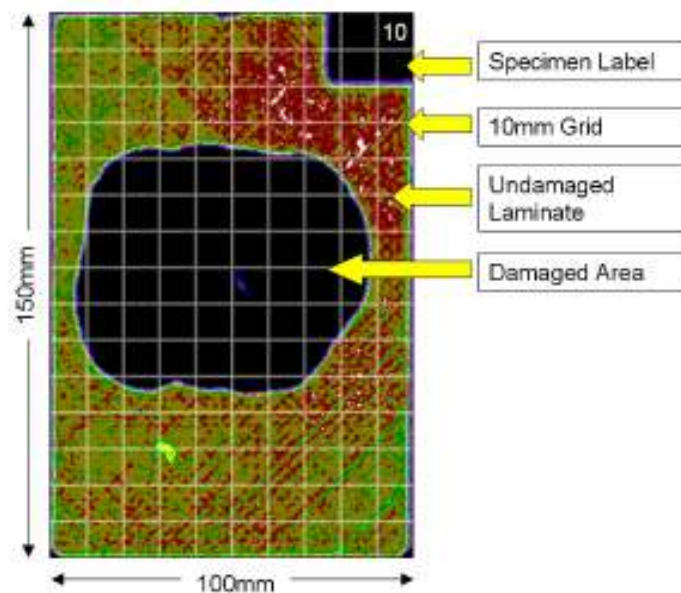


Figure 4.02 – C-Scan of 40J impact damage from Ø87 mm on 33ply painted, laminate with bronze mesh

#### ***4.5 – Measurements of impact damage surface topography***

##### ***4.5.1 – Width measurement with Vernier callipers***

The width of the surface flaws on all of the coupons was first measured approximately using a vernier calliper device, to the nearest 0.02 mm.

#### ***4.5.2 – Depth measurements with a depth gauge***

For all coupons, the surface flaw depth was measured through the centre of each flaw, with the coupon placed atop an open cylinder. The open cylinder allowed the coupon to sit flat despite the presence of back-face fibre break out. The depth measurements were made using a mechanical dial gauge (0.01 mm accuracy) mounted to a stand, as illustrated in figure 4.04. An arbitrary point on an unaffected area of surface, just outside of the area affected by the surface flaw, was used as the origin.



Figure 4.04 – Dial gauge measurement of surface flaw depth

#### ***4.5.3 – Depth gauge profiles***

Depth measurements were made across the 100 mm width of the surface of hemispherical impact damaged, fully finished coupons, through the centre of the surface flaw, using a dial gauge (0.01 mm accuracy) and a sliding track (see figure 4.05). Depth measurements were taken at 5 mm intervals outside of the surface flaw region (as determined from approximate vernier measurements), and at 1 mm intervals within the flawed area. The coupons were mounted to the slider by pressing them down onto lumps of putty, thus affording a stable mount and clearance room for back-face fibre breakouts. Plots of depth vs. track distance gave representations of the sectional profiles of the surface flaws. Figure 4.06 illustrates an example of a 30J, Ø20 mm impact on a 17ply painted laminate. The advantage of this method of data

representation is the ability to stretch the Y-Scale in order to better observe the surface flaw shape.

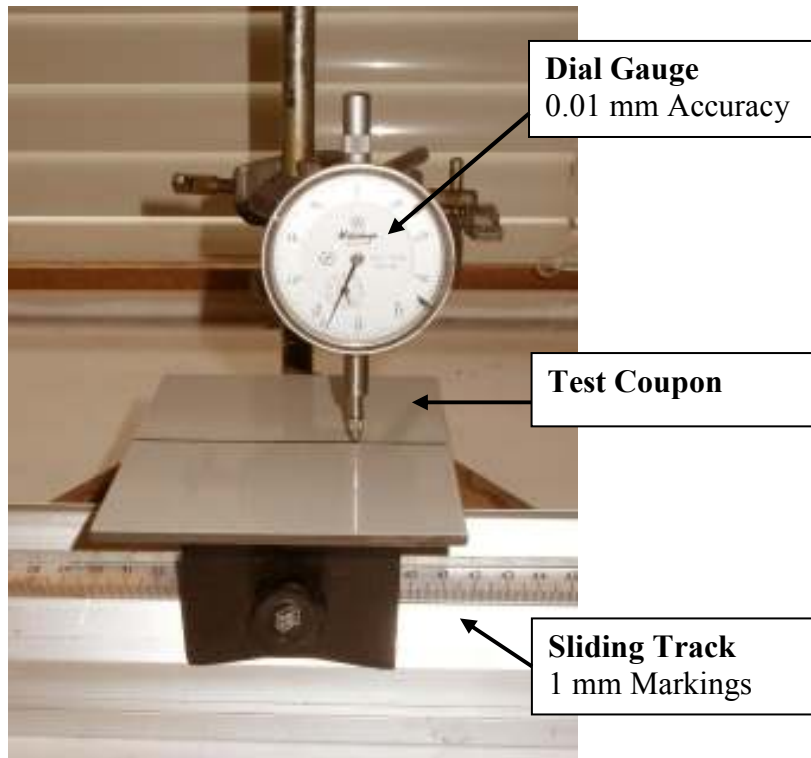


Figure 4.05 – Dial gauge setup for measuring vertical depth vs. horizontal distance.

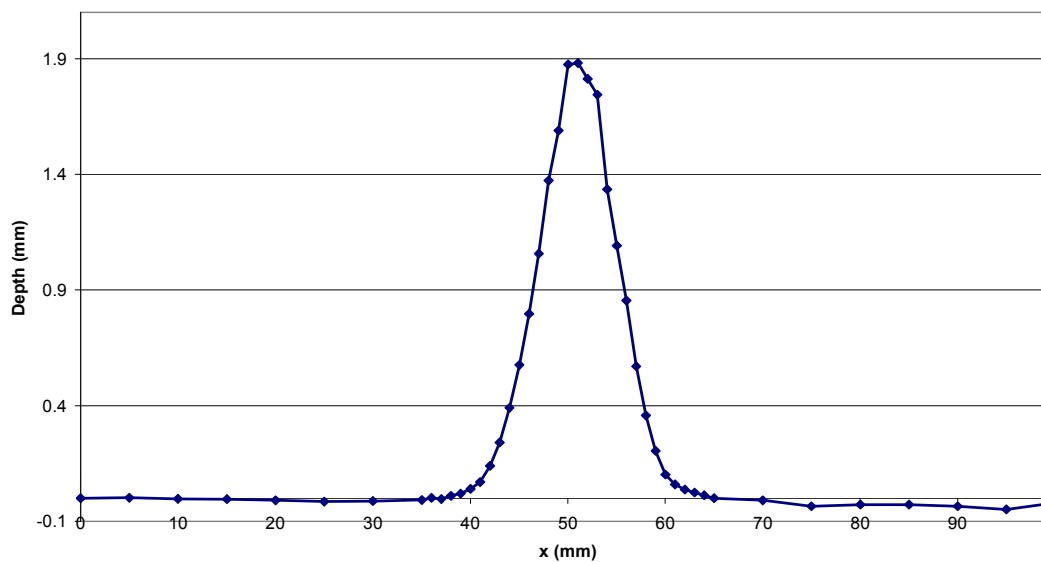


Figure 4.06 – example of graph representing section through surface flaw, produced from depth gauge measurements.

#### ***4.5.4 – CMM (Coordinate Measuring Machine) coupon surface digitisation***

A Renishaw Cyclone Series 2 touch-trigger probe CMM machine was used to produce digitised traces of hemispherical impact flawed, fully finished coupon surfaces using three dimensional data points with X, Y and Z coordinates (3D points cloud). The machine was set to scan with a pitch of 1 mm by 1 mm in the X & Y axes, with  $\pm 1\mu\text{m}$  accuracy in the Z-axis. The scanning area was 80 mm x 80 mm in size, centred approximately on the surface flaw on each coupon. The point cloud data was saved as IGES data, and imported into a computer aided design (CAD) file using CATIA. The CATIA system was used to produce section lines through the points cloud in a Z/Y plane through the transverse (100 mm) section of each coupon.

#### ***4.5.5 – Width measurements from depth gauge & CMM data***

In order to measure the surface flaws caused by hemispherical tip impacts, using the CMM data, the series of points representing the surface flaw centre, and a series of points on the coupon surface close to the flaw area were identified within the CMM point cloud data (see figure 4.07) by producing section lines through the points cloud. Once these two sections were isolated within the CMM points cloud, the other section lines were removed leaving only two section lines as seen in figure 4.07 & 4.08.

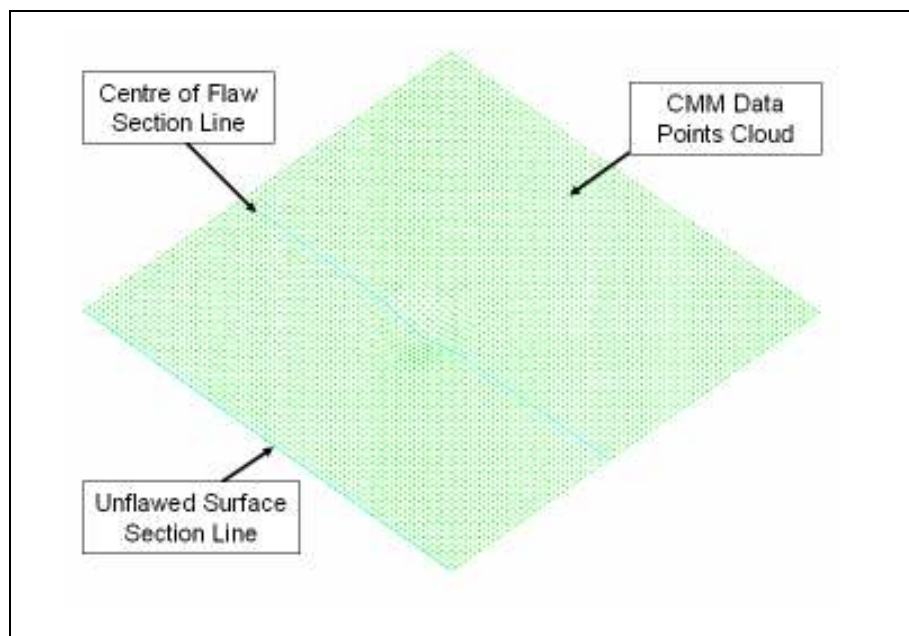


Figure 4.07 – Section line positions on CMM data points cloud

Vertical (Z-axis) depth measurements were made every 1 mm along the line (figure 4.08). The depth measurements were made using a second section line, made through the coupon surface outside of the flaw area, as the origin.

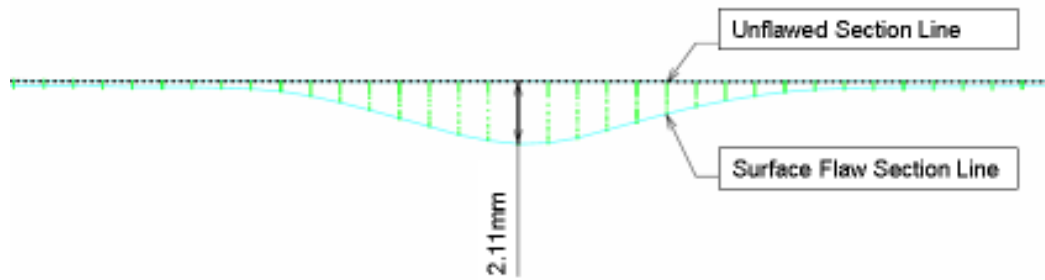


Figure 4.08 – section lines obtained from 2.11 mm deep surface flaw using CMM machine, vertical data lines are 1 mm spaced

The depth measurements from the CMM data were also plotted using Excel, and by placing them alongside the depth gauge measurements and subsurface damage width measurement from the C-Scans of each coupon, a clear picture of the damage morphology could be obtained (See Boulic, 2007). An example is given in figure 4.09.

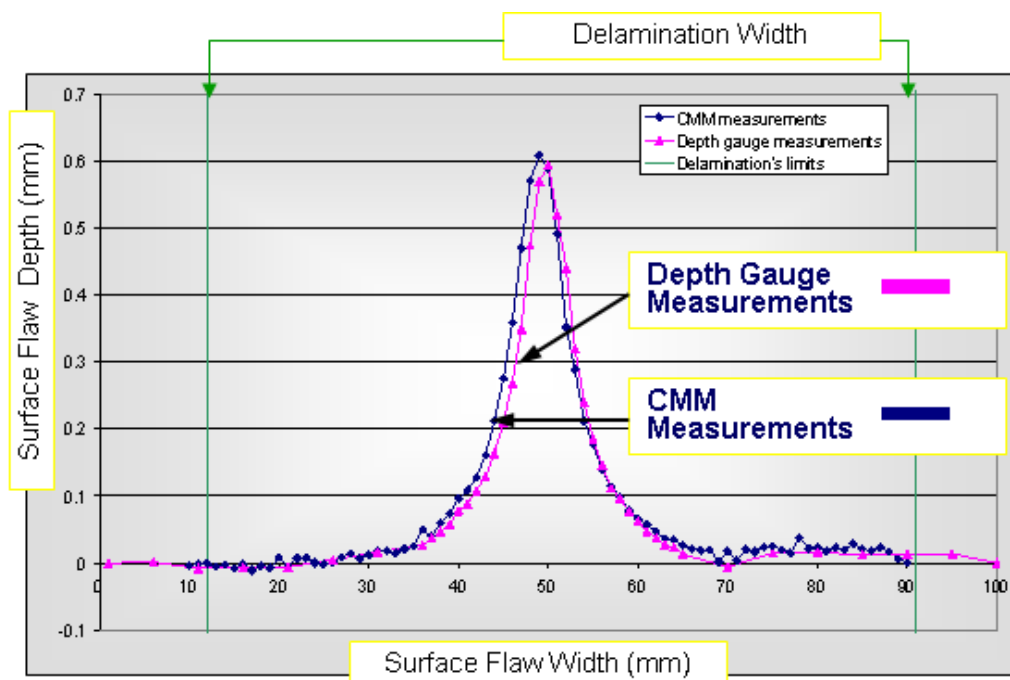


Figure 4.09 – typical graphical representation of depth gauge, CMM and C-Scan measurements of impact damage and surface flaw on a coupon.

The approximate flaw width measurements made using Vernier callipers were used to mark the estimated flaw endpoint regions on the surface flaw profiles. In these regions, the unflawed surface line was drawn by extending a line of best fit through data points that were known to represent an unflawed region. Using the vernier measurement regions as a guide, the first of three points, running towards the flaw



centre, in the marked region, that were consecutively lower than the unflawed surface line were identified. With two of such points identified on each side of the centre of the flaw, the flaw endpoints were marked. Flaw width was thus obtained by taking the distance between the two endpoints.

#### ***4.5.6 – Metallographic sectioning technique***

Selected fully finished, impact damaged coupons were cut into a 30 mm square, with the centre of the square placed at the centre of each surface flaw. The squares were set into resin, ground back and polished so that the section ran through the centre of the surface flaw.



Figure 4.10 – Section through 50J, Ø20 mm impact on 33ply painted, mesh covered laminate

A microscope fitted with a digital camera was used to produce multiple small digital images of the finished sections. The 3 mm x 3 mm images were then combined, and arranged in the correct sequence to produce a composite image (figure 4.10) which provides a high-resolution photographic view through the 30 mm section of damaged laminate.

#### ***4.6 – Reconstruction of surface flaws using geometric lines & arcs***

The sectional profiles of hemispherical surface flaws were recreated in a CATIA CAD system, by overlaying a set of geometric lines onto the section lines produced by the CATIA system through the CMM points cloud for the surface flaws. The section lines created by the CATIA system are splines, and are non-parametric, i.e. the shape of the section line is simply a collection of short, 2D lines running from point to point much like a dot-to-dot picture. New geometric lines with lengths and radii were overlaid to match the shape of the non-parametric splines, as seen in figure 4.11.



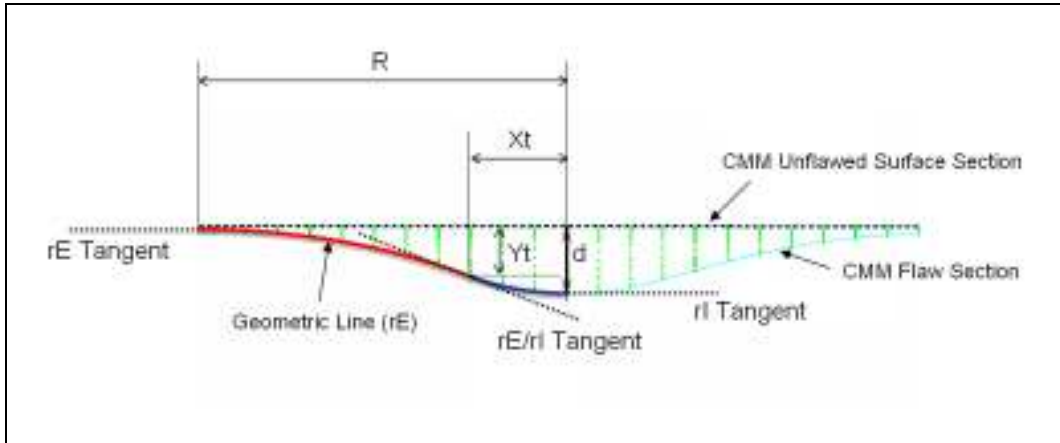


Figure 4.11 – Construction of geometric lines to match CMM data section lines

In order to ensure a smooth transition between the arcs used to reproduce the surface flaw section and the line representing original flat surface, without a visible join line, the tangency at the end of arc  $rE$  where it meets the planar surface was set to be horizontal (i.e. the same as the surface). To ensure symmetry, and not create a V shape at the centre of the flaw, the end of arc tangency of  $rI$  at the flaw centre line was constrained to be horizontal. A final tangency constraint was placed between the join of arcs  $rE$  and  $rI$ , in order to ensure a smooth, step-less transition between the arcs. These tangencies can be seen in figure 4.11.

The geometric variables of the lines were adjusted until the geometric line fitted as best as possible to the CATIA section splines through the CMM points data (see figure 4.11). From the new geometric fitted lines and arcs, it was possible to derive accurate values for the geometric variables used to describe the flaw shapes. The values that could be derived from this method are illustrated in figure 4.12.

Whilst actual impact dents may have had varying sectional profiles across the width of the dent, the characterisation data represent only the deepest section line, i.e. the central section line though each impact dent.

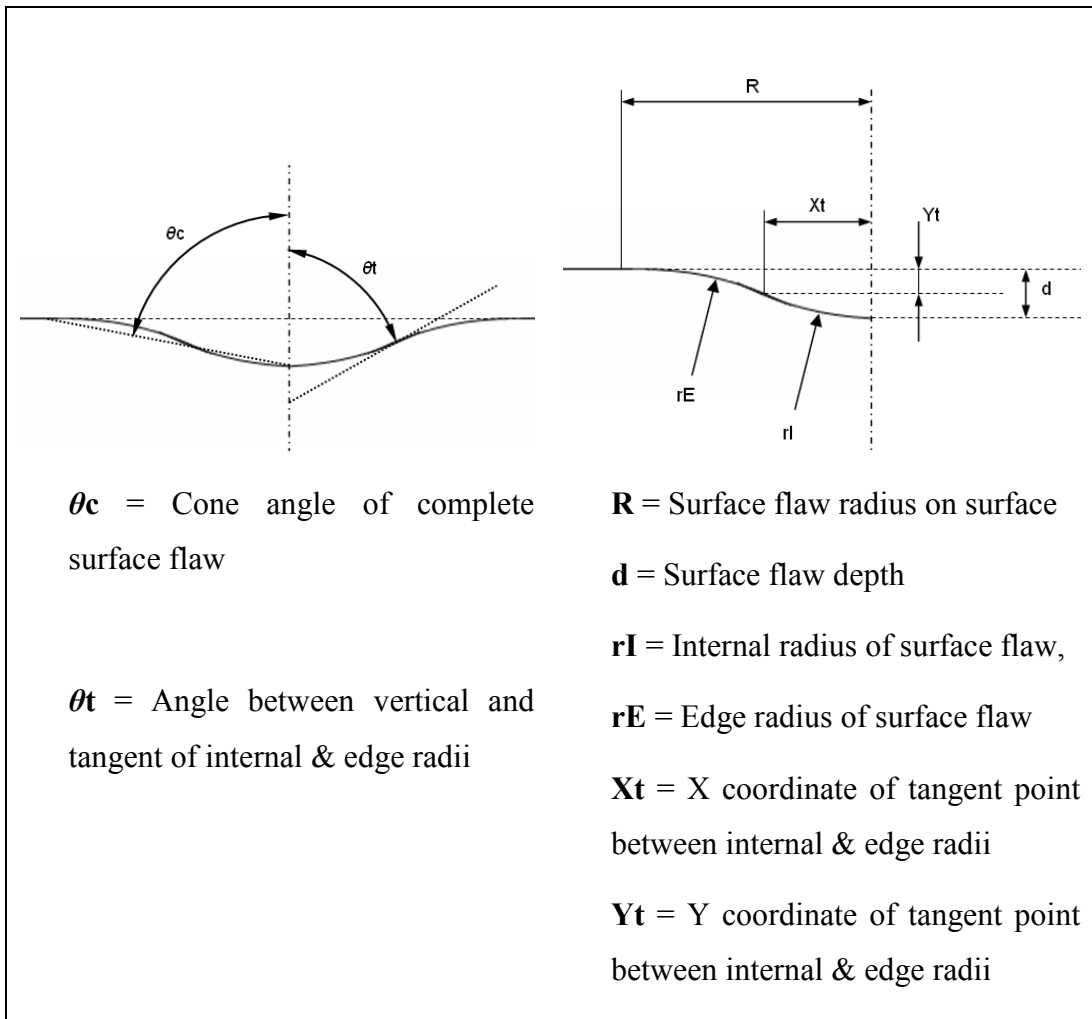


Figure 4.12 – Geometric variables used to reconstruct a surface flaw section

#### 4.7 – *Reproduction of impact flaws as 3D CAD data*

Representations of flaws were created using the Solid Works CAD program [SolidWorks 2000] by revolving geometric section lines around a vertical centre axis as illustrated in figure 4.13. The 3D revolved geometry was cut away from top surface of a 3D model of a flat panel, leaving a circular surface flaw on the panel surface.

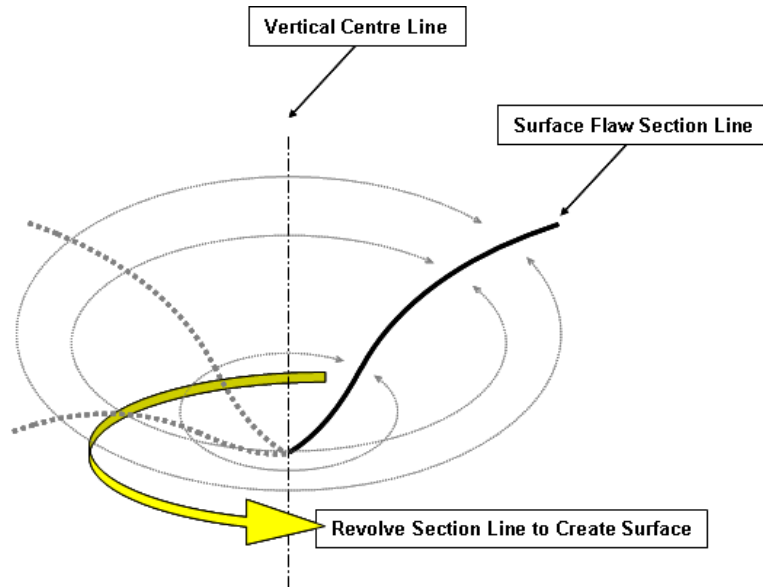


Figure 4.13 – Revolution of surface flaw section line to produce 3D flow surface

#### ***4.8 – Production of virtual facsimile specimens***

Sets of virtual specimens were produced by photo-realistically rendering 3D Solid Works [SolidWorks 2000] CAD models of panels containing 3D surface flaws. The 2500 pixel x 2500 pixel rendered images were saved as bitmap files. The photo-realistic images of each specimen represented an observer's view normal to the inspection surface of the panel. A gloss grey finish was replicated, and the simulated lighting direction was at 30 ° from the vertical plane and 30 ° from the plane normal to the surface (i.e. facing across, and down on to the panel, from the top right hand corner to the bottom left). The rendering parameters can be found in appendix A. Figure 4.14 illustrates an example of a virtual surface flaw that represents impact damage to a fully finished CFRP laminate, as used in the second series of virtual trials.

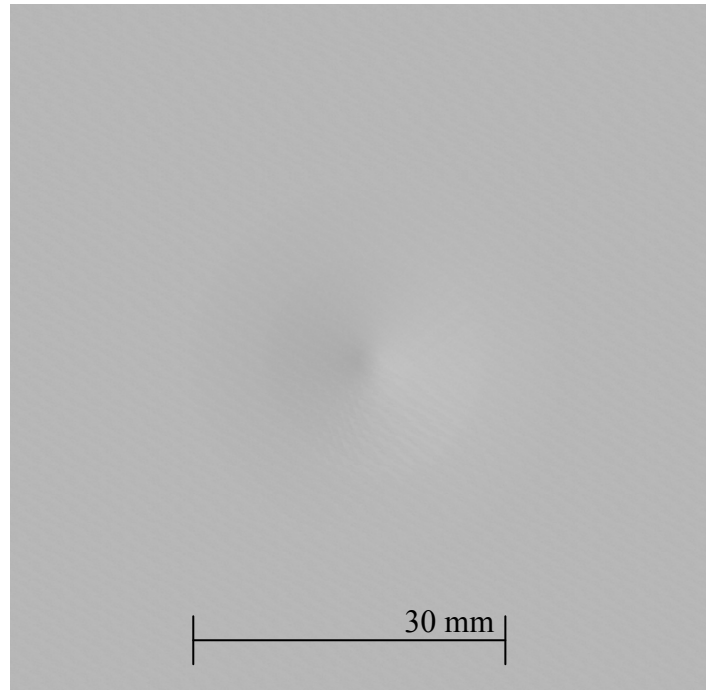


Figure 4.14 – Virtual specimen flaw, representing Ø20 mm/33ply 46J impact damage (Ø29.96 mm / 0.57 mm deep)

#### ***4.9 – Production of physical facsimile specimens***

The 3D CAD geometry of each surface flaw was NC machined, in specified locations, into 3 mm thick Plexiglas panels, and the surface flaw area was polished to return the flaw site to its original surface finish quality. Figure 4.15 illustrates a test piece that contains 12 surface flaws produced in this way, and can be compared with figure 4.16 which shows a photograph of an actual impact damage surface flaw on a painted/mesh laminate. The lighter area observed across the image in figure 4.15 and in the upper right quarter of figure 4.16 is the reflection of a lighting luminaire. Three specimen sets were produced by machining surface flaws into grey, white and blue Plexiglas panels, thus providing different coloured sets of panels without the need for painting.

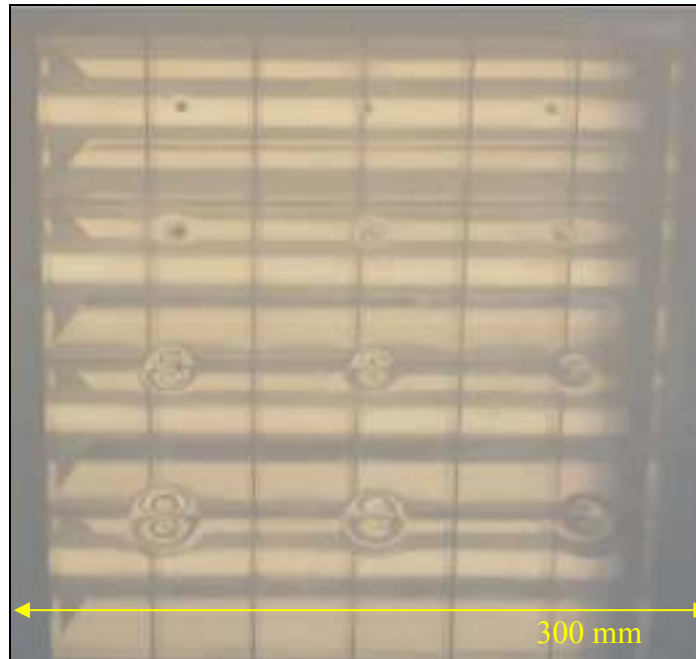


Figure 4.15 – Test piece containing machined surface flaws



Figure 4.16 – Impact damage surface flaw on a painted/ bronze mesh CFRP laminate

#### ***4.9.1 – Application of matt finish to physical specimens***

Upon completion of visual inspection trials with the gloss grey, white and blue panels, the flawed specimens received a thin coat of matt finish paint of the same colour. This allowed their use in reliability assessments of the effect of surface finish on visual inspection, without the need for new machining work. In order to reduce painting time, and costs, complete sets of unflawed panels were not produced. Instead, a smaller number of unflawed panels of each colour were prepared with matt finish, and were recycled into the specimen set during visual inspection trials in order to provide the required number of unflawed specimens.

#### 4.9.2 – CMM checking of physical specimens

Five selected machined flaws on each colour of specimen underwent CMM digitisation to check for conformity to the original specification. An example of a comparison between the CMM data, and the original flaw specification can be seen in figure 5.23. The CMM data taken from the machined flaw are barely distinguishable from the specified geometry, meaning that the machined flaw is the correct depth, correct width and correct, specified flaw profile / shape.

Flaw width measurements are difficult to obtain due to the difficulty in determining the ‘edge’ of the flaw surface and the exact centre point of the flaw. Instead, three Y-axis, or surface height, measurements of the CMM data were made using CATIA at the endpoint, the Xt point, and the centre point of the flaw, as shown in Figure 4.18. The discrepancy between the actual surface height and the specified surface height at the designated points was recorded in order to identify deviations from the specified flaw shape. Measuring surface height deviation at the endpoint of the flaw reveals whether the flaw has been machined to the correct width. A flaw of the correct width shows no surface height deviation, i.e. a measured value of 0 at the endpoint measurement. Measuring the flaw depth against the specified flaw depth reveals whether the flaw has been machined to the correct specified depth. Flaws that have been machined to the correct depth show a depth measurement deviation of 0. The surface height at Xt point of the flaw surface was measured in order to determine that the flaws had been machined to within acceptable shape tolerances. A surface height deviation of 0 at the Xt point shows that the transition between the internal and external radius of the sectional profile of the flaw is in the correct location, and thus the flaw shape has been correctly machined as specified.

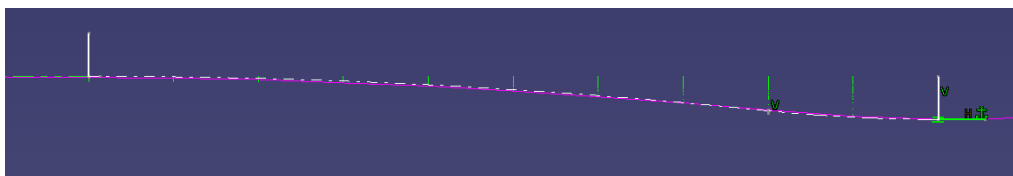


Figure 4.17 - CMM data (pink solid line) and specified geometry (white dashed line) of Ø22.2 mm/ 0.57 mm deep NC machined surface flaw

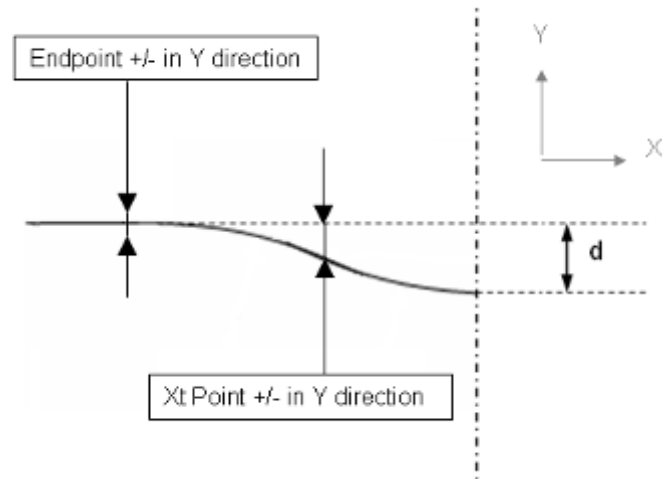


Figure 4.18 – Surface height checking points for CMM data vs. original specification

#### ***4.9.3 – Gloss measurements of physical specimens***

Novo Gloss dual-angle (20° & 60°) gloss meter measurements of the gloss level of each specimen colour & finish provided quantitative values for surface glossiness, and allowed comparisons with an actual aircraft surface finish. A gloss meter measures the intensity of light reflected by a surface from a light source of known intensity, and quantifies the amount of reflected light in terms of gloss units. Gloss measurements range from 0 to 100, with 100 being very glossy, i.e. the surface reflects light with 100% of original intensity. A matt finish surface will diffuse the light reflection, causing less light intensity to be detected, resulting in a lower gloss reading.

#### ***4.9.4 – Paint thickness measurement of physical specimens***

For the matt finish facsimile specimens, the thickness of the paint was measured. This was accomplished by metallographic sectioning of samples of a painted Plexiglas test piece. Figure 4.19 details the image obtained using a microscope. The measurement of the paint thickness was made using the microscope's image processing software. The thickness was measured in several different places, and was found to be consistently within 12µm to 20µm.

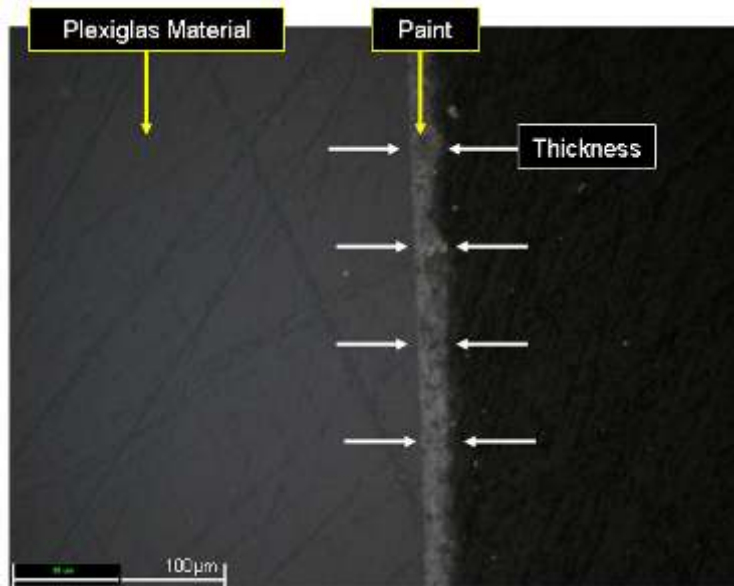


Figure 4.19 – Section of painted Plexiglas material used for thickness measurements

#### 4.10 – Flaw and specimen characteristics

##### 4.10.1 – Specimens for virtual trial 1 (series 1)

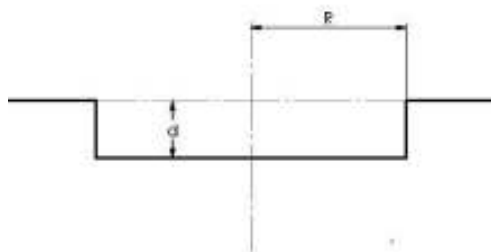


Fig 4.20

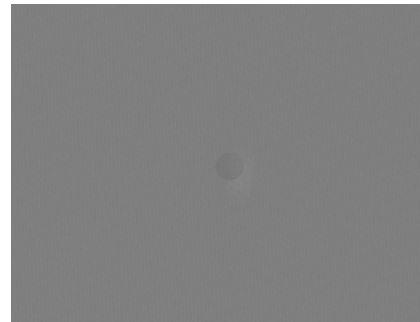


Figure 4.21

The aim of the first trial was to determine the effect of defect width on detectability. For this, circular flat-bottomed flaws were used, as illustrated in Figure 4.20 & 4.21.

The flaws were sized with widths (R) between  $\text{Ø}1$  mm and  $\text{Ø}30$  mm in intervals of 1 mm. The depth (d) of all the flaws was 1 mm. The flaws were positioned onto single 750 mm x 750 mm panels, using random coordinates. The coordinates used are detailed in appendix B. Figure 4.21 illustrates a typical flaw as used in this trial.

The display sequence of the panels was randomised. The 30 panels containing flaws were intermixed with a further 90 unflawed panels, giving 120 panels in the specimen



set. Each panel was displayed onto a white screen for 5 seconds, with an interval of 2 seconds between each panel. The total trial time was approximately 14 minutes.

#### 4.10.2 – Specimens for virtual trial 2 (series 1)

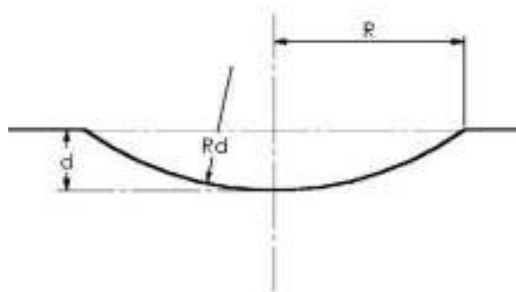


Fig 4.22

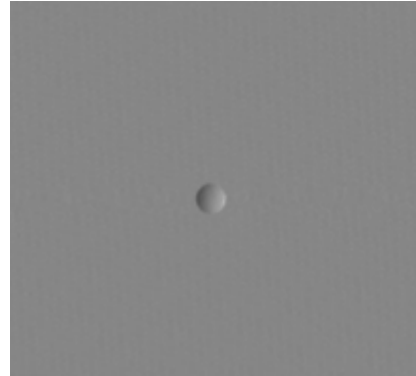


Figure 4.23

The aim of the second trial was to determine the effect of flaw depth on detectability. For this, circular semi-spherical flaws were used, as illustrated in Fig 4.22. The flaw width (R) and depth (d) were set according to design. The flaw radius (Rd) cannot be controlled, as it is dependent on R and d. The values were simply recorded. Figure 4.23 details an example of a flaw used in Trial 2.

The flaws were positioned onto 750 mm x 750 mm panels, using random coordinates produced using the method previously described. A margin of 20 mm from each edge of the panel, leaving an area of 710 mm x 710 mm for flaw positioning. The coordinates used are detailed in appendix B.

Three flaw widths were used for Trials 2 & 3. These were chosen as the 50% POD width, the 70% POD width and the 90% POD width from Trial 1. The reason for including three flaw widths was to investigate whether wider flaws might in fact be less visible due to the increases in the flaw radii (Rd). The three sets of flaw widths were thus Ø4.5 mm, Ø6.5 mm and Ø12 mm. The flaw depths were separated by intervals of 0.1 mm. For the Ø4.5 mm wide flaws, the depths spanned a range from 0.1 mm deep to 1.5 mm. For the Ø6.5 mm wide flaws, the depths ranged from 0.1 mm to 1.3 mm deep. The Ø12 mm wide flaws spanned a depth range of 0.1 mm to 1.1 mm. The flaw depth ranges being investigated required a greater number of flaws, and the trial was subsequently designed to include 39 panels containing flaws, with a further 117 unflawed panels being included to bring the total number of panels to 156.

The specimen and flaw characteristics are detailed in appendix B. The specimen display order was randomised, as detailed in appendix B. Each panel was displayed for 5 seconds with 2 seconds interval. The total trial length was approximately 18½ minutes.

#### 4.10.3 – Specimens for virtual trial 3 (series 1)

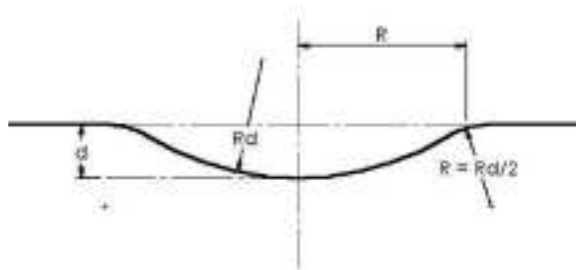


Figure 4.24

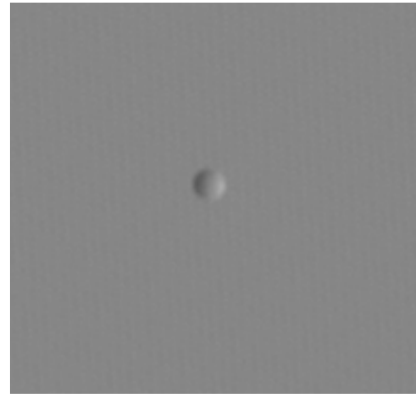


Figure 4.25

The aim of the third trial was to determine whether softening the flaw profile had any effect on detectability. For this, circular semi-spherical flaws with blended edges were used, as illustrated in figure 4.24. The flaw width ( $R$ ) and depth ( $d$ ) were set according to design. The flaw radius ( $R_d$ ) cannot be controlled, as it is dependent on  $R$  and  $d$ . The values were simply recorded. The edge radius was set at half that of the flaw radius, i.e.  $R_d/2$ . This provided a constant ratio between the edge blend and the size of the flaw and avoided introducing further variables. Figure 4.25 details an example of a flaw used in Trial 3.

The flaws were positioned onto 750 mm x 750 mm panels, using random coordinates as described in appendix B. The same flaw depths as those used in Trial 2 were used in Trial 3. The flaw and panel characteristics are detailed in appendix B. The specimen display order was randomised as detailed in appendix B, with 39 panels containing flaws out of the total 156. Each panel was displayed for 5 seconds with 2 seconds interval. The total trial length was approximately 18½ minutes.

#### 4.10.4 – Specimens for virtual trial 4 (series 1)

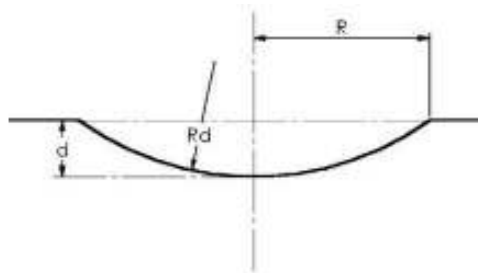


Figure 4.26

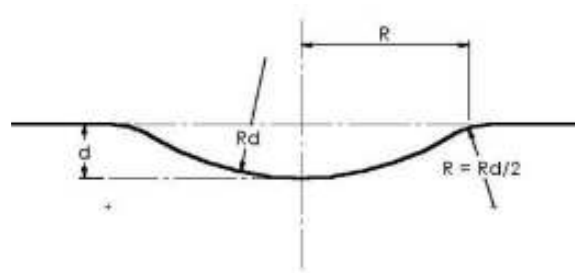


Figure 4.27

The aim of the fourth trial was to determine the effect of depth and the effect of flaw shape on detectability. This helped provide information on whether small, acute flaws gave different detectability to wider, shallower flaws.

For this trial, circular semi-spherical flaws were used, with both a hard edge and a blended edge, as illustrated in figures 4.26 & 4.27. Using both types of contour allowed a direct comparison between the detectability of each contour type.

The flaw width ( $R$ ) and depth ( $d$ ) were set according to design. The results of Trial 2 indicated that a flaw depth ( $d$ ) 0.155 mm would give approximately 50% POD. Therefore, the flaws for Trial 4 were all designed with 0.155 mm depth and their widths varied from 3 mm to 30 mm. The flaw radius ( $Rd$ ) cannot be controlled, as it is dependent on  $R$  and  $d$ . These values were simply recorded. The edge radius for the blended edge flaws was set at half that of the flaw radius, i.e.  $Rd/2$ . The flaws were positioned onto 750 mm x 750 mm panels, using random coordinates produced using the method previously described. The flaw and panel characteristics are detailed in appendix B.

The specimen set for Trial 4 contained 44 flawed panels and 132 unflawed panels, giving 176 panels in total. Within the 44 flawed panels, 4 flaw sizes were duplicated i.e. two panels contained the same flaw size (in different locations). This allowed checking of the consistency of the participant's responses. The panels were displayed for 5 seconds with a 2 seconds interval. The inspection time was approximately 21 minutes.

#### ***4.10.5 – Specimens for virtual trial 5 (series 2) and trials with facsimile specimens***

A total number of 32 surface flaws conforming to the geometry relationships for the Ø20 mm and Ø87 mm impactors on 17ply & 33ply laminates, as given in the results chapter, were designed, thus giving 8 sizes of flaw for each “type” of flaw geometry. Facsimile specimens of 3 mm thick, 600 mm x 600 mm panels containing the aforementioned surface flaws were designed as 3D CAD data. Virtual specimens were created by photo-realistic rendering of the CAD data. Physical specimens were reproduced by NC machining the surface flaws into Plexiglas (PMMA) [Degussa, 2006] material.

A single set of virtual specimens was produced in a grey colour. Six sets of facsimile specimen panels containing NC machined surface flaws were produced for the visual inspection trials:

- Gloss grey specimens (Plexiglas Grey 812)
- Gloss white specimens (Plexiglas White 003)
- Gloss blue specimens (Plexiglas Blue 601)
- Matt painted grey specimens (grey primer)
- Matt painted white specimens (white primer)
- Matt painted blue specimens (RAL 5002 Ultramarine Blue)

The facsimile specimen panels were labelled on the reverse (non-inspection) side, in order to identify their panel number, flawed/ unflawed status, surface colour and surface finish.

In order to set the flaw size range, based on realistic values of impact energy, upper values of impact energy for each flaw type were set as the maximum energy observed in coupon testing before the impact flaw exhibited surface cracking or severe distortion of the entire coupon surface occurs. The lower value of the impact energy range was set at that, which, using the relationships listed in the results chapter, gave a flaw depth of 0.1 mm, or a positive value for  $X_t$ . Using these impact energy ranges and the relationship for flaw width as a function of impact energy, a series of 8 flaw widths, spaced with even width intervals was produced, as shown in table 4.02.

Ø20 mm/17ply		Ø20 mm/33ply		Ø87 mm/17ply		Ø87 mm/33ply	
Energy (J)	Width (mm)	Energy (J)	Width (mm)	Energy (J)	Width (mm)	Energy (J)	Width (mm)
7.0	9.35	5.0	7.48	17.5	10.50	16.8	14.00
9.7	11.99	11.4	10.97	27.1	15.46	21.5	18.49
12.4	14.63	17.9	14.46	36.8	20.43	26.1	22.99
15.1	17.26	24.3	17.95	46.4	25.39	30.7	27.49
17.9	19.90	30.7	21.43	56.1	30.36	35.4	31.98
20.6	22.54	37.1	24.92	65.7	35.32	40.0	36.48
23.3	25.18	43.6	28.41	75.4	40.28	44.7	40.98
26.0	27.82	50.0	31.90	85.0	45.25	49.3	45.47

Table 4.02 – Width/ Energy ranges for realistic flaw sizes

Using the width & energy values in table 4.02 and the energy/ depth model described in the results chapter to calculate flaw depths, a plot of flaw width vs. flaw depth was produced, as seen in figure 4.28. As can be seen in figure 4.28, using an even width interval gives 9 flaws greater than 30 mm wide and 6 flaws deeper than 0.6 mm.

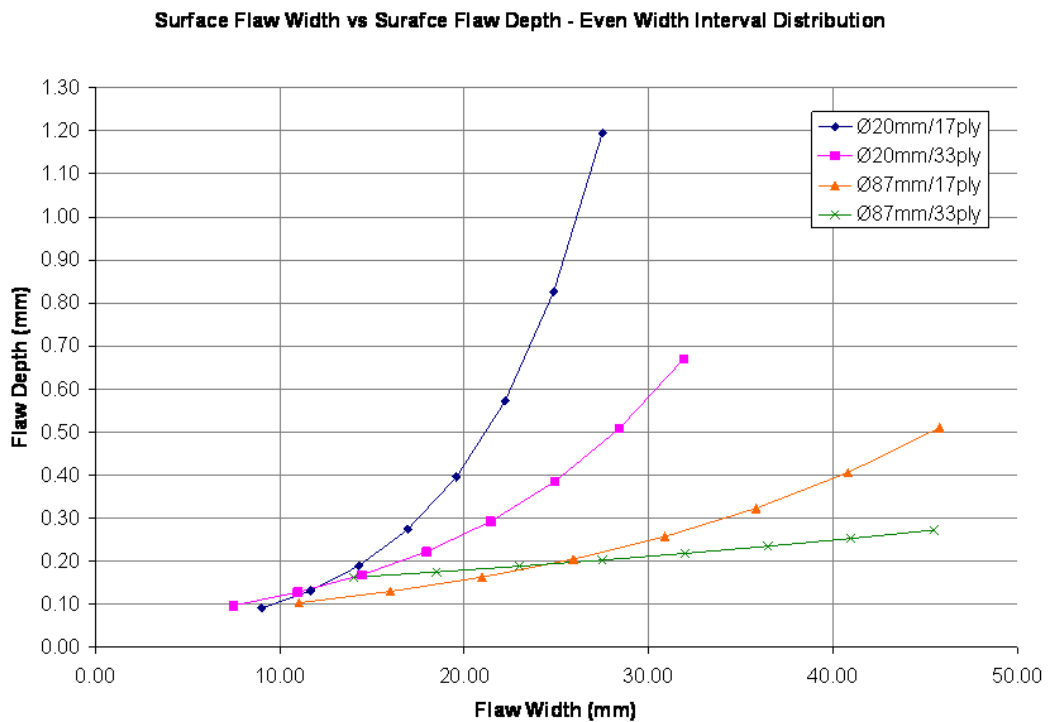


Figure 4.28 – Plot of flaw widths vs. flaw depths with even distribution between flaw widths

As stated in published guidelines on reliability assessment design, “specimens containing flaws so large that they are always found, and flaws so small that they are

*always missed*”, are not useful to the experiment [AGARD 1993]. Advice on flaw sizes also cites the “*tendency to include too many "large" flaws*” in reliability assessments [AGARD 1993]. In order to reduce the number of very wide or very deep flaws within the experiment, the size distribution was modified in order to include a greater number of small to mid width & depth flaws in the specimen set without increasing the overall number of flaws. The natural log of each of the flaw widths in table 4.02 was calculated, as seen in table 4.03. An interval that would space the natural log values across a similar range to the original log values was chosen. I.e. if the original range was 2.235 to 3.326, an interval of 0.15 was used to space new log values across a range of 2.200 to 3.250. Using the exponential of the evenly spaced log intervals, a new value was obtained for each flaw width. This resulted in a new set of flaw widths, which are given in table 4.03.

Ø20 mm/17ply				Ø20 mm/33ply			
Original Width (mm)	ln Width	New Value	New Width (mm)	Original Width (mm)	ln Width	New Value	New Width (mm)
9.350	2.235	2.200	9.025	7.480	2.012	2.000	7.389
11.988	2.484	2.350	10.486	10.969	2.395	2.200	9.025
14.626	2.683	2.500	12.182	14.457	2.671	2.400	11.023
17.264	2.849	2.650	14.154	17.946	2.887	2.600	13.464
19.902	2.991	2.800	16.445	21.434	3.065	2.800	16.445
22.540	3.115	2.950	19.106	24.923	3.216	3.000	20.086
25.178	3.226	3.100	22.198	28.411	3.347	3.200	24.533
27.816	3.326	3.250	25.790	31.900	3.463	3.400	29.964
Ø87 mm/17ply				Ø87 mm/33ply			
Original Width (mm)	ln Width	New Value	New Width (mm)	Original Width (mm)	ln Width	New Value	New Width (mm)
10.499	2.351	2.400	11.023	13.995	2.639	2.650	14.154
15.463	2.738	2.600	13.464	18.492	2.917	2.800	16.445
20.427	3.017	2.800	16.445	22.989	3.135	2.950	19.106
25.391	3.234	3.000	20.086	27.486	3.314	3.100	22.198
30.356	3.413	3.200	24.533	31.983	3.465	3.250	25.790
35.320	3.564	3.400	29.964	36.480	3.597	3.400	29.964
40.284	3.696	3.600	36.598	40.977	3.713	3.550	34.813
45.248	3.812	3.800	44.701	45.474	3.817	3.700	40.447

Table 4.03 – Values for flaw widths with even interval between natural log of width

The flaw widths in table 4.03 and the model for energy as a function of flaw width were used to calculate new energy values, which are listed in table 4.04. A second plot of flaw width vs. flaw depth, as seen in figure 4.29, was produced using the new flaw widths and energies in table 4.04, and again the energy/ depth models described in the results section. On this plot, it can be seen that the modified distribution includes only 4 flaws wider than 30 mm and 1 flaw greater than 0.6 mm deep.

Ø20 mm/17ply		Ø20 mm/33ply		Ø87 mm/17ply		Ø87 mm/33ply	
Energy (J)	Width (mm)	Energy (J)	Width (mm)	Energy (J)	Width (mm)	Energy (J)	Width (mm)
11.9	9.03	4.8	7.39	18.5	11.02	11.7	14.15
14.3	10.49	7.8	9.03	23.3	13.46	13.2	16.44
17.0	12.18	11.5	11.02	29.1	16.44	14.9	19.11
20.2	14.15	16.0	13.46	36.1	20.09	17.0	22.20
23.9	16.44	21.5	16.44	44.8	24.53	19.3	25.79
28.2	19.11	28.2	20.09	55.3	29.96	22.1	29.96
33.2	22.20	36.4	24.53	68.2	36.60	25.3	34.81
39.0	25.79	46.4	29.96	83.9	44.70	29.0	40.45

Table 4.04 – Revised surface flaw widths & energies

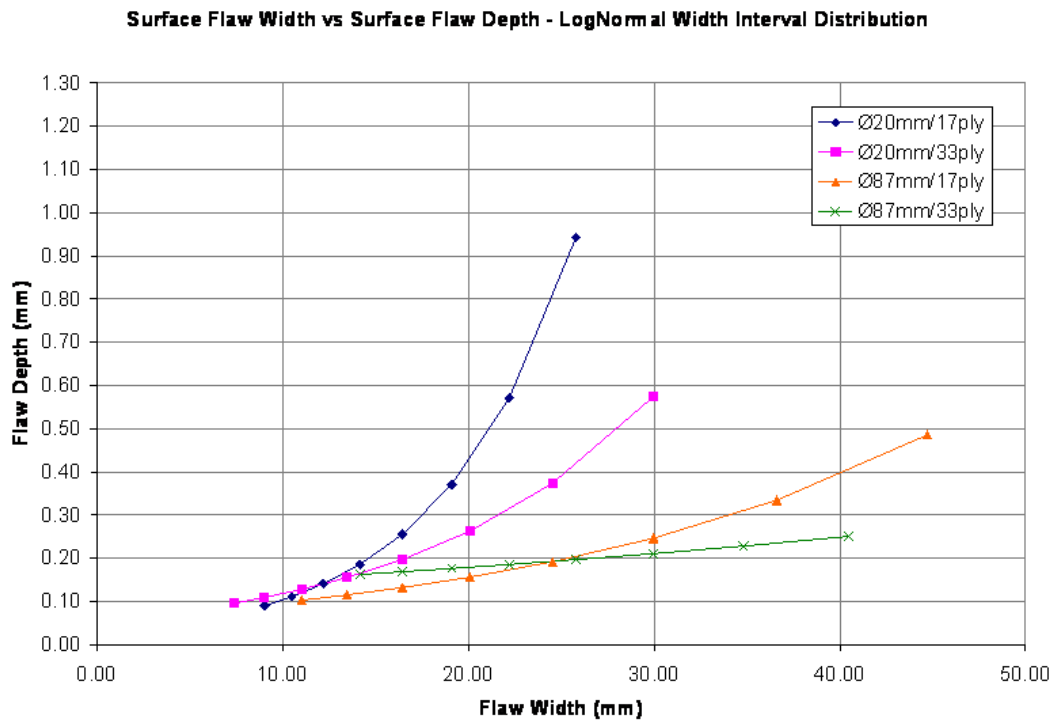


Figure 4.29 – Graph of flaw widths vs. flaw depths with even distribution between lognormal of flaw widths

By using the flaw widths in table 4.04 and the geometry variable models derived in the results chapter to calculate the flaw depths,  $X_t$  values and  $Y_t$  values as a function of flaw energy, the flaw geometry variables for 32 surface flaws were calculated. Table 4.05 lists the variable sizes required to reproduce the flaws in a CAD system. The geometric variables in table 4.05 were used to construct the 2D section lines for each of the 32 flaws. It should be noted that the values of  $r_E$  and  $r_I$  are driven by the



position of  $X_t$  and  $Y_t$  due to the tangency constraints between the curves and the planar surface (see figure 4.11). Their calculations were thus not required as  $X_t$  and  $Y_t$  were specified.

Each of the 32 flaws were placed into random locations on 16 flawed specimen panels, using randomised X and Y coordinates. A margin of 50 mm from the panel edges was used in order to avoid flaws reaching the panel edges. The placement order of the panels was also randomised, such that each panel contained up to 3 flaws of different sizes and types. The specifications for each of the flawed panels are given in table 4.06. The production drawings for the specimens are given in appendix C.

Ø20 mm/17ply					Ø20 mm/33ply				
Energy (E) (J)	Width (2R) (mm)	Depth (d) (mm)	$X_t$ (mm)	$Y_t$ (mm)	Energy (E) (J)	Width (2R) (mm)	Depth (d) (mm)	$X_t$ (mm)	$Y_t$ (mm)
6.7	9.03	0.09	1.352	0.056	4.8	7.39	0.10	0.303	0.089
8.2	10.49	0.11	1.723	0.071	7.8	9.03	0.11	0.351	0.102
9.9	12.18	0.14	2.154	0.093	11.5	11.02	0.13	0.410	0.119
11.9	14.15	0.19	2.656	0.127	16.0	13.46	0.16	0.481	0.145
14.3	16.44	0.26	3.238	0.183	21.5	16.44	0.20	0.568	0.183
17.0	19.11	0.37	3.915	0.280	28.2	20.09	0.26	0.675	0.245
20.2	22.20	0.57	4.701	0.460	36.4	24.53	0.37	0.805	0.348
23.9	25.79	0.94	5.614	0.816	46.4	29.96	0.57	0.965	0.535
Ø87 mm/17ply					Ø87 mm/33ply				
Energy (E) (J)	Width (2R) (mm)	Depth (d) (mm)	$X_t$ (mm)	$Y_t$ (mm)	Energy (E) (J)	Width (2R) (mm)	Depth (d) (mm)	$X_t$ (mm)	$Y_t$ (mm)
18.5	11.02	0.10	1.681	0.077	17.0	14.15	0.16	0.184	0.136
23.3	13.46	0.12	2.072	0.082	19.3	16.44	0.17	0.749	0.139
29.1	16.44	0.13	2.549	0.089	22.1	19.11	0.18	1.407	0.141
36.1	20.09	0.16	3.132	0.098	25.3	22.20	0.19	2.171	0.145
44.8	24.53	0.19	3.844	0.110	29.0	25.79	0.20	3.058	0.149
55.3	29.96	0.25	4.713	0.128	33.3	29.96	0.21	4.090	0.154
68.2	36.60	0.33	5.775	0.152	38.3	34.81	0.23	5.288	0.160
83.9	44.70	0.49	7.072	0.189	44.1	40.45	0.25	6.679	0.167

Table 4.05 – Geometric variables used to define size of specimen flaws

Panel Number	Number of Flaws	Flaw Number	Section Number	Order	X Coordinate	Y Coordinate	Flaw Type	Energy (J)	R (mm)	d (mm)	Xt (mm)	Yt (mm)	rI (mm)	rE (mm)	$\theta_t$ (°)	$\theta_c$ (°)
1	1	1	A-A	1	290	490	Ø20mm/17ply	7	4.51	0.09	1.35	0.06	34	79	87.7	177.7
2	1	19	B-B	2	480	160	Ø87mm/17ply	29	8.22	0.13	2.55	0.09	81	179	88.8	178.2
3	1	12	C-C	3	490	80	Ø20mm/33ply	16	6.73	0.16	0.48	0.15	10	131	87.9	177.4
4	1	10	D-D	4	290	90	Ø20mm/33ply	8	4.51	0.11	0.35	0.10	7	86	87.8	177.2
5	1	6	E-E	5	190	310	Ø20mm/17ply	17	9.55	0.37	3.91	0.22	51	73	85.6	175.6
6	2	24	F-F	6	50	350	Ø87mm/17ply	84	22.35	0.49	7.07	0.34	161	349	88.4	177.5
		22	G-G	7	270	400	Ø87mm/17ply	55	14.98	0.25	4.71	0.17	141	308	88.1	178.1
7	2	20	H-H	8	160	440	Ø87mm/17ply	36	10.04	0.16	3.13	0.11	98	217	88.2	178.2
		7	I-I	9	490	60	Ø20mm/17ply	20	11.10	0.57	4.70	0.33	46	62	84.1	174.1
8	2	25	J-J	11	170	200	Ø87mm/33ply	17	7.08	0.16	0.18	0.16	4	152	87.4	177.4
		31	K-K	10	500	340	Ø87mm/33ply	38	17.41	0.23	5.29	0.16	200	152	88.5	178.5
9	2	8	L-L	12	330	260	Ø20mm/17ply	24	12.90	0.94	5.61	0.53	39	50	81.7	171.6
		13	M-M	13	470	470	Ø20mm/33ply	22	8.22	0.20	0.57	0.19	12	157	87.2	177.3
10	2	27	N-N	14	260	80	Ø87mm/33ply	22	9.55	0.18	1.41	0.15	37	216	87.8	177.9
		26	O-O	15	330	310	Ø87mm/33ply	19	8.22	0.17	0.75	0.16	18	181	87.6	177.6
11	2	16	P-P	16	110	60	Ø20mm/33ply	46	14.98	0.57	0.96	0.53	13	184	85.6	175.6
		4	Q-Q	17	180	490	Ø20mm/17ply	12	7.08	0.19	2.66	0.12	49	82	86.9	177.0
12	3	18	R-R	18	180	80	Ø87mm/17ply	23	6.73	0.12	2.07	0.08	58	131	88.0	178.0
		15	S-S	20	230	290	Ø20mm/33ply	36	12.27	0.37	0.81	0.35	13	190	86.5	176.5
		30	T-T	19	460	250	Ø87mm/33ply	33	14.98	0.21	4.09	0.15	146	388	88.4	178.4
13	3	14	U-U	23	200	370	Ø20mm/33ply	28	10.04	0.26	0.68	0.24	13	181	87.0	177.0
		28	V-V	21	340	120	Ø87mm/33ply	25	11.10	0.19	2.17	0.15	63	261	88.0	178.1
		9	W-W	22	420	490	Ø20mm/33ply	5	3.69	0.10	0.30	0.09	6	63	86.9	177.0
14	3	3	X-X	25	110	530	Ø20mm/17ply	10	6.09	0.14	2.15	0.09	47	86	87.4	177.4
		21	Y-Y	26	250	210	Ø87mm/17ply	45	12.27	0.19	3.84	0.13	124	272	88.2	178.2
		29	Z-Z	24	280	540	Ø87mm/33ply	29	12.90	0.20	3.06	0.15	99	317	88.2	178.2
15	3	11	AA-AA	29	190	340	Ø20mm/33ply	12	5.51	0.13	0.41	0.12	9	108	87.3	177.3
		5	AB-AB	28	480	200	Ø20mm/17ply	14	8.22	0.26	3.24	0.16	51	79	86.4	176.4
		17	AC-AC	27	290	290	Ø87mm/17ply	19	5.51	0.10	1.68	0.07	46	106	87.9	177.9
16	3	23	AD-AD	30	60	440	Ø87mm/17ply	68	18.30	0.33	5.78	0.23	160	347	87.9	177.9
		32	AE-AE	31	370	340	Ø87mm/33ply	44	20.22	0.25	6.68	0.17	270	548	88.6	178.6
		2	AF-AF	32	450	430	Ø20mm/17ply	8	5.24	0.11	1.72	0.07	41	84	87.6	177.6

Table 4.06 – Specimen panel details

#### ***4.11 – Display of virtual specimens to participants***

The virtual specimens were displayed onto a large, clean, white display screen using a Sanyo PLC-XW20A colour projector connected to a laptop computer, as illustrated in figure 4.30. The need for 'keystone adjustment' was eliminated by placing the projector on a 1.1m high stand. This ensured that the display image was projected without shape distortion or stretching. The display size was checked and adjusted to ensure the virtual specimen panels were displayed at the correct size. Blinds were drawn across all windows to maximise projection clarity, and a desk lamp was provided to allow participants to see their answer sheets. The lamp was placed such that its beam did not interfere with the projected display. A single operator was required to run and moderate the projected specimen trials.

The participants were seated slightly offset to the centre of the display, and within 1.2m from it, as seen in figure 4.30. The slight offset, which is exaggerated in the diagram, was required to stop the heads of taller participants interrupting the projection beam.

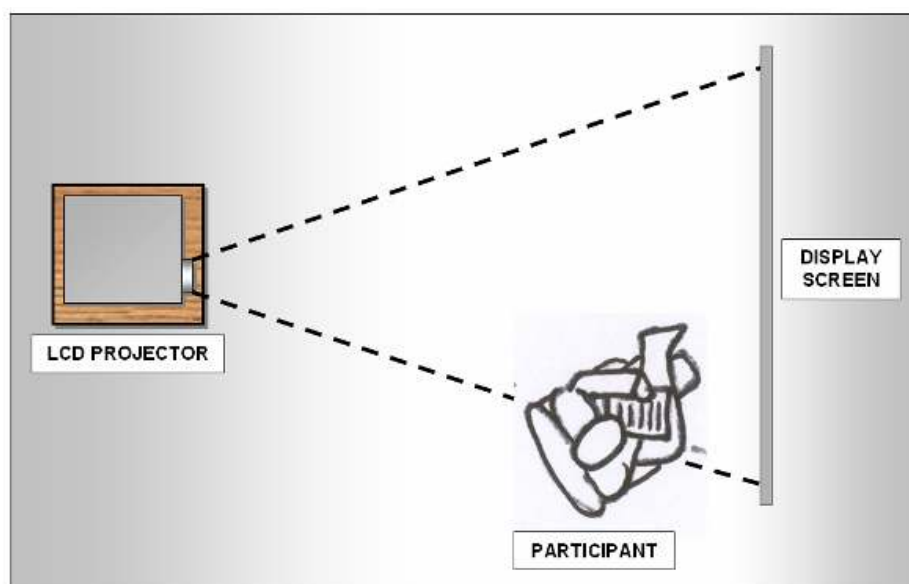


Figure 4.30 – Virtual trials setup

The virtual specimen bitmaps were arranged in a predetermined random order in a Microsoft PowerPoint presentation file. The operator started the PowerPoint presentation once the participants were ready, and each panel was displayed for 5

seconds, with an interval between each panel. For the first series of trials, specimens were displayed in rapid succession with a short (2 seconds) blank screen interval between each specimen. For the second series of virtual trials, a longer interval of 20 seconds was used to simulate the time required to change specimen panels over when physical facsimile specimens were used. A countdown timer and three bleeps alerted the participants of when the next panel would appear. For all trials, the panel numbers were displayed with the panels and for the second series of trials, the number of the next panel was displayed during the “changeover” sequence.

#### ***4.12 – Display of physical facsimile specimens to participants***

A pivoted display stand was used to display the physical specimens to the participants (see figures 4.31 & 4.32). The design of the stand allowed the participants to inspect the panel, after which the operators swung the panel round and replaced it with the next specimen, without the participants seeing the changeover.

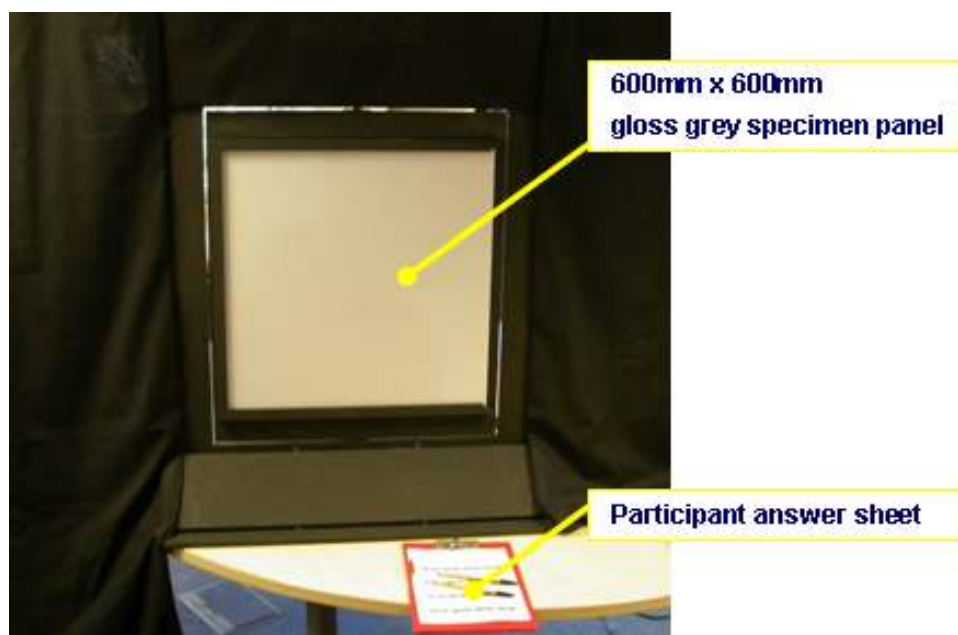


Figure 4.31 – Specimen display stand for visual inspection trials

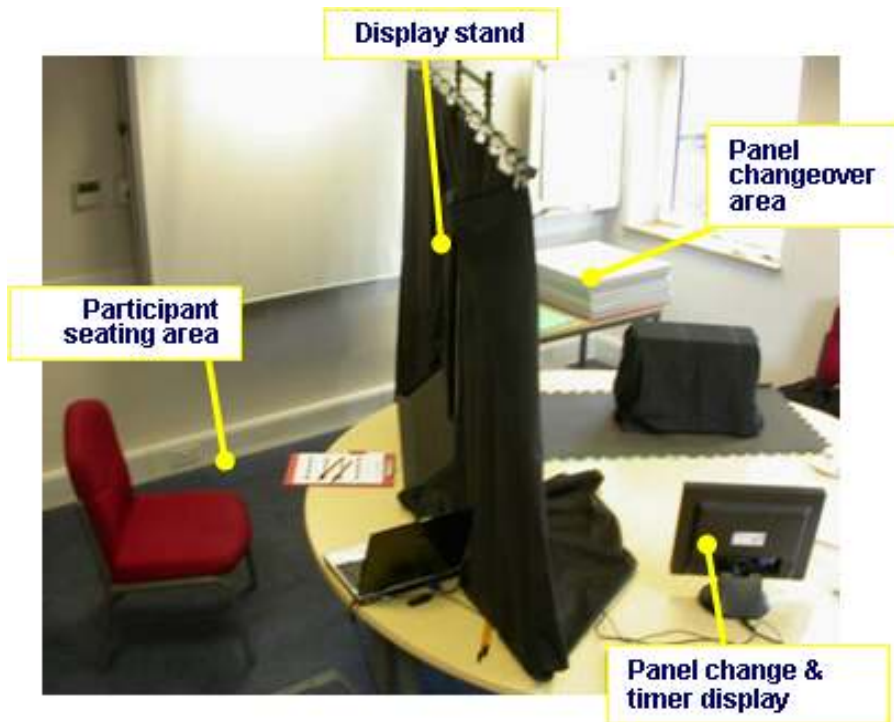


Figure 4.32 – Specimen display stand setup in meeting room

Figures 4.31 and 4.32 show the inspection trials experiment as it was set up. The display stand was table mounted, and curtains attached to it in order to provide a screen behind which the personnel performed the panel changeover. A small, detachable display curtain hid the panels from view whilst they were swung into the inspection position.

The lighting of the inspection task was provided by downwards reflecting fluorescent tube ceiling luminaires of the type commonly found in office buildings. The lights were located above, and in line with the front of the inspection side of the display stand. A computer with a display screen and speakers was used to run a Microsoft PowerPoint presentation, which provided the audible and visual timing signals for the display curtain operations, and changeover of the panels. The display screen was hidden from the participants view in order to avoid alerting them as to whether a flawed or unflawed specimen would be shown next. The participants were given a clipboard and paper answer sheet, on which they marked their answers with a pen.

The participants were seated in a chair, viewing the panels normal to the inspection surface plane, in a position where the participant's eyes were 1.2m from the specimen

panels. The specimen panels were displayed individually, in a pre-determined, random order, for 5 seconds each. A regular interval of 20 seconds between each panel display was allowed for panel changeover. The complete task duration was 27 minutes.

Two operators were required to run the visual inspection trials, operator 1 to perform the panel changeover, and operator 2 to remove and replace the small display curtain and act as moderator.

After starting the PowerPoint timing presentation, operator 2 removed the display curtain on hearing a single beep from the computer, moved & held it clear of the display stand for a 5 seconds, and replaced it as instructed by a second beep from the computer. The display stand was swung round, and operator 1 removed the specimen panel, and replaced it with the next panel in the specimen display sequence. The computer display behind the display screen gave information on which panel to place into the display stand. An audible signal of three consecutive beeps sounded after 17 seconds, alerting the operators that the display stand & new specimen should now be ready in display position. After 20 seconds, a single beep sounded, thus repeating the process until the 64<sup>th</sup> panel was displayed.

For trials with gloss finish specimens, 48 unflawed specimen panels were available. This made it possible to stack the complete set of 64 (16 flawed/ 48 unflawed) specimens in the correct display sequence prior to beginning the first trial, ready for display to participants as instructed by the PowerPoint timing presentation. During the trial, the changeover operator re-stacked the specimens in reverse order, when removing them from the display stand. For the next trial, the specimens were displayed in reverse sequence. Two different timing presentations were used, one for forwards order trials and one for reverse order trials. A record was kept of which sequence the participants saw the specimens in by adding FO (forwards order) or RO (reverse order) into the serial number on each participants answer sheet.

For the inspection trials with matt finish specimens, only 16 unflawed specimens were available. In order to display the 48 required unflawed specimens, the set of 16 unflawed specimens were displayed cyclically. The specimen sequence was displayed

on the panel change screen (see figure 35.5) for these trials, and the flawed and unflawed specimens were kept in separate piles. The changeover operator chose the correct flawed specimen, or an unflawed specimen, as instructed by the panel change screen. Prior to the first trial with a matt finish specimen set, the flawed specimens were stacked in the correct order in which the display screen would request their display for inspection. Upon removing a flawed specimen from the display stand, operator 2 restacked the flawed panels in the reverse order ready for the next trial, in which the display sequence reversed, as described for the gloss specimens.

In any situation where a pause in the trial was required, the moderator stopped the inspection trial timer at the end of the display time for the current specimen, and re-started when convenient in order to avoid the possibility of distractions affecting participant performance during the trial.

#### ***4.13 – Participant briefing for visual inspection trials***

All participants were given a 10-minute briefing before undertaking a visual inspection trial. The briefing explained the experimental task, provided examples of the surface flaws that the participants would be asked to find, and gave instructions on how to complete the answer sheet.

Participants were advised of the trial duration and how many panels they would view. Where applicable, the participants were told whether panels would contain either single flaw or contain more than one flaw, and that some panels would be unflawed. The participants were advised that the panel display order had been randomised, and were told not to be anxious if they experienced a succession of panels on which they did not see flaws. The participants were not told how many flaws were in the specimen set, or how many flawed and unflawed specimen panels there were in the experiment. Participants were not told of the size range of flaws they would be expected to see. The participants were advised that their payment was not performance related, i.e. payment would not be increased for finding greater numbers of flaws, and deductions would not be made for missed flaws.

The participants were asked if they would normally wear corrective eyewear for medium to long-range vision, (i.e. to see presentation screens during lectures or for

driving), and if so, that they wear them during the trial. The participants were told that they could move their heads to a reasonable extent during the visual inspection trials, but persons moving excessively would be asked to reduce the amount by which they moved their viewing position. When undertaking trials with physical specimens, the participants were instructed not to touch the panels. After being briefed, the participants were given a clipboard, pen, and answer sheet. The answer sheet was marked with a serial number that identified the type of trial, the colour & finish of the panels (for physical specimens), the date of the trial, and the participant number.

#### ***4.14 – Experimental task for visual inspection trials participants***

The experimental task for the visual inspection trial experiments was for the participants to view each specimen panel and search for the presence of impact damage flaws. The participants were asked to signal the presence of suspected flaws by marking their responses on an answer sheet.

#### ***4.15 – Recording participant responses – series 1 virtual specimen trials***

The participants were asked to mark their responses down on a response sheet. The response sheet contained a box for each panel number. Within each box was a space for a mark against ‘yes’ or ‘no’. Participants were requested to use a tick, a cross or a line through the ‘yes/ no’ boxes in order to mark their response to each panel. Most complied, with only one individual choosing to ring the ‘yes/ no’ text instead of using the boxes provided. The hit/ miss results were obtained by overlaying an answer sheet onto the response sheets, and marking the response sheets as either a correctly identified flaw, a missed flaw or a false call. The results data was input into a Microsoft Excel spreadsheet and stored electronically.

#### ***4.16 – Recording participant responses– physical specimen & series 2 virtual specimen trials***

For the first series of trials, the flawed specimens contained only a single impact flaw, which allowed the use of a simple ‘yes’ or ‘no’ response from participants when identifying the presence of flaws.

For the second series of trials, the specimens contained up to 3 impact flaws on a single specimen panel, which negated the use of a yes/ no response sheet. Instead, the participants were asked to mark the location of suspected flaws on a diagrammatic representation of each individual specimen panel.



The diagrammatic answer sheets contained a diagram of each of the 64 specimen panels within the specimen sets. The diagrams, as seen in figures 4.33 & 4.34 illustrated the edge of the specimen panels, and a nine square guide grid to help the participants place their answers in the correct location. The participants were asked to mark the location of surface flaws with a cross (figure 4.33), and to put a line through the entire panel for any specimens that the participant deemed free of surface flaws (figure 4.34)

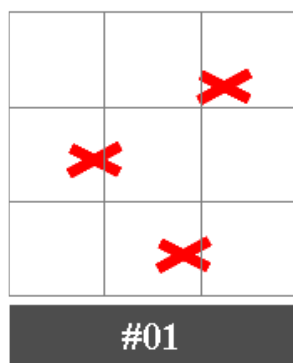


Figure 4.33 – Surface flaw Detected

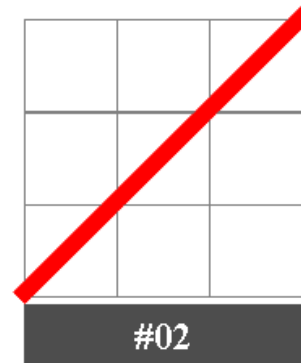


Figure 4.34 – No surface flaws detected

#### ***4.17 – Data collection method for visual inspection trials***

Hit/ miss data, and false call data were extracted from the answer sheets by comparing the answer sheets with marking sheets. For the first series of trials, correctly identified flaws, or hits, were denoted by ‘yes’ answers marked against panels known to contain flaws. Correct answers for unflawed panels were denoted by ‘no’ answers against those panels. Undetected flaws, i.e. misses, were denoted by ‘no’ answers against panels that were known to contain flaws. False calls were identified by ‘yes’ answers against panels that were known to be free of flaws.

For the second series of trials, in which the participants had to denote the location of suspected impact flaws, or flaws, the answer sheets were compared with a marking sheet that contained the actual locations of the 32 flaws within the specimen set. A ‘hit’ was made when the participant viewed a flawed specimen panel ,detected a flaw or flaws, and marked down the presence of each flaw in the correct position on the

diagram. A miss occurred when the participant did not detect a flaw, i.e. failed to make a mark in the correct position on the panel diagram or crossed the panel as unflawed despite having viewed a panel that actually contained flaws. False calls were classed as occurrences of participants marking the presence of a flaw on a panel, or an area of a panel, that was denoted on the marking sheet as being free of flaws. The moderator's criteria for successful detections, or hits, were as follows:

- For multiple surface flaws, the participant answer marks were expected to be in similar positions, or follow the same pattern as the flaws shown on the marking sheet.
- For the remaining flaw answer marks on a multiple flaw specimen, where the participant has missed one or more flaws, the above criteria applied, and participant answer marks were expected to be within a distance equal to the size of one grid square of the position shown on the marking sheet
- For single flaws, or for judging a borderline hit/miss for individual flaws on a multiple flaw specimen, the participant answer was expected to be within a distance equal to the size of one grid square of the position shown on the marking sheet.

The following additional criteria were set out before marking began:

- Any answer mark made by the participant not corresponding to a surface flaw on a specimen was to be deemed a false call. The number of false calls made by each participant was to be recorded, in case of the data being required for further analysis in other work.
- Some participants may believe they saw a surface flaw and marked it down, but then decided that what they saw may not have been a surface flaw, and crossed out their answer. In such cases, marking was to ignore crossed out marks that did not correspond to a surface flaw, as such marks were deemed the result of participants realising that they had made a false call and correctly crossing out their mistake.
- Where a participant correctly detected, and marked down a surface flaw, but subsequently crossed the answer out, the mark was recorded as a hit, as the participant must have had some cause to make the original mark.

The reason for adopting the described approach to marking was to include all occurrences of ‘detections’ (i.e. the participants eye detecting a target) in the results. The implications for the detection results are that for a very limited number of results, what the participant may have felt was a false call might actually be recorded as a hit. However, the implications of this treatment are insignificant given the very limited numbers of crossed out calls that were in flaw locations (<2) and the fact that the false call data were not to be used for determining operator bias as per signal detection theory (which, as described in chapter 2, is outside of the scope of this thesis).

The hit/ miss & false call data for each of the visual inspection trials were transferred into electronic format by recording them as Microsoft Excel data tables, one for each set of specimens used. The tables list each of the flaws within the specimen set, and each of the participant’s responses. A hit is recorded as 1 and a miss as 0.

#### ***4.18 – Participants – Series 1 trials (with virtual specimens)***

The trials were undertaken by participants from Cranfield University. Each participant was given £5.00 for a single trial. As an incentive to encourage participation & good attendance, participants attending all the trials in the series were given an extra £5.00. There were 18 participants in total; 4 of whom attended just one trial. 2 participants attended two of the trials, and 12 participants attended all three trials.

All participants were able to see the example flaws, and were thus deemed to have suitable eyesight for continuing with the trials. The ages of the participants were not recorded. However, the typical demographic of Cranfield University, and thus the participant ages, can be considered as generally being between 20 and 35 years old.

#### ***4.19 – Participants – Series 2 trials (physical & virtual specimens)***

As per series 1 trials, the participants for the second series of visual inspection trials were volunteers from Cranfield University, and were paid £5 for participating in a single trial. Actual aircraft inspectors were not required, as the trials constitute a reliability assessment that simulates the inspection task [see Gallwey & Drury, 1986].

The daily schedule of 6 trials per day allowed the operators sufficient time to absorb late participant arrivals and minor delays during trials. Delays mostly arose in early

trials due to participants keen to ask numerous questions during the briefing. To accommodate participant availability for 6 inspection trials, two participants performed the inspection trial sat side-by-side. The possible advantage of being seated at a slight angle to the specimen panel was negligible, especially given that other participants were free to move their heads during inspection. The operators checked, and found that the view of a panel, and surface flaw, at a slight angle was indiscernible to the view from exactly 90° to the panel. The results from these trials showed no difference to trials with a single participant.

Participant 12 experienced some eyestrain during an inspection trial with matt white specimens, and experienced difficulty deciding between being better able to inspect with or without their glasses. The operators offered to pause, or stop the trial, but the participant expressed a wish to continue, and inspected without glasses thereafter. The results for this trial did not appear significantly different to any other participants, and were thus included in the experimental results. Apart from this isolated case, there were no other indications from participants that they were becoming bored, or suffering from fatigue.

## ***Chapter 5 – Experimental Results***

### ***5.1 – Impact damage to CFRP laminates***

Examples of impact damage to painted, mesh incorporating and unfinished CFRP laminate coupons were produced using falling weight apparatus at a range of impact energies. The impact events resulted in surface indentations (flaws), subsurface delaminations and back face fibre breakout, in a manner consistent with the typical impact damage behaviour of CFRP laminate materials. The visual appearance of the impact damage to the unfinished coupons was typical of that reported in other studies, i.e. a surface flaw with surface breaking cracks appearing in the upper plies of the laminate. Impacts to the painted, mesh incorporated<sup>2</sup> coupons also resulted in surface flaws, although their visual appearance was more ‘rounded’ than on the unfinished coupons and surface breaking cracks did not appear on the painted coupons unless the

---

<sup>2</sup> The term ‘painted’ shall be used forthwith to refer to CFRP laminate containing a single layer of bronze lightning strike mesh and having a primer & topcoat paint finish. The term ‘unfinished’ shall be used to refer to CFRP laminate without mesh layers or painted finishes.

impact tip penetrated or buckled the laminate (which occurred at varying energy levels depending on the laminate thickness and impactor geometry). The results of the impact damage experiments, which identify differences in impact damage morphology between painted and unfinished laminates, are described forthwith.

#### ***5.1.1 – Basic measurements of impact flaw morphology for fully finished CRFP laminates***

The surface area and depth of the surface flaws on each of the impacted coupons was measured as per 4.5.1 & 4.5.2. The associated delamination size was obtained using ultrasonic C-Scan methods as per 4.4. The measurements obtained by these methods are given in table 5.01. Some of the impacts by the flat cylindrical impactor produced more than one damage zone, in which cases the maximum indentation depth is given, along with the total damaged surface area and delamination area.

			Coupon No	Impact Energy (J)	Flaw Depth (mm)	Flaw Area (mm <sup>2</sup> )	Delamination Area (mm <sup>2</sup> )		Coupon No	Impact Energy (J)	Flaw Depth (mm)	Flaw Area (mm <sup>2</sup> )	Delamination Area (mm <sup>2</sup> )
Ø20mm Impactor	17 Ply	Painted	27	5	0.09	16	400	Unfinished	U13	5	0.09	20	350
			26	10	0.09	28	500		U14	10	0.15	79	600
			25	15	0.03	95	1050		U15	15	0.35	255	1150
			24	20	0.7	214	1900		U16	20	0.91	284	1800
			23	30	1.85	255	2400		U17	30	2.36	346	2600
Ø87mm Impactor	17 Ply	Painted	95	5	0.015	29	0	Unfinished	U18	5	0	0	100
			94	10	0.07	380	700		U19	10	0.08	64	700
			93	15	0.07	615	900		U20	15	0.09	79	3500
			29	20	0.06	700	2000		U21	20	0.14	150	4100
			88	30	0.03	491	3400		U22	30	0.17	177	7400
			92	30	0.1	804	6600		U23	40	0.19	314	-
			30	40	0.11	1100	4900		U24	50	N/A	8500	9700
			89	40	N/A	N/A	10000		-	-	-	-	-
			90	50	N/A	N/A	10700		-	-	-	-	-
Ø70mm Flat Cylinder	17 Ply	Painted	36	10	0.07	500	170	Unfinished	U25	10	0.01	124	400
			37	15	0.15	520	850		U26	15	0.1	596	800
			38	20	0.15	536.5	1100		U27	20	0.15	690	1150
			40	30	0.2	1480	1400		U28	30	0.24	725	1600
			39	40	0.3	3960	1900		U29	40	0.56	1443	1650
Tool Shaped Impactor	17 Ply	Painted	34	5	0.01	8	0	Unfinished	U30	5	0	0	50
			33	10	0.01	9	175		U31	10	0.04	88	600
			32	15	0.07	15	1100		U32	15	0.13	200	1350
			35	17.5	0.9	135	1500		U34	17.5	N/A	252	1800
			31	20	1.5	150	2500		U35	20	N/A	210	1900
Ø20mm Impactor	33 Ply	Painted	2	5	0.01	10	0	Unfinished	U38	5	0	0	0
			3	10	0.01	13	78		U39	10	0.12	50	900
			4	15	0.14	79	1300		U40	15	0.18	95	1100
			5	20	0.22	113	1550		U41	20	0.24	154	1600
			6	30	0.27	177	2800		U42	30	0.37	430	2500
			7	50	0.86	255	4900		U43	50	0.84	620	4600
			Ø87mm Impactor	33 Ply	Painted	9	20		0.12	314	2700	Unfinished	U44
8	30	0.19				380	3500	U45	30	0.21	616		3600
10	40	0.21				531	5100	U46	40	0.3	755		4500
11	50	0.21				707	6400	U47	50	0.38	804		6000
12	60	0.22				908	7000	U48	60	0.44	1195		7200
13	70	0.23				962	8900	U49	70	0.35	1964		9000
Ø70mm Flat Cylinder	33 Ply	Painted				18	10	0	0	0	Unfinished		U50
			19	20	0	0	0	U51	20	0		0	0
			20	30	0.01	2800	20	U52	30	0.01		30	50
			21	40	0.01	3150	30	U53	40	0.01		186	100
			1	50	0.01	3500	60	U54	50	0.15		347	1100
			70	60	0.03	3500	700	U55	60	0.06		334	1400
			Tool Shaped Impactor	33 Ply	Painted	14	20	0.18	15	2300		Unfinished	U56
15	30	0.22				18	3200	U57	30	0.26	103.5		3800
16	40	0.23				24	5100	U58	40	0.37	127.5		4900
17	50	0.43				24	5400	U59	50	N/A	184.5		5600

Table 5.01 – Measurements of impact damage on CFRP coupons

### 5.1.2 – Relationship between flaw and subsurface damage sizes

The images obtained from the C-Scanning of the coupons provide useful comparisons between the subsurface damage size and the visible surface damage size. Examples of photographs of impact damage to painted CFRP coupons and the associated C-Scan image are provided in figures 5.01 to 5.03. These examples indicated that the subsurface damage caused by impact to a fully finished laminate extends further than the visible surface flaw regions.

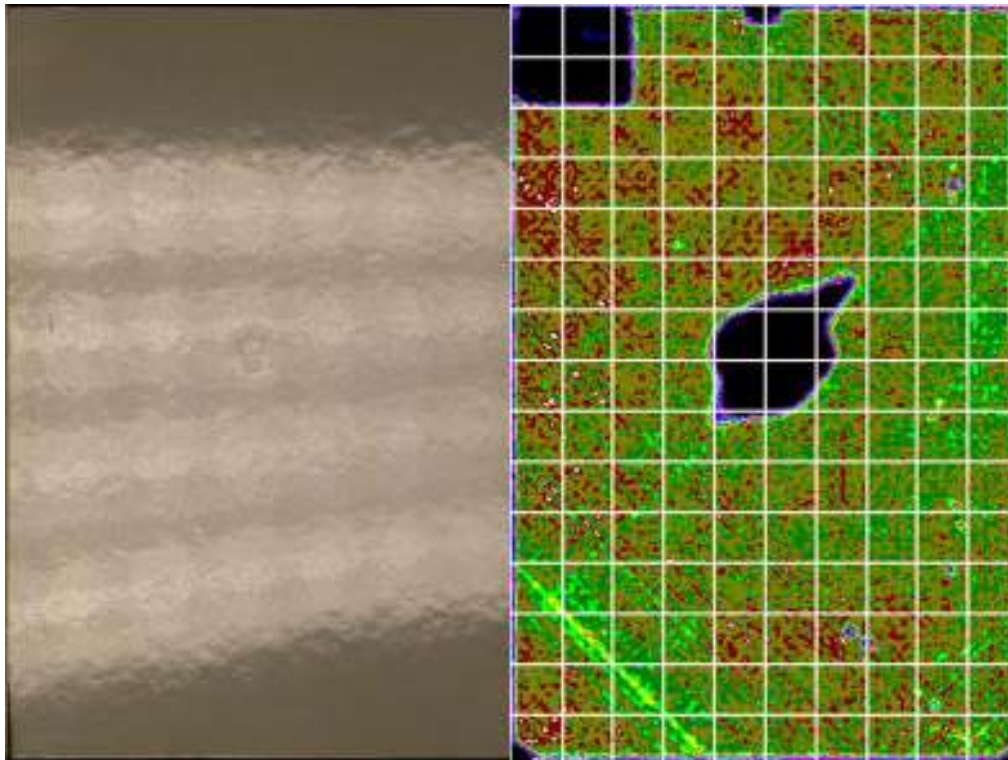


Figure 5.01 – Photograph and C-Scan of 10J / Ø20 mm impact on 17ply painted CFRP laminate

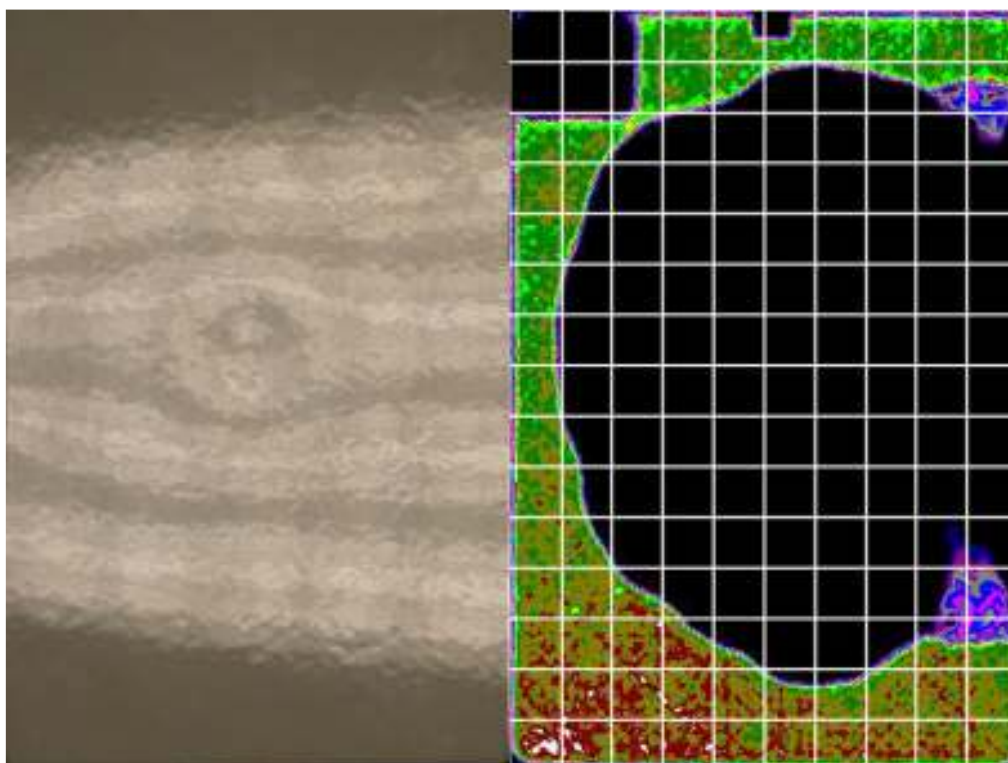


Figure 5.02 – Photograph and C-Scan of 70J / Ø87 mm impact on 33ply painted CFRP laminate

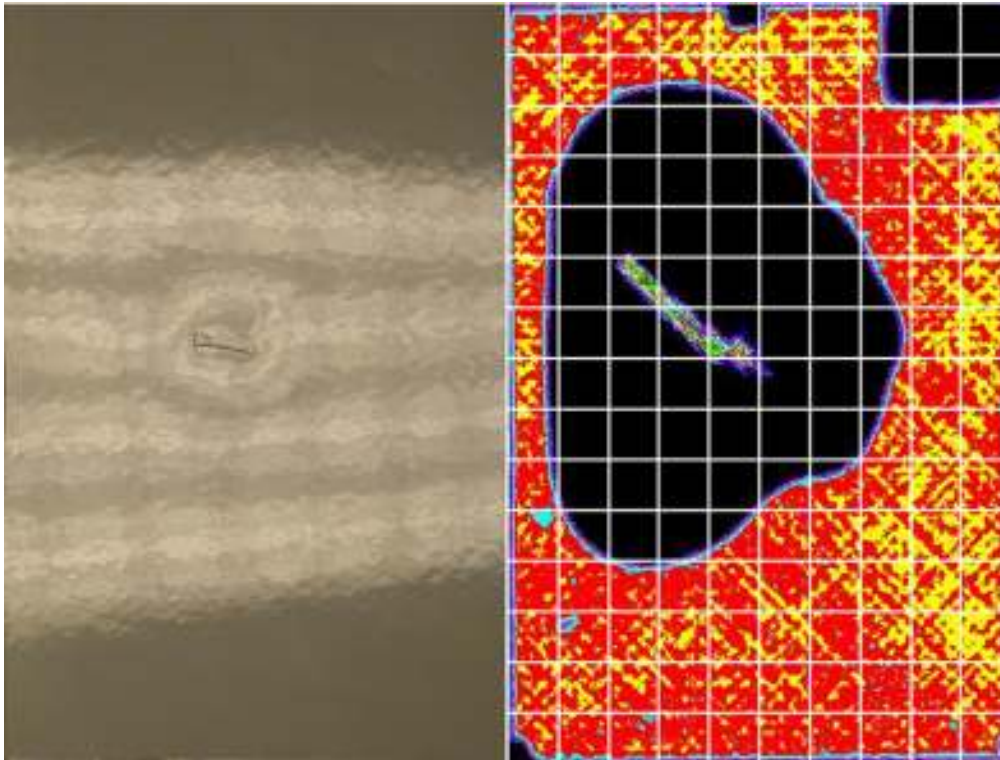


Figure 5.03 – Photograph and C-Scan of 50J / Wedge shaped impact on 33ply painted CFRP laminate

Figure 5.04 details a plot of delamination area vs. flaw area for all of the impact indentations on the fully finished CFRP coupons. From the plot, it can be seen that the subsurface delamination size varied depending on the size of the impactor and the impact energy. The general trend was for delamination area to increase in size as the flaw area increased. The disparity between flaw size and delamination size is also evident in figure 5.04. The delamination area produced by the 15J/ Ø87 mm impact on 17ply laminate was approximately 1.5 times the flaw area size, whilst the delamination produced by the 50J/ Ø87 mm impact on 33ply laminate was approximately 73 times the size of the surface flaw area.

Also of note is that the large flat cylindrical impact tip produced relatively small delamination areas ( $<2000 \text{ mm}^2$ ) for very large surface flaw areas ( $>1500 \text{ mm}^2$ ). In comparison, the smaller tool shaped impact tip produced large delamination sizes (up to  $5500 \text{ mm}^2$ ) with small surface flaw areas ( $<500 \text{ mm}^2$ ). The same comparison can be made for the larger (Ø87 mm) and smaller (Ø20 mm) hemispherical impact tips.



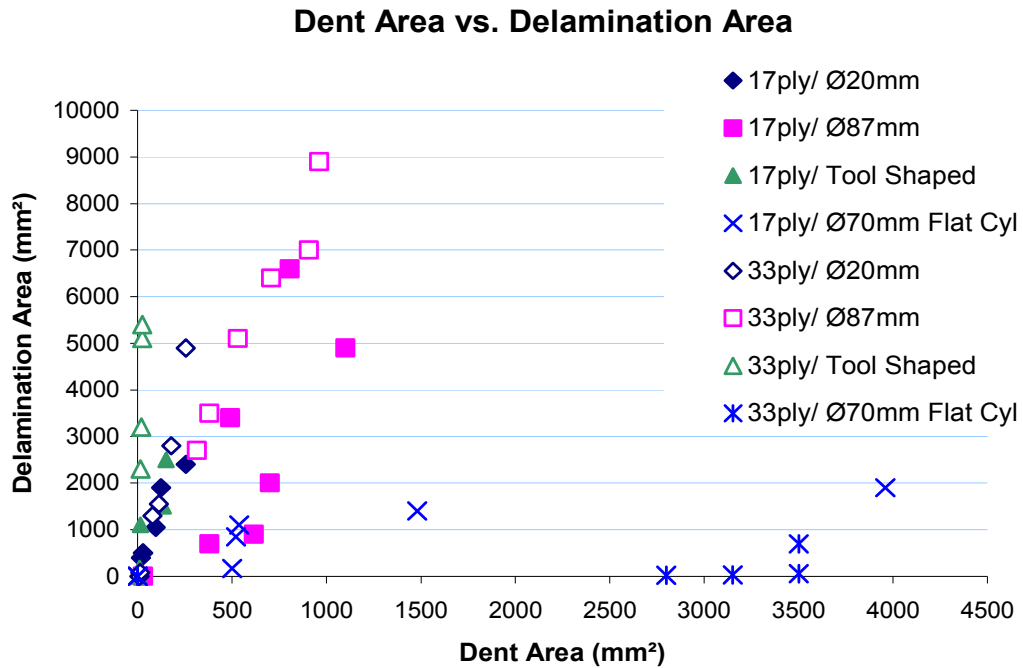


Figure 5.04 – Plot of surface flaw area vs. delamination area for impacts on fully-finished laminate

### 5.1.3 – Comparisons between impact damage on painted & unfinished laminates

Figures 5.05 – 5.18 illustrate a selection of photographs of impact-damage surface flaws that were created on painted and unfinished laminates. A photograph of each damaged coupon is given in appendix D. Comparisons between surface flaw appearance on the protected and unprotected laminates are also given.

#### Ø20 mm Impactor

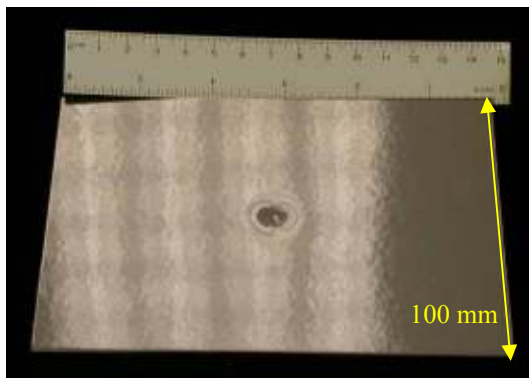


Figure 5.05 – rounded, circular surface flaw produced by 20J / Ø20 mm impact on 17ply painted laminate

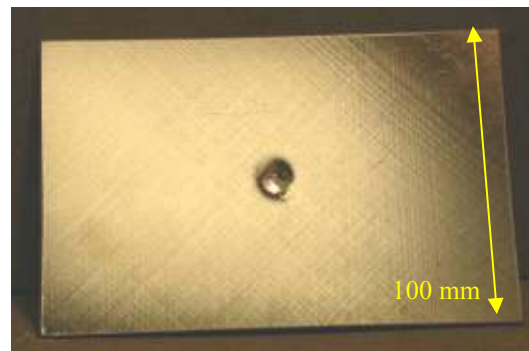


Figure 5.06 – jagged edged, circular surface flaw produced by 20J / Ø20 mm impact on 17ply unfinished laminate

The indentation of Ø20 mm hemispherical impact-damage surface flaws on painted laminates (figure 5.05), and unfinished laminates (figure 5.06), remained similar in shape. However, on unfinished laminates, the impact caused the upper plies to split, with small surface cracks becoming evident as seen in figure 5.08. The cracks were not seen on the painted laminate, as seen in figure 5.07.



Figure 5.07 – 15J / Ø20 mm impact on 17ply painted laminate

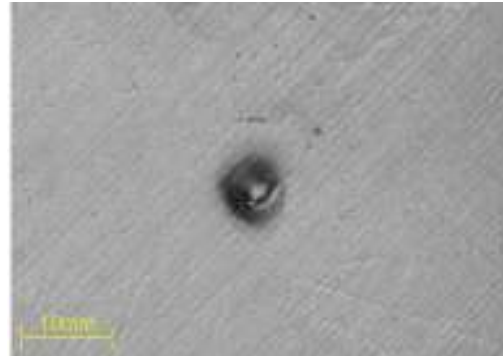


Figure 5.08 – 15J / Ø20 mm impact on 17ply unfinished laminate

As seen in figures 5.05 to 5.08, the typical visual appearance of Ø20 mm impactor surface flaws was a circular, rounded depression. As a general trend, increasing impact energy resulted in deeper surface flaws, and greater flaw areas. Surface flaw sizes reached a maximum of 1.85 mm deep / 255 mm<sup>2</sup> on the painted coupons and 2.36 mm deep / 346 mm<sup>2</sup> on the unfinished coupons. Figure 5.09 illustrates a plot of surface flaw depth vs. impact energy, produced using the values in table 5.01. The plot in figure 5.09 shows that the flaws on unfinished coupons vary from being 0.1 to 2.0 mm deeper than for the same impact conditions on the painted coupons. The plot of impact energies vs. flaw areas in figure 5.10 illustrates how flaw areas are between 4 mm<sup>2</sup> and 300 mm<sup>2</sup> larger on the unfinished coupons than for the same impact conditions on the painted coupons.

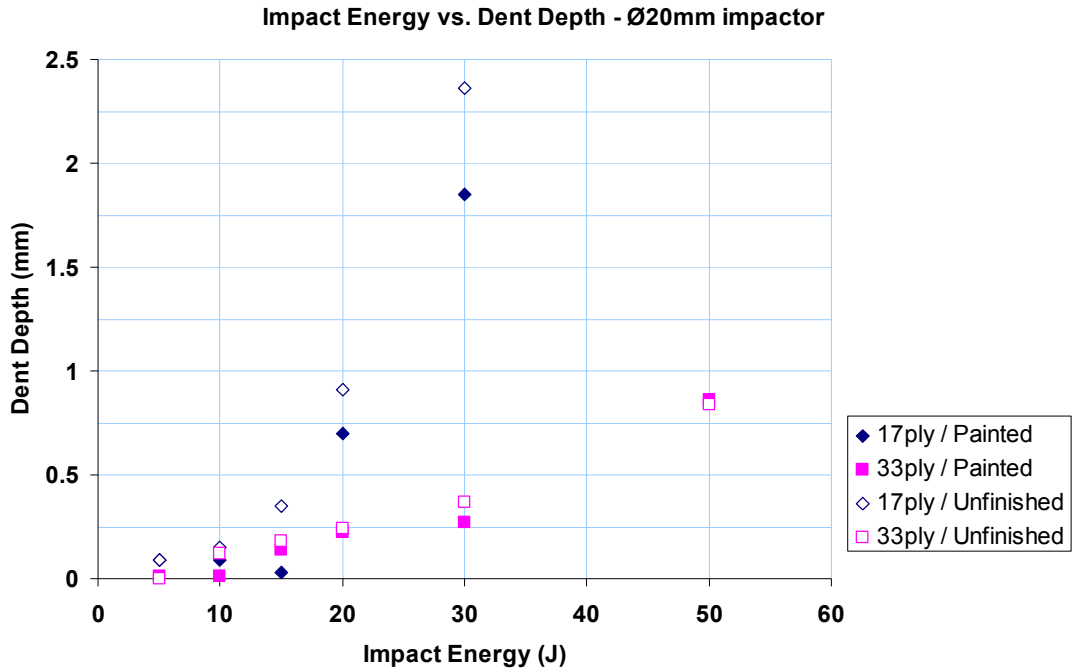


Figure 5.09 – Impact energy vs. Flaw depth plot for Ø20mm impactor

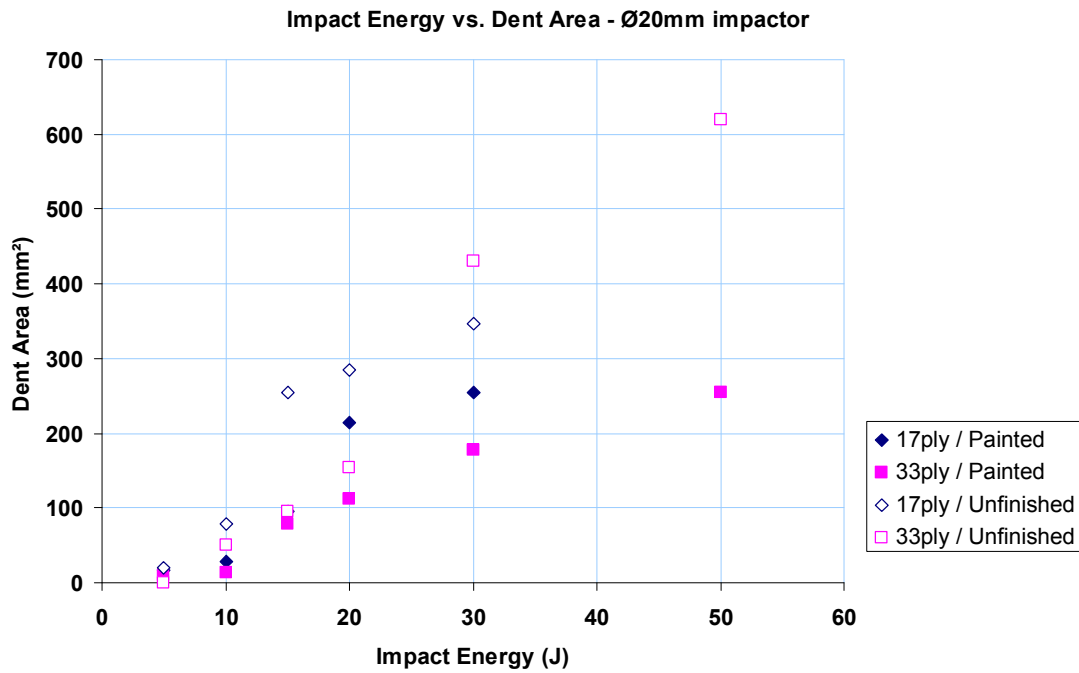


Figure 5.10 – Impact energy vs. Flaw area plot for Ø20mm impactor

## Ø87 mm Impactor



Figure 5.11 - surface flaw produced by 30J / Ø87 mm impact on 17ply painted laminate

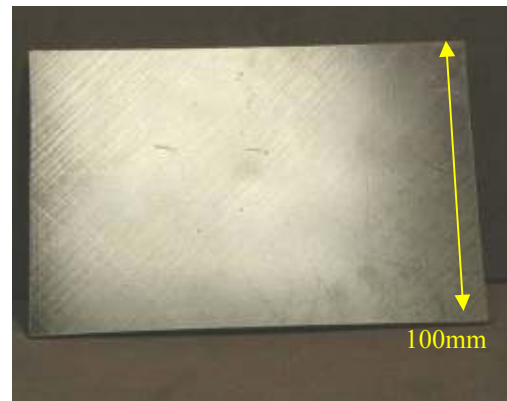


Figure 5.12 –surface flaw produced by 30J / Ø87 mm impact on 17ply unfinished laminate

The appearance of Ø87 mm hemispherical impact-damage surface flaws on painted laminates (figure 5.11), and unfinished laminates (figure 5.12), was very similar. Surface breaking cracks did not appear on either the painted or unfinished coupons when impacted by the Ø87 mm impactor. Typical visual appearance of surface flaws was a rounded, circular indentation type flaw. As seen in the plot in figure 5.13, flaw depths remained below 0.5mm despite energy levels of up to 70J and the flaws, for the same impact conditions, were deeper on unfinished coupons than on painted coupons. However, as seen in the impact energy vs. flaw area plot in figure 5.14, the flaw areas produced by the Ø87 mm impactor were smaller on the painted 33ply coupons than on the unfinished 33ply coupons.

Also noted in figure 5.14 are the significantly lower flaw areas measured on the unpainted coupons compared to the painted coupons impacted by the 87 mm impactor. This apparent discrepancy is evident when figure 5.11 and figure 5.12 are compared. The visibly affected flaw area on the 33ply painted coupon (figure 5.11) appears larger in the photograph than the flawed area exhibited in a similar photograph of the same impact (30J / Ø87mm) on a 33ply unpainted laminate. The reason for the discrepancy in flaw width measurements is thus attributed to the impact causing deformation to the bronze mesh on the painted laminate, which spreads across a greater area than the simple impact dent produced on the unpainted laminate. Thus this phenomenon does not occur with the Ø20 mm impacts due to the impact causing more of a puncture into the laminate surface as opposed to a simple depression.

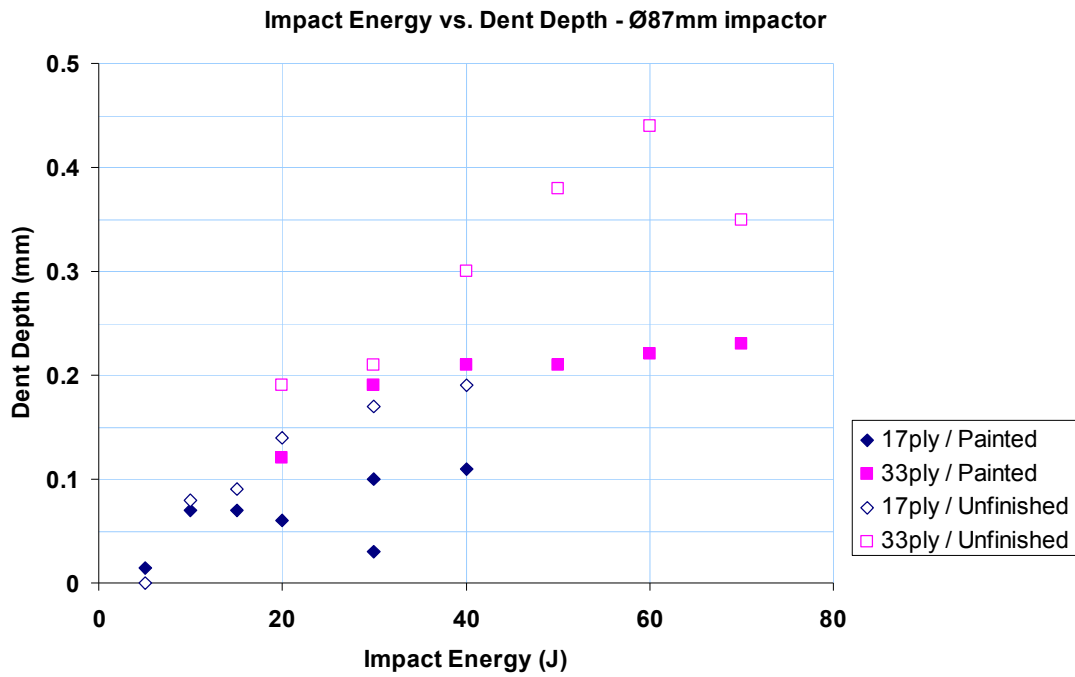


Figure 5.13 – Impact energy vs. Flaw depth plot for Ø87mm impactor

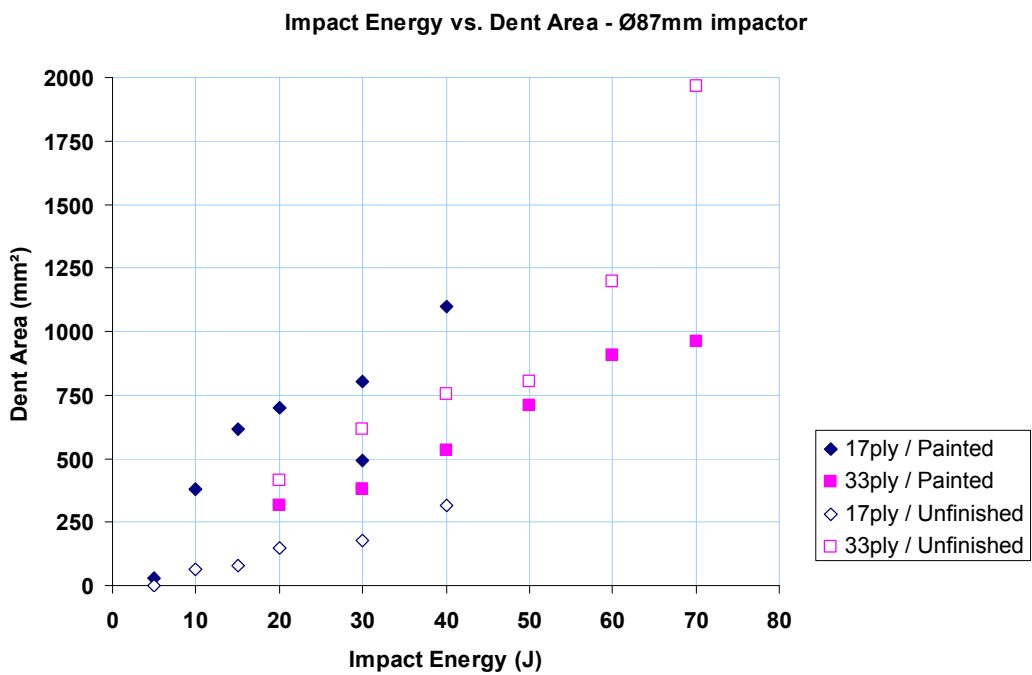


Figure 5.14 – Impact energy vs. Flaw area plot for Ø87mm impactor

### Ø70 mm Flat Cylindrical Impactor

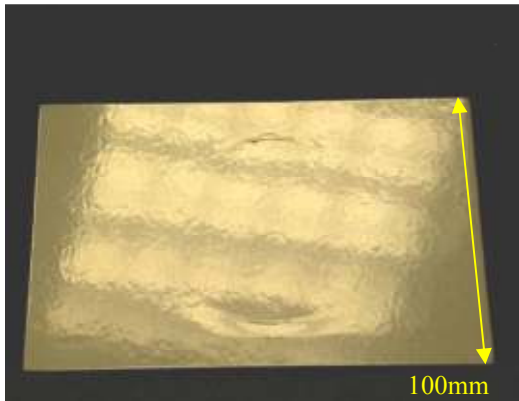


Figure 5.15 - 30J / Ø70 mm flat cylinder impact on 17ply painted laminate produced two distinct surface flaw areas with circular shaped depressions (0.2 mm deep)

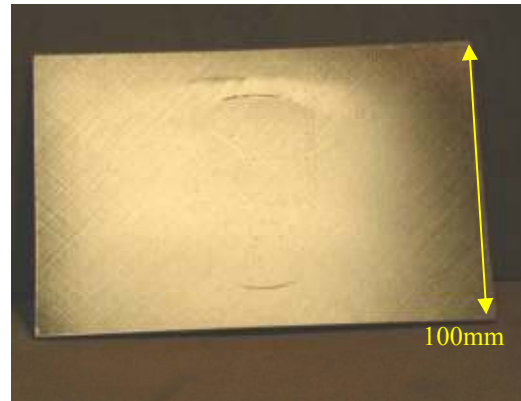


Figure 5.16 - 30J / Ø70 mm flat cylinder impact on 17ply unpainted laminate produced two surface flaw areas with deeper (0.24 mm), less complete circular shaped depressions

The typical visual appearance of surface flaws was a circular impression on the surface, which became more pronounced as impact energy increased. Some impacts from the Ø70 mm cylindrical impactor resulted in two surface flaw sites that appeared as sections of a circular depression. These can be seen clearly in figure 5.17, which illustrates a C-Scan of a painted coupon impacted by the Ø70 mm cylindrical impactor.

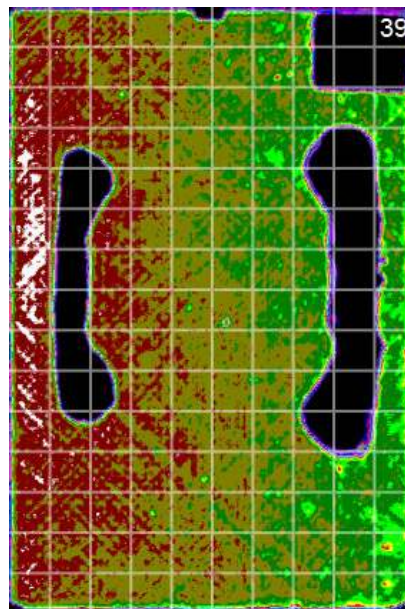


Figure 5.17 – C-Scan of 30J / 70 mm cylindrical impact on painted 17ply coupon

On the painted laminates (figure 5.15), the impact from the flat cylinder appeared to leave a less deep depression in the surface than the other types of impactor, but affected a greater area, giving the visual appearance of a far more serious surface flaw than was actually present. The depressions generally formed more of a complete circle on the painted coupons than on the unfinished coupons (figure 5.16).

### Wedge Shaped Impactor

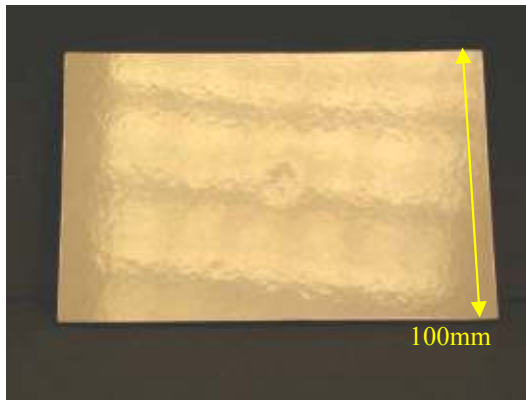


Figure 5.18 - 15J / tool shaped impact on 17ply painted laminate produced a small depression in surface

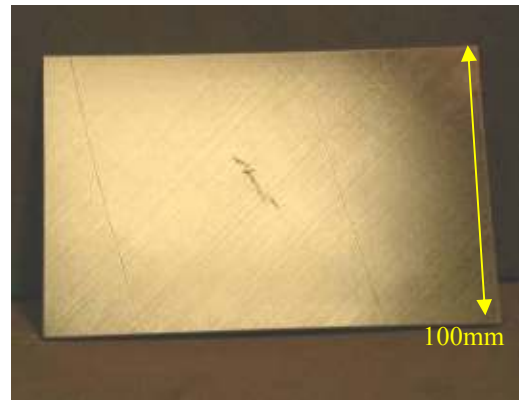


Figure 5.19 - 15J / tool shaped impact on 17ply unfinished laminate produced a small depression and surface cracking

The appearance of surface flaws on painted laminates (figure 5.18), and unfinished laminates (figure 5.19), remained similar in shape. However, on unfinished laminates, the impact caused the upper plies to split, with surface cracks becoming evident as seen in figure 5.19. Typical visual appearance of surface flaws is a small, rectangular impression, which at higher impact energies became surrounded by a shallow depression. The delamination sizes caused by the tool shape impacts are particularly large compared to the size of the surface indentation, as illustrated in figure 5.03, for both painted and unfinished laminates.

From observing the impact damage flaws on both fully finished and unfinished laminates, the following summary was made:

- There were differences in surface flaw appearance depending on the laminate finish. Surface breaking cracks occurred in flawed regions on the unfinished laminates even at low (<15J) impact energies, whereas such cracks only began to appear on the fully finished laminates once the impactor had caused laminate penetration. The energy level required for penetration of the painted laminates

varied from 30J with the Ø20mm / 17ply impacts to 50J for the Ø20mm / 33ply impacts. The hemispherical impact flaws on the unfinished laminates appeared to have jagged edges, whereas the flaws on the fully finished coupons were best described as having a ‘smooth, rounded’ flaw shape.

- The impactor shape affected the flaw topography. The hemispherical shaped impactors produced rounded, soft ‘edged’ flaws, whereas the tool shaped and flat cylindrical impactors produced flaws, or flaws with defined, i.e. ‘hard’ edges.
- Impact energy and severity of the surface flaw profile were not considered positively correlated. Higher energy impacts (>30J) from the Ø87 mm impactor appeared to affect large surface areas (>300 mm<sup>2</sup>), and produce flaws with low depths (<0.5mm) and very smooth sectional profiles. These ‘shallow’ surface profiles were felt to be far less discernable to the observer than the lower energy (<30J), smaller area (<300 mm<sup>2</sup>) and greater depth (up to 1.85 mm) Ø20mm impacts which were said to have more ‘acute’ surface indentation profiles.

#### ***5.1.4 – Characterisation of surface flaws from hemi-spherical objects***

The images from the metallographic sectioning performed by Boulic made it possible to visualise the impact damage morphology in sectional profile, and identify a geometric shape within the surface flaw that could be used to describe hemispherically shaped impact damage surface flaws. Figures 5.20 & 5.21 illustrate metallographic sections through hemispherical tip impact flaws on fully finished CFRP coupons. Above the section photograph, figures 5.20 & 5.21 illustrate a non-geometric line, which was overlaid using Photoshop image editing software, onto the upper ply of the laminate in order to show the sectional profile of the surface indentation. Each of the surface flaws in Boulic’s work had similar basic geometric shapes i.e. an internal and external radius (see ‘geometric shape’ in figure 5.20 & 5.21). It was thus possible to describe and recreate the sectional profile of the indentations using these geometric lines by constructing the lines in a CAD system (see chapter 4.6 & 4.7) using a common set of geometric variables, as described in figure 5.22, in order to define the lines. These geometric variables were adopted for quantitatively describing the sectional profile of each of the impact-damage flaws produced by hemispherical tips on the painted CFRP coupons.



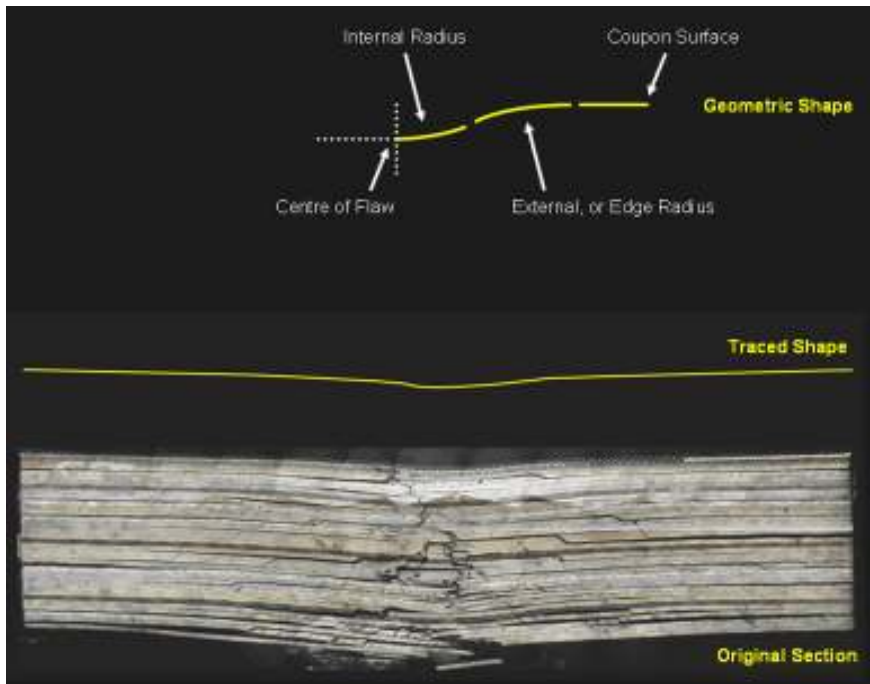


Figure 5.20 – Ø20 mm/50J Surface flaw on a 33ply coupon

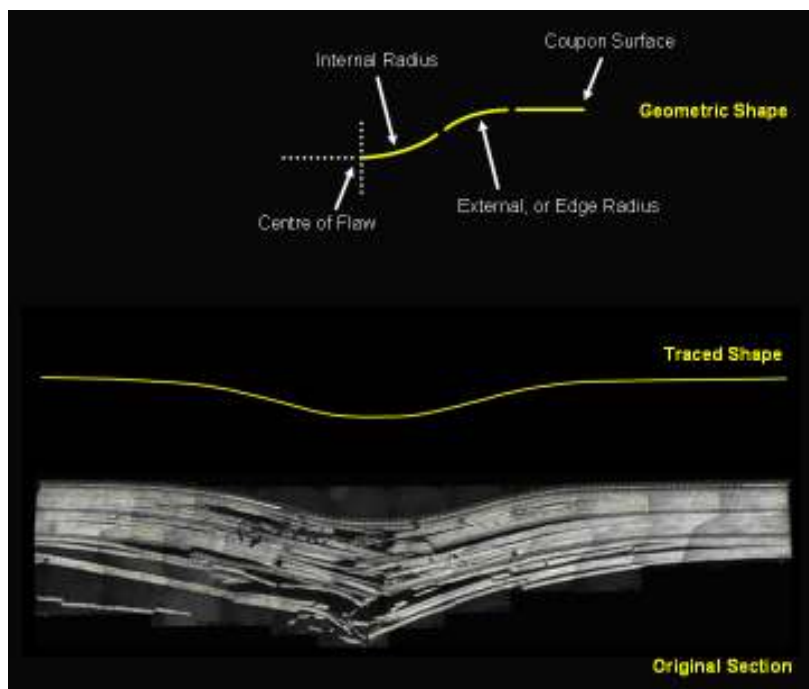


Figure 5.21 – Ø20 mm/ 30J Surface flaw on a 17ply Coupon

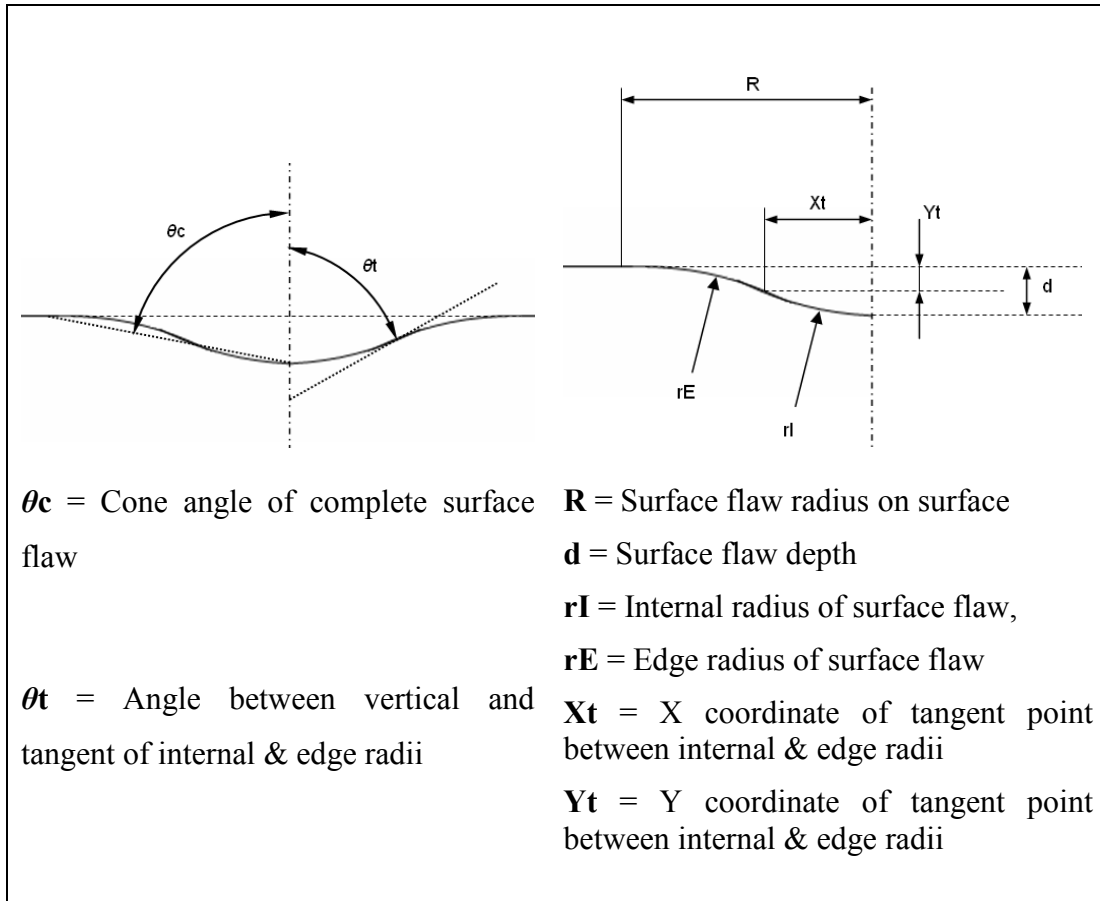


Figure 5.22 – Geometric variables used to reconstruct a surface flaw section

### 5.1.5 – Quantitative measurements of surface flaw topographies

CMM data of a set of 26 surface flaws on impact damaged, painted CFRP coupons was used to obtain depth measurements, width measurements and values for the geometric variables listed in figure 5.22, as per the method described in chapter 4.5 & 4.6. The measurements obtained are given in table 5.03.

Impactor Size	Thickness	Energy (J)	R [w/2] (mm)	d (mm)	rI (mm)	rE (mm)	Xt (mm)	Yt (mm)	$\theta_t$ (°)	$\theta_e$ (°)
Ø20 mm	17ply	5	2.5	0.11	11.78	16.68	1.03	0.06	84.96	87.48
		10	6	0.07	85.73	171.45	2	0.05	88.66	89.33
		15	10.75	0.32	58.84	121.89	3.5	0.22	86.59	88.29
		20	11	0.67	8.22	82.15	1	0.61	83.01	86.5
		30	15	2.11	5.44	48.94	1.5	1.9	73.99	81.99
	33ply	15	6	0.17	6.9	96.63	0.4	0.16	86.68	88.34
		20	7.5	0.2	9.57	134.02	0.5	0.18	87.01	88.5
		20	8	0.19	12.64	155.88	0.6	0.18	87.28	88.64
		30	11.5	0.19	24.09	322.21	0.8	0.18	88.1	89.05
		50	15	0.86	8.75	122.49	1	0.8	83.44	86.72
	50	16.5	0.61	13.54	209.92	1	0.57	85.77	87.88	
Ø87 mm	17ply	10	2.5	0.12	10.42	84.5	1	0.12	84.5	87.25
		15	6	0.11	41.68	125.04	1.5	0.08	87.94	88.97
		20	5	0.08	46.89	109.4	1.5	0.06	88.17	89.08
		20	6.5	0.18	36.14	81.31	2	0.12	86.83	88.41
		30	8	0.02	666.67	1466.67	2.5	0.01	89.79	89.89
		40	11	0.21	91.7	196.5	3.5	0.14	87.81	88.91
		40	11.25	0.45	43.82	97.03	3.5	0.31	85.42	87.71
	33ply	20	6.5	0.14	78.69	204.6	2.5	0.1	88.18	89.09
		30	10.5	0.18	101.55	203.1	3.5	0.12	88.02	89.01
		40	14	0.3	104.01	219.57	4.5	0.21	87.52	88.76
		40	30	0.26	286.48	1442.42	5	0.26	89.01	89.5
		50	23	0.37	203.73	517.16	6.5	0.26	88.17	89.09
		60	20	0.28	286.79	430.19	8	0.17	88.4	89.2
		60	35	0.29	521	1893.82	13	0.13	88.57	89.53
	70	31	0.34	659.17	750.09	14.5	0.18	88.74	89.37	

Table 5.03 – Table of geometric variable data obtained from surface flaws on painted, mesh incorporated CFRP laminate coupons

### 5.1.6 – Relationships between impact flaw geometry variables

The data in table 5.03 were plotted using Excel scatter-plots in order to identify relationships between the geometric variables. The data points were assessed in terms of the general trend, or data shape, and suitable best-fit lines were added. Plots of surface flaw width vs. impact energy, surface flaw depth vs. energy, surface flaw width vs. Xt value, and surface flaw depth vs. Yt value were produced, and are given in figures 5.23 to 5.26.

The data on the plot (figure 5.23) of impact energy and surface flaw radius R, i.e. ½ the flaw width, were fitted with linear best-fit lines. The fit equation, as shown on the

plot, for each of the impactor/ laminate thickness combinations allow the surface flaw width (2R) to be modelled as a function of impact energy and vice versa. Variations in the relationships were observed for each type of impactor on the two laminate thicknesses, resulting in 4 different relationships.

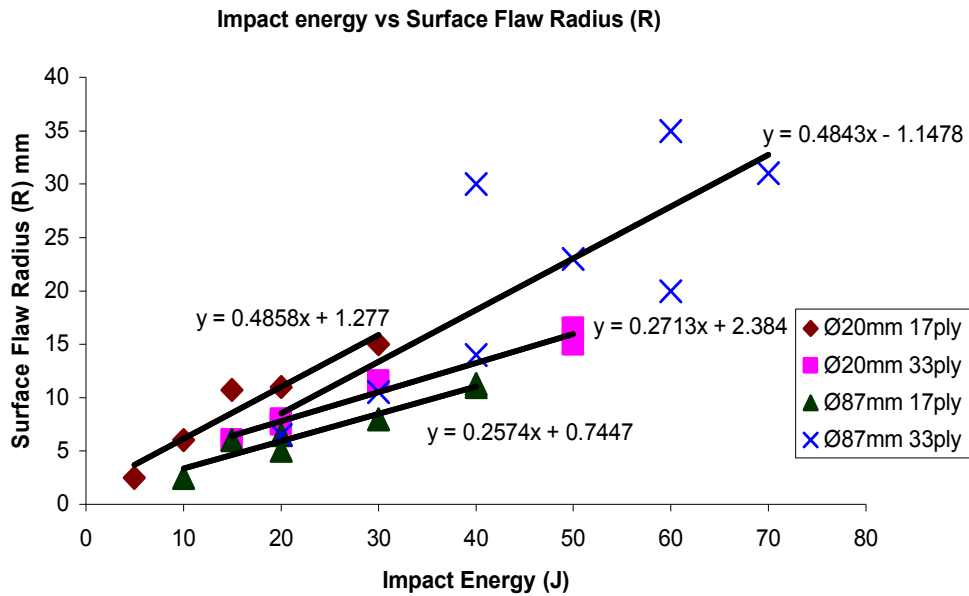


Figure 5.23 – Plot of impact energy vs. surface flaw radius with linear lines of best fit

The data on the plot of surface flaw depth vs. impact energy (figure 5.24) was best fitted by an exponential model. The data for the Ø20 mm/ 17ply flaws exhibited a comparatively high rate of increase in flaw depth as impact energy increased from 10J to 30J. The remaining impactor type / laminate thickness combinations exhibited lower rates of increase in depth with increasing impact energy. Each impactor / thickness combination resulted in a different relationship between impact energy and flaw depth.

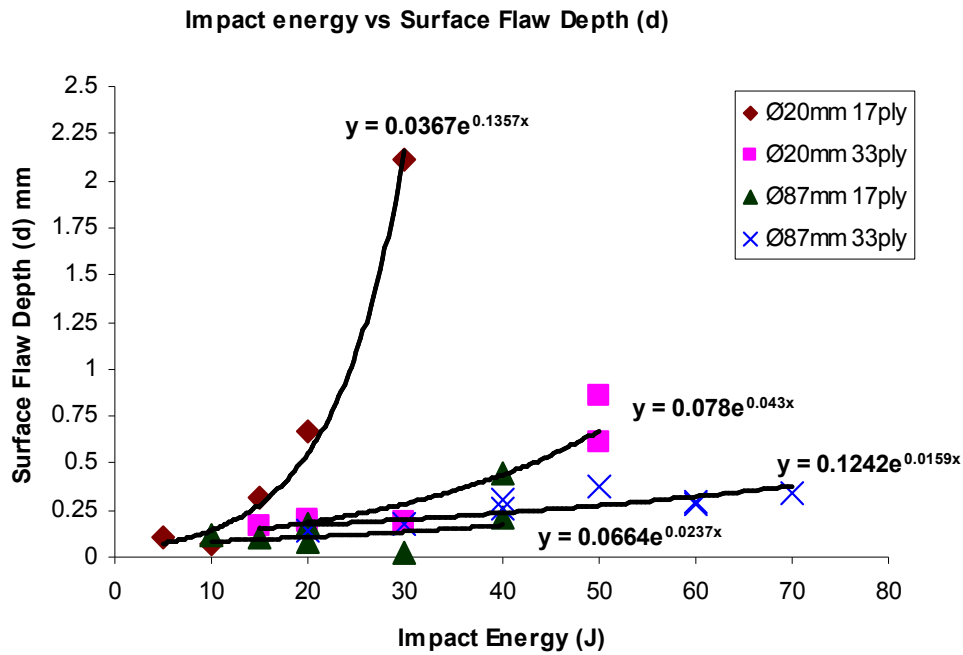


Figure 5.24 – Plot of impact energy vs. surface flaw depth with exponential lines of best fit

The data plotted in figure 5.25 were fitted with linear lines to represent the four different relationships between  $R$  ( $\frac{1}{2}$  flaw width) and the  $X_t$  point variable (see figure 5.22). The rate of increase in  $X_t$  with increasing values of  $R$  for the  $\text{Ø}20$  mm / 33ply flaws was comparatively lower than the other impactor / thickness combinations. The data plotted in figure 5.26 were also fitted with linear lines in order to represent the relationships between flaw depth and the  $Y_t$  geometric variable value. The linear best-fit lines shown in figure 5.26 exhibit comparatively less variation than the other relationships modelled in figures 5.23 – 5.25, suggesting that the increase in  $Y_t$  with increasing flaw depth was less affected by impactor / thickness variations.

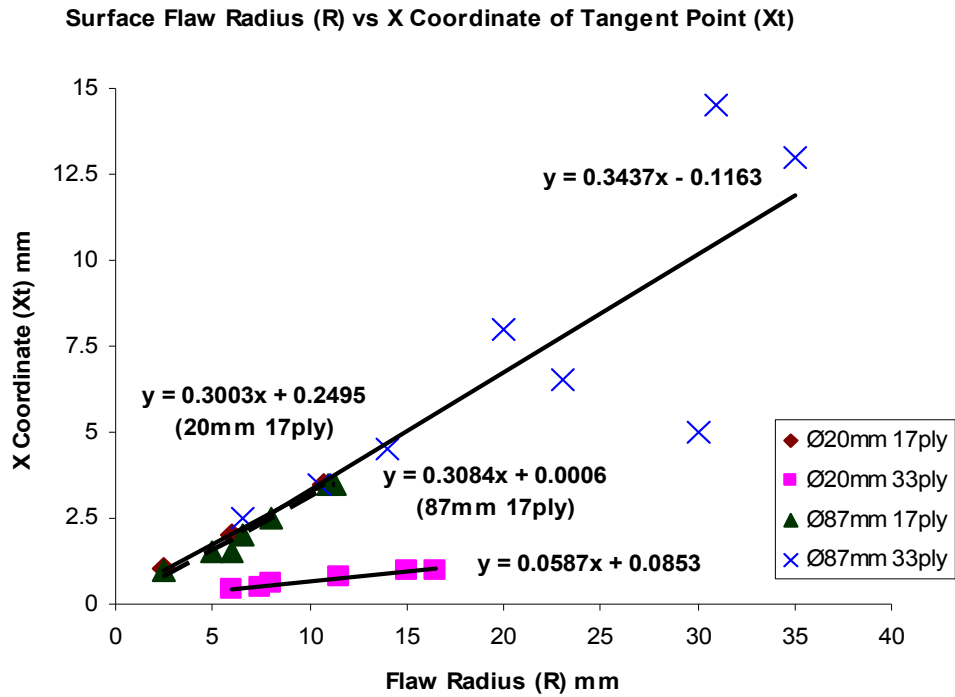


Figure 5.25 – Plot of surface flaw radius vs.Xt with linear lines of best fit

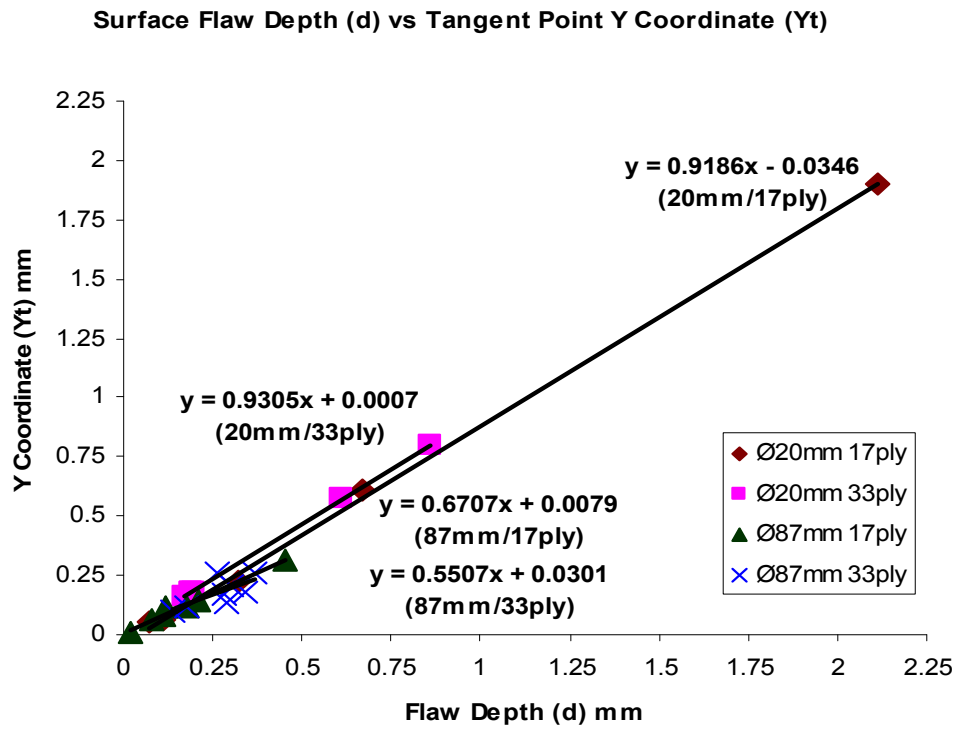


Figure 5.26 – Plot of surface flaw depth vs.Yt with linear lines of best fit

Table 5.04 gives the relationships obtained by the best fit-line method from tested coupons for two impactor sizes and two laminate thicknesses. Also given is the energy range for which the relationship remains valid. All the relationships are only valid for impacts greater than 4J; impacts below this energy level will not produce subsurface damage, and are thus irrelevant to this study. Impacts above the given limit will penetrate the laminate, or cause a significant shape change to the laminate, in which the case the surface flaw characteristics are outside the scope of this study, hence the use of an upper limit.

<b>17ply/ Ø20 mm</b>	<b>17ply/ Ø87 mm</b>
Energy $E = (R-1.277)/0.4858$	Energy $E = (R-0.7447)/0.2574$
Depth $d = 0.0367(\exp(0.1357E))$	Depth $d = 0.0664(\exp(0.0237E))$
X Point $X_t = (0.247E)-0.2933$	X Point $X_t = (0.0824E)+0.1555$
Y Point $Y_t = 0.0199(\exp(0.1553E))$	Y Point $Y_t = 0.0598(\exp(0.0137E))$
Applicable energy range: 4J -30J	Applicable energy range: 4J – 50J
<b>33ply/ Ø20 mm</b>	<b>33ply/ Ø87 mm</b>
Energy $E = (R-2.384)/0.2713$	Energy $E = (R+1.1478)/0.4843$
Depth $d = 0.078(\exp(0.043E))$	Depth $d = 0.1242(\exp(0.0159E))$
X Point $X_t = (0.0159E)+0.2263$	X Point $X_t = (0.2393E)-3.8805$
Y Point $Y_t = 0.0727(\exp(0.043E))$	Y Point $Y_t = 0.1198(\exp(0.0075E))$
Applicable energy range: 4J – 80J	Applicable energy range: 4J – 80J

Table 5.04 – Geometry variable relationships for impact damage surface flaws.

The relationships listed in table 5.04 were used to calculate the flaw energy (E) as a function of flaw width (2R) and the flaw depth (d), Xt value and Yt value as a function of impact energy (E) for chosen values flaw widths (2R). Using these values, the sectional profiles of representations of surface flaws caused by impacts, at energies within the ranges specified in table 5.04, from Ø20 mm & Ø87 mm tips on 17ply & 33ply fully finished CFRP laminate were able to be defined. By inputting the depth, R, Xt and Yt values, the geometric lines representing sectional profiles of impact damage flaws were created and associated 3D models of the flaws were produced in a 3D CAD system (see chapter 4.7).

## ***5.2 – CMM checking of physical facsimile specimens***

Five selected flaws on each colour of specimen underwent CMM measurement (as described in chapter 4.9.2) to check for conformity to the original specification, and table 5.05 details the findings. One can see in table 5.05 that the surface height measurements reveal no depth discrepancies, meaning that all the flaws were machined to the correct depth. Discrepancies between the specified surface height at the Xt point and the scanned surface height varied from 0.002 (#28 / white) to 0.050 (#7 / white) mm. The average discrepancy across all specimen colours for each measured flaw was between 1.9% and 8.5% of the specified surface height at the Xt point. As the average discrepancies were less than 10%, the machined flaws were all deemed to be within acceptable tolerance of the original specified shape. The surface height measurements at the flaw endpoints revealed that flaws 7, 9, 14, 20 & 28 had been machined with endpoint surface height discrepancies of less than 5% of the flaw depths across the three specimen colours. These flaws were thus deemed to be within an acceptable width tolerance. The measurements of flaw 9 revealed similar sizes of surface height discrepancies at the flaw endpoints, although due to flaw 9 being only 0.1mm deep, this translated into an average discrepancy of 15% of the total flaw depth. Despite this, and given that the surface height discrepancies for the endpoints of flaw 9 were all relatively small (<0.02mm), each example of flaw #9 was deemed to be the correct, specified width.



Flaw No	Check Point	Specified Surface Height	Surface Height Discrepancy			Average discrepancy across specimens
			Grey Specimen	White Specimen	Blue Specimen	
7	Endpoint	0 mm	0.044mm	-0.010mm	-0.023mm	0.0037mm (0.64% of depth)
	Xt Point	-0.329mm	0.018mm	-0.050mm	-0.005mm	-0.0123mm (3.75%)
	Centre (d)	-0.57mm	0mm	0mm	0mm	0mm
9	Endpoint	0mm	-0.019mm	-0.013mm	-0.013mm	-0.0150mm (15% of depth)
	Xt Point	-0.092mm	-0.007mm	-0.008mm	-0.004mm	-0.0063mm (6.88%)
	Centre (d)	-0.1mm	0mm	0mm	0mm	0mm
14	Endpoint	0mm	-0.011mm	-0.017mm	-0.011mm	-0.0130mm (5% of depth)
	Xt Point	-0.243mm	0.000mm	0.007mm	0.007mm	0.0047mm (1.92%)
	Centre (d)	-0.26mm	0mm	0mm	0mm	0mm
20	Endpoint	0mm	0.019mm	-0.007mm	0.010mm	0.0073mm (4.58% of depth)
	Xt Point	-0.11mm	-0.011mm	-0.004mm	-0.013mm	-0.0093mm (8.48%)
	Centre (d)	-0.16mm	0mm	0mm	0mm	0mm
28	Endpoint	0mm	0.027mm	-0.011mm	0.012mm	0.0093mm (4.91% of depth)
	Xt Point	-0.153mm	-0.014mm	-0.002mm	-0.010mm	-0.0087mm (5.66%)
	Centre (d)	-0.19mm	0mm	0mm	0mm	0mm

Table 5.05 – +/- Y-Axis measurements from CMM data of specimen surface flaws

### 5.3 – Gloss measurements of physical facsimile specimens

Table 5.06 gives the measurements made from the panels using a Novo Gloss dual-angle (20°, 60°) gloss meter.

Panel/ Specimen Colour	Gloss units (measurement angle)
Gloss Grey	84.666 (60°)
Gloss White	88.033 (60°)
Gloss Blue	79.833 (60°)
Matt Grey	1.733 (60°)
Matt White	7.766 (60°)
Matt Blue	0.533 (60°)

Table 5.06 – Gloss measurements of specimens

The gloss-finish Plexiglas specimens are no glossier than one would expect a painted aircraft structure to be [Akzo Nobel 2006 & 2008; PPG 2003; Guseva 2003], and the matt

finish grey and blue specimens are below the maximum gloss level that one would expect from a matt finish aircraft structure [Akzo Nobel 2006 & 2008; PPG 2003]. For the matt white finish specimens, the gloss reading of 7.766 gloss units is low enough to be considered as a matt finish, despite being slightly higher than that specified by aircraft paint manufacturers for matt finish aircraft paint [Akzo Nobel 2006 & 2008; PPG 2003].

#### ***5.4 – Results of visual inspection trials with virtual specimens – series 1***

After collecting the hit/miss data from the answer sheets as described in chapter 4, the number of participants correctly detecting each flaw was divided by the number of inspections for each flaw to provide the detection rate as a percentage. I.e. for a flaw inspected by 17 participants, and detected by only 15 of those participants, the detection rate would be 88%. Presenting detection results as a % value allows comparison between results from trials that used different numbers of participants.

##### ***5.4.1 – Results of trial 1***

Trial one was successfully undertaken by 7 participants. The main purpose of trial 1 was to determine a width of flaw that gave approximately 50% detectability. Trial 1 also served as a dress rehearsal for the virtual trials methodology hence the low number of participants. The hit/ miss data for trial 1 are presented in appendix E. From the hit/miss data, it was possible to produce the scatter plot seen in figure 5.27, which gives the percentage of participants that successfully detected each flaw. The data on the plot in figure 5.27 show a general trend for flaw detectability to reach over 85% for flaws wider than Ø6 mm. The key observations from the scatter plot were that:

- Flaws below 5 mm wide, at a depth of 1 mm, resulted in 0% detections.
- Detection of flaws greater than 6 mm wide varied between 85% and 90%

The variation in detection between 85% & 100% for flaws over 6 mm wide is accounted for by the fact that the response of a single participant was sufficient to impart variation of 15% in the total detectability result for a single flaw. Reviewing the hit/ miss data in appendix E reveals that the 15% variation in results for flaws >6 mm wide was caused solely by the responses of participant 2. The reason for the discrepancy between participant 2 and other participant results is unknown.

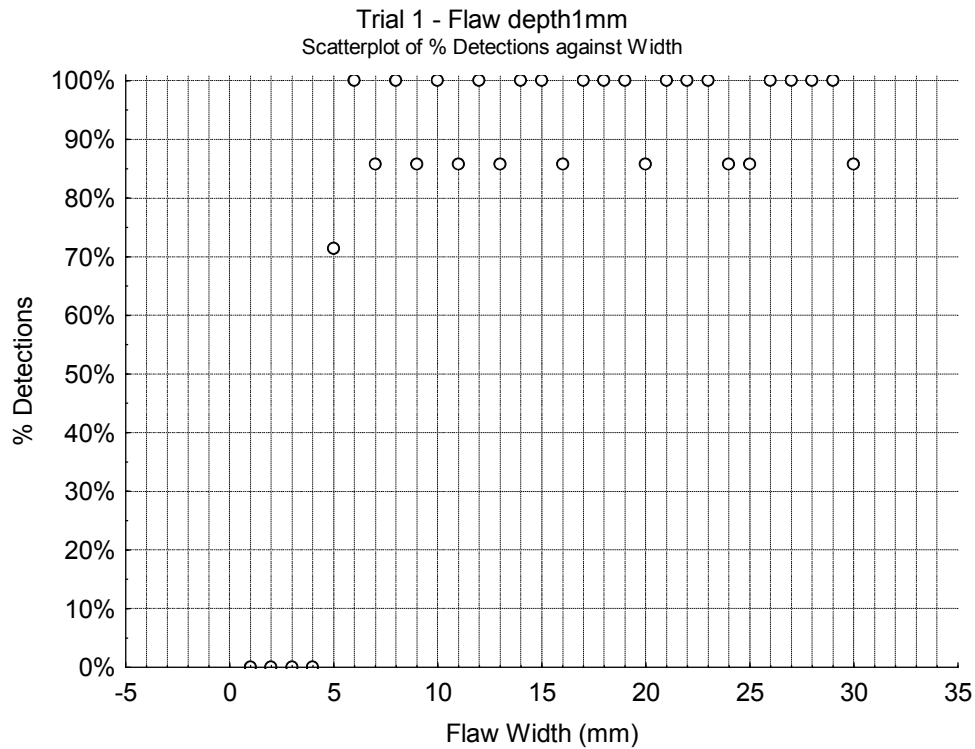


Figure 5.27 – Scatter plot of results from Trial 1 with virtual specimens

The results data from trial 1 were analysed using the log-odds/ range interval method [Bullock et al. 1994] in order to determine the POD curve seen in figure 5.28. The data and calculations used to generate the POD curve are given in appendix F. Using the POD curve for trial 1, it was determined that a flaw size of Ø4.5 mm would give approximately 50% POD, a flaw size of Ø6.5 mm would give approximately 70% POD and >90% POD could be expected for flaws >Ø12 mm. The data for trial 1 also indicated that for a flaw depth of 1mm, the detection rates (figure 5.27), or POD (figure 5.28), increased with increasing flaw width.

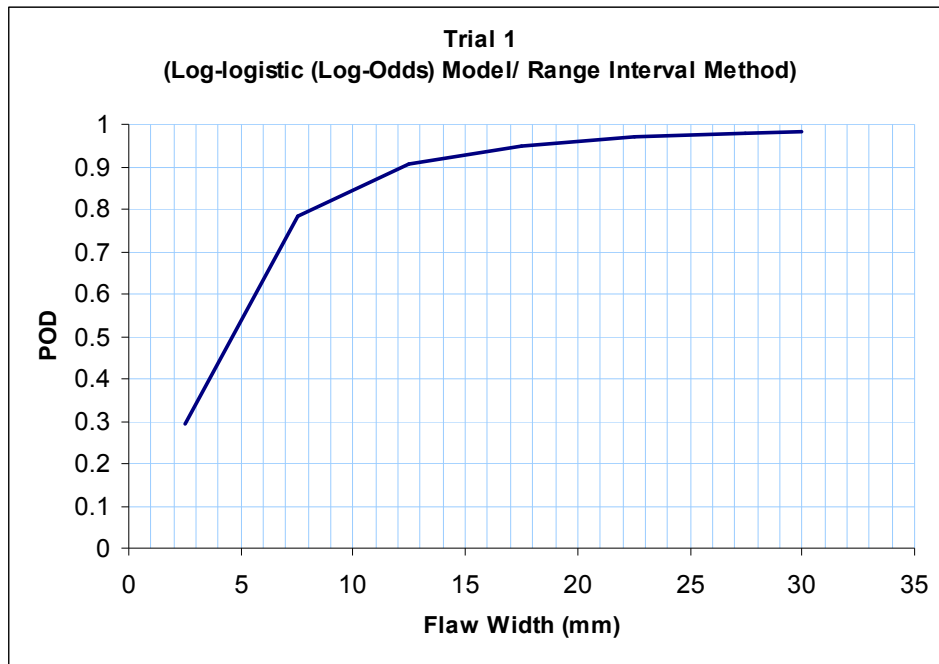


Figure 5.28 – log-odds/ RIM POD curve produced from trial 1 data

#### 5.4.2 – Results of trials 2 and 3

Trials 2 and 3 also utilised virtual specimens, and were both undertaken by 15 participants. The virtual trials methodology, utilising a projector to display the virtual specimens was again successfully implemented, and all participants successfully completed their trials.

As described in chapter 4.10, the virtual specimens for Trial 2 contained hard edged, hemispherical shaped circular flaws representing hard-edged flaws. Trial 3 contained the same sizes of surface flaws, with the addition of a radius, or blended edge to the flaw, thus resulting smoother flaw profiles. The following flaws were included in the specimen set:

- Ø4.5 mm flaws, 0.1 mm to 1.5 mm deep (50% POD width from trial 1)
- Ø6.5 mm flaws, 0.1 mm to 1.3 mm deep (70% POD width from trial 2)
- Ø12 mm flaws 0.1 mm to 1.1 mm deep (90% POD width from trial 3)

From the hit/miss data presented in appendix E for trials 2 & 3, the percentage of participants successfully detecting each flaw was calculated. Scatter plots of the detection percentage of each flaw vs. flaw depth, as seen in figures 5.29 to 5.31, were

produced by inputting the % detection data into Statistica [Statsoft Inc. 2008]. Figure 5.29 illustrates the results of both trial 2 & 3 using Ø4.5 mm wide flaws, and for flaw depths of below 0.5 mm, there are inconsistent differences in the detectability of the hard edge and blended edged flaws. There is considerable scatter in this flaw depth range, with the detection % for blended edge higher than hard edged for the 0.2, 0.4 & 0.5 mm deep flaws and vice a versa for the 0.1 & 0.3 mm deep flaws. Thus, for the Ø4.5 mm wide flaws, it is not possible to identify any consistent effect on detection rate (% detections) due to the different flaw profiles.

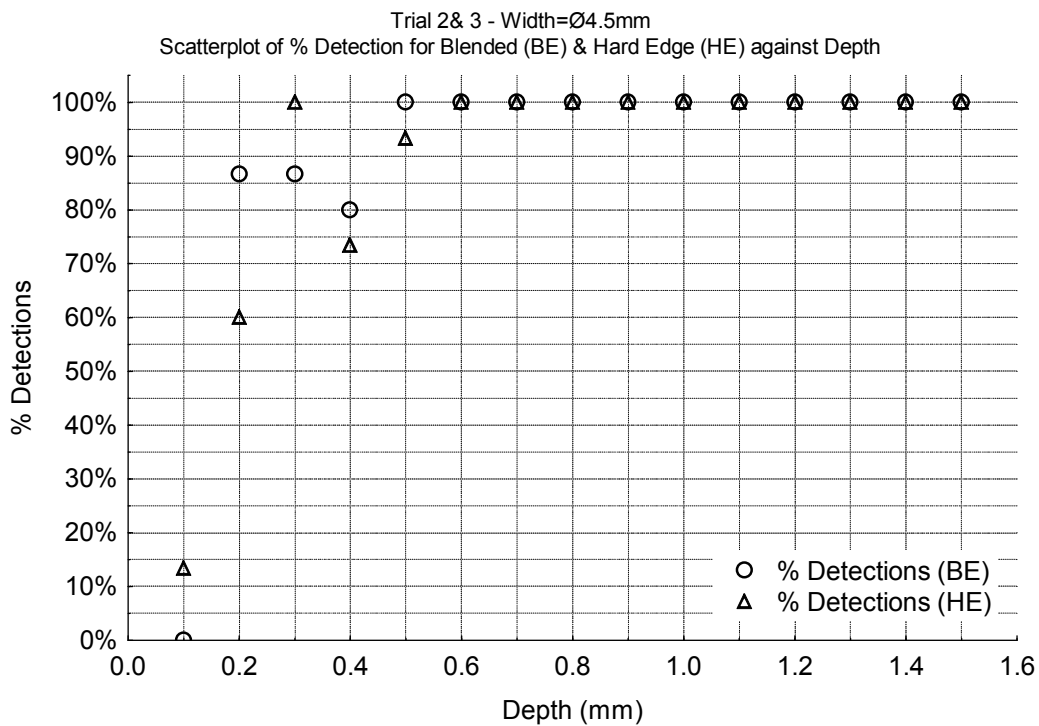


Figure 5.29 – Scatter plot of detection results for Ø4.5 mm flaws on virtual specimens

The hit/miss data from the Ø6.5 mm flaws in trial 2 & 3 (see appendix E) are summarised by the scatter plot given in figure 5.30. The results for hard edged and blended edged flaws are similar for flaws greater than 0.2 mm deep. However, the detection rates for the 0.1 mm deep flaw are over 20% greater for the hard-edged flaws, suggesting that the detectability of this size (0.1 mm deep/ Ø6.5 mm) of flaw was reduced by the addition of a blended edge. For the flaws, of both types, of depths <0.5 mm, the detection rate is consistently over 90%, compared to the lower rates for the same flaw depths for Ø4.5 mm wide flaws. This suggests that the increased flaw width resulted in increased detectability for < 0.5 mm deep flaws.

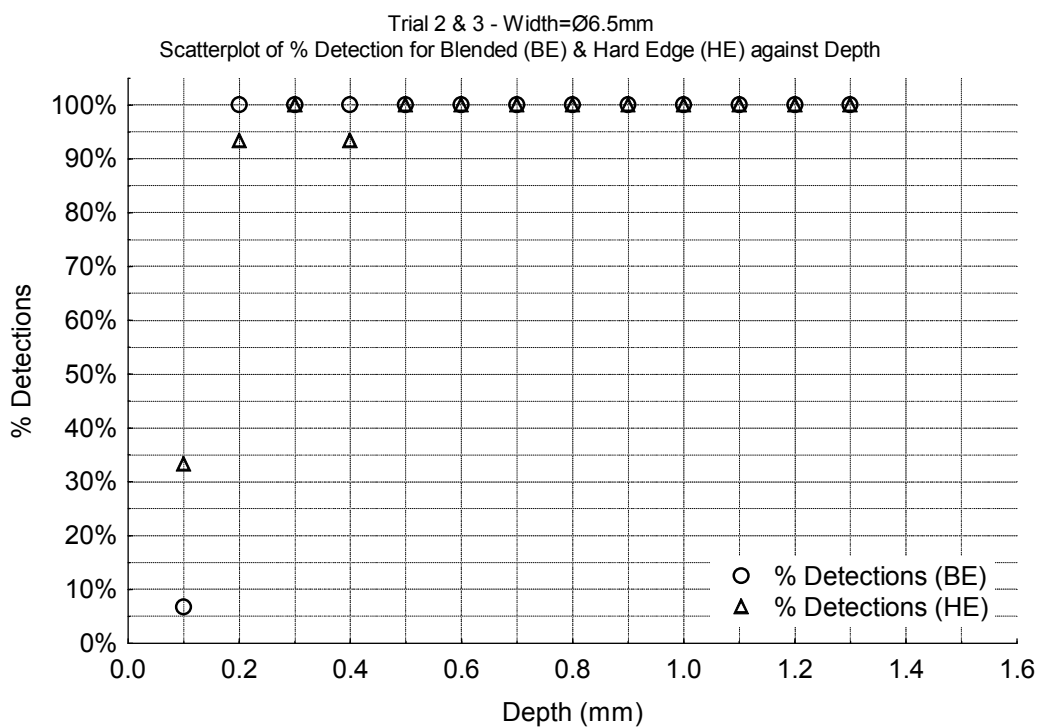


Figure 5.30 – Scatter plot of detection results for Ø6.5 mm flaws on virtual specimens

The hit/miss data (appendix E), and detection rate results for the Ø12 mm wide flaws are summarised by the scatter plot in figure 5.31.

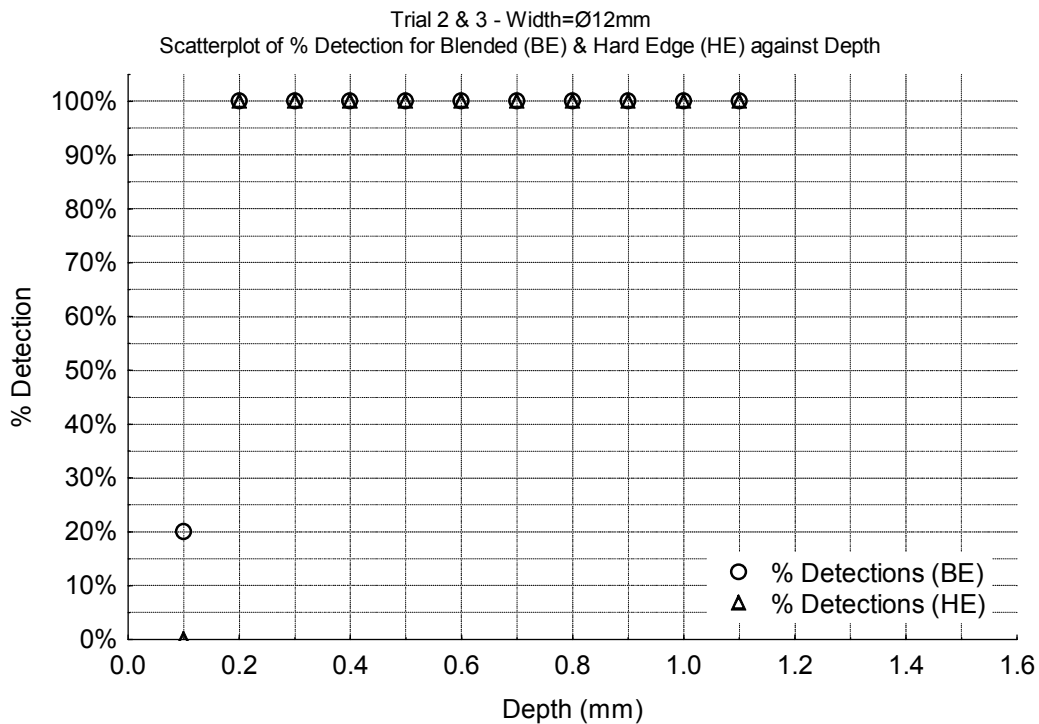


Figure 5.31 – Scatter plot of detection results for Ø12 mm flaws on virtual specimens

For a flaw width of Ø12 mm, and depth >0.2 mm, the flaws were detected by all the participants. None of the participants were able to detect the 0.1 mm deep, Ø12 mm hard-edged flaw.

The results from trial 2 with the Ø4.5 mm and Ø6.5 mm hard-edged flaws were plotted as POD curves, as seen in figure 5.32 (see appendix F for POD curve calculations). The Ø4.5 mm flaw data indicated 50% POD at 0.15 mm deep and 90% POD at approximately 0.3 mm deep. The Ø6.5 mm flaws returned a minimum of 65% POD for the 0.1 mm deep flaws, and the 90% POD size was estimated at 0.25 mm deep. The data from the Ø12 mm flaws could not be plotted as a POD curve due to only a single flaw returning less than 100% detections, which results in insufficient data points to construct the regression & POD curves from.

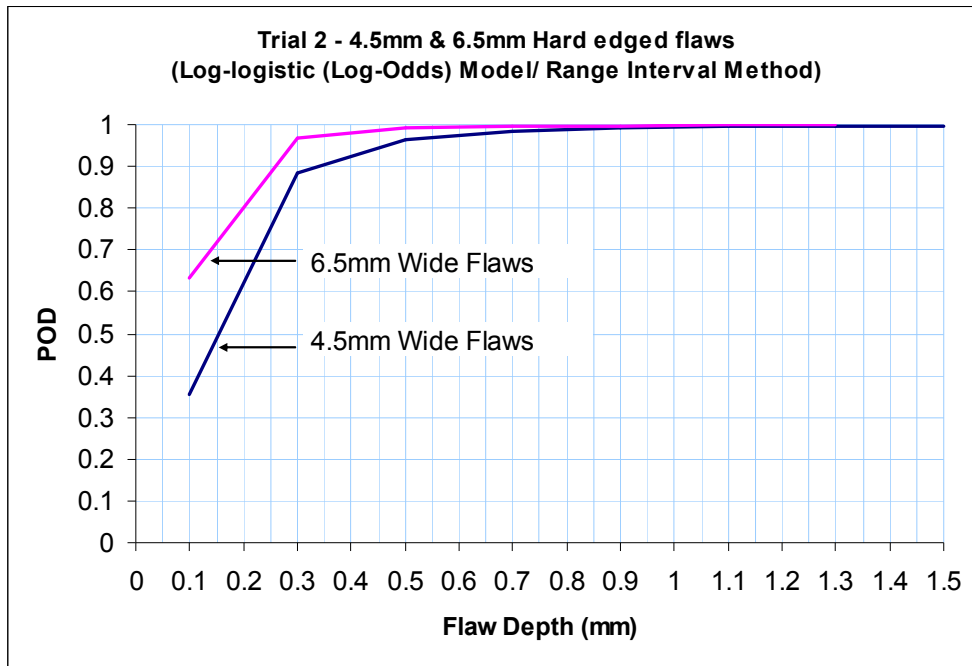


Figure 5.32 – POD curve from results of trial 2

As for the results of trial 2, the results from trial 3 were also plotted as POD curves (see appendix F). However, only the detection data from the Ø4.5 mm flaws could be plotted, due to the low frequency of <100% detections for the other flaw sizes. The POD curve for trial 3 is given in figure 5.33, and it can be seen that for the blended edge, Ø4.5 mm flaws, the 50% POD size is approximately 0.125 mm deep.

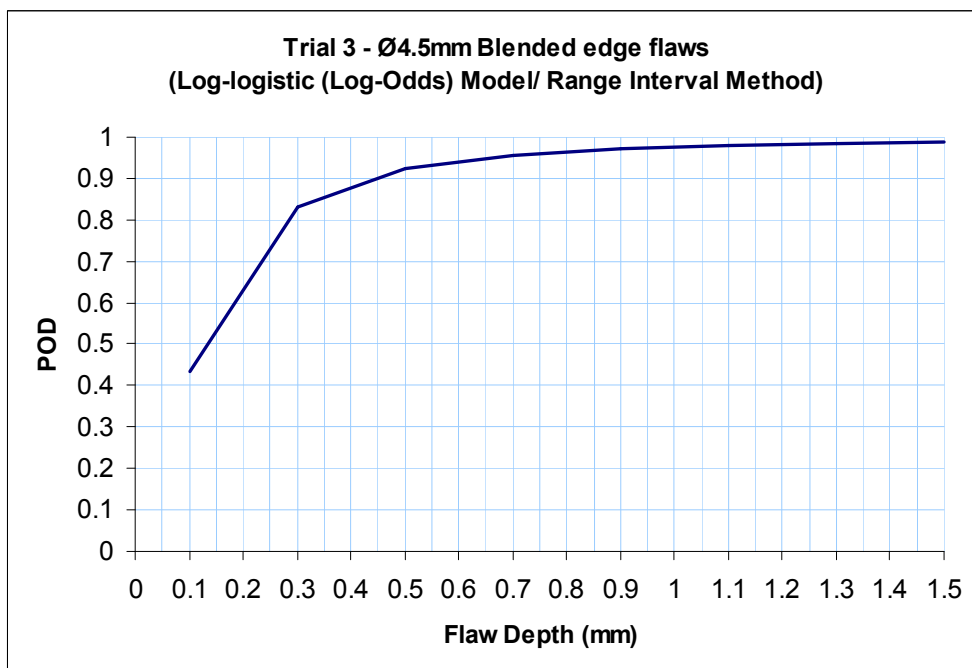


Figure 5.33 – POD curve from results of trial 3



The observations made from the results of trials 2 and 3 were:

- For flaws between 0.2 mm and 0.6 mm deep, and of widths of Ø4.5 mm, Ø6.5 mm and Ø12 mm, the detectability was greatest for the wider flaws.
- Flaws less than 0.1 mm deep gave less than 50% detectability
- Flaws greater than 0.6 mm deep were detected by all participants, irrespective of the flaw width.
- 50% POD occurred for Ø4.5 mm flaws at a flaw depth of 0.15 mm deep for hard-edged flaws, and at a depth of 0.125 mm for blended edged flaws.
- There was insufficient difference in the POD data for the Ø4.5 mm flaws, and no comparisons available for the Ø6.5 mm & Ø12 mm flaws in order to quantify the effect of the blended edge on detectability
- Due to trials 2 & 3 using only 3 values of flaw width, the effects of varying flaw width at lower flaw depths (<0.5 mm) on detectability could not be demonstrated

#### ***5.4.3 – Results of trial 4***

The virtual specimens used in trial 4 contained both hard and blended edged flaws, all of 0.15 mm depth and of widths ranging from 3 to 30 mm. The % detection data for each flaw, as calculated from the hit/miss data (see appendix E) returned by the 14 participants are summarised in the scatter plot shown in figure 5.34. As seen in figure 5.34, the blended and the hard-edged flaws returned similar results for the flaws up to Ø15 mm in size, thus providing little evidence that the addition of a blended edge had any significant effect on detection rates. As seen in figure 5.34, for flaws >Ø15 mm and with the exception of the Ø28 mm flaw, the detection % for the blended edge flaws were lower than the hard-edged flaws of the same width. A difference of up to 75% in detection rates was seen for the 22 mm flaw, and detection rates for the blended edge flaws at 22, 26 and 30 mm wide were less than 10%, compared to between 85% and 40% for the same size hard-edged flaws. Apparent in figure 5.34 is that the detection % does not increase with flaw width. Instead, the shape of the data plots is such that the detection % increases with flaw width until Ø15 mm. For flaws >Ø15 mm, the detection percentages become scattered, with flaws of similar sizes such as the Ø20 ~ Ø25 mm range exhibiting considerable variation in detection percentage (<10% to 50% for blended edge flaws).



Figure 5.34 – Scatter plot of detection results from trial 4

POD analysis of the detection data from trial 4 was performed (appendix F) in order to attempt to reduce the scatter seen in figure 5.34 and help improve the distinction of trends within the data. The detection data from trial 4, as represented in figure 5.34, presented a novel issue in terms of POD analysis, in that as flaw width increased, the detectability reached a peak before reducing again, albeit with considerable scatter. When the probability values for the data were calculated, (as seen in appendix F), the hard-edged flaws within the 3 mm to 9 mm flaw width returned increasing probability values as the flaw width interval size increased. For flaws within the 11 mm to 29 mm width intervals, the probability values reduced with increasing flaw width.

In order to plot a POD curve that reflected both increasing and decreasing POD with increasing flaw width, two values for  $\alpha$  &  $\beta$  were produced using RIM/ regression analysis [Bullock et al. 1994]. The first  $\alpha$  &  $\beta$  values were obtained for the 3 mm to 9 mm flaw width intervals. The second  $\alpha$  &  $\beta$  values were obtained for the 11 mm to 29 mm flaw width intervals. To create the POD curve, the POD function was run using the first set of  $\alpha$  &  $\beta$  values with the detection data for the 3 mm to 9 mm flaw width intervals, and the values recorded. The same was done for the 11 mm to 29 mm flaw

size intervals, this time using the second set of values for  $\alpha$  &  $\beta$ . The resulting POD curve (figure 5.35) combines all of the function outputs, and plots them against the corresponding flaw size interval, hence, the curve having a clear ‘switch’ point as POD begins to reduce.

The POD curve produced from the detectability data from trial 4 is presented in figure 5.35. The full data tables can be seen in appendix F. For both types of flaws, the 3 mm to 11 mm flaw width intervals gave increasing detectability with increasing flaw width, and the 13 mm to 29 mm flaw width intervals gave decreasing detectability with increasing flaw width. As seen in figure 5.35, the POD curves for the blended and hard edged flaws were similar for flaws up to 10 mm wide. The POD curves also indicate a greater rate of decrease in POD with increasing flaw width for the blended edge flaws than that of the hard-edged flaws greater than 11 mm wide.

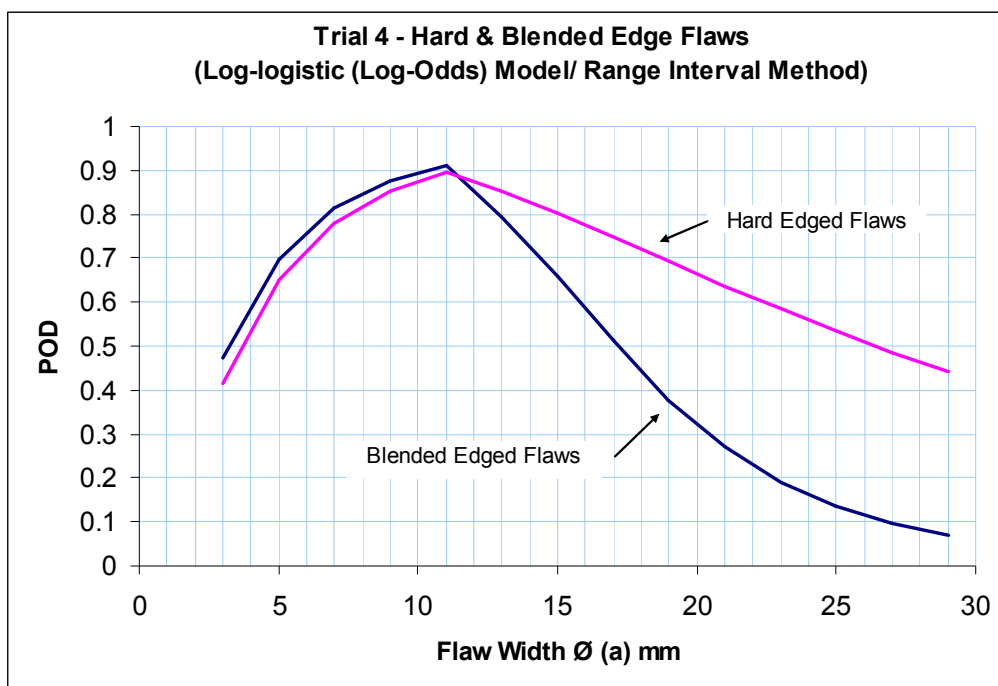


Figure 5.35 – Comparison of POD vs. flaw width for hard edged and blended edge flaws, from results of trial 4

As seen in the scatter plot in figure 5.34, for all but one flaw greater than >15 mm wide, the detectability is lower for the equivalent sized blended edge flaw than the hard edged flaw. The difference varies from between approximately 10% and 75% lower detection rate for the blended edge flaws. The POD analysis of the results data similarly indicate lower detectability for the blended edge flaws greater than >15 mm

wide. The results from trial 4 suggest that a hard-edged, 0.15 mm deep, hemispherical shaped flaw would be detected with greater than 50% POD so long as it is *between* 3.8 mm and 26 mm wide. However, the results from the blended edge flaws suggest that a 0.15 mm deep hemispherical flaw will only >50% detectable up to a width of Ø17 mm.

#### **5.4.5 – Summary of results from series 1 of virtual trials**

The results from the first series of virtual trials can be summarised as follows:

- <Ø5 mm flaws with blended edges returned detection rates less than 90% and approaching 0% for flaw depths <0.5 mm in trial 3.
- For flaws of the same width and >Ø15mm, flaws with blended edge shapes were generally less detectable than flaws with hard-edged shapes in trial 4, with the discrepancy in detection percentage varying from <10% up to >75%.
- For a constant flaw depth of 0.15 mm, detection rates for wide flaws (>Ø15 mm) reduced with increasing flaw width for the blended edge flaws, which are similar in size and shape to impact flaws observed on fully finished CFRP laminate coupons.

#### **5.5 – Results of visual inspection trials – series 2**

The second series of visual inspection trials to assess the reliability of visual inspection for composite aircraft structures was performed using volunteer participants and both virtual specimens and physical facsimile specimens, as described in chapter 4.10. A single trial constituted visual inspections of a set of 600 mm x 600 mm specimen panels, by an individual participant. The trial length was approximately 30 minutes, of which 10 minutes were set aside for briefing and the remaining 20 minutes were for performing the inspection. Seven sets of trials were performed:

1. Visual Inspection Trials with grey virtual specimens – 15 participants
2. Visual Inspection Trials with gloss grey specimens – 15 participants
3. Visual Inspection Trials with gloss white specimens – 16 participants
4. Visual Inspection Trials with gloss blue specimens – 16 participants
5. Visual Inspection Trials with matt grey specimens – 17 participants

6. Visual Inspection Trials with matt white specimens – 18 participants
7. Visual Inspection Trials with matt blue specimens – 20 participants

Each trial was successfully implemented, and all participants successfully completed their trials. In each trial, the participants marked their answers as detailed in chapter 4.14. After completion of trials with each colour / finish, the answer sheets were checked against a marking sheet in order to identify correct detections, missed flaws and false calls, as described in chapter 4.15. The results of each trial are presented forthwith.

#### ***5.5.1 – Results data for series 2 visual inspection trials***

The results of each of the visual inspection trials were originally recorded as a set of simple hit/ miss data as seen in appendix G. The detection % for each surface flaw was calculated by dividing the total number of successful detections for each flaw by the total number of participants that inspected each flaw. Using this value instead of the total number of hits for each flaw allowed the results of trials with different numbers of participants to be compared. A table of the detection percentage for each of the flaws in each specimen set is given in table 5.07.

Flaw Type	Flaw Number	Flaw Size		% Detections						
		Width (mm)	Depth (mm)	Projector	Gloss Grey	Matt Grey	Gloss White	Matt White	Gloss Blue	Matt Blue
Ø20 mm/17ply	1	9.03	0.09	0%	33%	41%	6%	0%	44%	5%
	2	10.49	0.11	7%	7%	35%	19%	22%	44%	10%
	3	12.18	0.14	0%	87%	71%	75%	39%	75%	10%
	4	14.15	0.19	20%	93%	94%	100%	94%	69%	45%
	5	16.44	0.26	80%	27%	35%	75%	94%	69%	50%
	6	19.11	0.37	100%	100%	94%	100%	100%	69%	95%
	7	22.2	0.57	100%	93%	94%	81%	89%	81%	50%
	8	25.79	0.94	100%	100%	100%	100%	100%	100%	100%
Ø20 mm/33ply	9	7.39	0.1	7%	13%	12%	6%	6%	25%	0%
	10	9.03	0.11	0%	27%	29%	19%	39%	6%	5%
	11	11.02	0.13	0%	80%	100%	75%	56%	31%	5%
	12	13.46	0.16	0%	20%	18%	13%	0%	50%	0%
	13	16.44	0.2	40%	20%	47%	50%	33%	63%	10%
	14	20.09	0.26	60%	93%	100%	100%	94%	69%	60%
	15	24.53	0.37	100%	93%	94%	88%	100%	56%	95%
	16	29.96	0.57	100%	100%	100%	100%	100%	81%	85%
Ø87 mm/17ply	17	11.02	0.1	0%	33%	24%	13%	39%	38%	5%
	18	13.46	0.12	0%	33%	29%	38%	44%	6%	5%
	19	16.44	0.13	13%	13%	24%	13%	6%	56%	10%
	20	20.09	0.16	7%	67%	71%	81%	67%	75%	30%
	21	24.53	0.19	33%	100%	88%	81%	61%	38%	50%
	22	29.96	0.25	73%	93%	88%	75%	33%	81%	40%
	23	36.6	0.33	47%	93%	100%	100%	89%	56%	75%
	24	44.7	0.49	67%	100%	88%	94%	78%	69%	85%
Ø87 mm/33ply	25	14.15	0.16	20%	87%	53%	81%	56%	19%	45%
	26	16.44	0.17	27%	53%	65%	56%	50%	19%	25%
	27	19.11	0.18	7%	80%	41%	50%	17%	38%	25%
	28	22.2	0.19	27%	60%	47%	50%	83%	56%	15%
	29	25.79	0.2	47%	73%	53%	38%	22%	75%	15%
	30	29.96	0.21	27%	40%	35%	19%	17%	50%	10%
	31	34.81	0.23	20%	27%	59%	13%	0%	50%	0%
	32	40.45	0.25	7%	67%	59%	6%	22%	44%	0%

Table 5.07 - % of detection for each flaw on each colour & surface finish

Whilst it is possible to plot simple graphs of percentage of detections vs. flaw width, or flaw depth, such graphs are unable to illustrate flaw depth at the same time. Similarly, simple graphs of detections vs. flaw depth are unable to convey the fact that two flaws of the depths may have different widths. As flaw visibility is believed to be dependent on both width and depth, it is of little use to attempt to base conclusions on graphs that only list one of the variables.

To allow display of both the width and depth of a surface flaw at the same time as the percentage of detections, 2D plots of detection percentage vs. flaw width & flaw depth were produced. Figures 5.36 to 5.42 illustrate matrices of detection percentages for surface flaws on the grey virtual specimens, and the gloss & matt grey, white and blue facsimile specimens. The flaw depth range was split into 18 equal intervals of 0.05 mm depth and the flaw width range was split into 8 equal intervals of 5 mm width. Each flaw in the specimen set was assigned to the appropriate size interval, and the detection percentages of all the flaws within each interval range were averaged, thus providing a single percentage detection value for all of the flaws within a given depth / width interval.

Average % Detections from Grey Virtual Specimens								
Depth Range	Width Range:							
	5.1 - 10.0mm	10.1 - 15mm	15.1 - 20mm	20.1 - 25mm	25.1 - 30mm	30.1 - 35mm	35.1 - 40mm	40.1 - 45mm
0.05 - 0.099		0%						
0.1 - 0.149	7%	1%	13%					
0.15 - 0.199		13%	13%	30%				
0.20 - 0.249			40%		37%	20%		
0.25 - 0.299			70%		73%			7%
0.30 - 0.349							47%	
0.35 - 0.399			100%	100%				
0.40 - 0.449								
0.45 - 0.499								67%
0.50 - 0.549								
0.55 - 0.599				100%	100%			
0.60 - 0.649								
0.65 - 0.699								
0.70 - 0.749								
0.75 - 0.799								
0.80 - 0.849								
0.85 - 0.899								
0.90 - 0.949					100%			

Figure 5.36 – Matrix of detection percentages arranged by flaw width and flaw depth, obtained using virtual grey specimens

Average % Detections from Gloss Grey Specimens								
Depth Range	Width Range:							
	5.1 - 10.0mm	10.1 - 15mm	15.1 - 20mm	20.1 - 25mm	25.1 - 30mm	30.1 - 35mm	35.1 - 40mm	40.1 - 45mm
0.05 - 0.099		33%						
0.1 - 0.149	13%	45%	13%					
0.15 - 0.199		67%	67%	80%				
0.20 - 0.249			20%		57%	27%		
0.25 - 0.299			60%		93%			67%
0.30 - 0.349							93%	
0.35 - 0.399			100%	100%				
0.40 - 0.449								
0.45 - 0.499								100%
0.50 - 0.549								
0.55 - 0.599				93%	100%			
0.60 - 0.649								
0.65 - 0.699								
0.70 - 0.749								
0.75 - 0.799								
0.80 - 0.849								
0.85 - 0.899								
0.90 - 0.949					100%			

Figure 5.37 – Matrix of detection percentages arranged by flaw width and flaw depth, obtained using gloss grey specimens

Average % Detections from Matt Grey Specimens								
Depth Range	Width Range:							
	5.1 - 10.0mm	10.1 - 15mm	15.1 - 20mm	20.1 - 25mm	25.1 - 30mm	30.1 - 35mm	35.1 - 40mm	40.1 - 45mm
0.05 - 0.099		41%						
0.1 - 0.149	12%	48%	24%					
0.15 - 0.199		55%	59%	68%				
0.20 - 0.249			47%		44%	59%		
0.25 - 0.299			68%		88%			59%
0.30 - 0.349							100%	
0.35 - 0.399			94%	94%				
0.40 - 0.449								
0.45 - 0.499								88%
0.50 - 0.549								
0.55 - 0.599				94%	100%			
0.60 - 0.649								
0.65 - 0.699								
0.70 - 0.749								
0.75 - 0.799								
0.80 - 0.849								
0.85 - 0.899								
0.90 - 0.949					100%			

Figure 5.38 – Matrix of detection percentages arranged by flaw width and flaw depth, obtained using matt grey specimens

Average % Detections from Gloss White Specimens								
Depth Range	Width Range:							
	5.1 - 10.0mm	10.1 - 15mm	15.1 - 20mm	20.1 - 25mm	25.1 - 30mm	30.1 - 35mm	35.1 - 40mm	40.1 - 45mm
0.05 - 0.099		6%						
0.1 - 0.149	6%	40%	13%					
0.15 - 0.199		65%	62%	66%				
0.20 - 0.249			50%		29%	13%		
0.25 - 0.299			88%		75%			6%
0.30 - 0.349							100%	
0.35 - 0.399			100%	88%				
0.40 - 0.449								
0.45 - 0.499								94%
0.50 - 0.549								
0.55 - 0.599				81%	100%			
0.60 - 0.649								
0.65 - 0.699								
0.70 - 0.749								
0.75 - 0.799								
0.80 - 0.849								
0.85 - 0.899								
0.90 - 0.949					100%			

Figure 5.39 – Matrix of detection percentages arranged by flaw width and flaw depth, obtained using gloss white specimens

Average % Detections from Matt White Specimens								
Depth Range	Width Range:							
	5.1 - 10.0mm	10.1 - 15mm	15.1 - 20mm	20.1 - 25mm	25.1 - 30mm	30.1 - 35mm	35.1 - 40mm	40.1 - 45mm
0.05 - 0.099		0%						
0.1 - 0.149	6%	40%	6%					
0.15 - 0.199		50%	45%	72%				
0.20 - 0.249			33%		20%	0%		
0.25 - 0.299			94%		33%			22%
0.30 - 0.349							89%	
0.35 - 0.399			100%	100%				
0.40 - 0.449								
0.45 - 0.499								78%
0.50 - 0.549								
0.55 - 0.599				89%	100%			
0.60 - 0.649								
0.65 - 0.699								
0.70 - 0.749								
0.75 - 0.799								
0.80 - 0.849								
0.85 - 0.899								
0.90 - 0.949					100%			

Figure 5.40 – Matrix of detection percentages arranged by flaw width and flaw depth, obtained using matt white specimens



Average % Detections from Gloss Blue Specimens								
Depth Range	Width Range:							
	5.1 - 10.0mm	10.1 - 15mm	15.1 - 20mm	20.1 - 25mm	25.1 - 30mm	30.1 - 35mm	35.1 - 40mm	40.1 - 45mm
0.05 - 0.099		44%						
0.1 - 0.149	25%	33%	56%					
0.15 - 0.199		46%	44%	47%				
0.20 - 0.249			63%		63%	50%		
0.25 - 0.299			69%		81%			44%
0.30 - 0.349							56%	
0.35 - 0.399			69%	56%				
0.40 - 0.449								
0.45 - 0.499								69%
0.50 - 0.549								
0.55 - 0.599				81%	81%			
0.60 - 0.649								
0.65 - 0.699								
0.70 - 0.749								
0.75 - 0.799								
0.80 - 0.849								
0.85 - 0.899								
0.90 - 0.949					100%			

Figure 5.41 – Matrix of detection percentages arranged by flaw width and flaw depth, obtained using gloss blue specimens

Average % Detections from Matt Blue Specimens								
Depth Range	Width Range:							
	5.1 - 10.0mm	10.1 - 15mm	15.1 - 20mm	20.1 - 25mm	25.1 - 30mm	30.1 - 35mm	35.1 - 40mm	40.1 - 45mm
0.05 - 0.099		5%						
0.1 - 0.149	0%	7%	10%					
0.15 - 0.199		30%	27%	33%				
0.20 - 0.249			10%		13%	0%		
0.25 - 0.299			55%		40%			0%
0.30 - 0.349							75%	
0.35 - 0.399			95%	95%				
0.40 - 0.449								
0.45 - 0.499								85%
0.50 - 0.549								
0.55 - 0.599				50%	85%			
0.60 - 0.649								
0.65 - 0.699								
0.70 - 0.749								
0.75 - 0.799								
0.80 - 0.849								
0.85 - 0.899								
0.90 - 0.949					100%			

Figure 5.42 – Matrix of detection percentages arranged by flaw width and flaw depth, obtained using matt blue specimens

The detection matrices are useful for comparing the detection rates of a particular size range. For example, it can be seen that for flaws within the 0.1 to 0.149 mm depth and 5.1 to 10 mm width range, the detection rate never exceeds 25% (Gloss Blue). Likewise, it is also possible to identify that the flaw size range 0.9 to 0.949 mm deep and 25.1 to 30 mm gives 100% detection on the virtual specimens and all variations of the facsimile specimens. However, the effects of width, depth, colour and surface finish on detection rates are difficult to discern using matrices.

A second method of presenting the results was to use Statistica statistical data analysis software [Statsoft Inc. 2008] to produce scatter graphs, with the percentage of participants detecting each flaw plotted against the corresponding flaw depth and flaw width of each flaw (see figures 5.43-5.49, and appendix H). A natural log scale is used for the X and Y-axis, allowing greater separation of the individual data points at

lower values of width and depth. The scatter plots allowed the detection percentage for each flaw to be seen, and compared, in terms of depth and width, against the other flaws in the specimen set. For example, in figure 5.44 it can be seen that on the gloss grey specimens, there is no clear correlation between flaw width and detection %. However, all the flaws over 0.3 mm deep were detected by more than 90% of participants. On gloss grey specimens, there were instances of greater than 90% detection when flaws were below 0.3 mm. On gloss blue specimens, however, there were no instances of greater than 90% detection when flaw depth was below 0.3 mm.

The scatter plots were also useful for comparing the detectability of individual flaws across the range of surface colours and finishes. For example, it can be seen that the detection of the 44.7 mm/ 0.49 mm deep flaw varied between 69% on gloss blue specimens and 100% on gloss grey specimens.

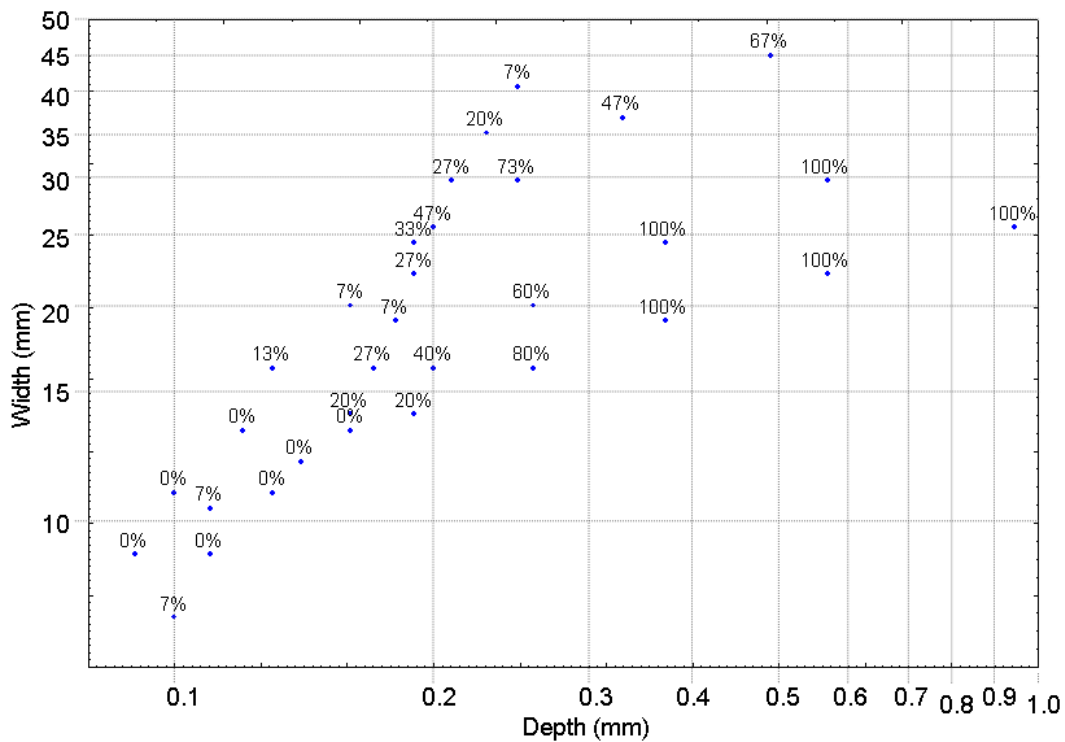


Figure 5.43 – Scatter plot of % of participants detecting each flaw vs. flaw depth & width for virtual grey specimens

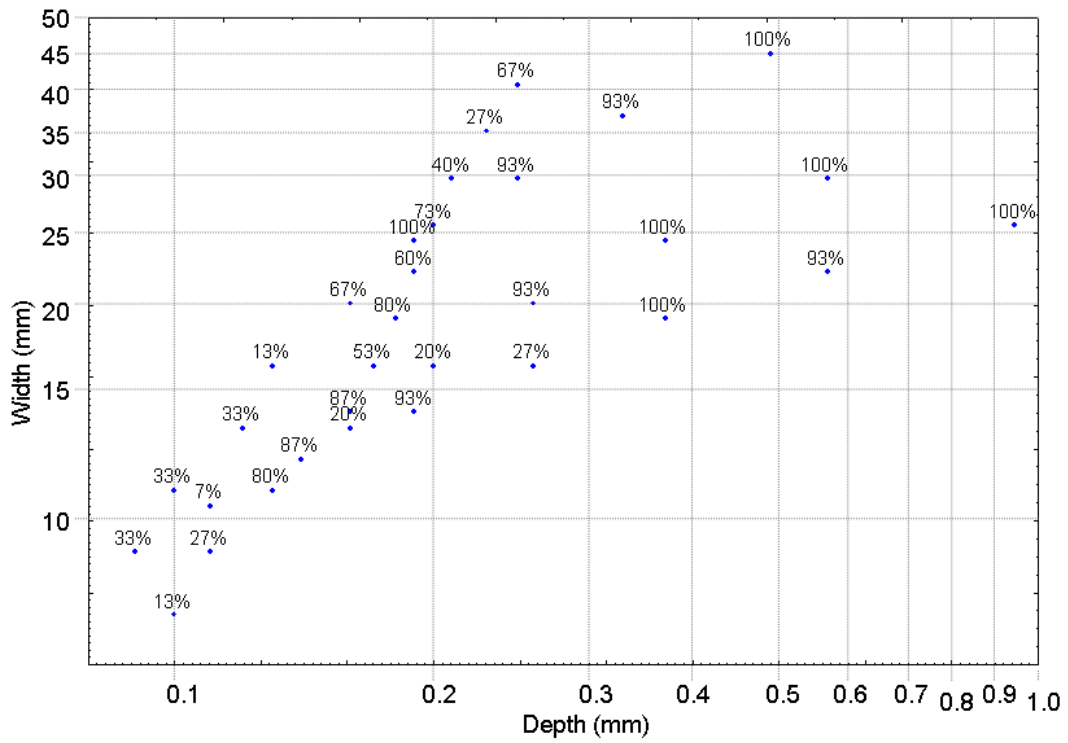


Figure 5.44 – Scatter plot of % of participants detecting each flaw vs. flaw depth & width for gloss grey specimens

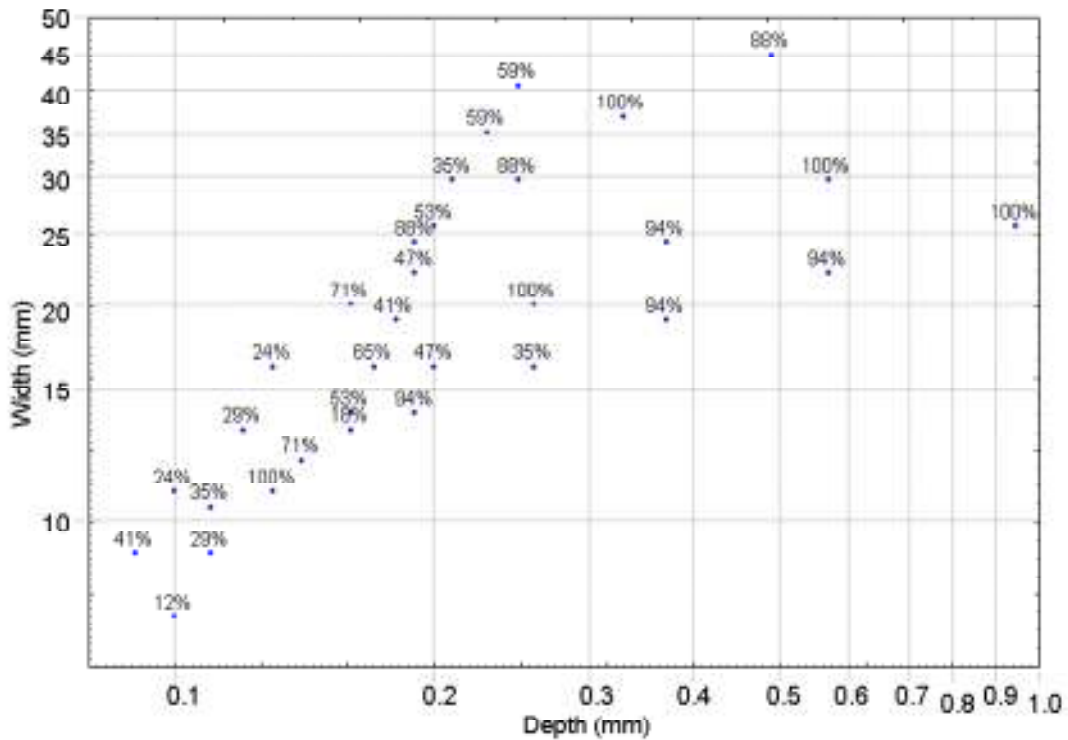


Figure 5.45 – Scatter plot of % of participants detecting each flaw vs. flaw depth & width for matt grey specimens

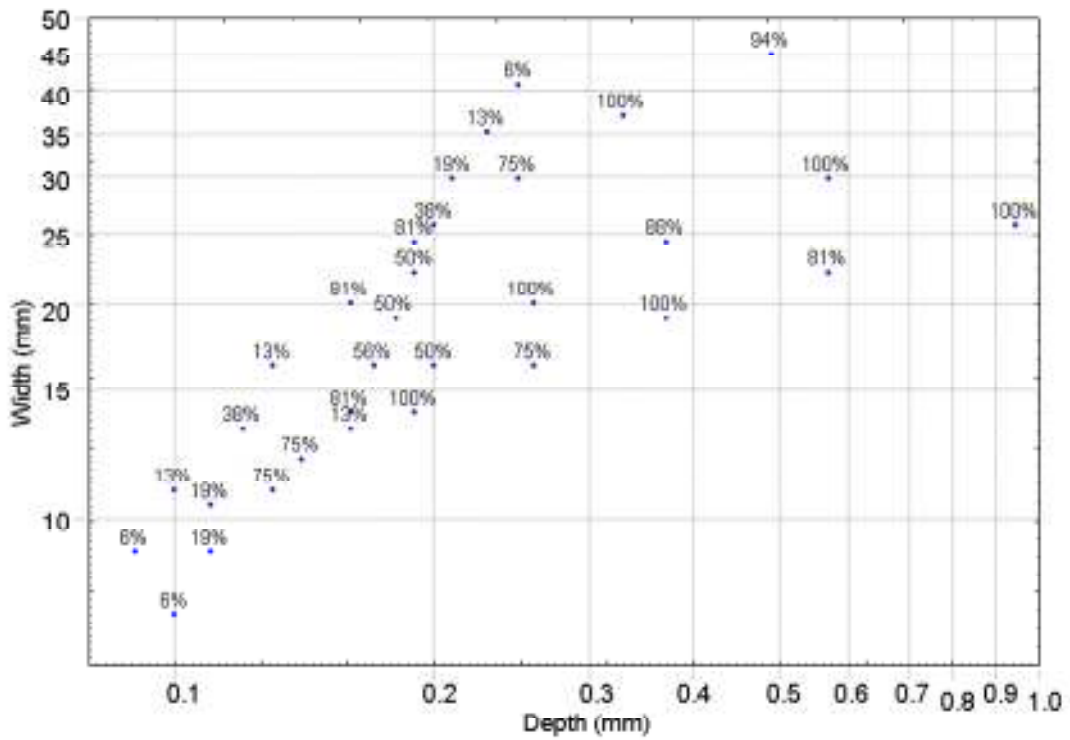


Figure 5.46 – Scatter plot of % of participants detecting each flaw vs. flaw depth & width for gloss white specimens

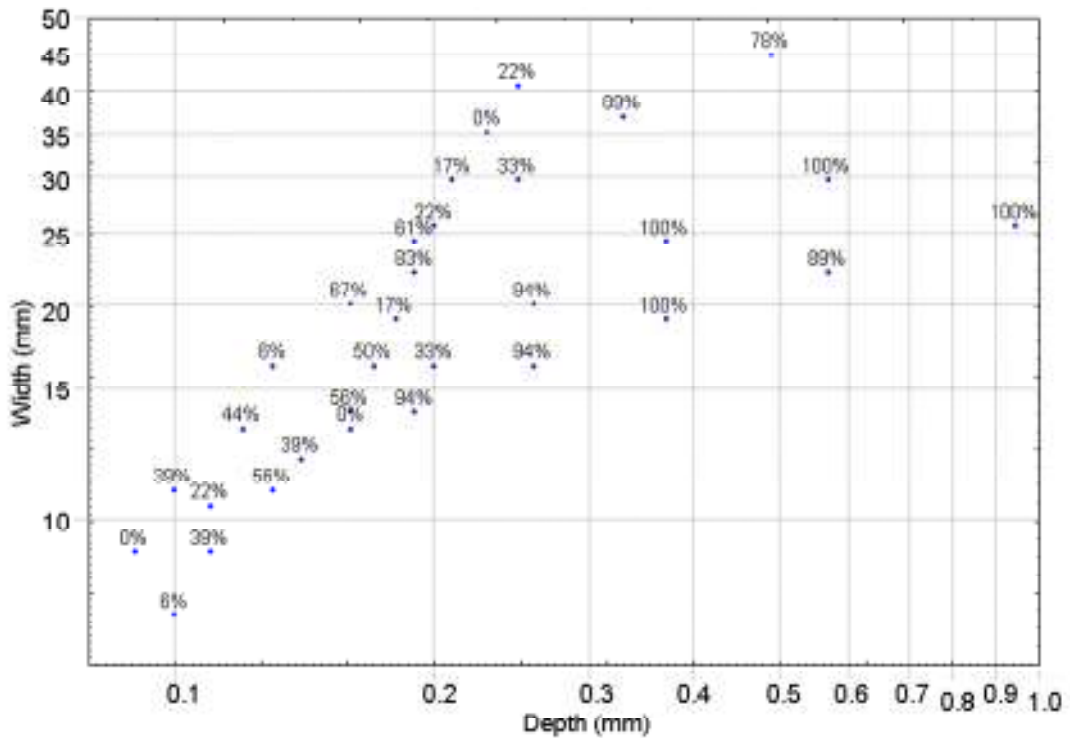


Figure 5.47 – Scatter plot of % of participants detecting each flaw vs. flaw depth & width for matt white specimens

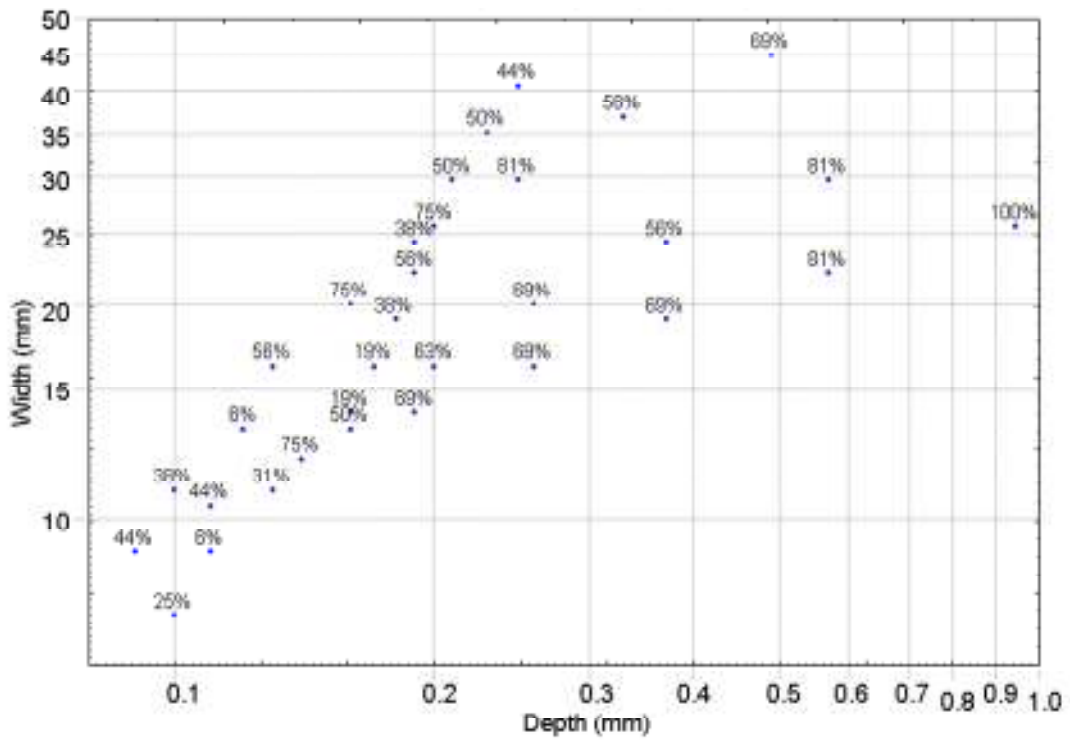


Figure 5.48 – Scatter plot of % of participants detecting each flaw vs. flaw depth & width for gloss blue specimens

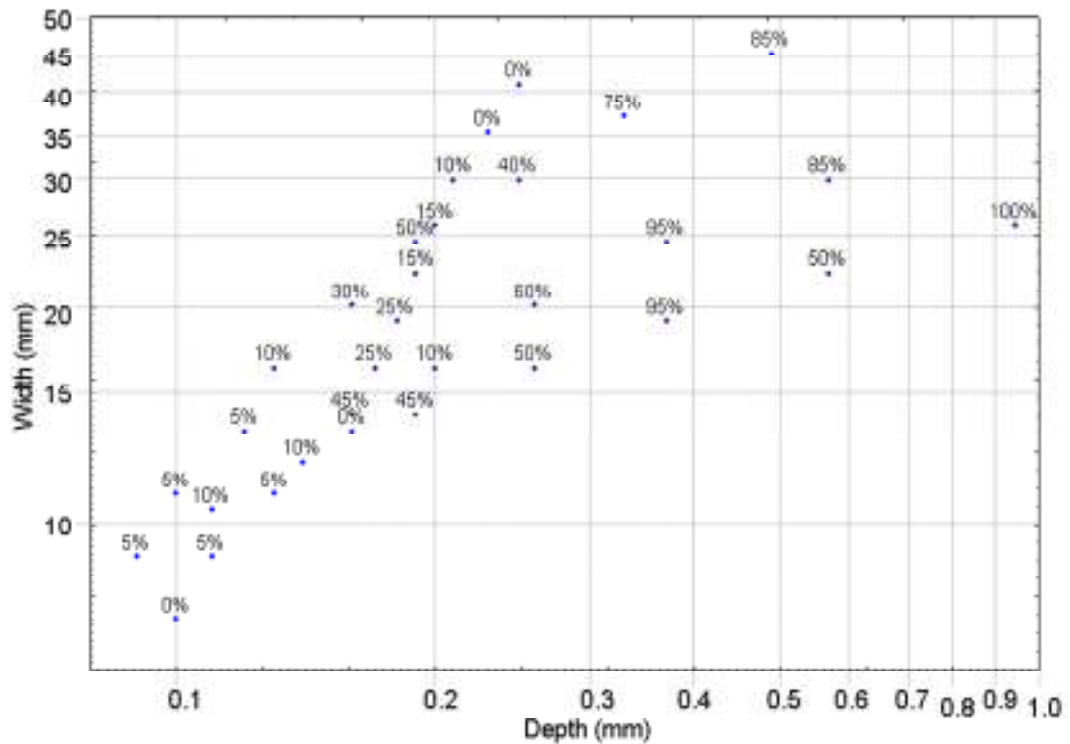


Figure 5.49 – Scatter plot of % of participants detecting each flaw vs. flaw depth & width for matt blue specimens

When viewing the scatter plots, it became apparent that the levels of detection percentage appeared to form bands, or contours, of constant detectability. In order to explore the possibility of detectability bands further, the wafer plot function of Statistica was used to fit the scatter plots with contours representing levels of detection percentage. The wafer plots are shown in figures 5.50 to 5.56, and in appendix H without annotations. The wafer plots also use a natural log scale on the X and Y-axis. The contours on the wafer plots are best-fit lines of constant detection percentage. The effects of flaw width and depth on detection rates, and the differences in detection rates obtained on different specimen colours and finishes were easily visualised on the wafer plots.

### ***5.5.2 – General Summary of results from series 2 trials***

All of the plots in figs 5.50 to 5.56 have a number of similar features, differing in detail with changes in sample colour and surface finish. At small values of depth and width percent detections are low and approach zero. The lower limit of the data is at flaws of 0.1 mm depth and 10 mm width. The upper limit of data is at flaws approaching 1 mm deep and 30-40 mm wide. Here detections approached 100%. The extent of the region of 90-100% detections varied depending on the colour and surface finish of the samples. The region of high (90 to 100%) detection percentages generally extended in a ridge from a centralised region at the highest values of depth towards smaller values of width and depth. The shape of the high detection percentage region meant that at constant flaw depth the effect of increasing width was first to increase the detection percent, and then with further increases in width to decrease the detection probability. All the data sets from the physical facsimile specimens show some local contour anomalies, which probably reflect variability within the hit/miss data. However, the contours of the results obtained using virtual specimens exhibit far better defined contour lines and clear variations in detectability with variations in width for flaws of the same depths.

### ***5.5.3 – Detailed summaries of results from series 2 trials***

The wafer plot produced from the results of the trials with virtual specimens (figure 5.50) is similar in overall shape to the plots obtained from trials with physical facsimile specimens. However, the region of 90~100% detection is limited to flaws <Ø35 mm and >0.3 mm deep. Flaws below 0.2 mm deep failed to achieve >60%

detection and detection of flaws  $>\text{Ø}35$  mm varied, with detection increasing with depth from a minimum of 10% to a maximum of 90%.

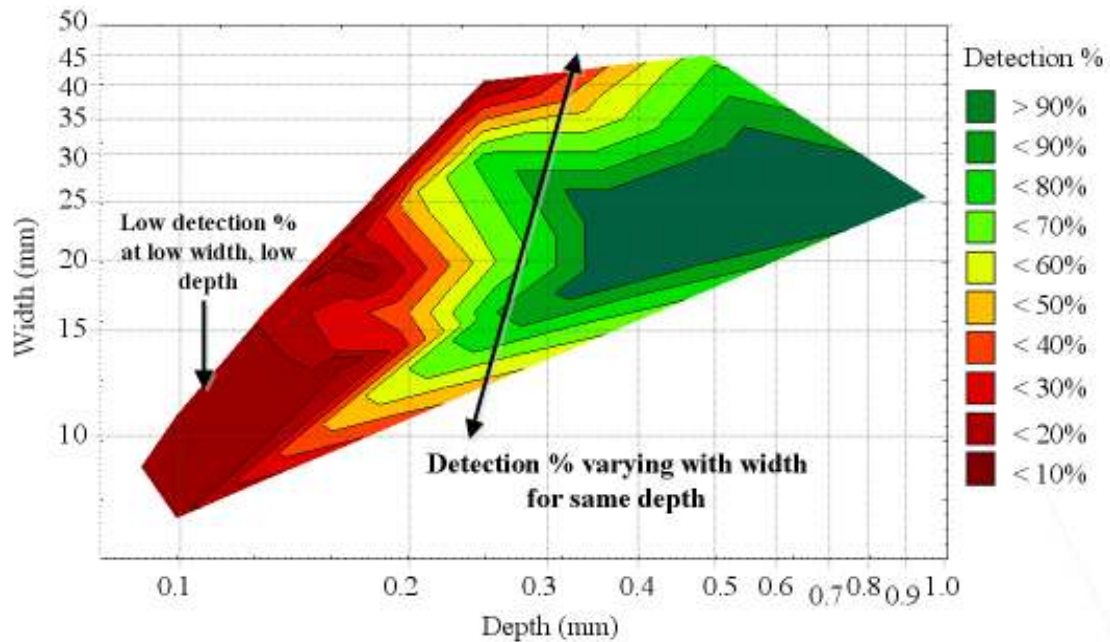


Figure 5.50 – Wafer plot of virtual grey specimen results with comments

In figure 5.51, the wafer plot of gloss grey results shows a large flaw depth and width region in which flaws were detected by over 90% of participants. The contours indicate that for flaws of small depth and width, the detection was at its lowest rate. If a nominal flaw depth of 0.2 mm is chosen, the wafer plot illustrates that flaw detection rates can vary between <10% and >90% as width varies; i.e. detection can vary for the same depth of flaw, depending on the flaw width.

Figure 5.52 illustrates the wafer plot of the matt grey results. It can be seen that the matt finish has little effect on detectability of flaws greater than 0.25 mm deep; the region of 90-100% detection is similar in size and shape to the same region on the gloss grey diagram. There is a slight change to the contour shape for flaws of smaller width and depth, where the <10% detection band is no longer present. As also observed for the gloss grey specimens, the detection contours vary with width for constant depths. The overall implication is that there is little difference in detection rates on gloss and matt grey specimens.

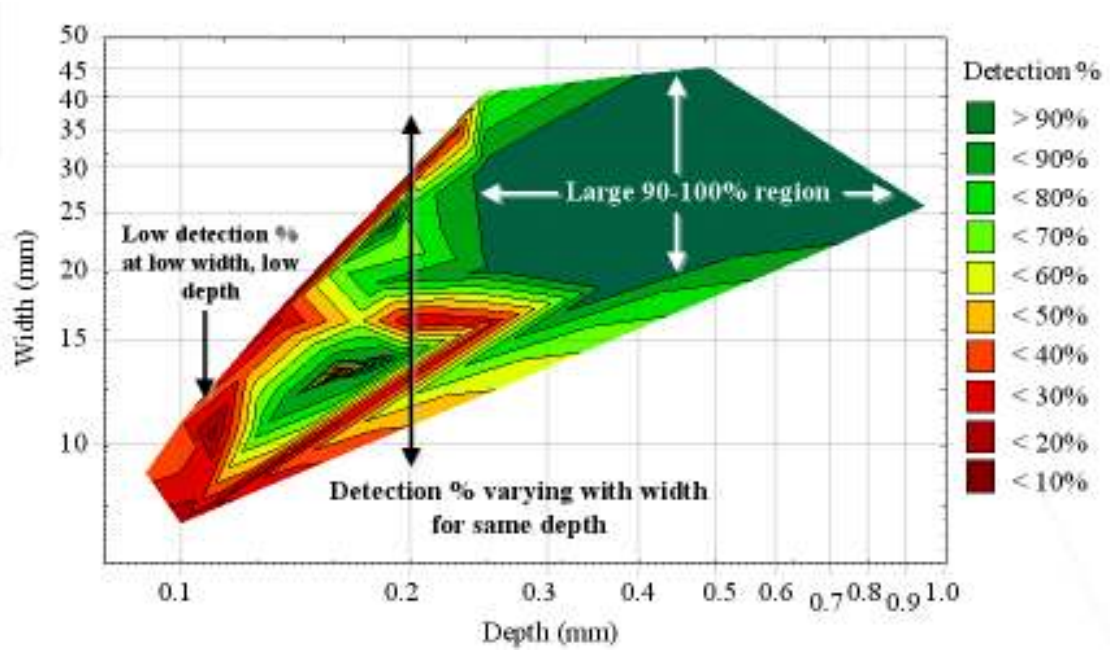


Figure 5.51 – Wafer plot of gloss grey specimen results with comments

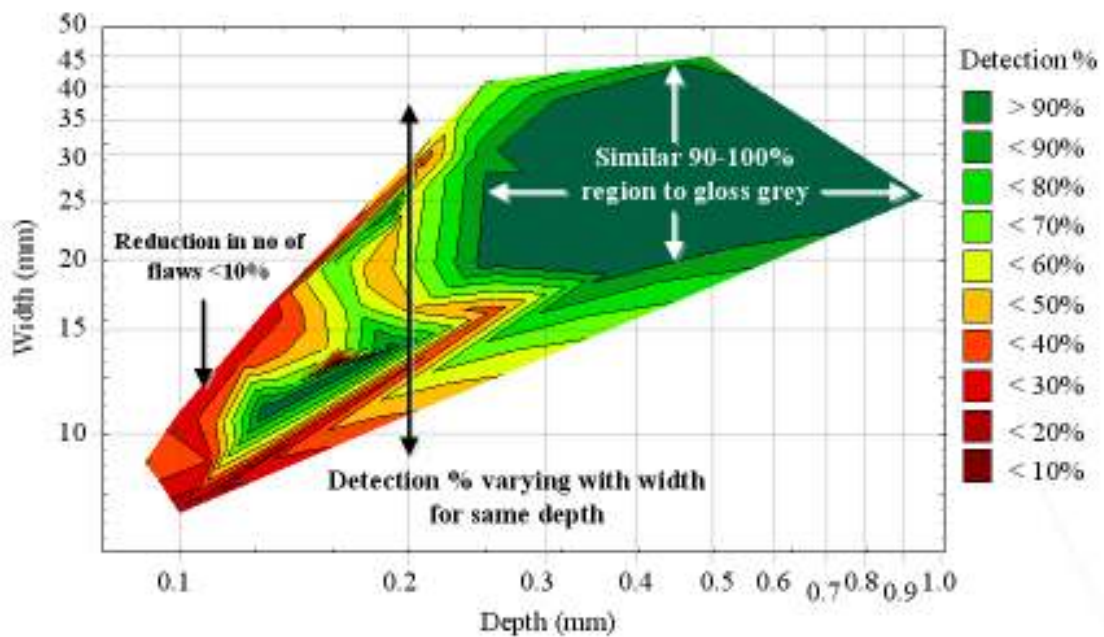


Figure 5.52 – Wafer plot of matt grey specimen results with comments

In figure 5.53, the wafer plot of the gloss white specimens illustrates that there are some differences compared to the results with grey specimens. The large area of 90-100% detection has changed shape slightly. For flaws between 0.2 mm - 0.3 mm deep, and >25 mm wide, the detection percentage reduces as width increases. However, for flaws below 0.2 mm deep, there is little difference to the detection



contours compared to the gloss and matt grey results. This implies that are slight differences in detection rates on gloss white specimens compared to gloss and matt grey specimens.

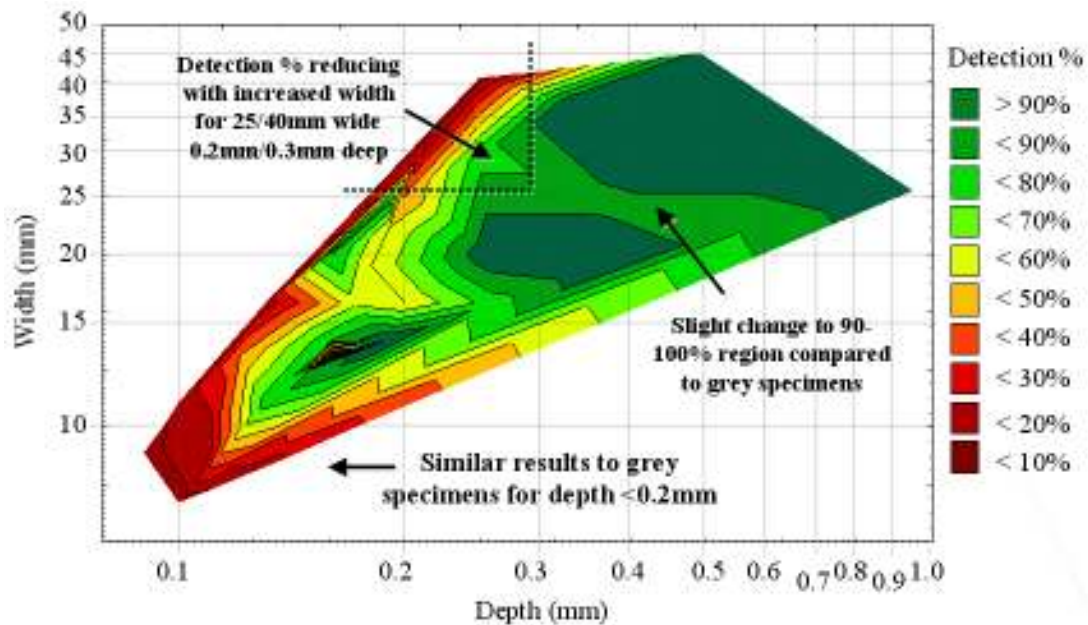


Figure 5.53 – Wafer plot of gloss white specimen results with comments

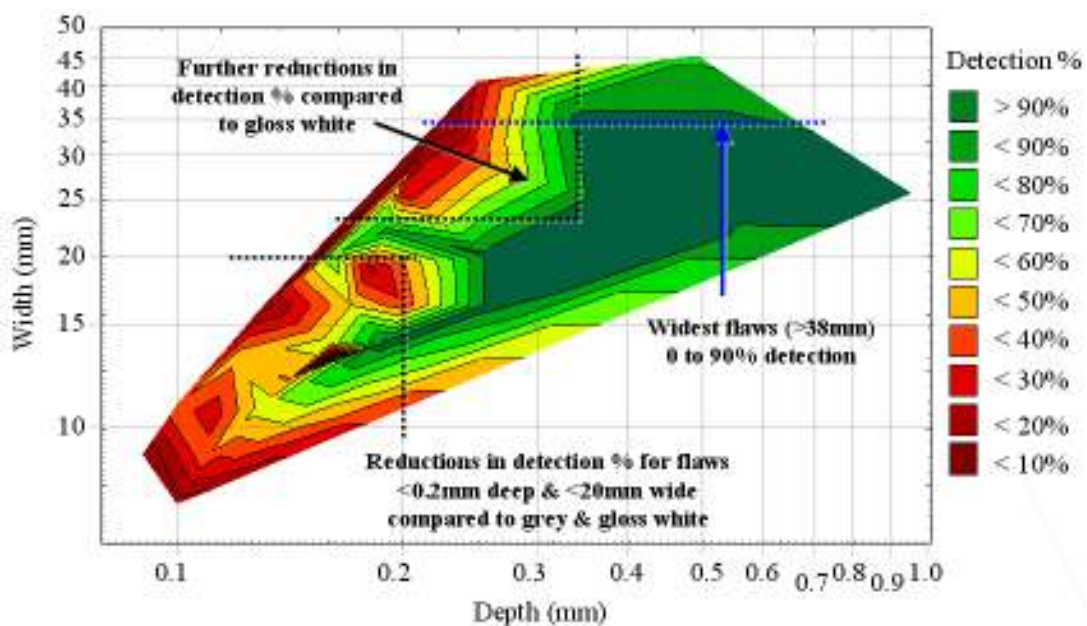


Figure 5.54 – Wafer plot of matt white specimen results with comments

In figure 5.54, which shows the results from matt white specimens, there are notable differences to the contour shapes on the gloss white results. The large area of >90% detection has changed shape, and no longer includes flaws wider than 38 mm. The detection of flaws >38 mm wide now varies from <10% to >90% depending on flaw

depth. For the flaws between 0.2 mm & 0.3 mm deep and >25 mm wide, there is greater variation in detection rates compared to the same region on the gloss white results. Detection of flaws <0.2 mm deep and <20 mm wide saw reduced rates on the matt white specimens compared to the gloss grey and white, and matt grey specimens. The results seen in figure 5.54 imply that the matt finish altered detection rates on the white specimens.

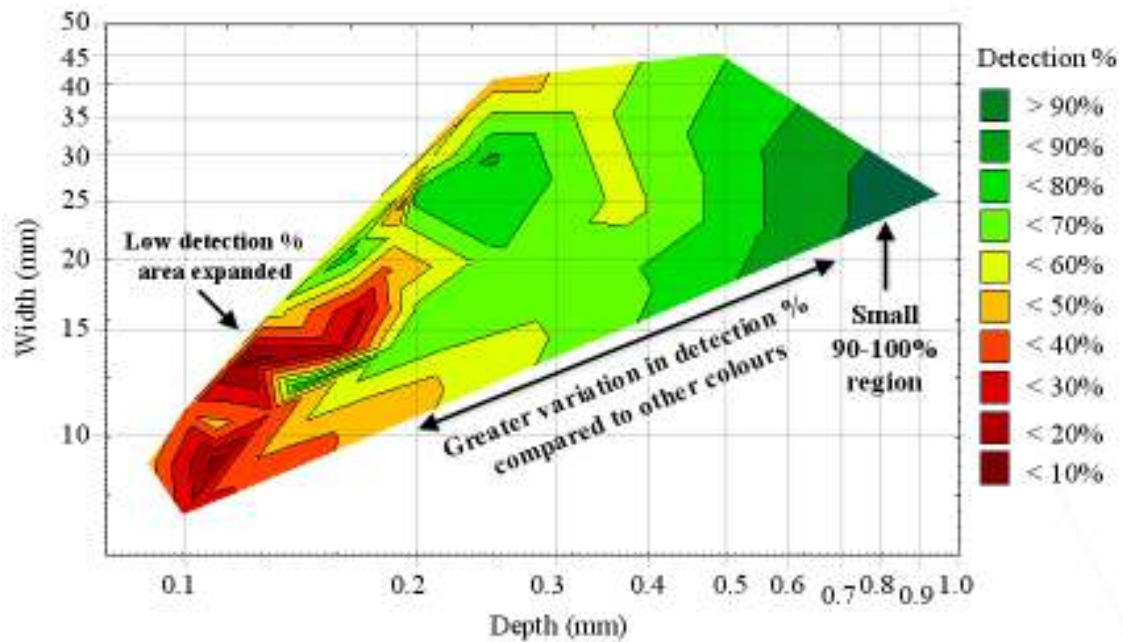


Figure 5.55 – Wafer plot of gloss blue results with comments

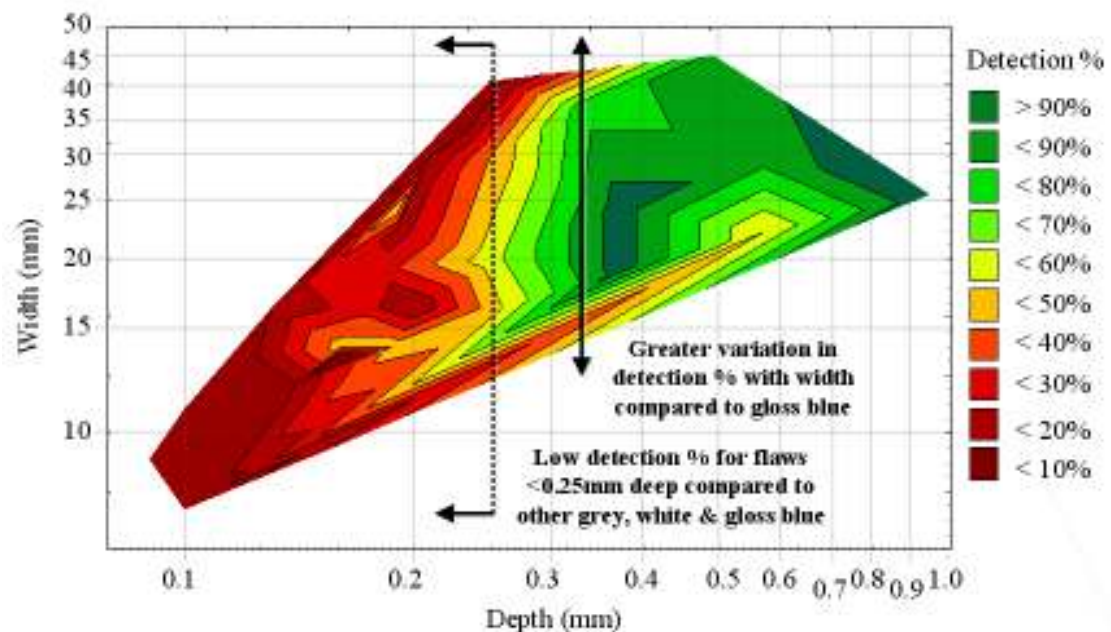


Figure 5.56 – Wafer plot of matt blue results with comments

Figure 5.55 shows the results obtained from the gloss blue specimens. In this plot, it can be seen that there is a significantly different shape to the detection contours compared to the results from grey and white specimens. The lower limit of the region of >90% detection has shifted to 0.7 mm deep compared to extending down to 0.25 mm deep for the results from the grey and white specimens. The detection contours for flaws >0.2 mm vary with flaw width from 60% to 80% detection compared to variations from <10% to >90% detection on the other plots (fig 5.51 – 5.54 & 5.56), i.e. flaw detections for the same flaw depth vary less with width on the gloss blues specimens. For the gloss blue specimens, in particular for flaws >0.2 mm deep, the detection contours vary less (0 to 30% variation vs. >50% variation) with width for flaws of the same depths than for the same region on grey & white specimens.

Figure 5.56 illustrates the results from the matt blue specimens. It can be seen in figure 5.56 that detection percentages for flaws 0.2 mm to 0.5 mm deep vary from <30% to >90% with width, compared to <50% to <80% on gloss blue specimens. It can also be seen that detection of flaws with <0.3 mm depth is reduced to below 50% for matt blue specimens. The results seen in figure 5.56 imply that a matt blue finish gives different detection results to a gloss blue finish.

## ***Chapter 6 – Discussion***

The visual inspection trials were performed in order to investigate the detection of 3D surface flaws that represent impact damage to a painted, mesh incorporated CFRP laminate. As detailed in chapter 5.1, falling weight impact damage to painted, mesh incorporated CFRP laminates produced a different surface topography, and different visual appearance to the same impact conditions on an unpainted, non-mesh laminate of the same thickness. Many of the examples of impact damage from hemispherical shaped objects to painted laminates, as presented in chapter 5.1, exhibited a 3D surface indentation, which was free of surface breaking cracks. However, the lack of published examples of impact damage to fully finished, painted monolithic CFRP laminates inhibits comparisons with other works.

The lack of published examples of impact damage to painted laminates also means that the obtained flaw geometry, or topography data cannot be compared to published works. However, the data obtained for flaw depth vs. impact energy plots, as seen in chapter 5.16, were best fitted by an exponential model or line, which is in keeping with results obtained on unfinished laminates [Brookes 2004]. The fit quality of the geometry variable relationships is discussed later in this chapter.

In previous published studies on reliability of visual inspection of composite materials, surface colour and surface finish were identified, but not demonstrated, as factors having the potential to affect visual inspection reliability [Erhart et al., 2004; Gant, 2007]. To date, no published study demonstrates the effects of both surface colour and surface finish on visual inspection reliability for impact damage to composite materials. The results presented in this thesis successfully demonstrate the effects of both surface colour and surface finish. Furthermore, the results demonstrate that colour and finish had interactive effects on visual inspection reliability.

A particularly noteworthy issue arising from the visual inspection trials results is the low detectability (<70%) of flaws representing impact damage from larger diameter objects (87 mm), at relatively high (60J) energy impacts on 33ply painted CFRP laminate. Traditionally, a 10, 15 or 20 mm impactor is used for impact testing and CAI studies on composite materials, and flaws representing lower energy (50J) impact

damage from a 20mm tip returned greater than 80% detection rates. The lack of published impact testing work using larger diameter (>25 mm) tips has resulted in few examples of larger size, higher energy impact damage to CFRP laminates. However, the impact damage examples presented in this thesis demonstrate significant differences between the flaw depth/impact energy and flaw width/ impact energy relationships for smaller and larger size hemispherical impactors. Furthermore, the visual inspection trials results lead to the previously unpublished suggestion that impact damage at relatively high impact energy from larger sized objects may be less detectable by visual inspection.

The “bigger is better” assumption for NDT reliability is inherent and deep rooted in the 20+ years of research into NDT system reliability assessment. However, the visual inspection reliability data presented in chapter 5.5 pose a significant challenge to the traditional reliability assessment assumption of increasing probability of detection (POD) with increasing flaw size. Within the results obtained from visual inspection trials with facsimile specimens, it is evident that flaw width and visual inspection reliability are not positively correlated for impact damage to painted CFRP laminates. In fact, as seen in figures 5.51 to 5.56, for flaw depths < 0.25 mm there is strong evidence that detection rates will be reduced for wider flaws (>30 mm). Whilst the results presented in chapter 5.5 demonstrate greater detection rates at greater depths, it is unfeasible to assume that all *types* of damage above a given depth threshold will have greater detectability. Whilst the results may support this assumption for a particular *type* of impact damage, i.e. a 20 mm hemispherical object, the results demonstrate that when the detectability of different *types* of impact damage are considered altogether, an increase in flaw depth does not necessarily correspond to an increase in detectability.

Published experimental paradigms and protocols are written solely with NDT of metallic structures, and inspection for cracks, in mind. In implementing a reliability assessment of visual inspection for three-dimensional impact damage to composite materials, it has become apparent that the established “metallic” experimental paradigms and protocols require a certain degree of interpretation in order to be applied to the experimental design. Hence, a rather poignant question; has the same

interpretation, if any, been made by each aircraft manufacturer when determining BVID sizes for composite structures?

Either because of inability to translate elements, or ignorance of existing paradigms & recommendations the specimens used in published work on visual inspection of composite aircraft structures [Erhart et al.; 2004, Gant 2007] fail to demonstrate constancy between experimental variables such as flaw geometries and sizes, lighting conditions, inspection environment and specimen set-up. The combination of these issues with variations in laminate type and surface finish treatments leads to an inability to make meaningful direct comparisons between detection results obtained by others and those presented in this thesis.

## ***6.1 – Experimental issues; impact damage***

### ***6.1.1 – Flaw width measurements on impact damaged CFRP coupons***

The examples of impact damage to coupons of painted, mesh incorporated CFRP laminate were produced according to manufacturer's specifications, and standard falling weight impact procedures were employed. However, there are currently no published standard procedures for characterising the subsequent surface flaw topographies. Various methods for characterising impact damage morphology are presented in this thesis, and whilst delamination size and flaw depth measurements were made with relatively high accuracy, width measurements presented a particular challenge.

Flaws with low depth and highly blended shapes presented the greatest challenge to making the distinction between flawed and unflawed surface. Small undulations in surface angle due to the paint finish caused such significant 'noise' in surface angle measurements. Such noise rendered useless any attempts to use differences in surface angle as indicators of where flaws finished and returned to having the same surface angle as the unflawed surface. The method described in chapter 4.5.5 was thus developed as a constant, workable solution to the width measurement challenge. The three depth measurement points described in chapter 4.5.5 are spaced at 1 mm intervals, and it is acknowledged that an error of a single point either side of the three chosen points was possible in determining three points with consecutively lower depths. Hence, the accuracy of the flaw width measurements was within +/- 5 mm for

each side of the flaw, resulting in an overall width measurement accuracy of +/- 10 mm.

Others [Brookes 2004] have reported the use of digital images and subsequent image processing to make width measurements. However, this method appears to use changes in surface angle to distinguish between flawed and unflawed surface. NDT methods such as moiré reflectology (D-Sight) also rely on changes in surface profile to quantify impact damage size. Autoclave cured, unpainted CFRP laminates typically have smooth surfaces, free of paint finish effects such as pinholes or orange peel which cause noise in profile or angle measurements. Use of peel plies during laminate processing presents a further source of surface profile noise, which may increase the difficulty in using a surface angle change threshold to identify flaw endpoints when measuring flaw widths.

Bearing in mind the surface angle or surface profile noise associated with paint finishes or peel plies, future work may wish to investigate the accuracy of flaw-width measurement methods or procedures for impact damage on fully finished CFRP laminates.

## ***6.2 – Experimental issues – visual inspection trials***

### ***6.2.1 – Inspection time***

For the series two visual inspection trials, a minimum of 20 seconds were required for change over of each panel, and a maximum of 30 minutes trial duration was imposed in order to avoid the onset of fatigue in participants. This resulted in a maximum display time for each specimen of 5 seconds for each of the 64 specimen panels. Drury, 1993 demonstrated that a search time of 5 seconds on a complex visual inspection task was the minimum required in order to identify the correct target amongst 10 others, although actual eye fixations on targets (i.e. detections of flaws as opposed to comparison between flaws to identify a particular target) occur in milliseconds rather than seconds [Megaw & Richardson, 1979]. The visual participants in the trials presented in this thesis were asked to perform the simpler task of identifying only the presence of flaws, as opposed to searching for all the flaws and making a decision between which one should be marked down. The display duration of 5 seconds was therefore considered more than adequate time to search the

specimen surface and *detect* several flaws. The ability of some participants to identify all three flaws on facsimile specimen panels during visual inspection trials suggests that the display of 5 seconds was in fact adequate, and that non-detections were as a result of flaws being too ‘small’ to detect, as opposed to participants having insufficient time to search the entire specimen surface. However, without the employing eye tracking equipment to determine participant visual search patterns, this can only remain a suggestion and cannot be considered hard evidence.

### ***6.2.2 – Use of novice inspectors in visual inspection trials***

The 600 mm x 600 mm panels were intended to represent a small inspection zone on an aircraft structure, and the surface flaws represented impact damage to a CFRP aircraft structure. The participants were shown examples of the facsimile flaws prior to each trial, and the visual inspection task was simply to identify the presence of *any* similar flaws on a specimen panel. The participants were not required to make judgements regarding the severity of each flaw or whether repair, or further NDT was required, as would normally be the case during a real inspection of an actual aircraft. Furthermore, the panels did not represent a particular section of aircraft structure, thus eliminating any expectancy of finding a particular type of damage. Any aviation experience or experience of composite materials would have had no bearing on the inspection outcome; hence, the use of novice participants. Furthermore, the work of Gallwey & Drury, 1986 demonstrated that novice and trained inspectors returned comparable results for tasks where inspector experience and expectancy were redundant in the task. The participant’s responses in the visual inspection trials therefore represent the simplest possible indication of whether a human eye, be it that of a novice or trained inspector, could or could not detect the presence of each flaw.

### ***6.2.3 – Lighting***

The visual inspection trials setup used only ambient lighting without additional directional lighting or sources of light ‘edges’, which are aids to detection of 3D surface flaws (see Faulkener & Murphy, 1979 and Lloyd & He, 1998). Gant, 2007 investigated the use of additional directional lighting and/ or flashlights and found subsequent improvements in detection rates for visual inspection of impact damage to composite aircraft structures. However, lighting conditions, lighting design and lighting availability in aircraft hangars will vary from facility to facility, making them difficult to represent in a single trial. Inspection surfaces may also be poorly lit due to



being on the underside of an aircraft or outside the range of available light sources, leading to reduced detection rates (as demonstrated by Gant, 2007 and Erhart et al., 2004).

The results of the visual inspection trials presented in section chapter 5.5 represent inspection under ambient light, which can be considered the basic lighting requirement for visual inspection (see Brombach et al., 2006). The detection results therefore represent a ‘baseline’ level of visual inspection reliability. The work of Gant and Erhart et al. suggests that the detection rates for flaws will be reduced due to inspection on under wing surfaces, and the work of Gant, 2007 and Lloyd & He, 1998 suggests detection rates would increase with the use of flashlights & lamps, additional directional light sources and grid or strip luminaires.

#### ***6.2.4 – Design of facsimile specimen flaws***

The design of the facsimile specimen flaws was based on relationships between impact energy, flaw width and the other variables (see chapter 5.1.6) that were derived by fitting lines to scatter plots of the CMM characterisation data from actual impact damaged painted CFRP laminate coupons (described in chapter 5.1.6). As can be seen in the plots, particularly in figures 5.23 & 5.25, the quality of fit varied depending on the impactor / laminate combination. However, the key objective for the characterisation work was to arrive at a method by which the sectional profile of impact damage from different impactor/ laminate combinations could be constructed for any given impact energy or flaw width. In order to avoid using several different model types (i.e. linear, logarithmic, exponential) for each geometry variable across the four combinations of impactor size and laminate thickness, the variance in fit quality was accepted, and only a single model type was adopted for each relationship. Improvements in fit quality could be obtained by producing further examples of falling weight impact damage in order to populate the same impact energy range at reduced impact energy intervals, with repeat examples at the same impact energy. Due to the inherent variability in flaw size and geometry of falling weight impact damage, and the approximate nature of the flaw geometry variable relationships, it was accepted that slight variations might occur between flaw geometries of actual flaws produced by others on similar CFRP test coupons and the facsimile flaws used

in the visual inspection trials. Such variations should not detract from the overall visual inspection reliability issues that arise from the visual inspection trials results.

The sizes and geometries of the facsimile specimens and machined flaws used in the visual inspection trials were based on characterisation data from actual examples of impact damage to CFRP laminate coupons. Close tolerances (<15% of the specified dimensions) to the original size and geometry specifications resulted in machined flaws that were the most authentic possible representations of impact damage flaws on painted CFRP laminates. Their authenticity could only be further improved by using more sophisticated computer aided machining methods whereby the impact damage flaws on the CFRP laminate coupons would be reproduced by machining a CMM digitisation of the damaged laminate surface into the specimen. Such a method might provide the means by which non-symmetrical, non-geometric flaws could be reproduced on facsimile specimens.

In reliability assessment experiments, it is traditional to vary only a single flaw size parameter or variable, which has conveniently only ever needed to be crack length for metallic NDT/ NDI reliability assessments. However, the sectional profiles of the differing surface topographies of impact damage to CFRP laminates could only be quantitatively described by using a series of geometric variables, which, as previously described, were interlinked by various relationships. A change in size or value for one variable subsequently resulted in a new value for the others. Varying a single flaw geometry value and holding the others constant would have broken the relationship to the other flaw geometry variables, i.e. the flaw geometry would no longer be representative of a particular impactor geometry/ laminate combination. In order to ensure authenticity to the Ø20 mm & Ø87 mm impact damage on 17 & 33 ply painted CFRP laminates whilst covering a broad range of realistically sized and shaped dents, the specimens for the series 2 trials contained flaws that had varying values of flaw width, flaw depth and other geometric variables as described in table 4.06. It was thus difficult to isolate the effect of a particular flaw geometry (flaw size) variable, or impactor geometry (flaw type) on visual inspection reliability within the results obtained.

### ***6.2.5 – Size range of physical trial results***

It is acknowledged that the results presented in chapter 5.5 cover a relatively narrow band of flaw widths and depths. Consequently, the question of detectability of flaws outside of this band arises. Accurate predictions of flaw detectability outside of the reported results would require further visual inspection experiments using an extended range of flaw sizes in order to populate detection data for the sizes not covered, allowing the contours produced in figures 5.50 to 5.56 to be extended. However, some discussion is made in the following sections of the possible implications for detectability of flaws outside of the range used.

### ***6.2.6 – significance of participant responses***

The physical specimen trials were undertaken by between 15 and 20 participants, hence a single participant's response could alter the detection rate for a single flaw by between 5% and 6.7%. Fifty participants would be required to reduce this figure to 2%, and 100 participants would be required for 1%. By reducing the variation in detectability for a single flaw imparted by a single participants answer, greater numbers of participants may also serve to improve the distinction of the detectability bands represented in the contour plots shown in figures 5.50 to 5.56. Increased participant numbers coupled with an increased flaw size range (as described above), would help increase the viability for using the contour plots described in this thesis as guides to impact damage detectability.

### ***6.2.7 – Generic applicability of physical trial results***

The visual inspection results obtained in the series 2 trials are considered representative of the visual inspection reliability of Ø20 mm & Ø87 mm impact damage to 17ply and 33ply painted CFRP laminates. In addition, the visual inspection trials results also represent visual inspection reliability of impact damage from any impactor size/ impact energy/ laminate combinations that produce non-surface breaking crack, 3D flaws with similar geometries to those used in the visual inspection experiments. Impact flaw geometries obtained by others may be compared to those presented in table 4.06, and if similar or matching geometries are obtained, the associated detectability of such flaws may be approximated from the results shown in chapter 5.5. It is important to note that the visual perception, and hence detectability of flaws exhibiting surface breaking cracks is different to that of

smoothly shaped 3D surface indentations, therefore such flaws are outside of the visual inspection reliability results presented in this thesis.

It is also noted in figures 5.50 to 5.56 that for each surface colour and finish combination, a region of >90% detections occurred. Whilst the range of widths and depths that fall into this region vary with colour and finish, it can be seen in figures 5.44 to 5.49 that a 25.79 mm wide, 0.94 mm deep facsimile dent representing 39J 20 mm hemispherical impact damage to a 17ply painted CFRP laminate was detected by all participants. Therefore, it can be said that for impact damage dents similar in size and shape to the described dent, >90% POD may be expected, regardless of surface finish or colour. However, the contour plots in figures 5.50 to 5.56 demonstrate that >90% detectability cannot be assumed for flaws of greater width or greater depth than the described flaw.

The results presented in chapter 5.1 demonstrate that for the same laminate type, the surface flaw geometry can vary depending on the impactor geometry and impact energy. Furthermore, it should be remembered that the surface flaw topographies and associated sub surface delaminations produced by falling weight impacts were established in this instance on 100 mm x 150 mm coupons manufactured from AS4/8552 pre-preg. In large-scale structures, the flaw topography and delamination size will be influenced by the compliance of the impacted structure as well as by the toughness and stiffness of the composite resin and fibre system used.

The flaws used in the visual inspection trials, and the detection results therefore represent only a small selection of the possible impact scenarios that could occur on aircraft in service. Thus, although the detection results obtained using various sizes and shapes of flaw on various colours and surface finishes will have generic applicability across all materials and structures where similar surface flaws occur, flaw topography, level of sub surface damage and subsequent flaw detectability needs to be determined by experiment for each application.

A specific question was posed to the author of this thesis regarding the applicability of the results data to existing damage detectability thresholds such as the 1.2 to 1.3 mm dent depth detectability threshold for GVI used by Airbus and the Boeing threshold

dent depth of 0.254 to 0.508 mm [Rouchon 2010]. The detection results reported in this thesis do not extend to the dent depths used by Airbus, but do cover the lower threshold value used by Boeing. At first glance, therefore, it would appear that the results imply that the 0.5 mm depth upper BVID threshold employed by Boeing is less conservative than the Airbus approach. Flaws within the 0.254 to 0.508 mm depth range were demonstrated to be less than 50% detectable, depending on colour and finish whereas detectability approached 100% for flaws approaching 1 mm in depth. However, if the detectability contours plotted in figures 5.50 to 5.56 were to be extended or extrapolated to cover a greater range of flaw depths and widths, it is plausible that the issue of reduced detectability for very wide flaws even at higher depths may present itself even above the dent depth threshold employed by Airbus. The implications of this possibility are discussed in later sections.

### ***6.2.8 – Existing experimental paradigms and protocols***

Extensive research was conducted in order to ensure that the visual inspection experiments carried out for this thesis conformed to existing experimental paradigms and followed guidelines & recommendations for NDT/ NDI reliability assessments. From this research, it is apparent that NDT/ NDI reliability for aircraft structures has predominantly been concerned with inspection for cracks in metallic structures. As a result, recommendations and guidelines for experimental design of NDT/ NDI reliability assessment, such as Spencer's generic protocol [Spencer et al. 1993] AGARD LS-190 [AGARD 1993] or MIL-HDBK-1823 [US DoD 2007] are written exclusively with inspection of metallic aircraft structures in mind.

#### **Translation of recommendations from 'metallic' to 'composite' context**

For 'metallic' inspection, it is relatively simple to implement or translate elements of the existing experimental paradigms and recommendations such as use of specimens that faithfully represent the aircraft structure under inspection, and use of flawed and unflawed specimens, with a 1:3 flawed to unflawed ratio. However, there is currently no established experimental paradigm or published recommendations to aid translation of these elements into reliability assessment of visual inspection of composite materials.

Whilst various barely visible damage (BVID) sizes have been published (Forsyth et al. 1998 & Rouchon 2009) for impact damage on composite materials, the details of how such sizes were determined are not available in the public domain. Damage tolerance for composite aircraft structures is intrinsically linked to BVID sizes, and despite the development of, and adherence to recommendations for metallic NDT/NDI reliability assessment protocols, there is little evidence available as to how such recommendations have been interpreted into protocols for determining BVID sizes for composite structures.

For the visual inspection trials presented in this thesis, the 3:1 recommendation [Spencer et al. 1993; AGARD 1993; US DoD 2007] was interpreted such that a single specimen constituted an ‘inspection site’, and for every specimen in the set that contained intentional damage or flaws, there were three more containing no intentional damage. When attempting to translate the 3:1 ratio recommendation from a ‘metallic’ to a ‘composites’ context, an issue of concern was that similar work such as Gant 2007 and Erhart et al. 2004 did not implement the recommendation. There was thus no published experimental precedent of how the recommendation should be translated or implemented.

Without an available precedent of conformity to experimental recommendations, the actual setup and size of specimens was also open to interpretation. Gant, 2007 used specimens that were pieced together to represent a composite wing structure, and presented it ‘on-aircraft’, thus representing inspection of an actual aircraft. The study by Erhart et al., 2004, however, used a single panel specimen from an actual aircraft, representing inspection of a single piece of damaged structure, presented in an isolated environment to an actual aircraft. Major airliner manufacturers have not published experimental procedures used for determining BVID sizes in the public domain, although there is evidence to suggest that large panels comprising many small size (100 x 100 mm) impact damaged coupons have been employed (see figure 6.01) [Fualdes 2006].

The methodology used in obtaining results for this thesis is believed be novel in presenting individual, large size (600 mm x 600 mm) faithful facsimiles of impact

damaged composite aircraft structure, whilst using a 3:1 unflawed specimen panel to flawed specimen panel ratio.



Figure 6.01 – Manufacturer's setup for visual inspection reliability assessment  
from Fualdes, 2006

### **Limitations of reliability assessments based on a single flaw size variable**

The word 'flaw' itself is a contentious issue, as for impact damage to a composite material, the resultant damage morphology is generally a surface indentation, which may or may not exhibit surface breaking cracks, beneath which lies subsurface delamination or cracking. Such damage cannot be simply described as a 'crack'. Whilst the use of the word 'dent' is more appropriate, dents are rarely described in published literature by more than their depth and/ or width. These measurements alone provide insufficient description of the surface flaw or dent topography, and as such, are not suitable flaw size variables on which models of flaw detectability can be solely based. Some description of flaw shape is required in order to be able to determine its detectability. The visual inspection trials results demonstrate that

detection rates did not always increase with increasing flaw depth or increasing flaw width. Furthermore, different shaped flaws, although similar in size returned different detection rates (such as flaw number 22, as demonstrated in table 5.07).

Current log based probability of detection (POD) models are unable to accommodate the above issues. Bi-variate plots of POD go some way to resolving the issue, by allowing POD to be calculated as a function of two variables. However, the accepted models and analysis methods for POD are logarithmic based, and unable to accommodate a situation in which detectability increases then decreases with increasing values of a given flaw size variable. As such, existing treatments for POD, which are recommended for use in NDT/ NDI reliability assessment, are unsuitable for use in assessment of the reliability of visual inspection for impact damage to composite aircraft structures.

### ***6.3 – Visual perception cues and visual inspection of impact damage***

The visual inspection trials results identify effects on detectability of flaws, representing impact damaged CFRP, due to surface colour and surface finish. These results were obtained using ambient, non-directional light, leaving the specimen panel surfaces free of reflections light sources, i.e. specular highlights. The area behind the participants was kept free of objects, thus any specular reflections on the panel surfaces were of a flat, light coloured wall.

Norman et al., 2004 identified that specular highlights aided 3D shape perception and Lloyd & He, 1998 identified positive correlation between ‘severity’ or ‘saliency’ of defects and their specular highlight area. Hence, if specular highlights were the influential factor affecting flaw detectability, greater differences would be expected between the contours plotted for detection of flaws on the highly specular, gloss specimens and detection of flaws on the diffuse, matt grey finish specimens. However, the fact that the contour plots of matt and gloss results (see figures 5.51 to 5.56) for each colour of specimens have similar features provides evidence that specular reflections and highlights had minimal role in the perception of the 3D surface flaws. Such evidence leads to the conclusion that much of the variation in detectability of surface flaws came from variations in shading cue saliency.



This is not to say, however, that the flaws on the grey (and other coloured) specimens failed to exhibit 'lighter' areas. Shading, and perceived colour as described in chapter 2.3, is a discrete visual cue, separate from specular highlights. Although the object shown in figure 2.28 has a matt finish, it still exhibits 'lighter' areas of shading. As deduced from Xiao & Brainard, 2008, and Norman et al., 2006, lighter areas appear on a shape when the surface slant is such that the colour shade reflected back to the observer is perceived as being lighter than neighbouring surfaces. A change in surface slant, such as that of an indentation on a flat surface, may result in a 'lighter' colour or 'darker' colour being observed, hence, the appearance of lighter and darker shaded regions where surface flaws are present (see again Xiao & Brainard 2008 and Norman et al. 2006).

Combining the modularity between shading cues and original the surface colour, for surface indentations, with the link between modularity & defect 'severity' raised by Lloyd & He provides an explanation for the results obtained from the visual inspection trials with physical specimens. Poor modularity between shading cues and the base colour will lead to the two being perceived as the same colour, making the shading imperceptible [Xiao & Brainard 2008], thus making the flaw difficult to detect.

### ***6.3.1 – Effects of surface colour & surface finish on modularity of visual perception cues***

Considering small width (<15 mm), low depth (<0.25 mm) flaws and larger, shallower shaped (>Ø35 mm/ <0.3 mm) flaws it is reasonable to suggest that the lighter and darker shading cues exhibited by such flaws occupy small surface areas, and/ or their modularity with the surface colour is low, resulting in poor saliency. Hence, the trend for lower detection rates for such flaws demonstrated on all colours of specimen (see figures 5.44 to 5.49). For the grey specimens, both lighter (tending towards white under white lighting) and darker areas (tending towards black under white lighting) of shading had modularity with the grey base colour, thus both may be perceived by the observer, if large enough. For the white coloured specimens, the darker shaded areas had increased modularity (being dark grey/ black against white), and greater saliency against the background colour. However, white is a 'light' colour, hence, surfaces whose slant causes them to reflect more light, and thus appear lighter than their neighbours are indistinguishable due to the lack of contrast i.e. low

modularity with the light base colour. The lack of improvement in detection rates for the gloss white over matt white specimens is thus explained by the following:

- Specular highlights, whilst they would also have poor modularity, were not present to aid perception [see Norman et al. 2004].
- The areas of lighter shading on both finishes had poor modularity with the base colour making them difficult to distinguish [see Xiao & Brainard 2008], thus making the flaws difficult to detect.

Conversely, for the blue specimens, the darker areas of shading had poor modularity with the dark base colour, reducing their saliency [Xiao & Brainard 2008] and thus explaining why detection contours for the blue specimens are somewhat different to those of the grey and white specimens. However, areas of lighter coloured shading had greater saliency, due to their increased modularity with the dark base colour, which implies that for flaws with higher detection rates, i.e. >0.5 mm deep, on the blue specimens, it is the lighter areas of shading that made them detectable. As described in chapter 2.3, specular, glossy surfaces produce small, precise highlights whereas a matt surface provides diffuse, less intense, but larger size lighter shaded areas. The reason for higher detection rates for flaws 0.3 to 0.4 mm deep on matt blue specimens, as seen in figure 5.56, is believed to be that the flaws exhibited larger, albeit less intense regions of lighter shading than the same flaws on the gloss blue specimens under the visual inspection trial lighting conditions.

The general trend for higher detection rates on grey specimens than on white and blue specimens is explained by the fact that both darker *and* lighter areas of shading had modularity with the grey base colour, i.e. the observer had the chance of detecting either or both cues, thus an increased chance of detecting the flaw.

### ***6.3.2 – Effect of surface colour & finish on specular reflection cues***

It is believed that due to the predominance of shading and shadow cues on the grey and white specimens, distortions in specular reflections of the light coloured wall behind the participants offered little advantage over the matt finish specimens, as supported by the relative similarity between the contour plots for gloss & matt finishes on grey and white specimens. Furthermore, the specular reflections of the light coloured wall on the light coloured specimens would have been faint, most likely

indiscernible, to the participants. However, for the gloss blue specimens it is conceivable that the contrast between the light reflected (specular) colour and the dark surface colour would have increased the saliency of specular reflection distortions, or increased the saliency of darker areas within the specular reflection caused by changes in surface slant at flaw sites.

### 6.3.3 – Effects of flaw shape on visual perception cues

The issue of shadow cues provides explanation for the scatter in detection rates, and thus irregularly shaped detection contours (as seen in figures 5.51 to 5.56). Although the lighting used was not directional, for some of the flaws on the specimens, the inclination of their internal surfaces may have been at sufficiently great an angle from the unflawed surface as to result in occlusion of the available light, as illustrated by figures 6.02 & 6.03.

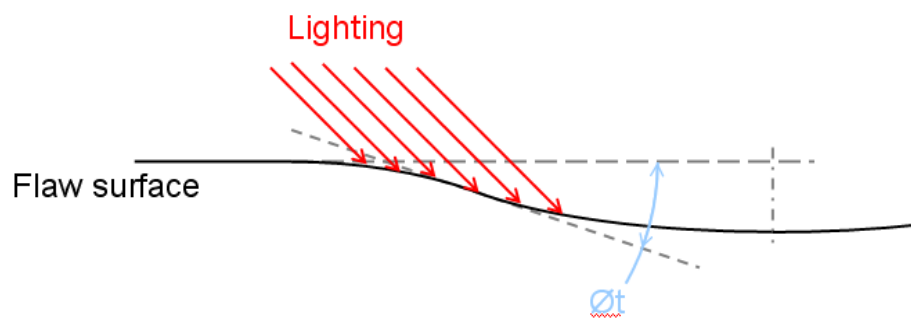


Figure 6.02 – Section through ‘shallow’ surface flaw with low value of  $\theta t$  and no occlusion shadow present

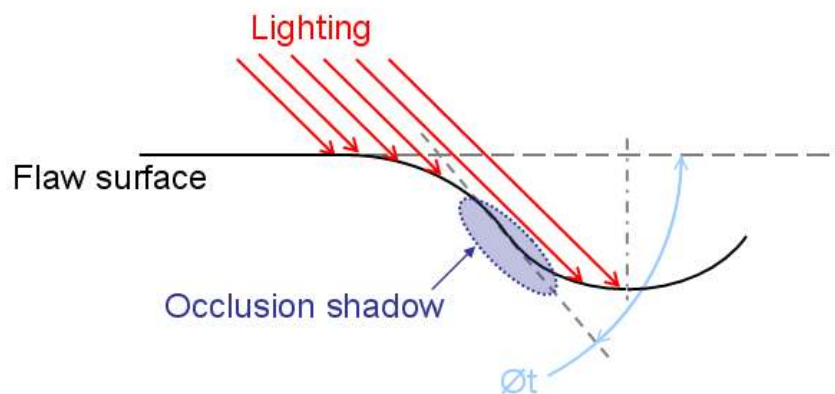


Figure 6.03 – Section through surface flaw with higher value of  $\theta t$  and subsequent occlusion shadow

For relatively shallow (i.e. >25 mm/ <0.3 mm deep) flaws such as those produced by larger radii (Ø87 mm) impactors even at high impact energies (>40J), the transition between the large sized internal and external radii occurs over relatively shallow angles, thus resulting in a ‘soft’ profile, and no occlusion shadow. The angle  $\theta_t$  between the curve endpoint tangency line (see figure 6.02) and the unflawed surface is relatively low for such flaws. However, for a ‘hard’ profile flaw, the sectional profile is such that the internal and / or external radii are small, and their transition occurs over a short distance, resulting in a large angle  $\theta_t$  between the tangency line (i.e. flaw surface) and the unflawed surface as seen in figure 6.03. For these ‘hard’ profiled flaws, such as flaw number 8 (see table 4.06), which typically represent high energy (>30J), smaller size (Ø20 mm) impactor damage to a CFRP laminate, an occlusion shadow has a greater likelihood of occurring, thus providing a further cue to aid visual detection.

Furthermore, changes in sectional profile shape translate into changes in surface slant, which, as the work of Norman et al., 2004 demonstrates, affect surface shape perceptibility. ‘Hard’ profile flaws will provide more significant changes in surface slant, than ‘soft’ profiled flaws (see figures 6.02 & 6.03), resulting in more salient, and thus more detectable changes in surface shading and colour.

For impact damage dents on CFRP laminates, the geometric variables that are driven by the dent shape profile are those that relate to the internal curvature (see figure 4.12). During the experimental design for the visual inspection trials with physical specimens described in this thesis, a decision was taken to distribute the flaw sizes by widths and depths (see chapter 4.10.5). The values for the internal curvatures were driven by maintenance of relationships to width and depth that were determined for 4 types of impact damage. Within the specimen set, few flaws had both similar widths and depths, meaning that for a given flaw width or depth, the effect of differences in internal geometry on dent detectability could not be isolated. Plotting detection results as a function of internal geometry variables would be meaningless without first isolating their effect from those of dent width and depth, i.e. holding width and depth constant for variations in internal flaw geometry. Isolation would be required in order to provide conclusive evidence as to the effect of internal geometry variables on detection rates.

However, holding a constant flaw depth and flaw width whilst varying internal geometry variables would mean that the resultant flaw shapes would not be representative of a single ‘type’ of impact damage across a range of impact energies on the same laminate.

#### ***6.2.4 – Role of head movements in visual perception/ inspection***

Whilst shading and shadow cues remain constant regardless of viewing angle under a constant lighting condition (see Gibson 1950a, & Kingdom 2008), the position of specular highlights and the appearance of specular reflections will alter with changes in viewing angle (see Norman et al. 2004) i.e. with head movements during visual inspection. Changes in specular reflection have been proven to enable identification of surface flaws (see Norman et al. 2004). Furthermore, by altering their viewing angle, participants may have been able to observe small specular highlights that were not present in the normal viewing angle. The virtual specimens used in the series 1 and series 2 trials were rendered such that the shading cues of each flaw were replicated for a constant viewing angle and constant lighting condition, and without specular highlights or reflections. When viewing the specimens, participants saw the same image regardless of whether they moved their heads, i.e. the cues appeared the same from every viewing angle. Comparing the detection contours obtained from virtual grey specimens with those obtained from physical gloss grey specimens reveals lower detection rates (40% ~ >90% vs. 80% ~ >90%) for >Ø30 mm / >0.3 mm deep flaws on virtual specimens. It is apparent that the detection contours are far more clearly defined, with less scatter for the <0.3 mm deep flaws on virtual specimens. Also apparent is the fact that flaws <Ø15 mm/ <0.2mm deep (small size) flaws achieve only up to 60% detection on virtual specimens compared to up to 100% on physical specimens. The only significant difference between each set of results is that the participants viewing the physical specimens were able to obtain a new, albeit perhaps very similar, view of each flaw by moving their head, unlike the fixed, single view offered by the virtual specimens. The results therefore demonstrate that head movement during visual inspection, and subsequent detection of (possibly very small) specular highlights & reflections (or changes to them) is advantageous to visual inspection for 3D surface flaws, such as those caused by impact damage to a CFRP laminate. This is consistent with the findings of Norman et al., 2004 & Todd et al.

1996, on the role of changes in specular highlights in shape perception. Therefore, there is sufficient evidence to state that, in order to provide accurate estimations of visual inspection reliability, virtual specimens must replicate the changes in visual cues that occur as the observer moves their head. Such specimens require a high-resolution display, capable of displaying real time photo-realistic renderings of the specimen surface that change in coordination with the participants head movements.

## ***6.4 – Implications for aviation safety***

### ***6.4.1 – Lighting for visual inspection tasks on composite structures***

For the visual inspection trials, the ceiling mounted diffuse lighting provided a luminance level such that the base colours of the grey, white and blue specimens appeared as those colours. The panels were viewed normal to their surface, thus eliminating reflections of light sources and specular highlights. Shadows were also minimised by the use of diffuse lighting. The lighting conditions thus provided an optimum balance between producing shadow, shading, specular reflection and specular highlight cues. However, lighting conditions for inspection of 3D surface flaws can be adjusted to increase the modularity, and thus saliency of specific cues in order to increase the likelihood of flaw detection.

The work of Faulkener & Murphy, 1979 and Brombach et al., 2006 provides evidence to suggest that improvements in detection rates on all specimens would be made by adding a directional light source, transverse to the specimen panel surface, whilst maintaining diffuse lighting, as used in the experimental setup. If transverse lighting were used, shadows would be cast by all surface flaws on all finishes, and specular highlights would become visible on gloss specimens, both of which undoubtedly enhancing flaw visibility, especially for the wider, less deep flaws ( $>0.35\text{mm}$ / $<0.25\text{mm}$ ). Such conditions represent the use of a flashlight or lamp held transverse to the inspection surface, and future work could evaluate the benefits offered by such equipment to inspection of light, mid, and dark coloured surfaces in either gloss or matt finishes.

For conditions where low luminance levels are present, surface colours may appear darker than their actual colour, resulting in reduced modularity between cast shadows or areas of darker shading and base colour. In such conditions, such as undersides of

aircraft structures, specular reflections, highlights and areas of lighter shading will have increased modularity against the background colour. Under lower levels of luminance, white surfaces may appear darker, thus lighter shading or specular highlights & reflections will have greater modularity against the surface colour whilst dark shading and shadows will retain reasonable modularity. For lighter coloured surfaces, reduced luminance levels will therefore be less detrimental to flaw visibility wherever sources of specular reflections or highlights (such as reflections of floor markings & lamps or highlights from lamps) are present.

Dark colours, on the other hand, will appear yet darker, and offer poor dark shading and shadow modularity under reduced luminance levels. The detection of surface flaws on a dark surface is believed to be predominantly based on detection of lighter shaded and highlight areas, due to the lack of modularity between dark shading or shadowed areas and dark base colours. Modularity between specular reflections and specular highlights is at its greatest on dark base colours. The work of Lloyd & He 1998 provides evidence that flaws or indentations may be detected simply by detection of specular highlights, and highlight modularity & size are good indicators of flaw detectability. It is therefore suggested that the detection of flaws on dark coloured glossy surfaces can be improved by providing lighting sources that produce specular highlights or specular reflections on the inspection surface. Lighting sources such as strip lights or grid lights produce linear specular reflections in which distortions are highly salient, and easily identified. The work presented in Aluze et al., 2002 and Lloyd & He 1998, provides evidence that such lighting will enhance the detectability of surface flaws, especially on darker colours. This leads to the suggestion that detection of impact damage flaws, and thus visual inspection reliability of composite aircraft structures would benefit from the provision of luminaires fitted with grids or strip type lighting.

#### ***6.4.2 – Implications for designers of composite material structures***

Aircraft maintenance documents such as structural repair manuals (SRM) commonly give repair criteria for composite structures based on the depth of the surface flaws, and delamination size. Whilst flaw depth may be acceptable as sole criteria for repair assessment, aircraft & aircraft structure designers cannot simply assume that all damage over a certain depth or width will be found. The results of the visual

inspection trials (as seen in chapter 5.5) demonstrate that flaws of small depth & width are difficult to detect, and that for a given flaw depth, wider flaws are also more difficult to detect. This trend is also apparent in results presented by Gant, 2007, as seen in figure 2.17. When the detection percentages obtained by Gant are plotted against flaw width, it is apparent that whilst greater detections are achieved for wider flaws, the widest flaw in the specimen set returns less than 90% detection. The visual inspection trials results, and the results presented by Gant provide evidence that a blanket ‘bigger is better’ approach is invalid for width of impact damage and associated detectability on composite aircraft structures.

Given the points discussed in chapter 6.1.1 regarding impact damage dent width measurements, it is acknowledged that such measurements are difficult to obtain compared to dent depth measurements. However, the results of the visual inspection trials presented in chapter 5 demonstrate that the probability of detection of a 3D surface flaw has both a width and depth component. Therefore, when determining the damage tolerance size, i.e. size of impact damage that can be found (or missed) on composite structures, the limit of visual inspection reliability should be considered in terms of both the surface flaw depth and the flaw width, as both are required in order to determine a surface flaw’s visibility.

Aircraft designers and regulatory bodies should not assume that visual inspection reliability of a composite aircraft structure increases for larger energy impacts, or impacts from larger objects. Table 6.01 gives the flaw characteristics of actual impact damage on a painted, mesh incorporated CFRP laminate coupon, produced during the flaw characterisation work described earlier in this report. Alongside, the characteristics of a similar sized flaw used in the visual inspection trials, and its detectability are given.



Actual surface flaws				Facsimile specimen flaws							
Impact conditions	Surface Flaw Width (mm)	Surface Flaw Depth (mm)	Delamination Width (mm)	Surface Flaw Width (mm)	Surface Flaw Depth (mm)	% Detections obtained					
						Gloss Grey	Matt Grey	Gloss White	Matt White	Gloss Blue	Matt Blue
Ø20 mm 17ply/ 5J	5	0.11	10	9.03	0.11	33	41	6	0	44	5
Ø20 mm 17ply/ 15J	21.5	0.32	26	19.11	0.37	100	94	100	100	69	95
Ø20 mm 33ply/ 20J	15	0.2	47	16.44	0.2	20	47	50	33	63	10
Ø20 mm 33ply/ 50J	30	0.86	79	29.96	0.57	100	100	100	100	81	85
Ø87 mm 17ply/ 20J	13	0.18	67	13.46	0.12	33	29	38	44	6	5
Ø87 mm 17ply/ 40J	22	0.21	100	24.53	0.19	100	88	81	61	38	40
Ø87 mm 33ply/ 20J	13	0.14	12	14.15	0.16	87	53	81	56	19	45
Ø87 mm 33ply/ 60J	40	0.28	83	40.45	0.25	67	59	6	22	44	0

Table 6.01 – Links between detectability and delamination sizes

From table 6.01, it is evident that a Ø24.53 mm/ 0.19 mm deep surface flaw, that could have 100mm wide impact delamination beneath, whilst being 100% detectable on a gloss grey specimen, was only detected by 38% of participants on a gloss blue specimen. Furthermore, a 0.25mm, 40.45mm wide surface flaw that could have 83mm of delamination beneath was undetectable on a matt blue surface, yet 67% detectable on a gloss grey surface. Of particular concern, is that the surface flaw that represents impact damage with 83mm wide delamination was no more than 67% detectable. The visual inspection trials results show that surface flaws, occurring from impacts that cause relatively large delamination widths, may be undetectable, or difficult to detect, depending on the surface colour and finish of the structure. For example, a flaw representing a 44J impact from an Ø87 mm impactor (or 60 mm of delamination) was not detected by any participants on a matt blue specimen, but was detected by 67% of participants on a gloss grey specimen. Whilst one may argue that NDT techniques such as tap-test and C-Scan should easily identify large areas of delaminated structure, one must remember that because the surface flaw of such damage could be undetectable, the NDT may never actually be requested.

#### 6.4.3 – Implications for aviation personnel

Aviation personnel may drop tools or objects onto an aircraft, or may cause impact damage to aircraft with ground handling equipment. The impact testing work

performed on mesh incorporated, painted composite laminate, as seen in chapter 5.1, provided evidence that impact damage can have a surface appearance that is more typical of a small dent on a metallic structure. The testing work also demonstrated that impact damage to a composite aircraft structure does not always produce a visible crack. Aviation personnel need to be made aware that damage with an appearance they may pass off as being an insignificant dent on a metallic structure could in fact be quite significant impact damage to a composite structure, and should be reported or further NDT requested.

The visual inspection trials show that for a 40.45 mm wide, 0.25mm deep surface flaw, which would represent significant impact damage to a 33ply laminate, there is between 30% and 100% chance of *not* detecting the damage, depending on whether the surface is glossy grey or matt blue. Aviation personnel must be made aware that they could produce impact damage that is impossible, or difficult to see, and should be encouraged to report any impact incident on a composite aircraft structure, regardless of whether or not they can see a surface flaw. If the person causing the impact is unable to see a surface flaw, the inspector performing a requested inspection or NDT may also be unable to locate the impact site. It may be beneficial to request that aviation personnel mark, or record the location of any known impact occurrence immediately, in order to avoid a requested NDT or further inspection being conducted in the wrong place. Due to the poor modularity and subsequent saliency of shading and shadow cues associated with dark coloured, matt finish surfaces, visual inspection personnel should be encouraged to be particularly vigilant when inspecting them.

## ***6.5 – Recommendations to industry & regulatory bodies***

### ***6.5.1 – Damage size assumptions***

Impact damage from large objects may cause wide, shallow surface dents, coupled with significant delamination. Despite being associated with significant hidden delaminations, wide, shallow surface flaws can be difficult to detect by visual inspection. Persons involved in the design and certification of composite aircraft structures are recommended against assuming that impact damage dents associated with large sub-surface delamination will be more reliably detected than dents with smaller sub-surface damage. A “bigger is more detectable” metric should not be applied to visual inspection reliability for impact damage to composite aircraft

structures. If such a metric is adopted, it is conceivable that significant delamination damage may be left un-repaired due to the associated surface indentation being non-detectable.

### ***6.5.2 - Damage reporting***

The results of the impact experiments on coupons of CFRP laminate demonstrate that a measurement of surface flaw depth alone cannot be used to determine delamination size for different impact dent scenarios. A measurement of surface flaw width and surface flaw depth may provide an improved estimate of delamination size, although for any given values of width and depth delamination size was seen to vary depending on impact conditions. Given that structural performance of composite aircraft structures is affected by delamination size, and that different delamination sizes can occur for the same surface flaw width and depths, it is recommended that only delamination size be used for repair criteria assessment. Consequently, it is recommended that unless sufficient data can be generated to categorise damage scenarios and resultant delamination size into surface flaw width and depth bands, all impact damage suspected during visual inspection is assessed using further NDT before a decision on repair or airworthiness is made.

### ***6.5.3 – Reporting culture***

If aviation personnel are to be encouraged to report all impact occurrences to composite aircraft, the aviation industry must be prepared for inspection or NDT by qualified personnel to be requested more frequently than with metallic aircraft structures. Aviation personnel should not be reprimanded for calling out impact occurrences that result in insignificant damage, or no damage being found, for fear of creating a non-reporting culture, which could lead to significant impact damage going unreported, undetected and un-repaired. Although further NDT of all flaws suspected during visual inspection implies an increased frequency of flaw detections and NDT operations, this does not imply that the frequency of impact events to aircraft will increase.

### ***6.5.4 – Effects of surface colour, finish & lighting***

Detection rates of 3D surface flaws produced by impact damage were affected by flaw depth and flaw width, surface colour and finish. The lighting conditions available during inspection could also affect the reliability of visual inspection of 3D surface flaws. When assessing the reliability of visual inspection of composite structures,

attention must be paid to colours and finish of the inspection area, what the available lighting conditions will be, and the size and shape of the damage that is actually likely to occur. For example, inspection reliability data for relatively deep, flaws of small width on gloss grey structures that are brightly lit by grid lights could be used for calculation of damage tolerance sizes. In a worse case scenario, if the structure when in service is actually painted gloss blue, is located on a poorly lit fuselage underside, and suffers impact damage causing significant subsurface damage and a wide, shallow flaw, the flaw will have much reduced probability of detection than originally. If the flaw is not detected, the repair will not be made, and the structure may continue to fly with an airworthiness hazard. Therefore, it is recommended that if highly conservative estimates are sought for determining the base values on which visual inspection reliability for impact damage to composite aircraft structures can only ever improve, dark coloured matt finishes should be replicated and lit solely by low luminance level ambient lighting.

It also recommended that when assessing visual inspection reliability for impact damage to composite aircraft structures, attention should also be paid to the gloss levels of the inspection surface. If the gloss level of a structure's finish degrades after several months of service, such as reported by Guseva et al. 2003, the visual inspection reliability for that structure could be negatively affected. Visual inspection reliability may need to be demonstrated for a worst-case gloss degradation scenario.

#### ***6.5.5 – Flaw significance/ perceived severity***

Consideration must be paid to the likely interpretation of flaw significance by personnel whose experience has been with metallic structures. Such personnel may be accustomed to the presence of shallow, insignificant surface dents on a metallic structure, which pose no airworthiness issues. However, the same personnel may be unaware that similarly shaped dents on a composite structure could be an indication of significant sub-surface damage, and failure to instigate further investigation or repair could have severe airworthiness implications.

#### ***6.5.6 – Reliability assessment protocols***

There is currently a wealth of published literature available to assist in the design of reliability assessment experiments concerning NDT/ NDI procedures for metallic aircraft structures. However, this literature currently requires significant interpretation

before it can be applied to reliability assessment of visual inspection of composite materials. Regulatory bodies should ensure that a common set of experimental protocols are being used in determining visual inspection reliability and subsequent BVID sizes for composite aircraft structures, and consider publishing a recommended protocol or experimental design guidelines/ recommendations.

## ***Chapter 7 – Future Work***

The following sections describe areas where the work presented in this thesis has identified the possibility or requirement for future work.

### ***7.1 – Expansion of flaw size range***

A better understanding of width/depth effects on detection rates may be obtained by expanding the flaw size range in future experiments. However, the values of the flaw geometry variables for such flaws may extend to width/ depth combinations that fall outside the relationships for Ø20 mm & Ø87 mm hemispherical impacts on 17ply & 33 ply painted CFRP laminates. In such instance, it would be beneficial to vary only a single flaw geometry variable at a time, whilst using constant relationships to the other flaw geometry variables, in order to isolate the effects of each in visual inspection reliability. For example, if flaw widths were varied at constant flaw depths, and vice a versa, with constant relationships between the other flaw geometry variables, a 3D surface plot of detectability as function of both flaw depth and flaw width could easily be produced. However, as the visual inspection trials results show (see chapter 5.5), the detectability may not always be greater for wider flaws, whilst still being low for the smallest width flaws at a constant flaw depth. As widely accepted logarithmic based POD functions are unable to model detectability that both increases and decreases with increasing flaw size, the application of traditional POD models to the data will remain unfeasible.

### ***7.2 – Experimental protocols/ guidelines***

The current publications concerning design of NDT/NDI reliability assessments such as LS190 [AGARD 1993], MIL HDBK 1823 [US DoD 2007] and the Generic Protocol produced by Spencer et al., 1993 were written in the context of inspection of metallic aircraft structures. However, many of the recommendations within these documents such as specimen characteristics & numbers, flaw size ranges, flaw

densities and flawed/ unflawed ratios are valid regardless of context, although they require interpretation depending on the process under assessment.

However, despite the many published BVID sizes, there are currently no published protocols or experimental recommendations for assessing visual inspection reliability, and thus BVID sizes, for composite aircraft structures. Future work should consider the valuable recommendations and protocols that have been published for design of NDT/NDI reliability assessment experiments, and apply them in the context of visual inspection of composite aircraft structures. The aim for such work should be to arrive at a set of protocols or recommendations that ensure consistent experimental practices are employed in determining visual inspection reliability and BVID sizes for composite aircraft structures under realistic conditions. The objectives would be to standardise the design of flaws, specimens, experimental setup, lighting and data collection methods used in determining visual inspection reliability and BVID sizes for composite aircraft structures.

### ***7.3 – Alternative Visual Inspection Trials Methodology***

The visual inspection trials described in this thesis (chapter 4.12) were performed using flat specimen panels presented vertically upright, with the inspection surface normal to the participants. It is acknowledged that this represents only a single inspection condition, and that visual inspection of an actual aircraft will involve the inspection of surfaces at various angles, such as fuselage skin, wings skins, and horizontal & vertical stabiliser skins. The work of Erhart et al. 2004 demonstrates that different viewing angles and under-wing inspections conditions are likely to produce different inspection results. The results presented in this thesis also demonstrate that an inspector's ability to move around the inspection area must not be discounted as an aid to visual inspection. The work of Aluze et al. 2002 and Lloyd & He, 1998 demonstrates that grid or strip lighting will also benefit visual inspection performance.

Furthermore, the surface flaws used in this experiment represent only 8 sizes of 4 flaw types. Whilst the experiment has successfully investigated the effects of surface colour and surface finish on visual inspection reliability, it would be desirable to expand the number different sizes of each flaw type, in order to produce more information on how the flaw geometry affects visual inspection reliability. However,

using the current experimental methodology would require that the total inspection time is increased to over 30 minutes, which may lead to participant fatigue or boredom.

A solution to providing a more realistic inspection scenario, and a solution for increasing the number of specimens inspected in a single visual inspection trial, would be to arrange square specimen panels containing realistically shaped flaws into a mock up aircraft shape, as seen in figure 7.01.

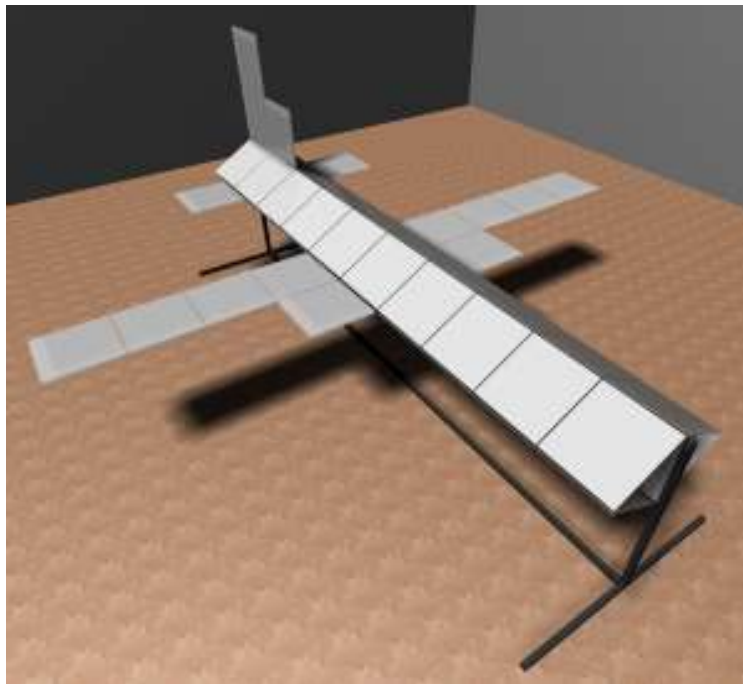


Figure 7.01 –Specimen panels arranged into an aircraft shape

A single participant, or several participants, would inspect the entire “aircraft”, and a maximum inspection time could be imposed if desired. The participants would be asked to search for surface flaws on each of panels, and mark their location on a diagram. The specimen panels would be a mix of flawed and unflawed panels, and with this arrangement, it is possible to increase the total number of specimens, thus increasing the number of surface flaws that can be included in the experiment, without increasing total inspection time. A further advantage to this arrangement is that it allows panels to be placed in different positions, in order to simulate horizontal and vertical topside and underside surfaces. As seen in figure 7.02, to inspect the underside surfaces, the inspector must view the underside panels from below, against

a bright background. Any effects on visual inspection performance due to this lighting condition and accessibility constraint would be revealed in the inspection results.

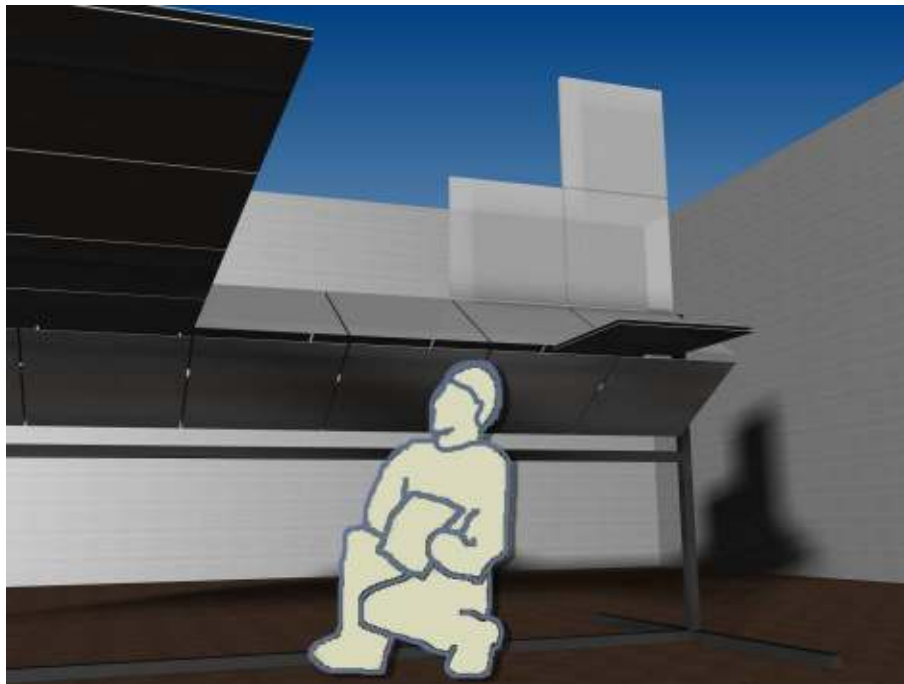


Figure 7.02 – Inspection of the panels representing the underside of an aircraft

If the specimens were laid out to represent an aircraft, or section of aircraft structure, the participants would expect to walk around the specimens and inspect from different angles. Due their ability to view each panel from a variety of angles, the participants would also observe specular reflections and specular highlights on glossy specimen panels laid out as in figure 7.01. The introduction of specular reflection and specular highlight visual perception cues may reveal greater differences in visual inspection performance on matt and gloss finishes than those demonstrated in the results obtained for this thesis. Because arranging the specimens as illustrated in figure 7.01 would inherently introduce specular reflection cues into the experiment, the effects on visual inspection performance due to different lighting designs such as grid luminaires or strip lights could also be investigated by incorporating them into the setup.

Arranging the panels into an aircraft shape would also factor inspector expectation into the experiment. For example, an aircraft inspector may expect to see damage aft of a wheel well, where stone & foreign object damage (FOD) is common. However, the inspector would not expect to see the same damage on the topside of a wing. An impact damage flaw may be detected in a wheel well, or under wing location, yet missed on the top surface of the wing. This would raise the question of whether the



inspector missed the damage or flaw on the topside of the wing because it was too small for them to see, or because they did not expect to see damage in that location. In a scenario where an aircraft is being simulated, it is expected that an inspector will use their experience to determine where they would expect to find damage, and concentrate their visual inspection on that area [see Gallwey & Drury 1986]. An untrained participant, however, would be more likely to look everywhere for the damage or flaws. Therefore, it is foreseeable that the value of prior experience or damage location expectancy could be quantified by conducting trials with trained inspectors and trials with novice participants.

#### ***7.4 – Paint Patterns***

By using either the original visual inspection trials methodology (see chapter 4.12), or the aforementioned alternative setup, it would be advantageous to investigate the effect of a paint pattern on visual inspection reliability. There is some concern that a pattern could disguise the shadow and shine cues provided by a surface flaw to an extent that the flaw detectability reduces, or the flaw becomes undetectable. In fact, this forms the basis of how camouflage works. Furthermore, the camouflaging effect of a paint pattern would be exacerbated by the fact that impact damage on an aircraft structure will not always be geometrically shaped, especially if caused by an irregularly shaped object. However, in order to produce a pattern on a specimen panel, a suitable production method must be researched and tested to ensure that the pattern is consistently the same on each specimen, and that the production process does not alter the flaw characteristics.

#### ***7.5 – Curved specimen panels***

The specimen panels used in the visual inspection trials were all flat panels, representing impact damage to a flat laminate. Aircraft surfaces are generally curved. The surface flaw due to impact damage may be different in shape & size on a curved laminate panel to the flaw on a flat laminate, due to internal material stresses & relaxation at the flaw site. A more realistic assessment of visual inspection reliability could use curved specimen panels that represent impact damage to a curved shaped composite aircraft structure.

### ***7.6 – State of knowledge of pilots, maintenance & ground crew personnel***

Whilst this study assessed the reliability of visual inspection of surface flaws due to impact damage on a composite aircraft structure, the participants in the experiments were all given examples of surface flaws prior to inspecting, i.e. they all knew what to look for. There is some concern that not all aviation personnel are aware of what a surface flaw due to impact actually looks like on a composite aircraft structure. In fact, the early stages of this study required work to address this lack of information. Therefore, in order to assess whether there is an industry wide knowledge deficit, and what future training may be required, it would be beneficial to study the current state of knowledge regarding impact damage to composite aircraft within aviation personnel groups i.e. pilots, maintenance personnel and ground crew.

## ***Chapter 8 – Conclusions***

### ***8.1 – Impact damage to fully finished CFRP laminates***

1. Impact experiments on CFRP laminate coupons demonstrated that the widely reported visual appearance of impacts to unfinished laminates is not typical of impact events on actual aircraft structures.
2. The experimental results demonstrate that impact damage to painted, bronze lightning strike protection mesh incorporated CFRP produces smoothly shaped, crack free dents that offer different visual perception cues to the rough edged, cracked surfaces of impact damage sites on unfinished laminates.
3. For a typical finished aerospace CFRP laminate, higher energy (40J) impact damage from a larger (87 mm) diameter hemispherical object resulted in damage with a lower depth (0.21 mm vs. 0.67 mm), and greater delamination (4900 mm<sup>2</sup> vs. 1900 mm<sup>2</sup>) than lower energy (20J) impact damage from a smaller (20 mm) diameter object.

### ***8.2 – Visual inspection reliability of impact damage dents***

4. The detection results obtained using facsimile specimens of hemispherical impact damage to CFRP laminates in visual inspection trials are consistent with theories of visual perception of surface slant & shading, occlusion shadows, specular highlights and specular reflections.
5. Using facsimile specimens in visual inspection trials, increased detection rates were observed with larger depths & widths of impact damage dents, but the positive effect of depth on detection rate was mitigated by a negative effect of width on detection rates for relatively large widths.
6. The visual inspection trials demonstrate that the detectability of *all* impact damage producing damage of a given width or depth cannot be considered the same.
7. The results of the trials with facsimile specimens demonstrate that impact damage dents associated with large subsurface delamination (as per conclusion 3) were less reliably detected by visual inspection than impact damage associated with smaller subsurface delamination (as per conclusion 3).

8. Visual inspection reliability cannot be accurately modelled by probability of detection estimates based solely on dent width, dent depth, impact energy or delamination size for impact damage to composite aircraft structures.
9. Visual inspection using 2D projected images of virtual specimens provides a time and cost efficient tool for developing experimental methodologies, or for generating detection data on which to base experimental design engineering judgments for visual inspection assessment experiments.
10. Visual detection results obtained using static 2D display specimens cannot not considered directly comparable to inspection of a physical specimen due to the inability to replicate the changes in visual perception cues on a 3D surface that occur during head movements.

### ***8.3 - Effects of surface finish and colour on visual inspection reliability***

11. In the detection results obtained with facsimile specimens of impact damage to CFRP specimens, a region of 90-100% detection occurred in all specimens at the largest depths and widths. The size and location of this region varied with surface finish and colour.
12. The grey surface colour provided the optimum modularity between light and dark shading cues, resulting in optimum cue saliency and the largest range of flaw sizes returning >90% detection (0.25 ~ 0.95 mm deep & Ø20 ~ Ø45 mm wide).
13. Poor modularity of lighter areas of shading reduced the visibility of flaws on white coloured specimens, reducing the saliency of lighter shaded areas, hence a reduction in the range of flaw sizes returning >90% detection (0.3 ~ 0.95 mm deep & Ø25 ~ Ø40 mm wide).
14. Increased modularity of lighter areas of shading on blue coloured specimens was mitigated by poor modularity of darker areas of shading and poor modularity of shadow cues against the dark background colour, reducing their saliency, hence the smallest range of flaw sizes returning >90% occurring on the blue specimens (0.7 ~ 0.95 mm deep & Ø25 ~ Ø30 mm wide).
15. Specular highlights were not visible to the observer, and specular reflections had insufficient saliency against the grey and white surface colours for distortions caused by flaws to be perceived, hence, the relative similarity between the results obtained from matt and gloss specimens in these colours.

16. The gloss blue specimens exhibited salient specular reflections, and distortions in the reflections caused by the flaws made the flaws visible, hence the lower number of flaws (12 flaws) returning <50% detection compared to the matt blue specimens (25 flaws) which were devoid of specular reflections.

#### ***8.4 – Visual inspection reliability for composite aircraft structures***

17. Visual inspection reliability for composite aircraft structures must be demonstrated for impact damage to the actual laminate surface finishes seen by a field inspector and not bare, unfinished laminates.
18. Visual inspection detection thresholds such as 50% probability of detection, (POD), 90% POD or barely visible (BVID) must not be considered in terms of either dent depth OR dent width alone. As a minimum, both the indentation width and the indentation depth are required to determine detectability thresholds.
19. In order to accurately model visual inspection reliability of impact damage to composite aircraft structures, a multi-variate POD analysis method must be developed.
20. Due to the significant effects of surface colour and finish, visual inspection reliability for composite aircraft structures must be demonstrated on at least one light, one mid and one dark colour in finishes typical for that structure in order to determine best and worst case reliability scenarios.

## References

- Abdallah, E. A., Bouvet, C., Rivallant, S., Broll, B. and Barrau, J. (2009), "Experimental analysis of damage creation and permanent indentation on highly oriented plates", *Composites Science and Technology*, vol. 69, no. 7-8, pp. 1238-1245.
- Abrate, S. (1998), *Impact on Composite Structures*, Cambridge University Press, Cambridge, UK.
- Aerospatiale (1991), *Substantiation of Composite Parts - Impact Detectability Criteria*, 440 225/91.
- AGARD (1993), *A recommended methodology for quantifying NDE/NDI based on aircraft engine experience*, AGARD-LS-190, Advisory Group for Aerospace Research and Development, North Atlantic Treaty Organization, 7 rue Ancelle, 92200 Neuilly-sur-Seine, France.
- Airbus (2009), *A350 XWB Programme Update January 2009*, Airbus Press Office, 31707 Blagnac, France.
- Airbus (2009), *Airbus A350 Fuselage Production*, available at: [http://www.airbus.com/en/aircraftfamilies/a350/efficiency/by\\_design/fuselage.html](http://www.airbus.com/en/aircraftfamilies/a350/efficiency/by_design/fuselage.html) (accessed 16 June 2009).
- Airbus (2003), *Airbus A340-200/300 Structural Repair Manual 41st Revision Jan 01/03*, A340 SRM, Airbus Customer Services, Technical Data Support and Services, 31707 Blagnac Cedex, France.
- Airbus (2002), *Airbus A340 Aircraft Maintenance Manual*, A340 AMM, Airbus Customer Services, Technical Data Support & Services, 1, rond-point Maurice Bellonte, 31707 Blagnac Cedex, France.
- Aktaş, M., Atas, C., İçten, B. M. and Karakuzu, R. (2009), "An experimental investigation of the impact response of composite laminates", *Composite Structures*, vol. 87, no. 4, pp. 307-313.
- ANAC (2008), *Eclipse High Solids Polyurethane Topcoat*, Technical Data, June 2008, Akzo Nobel Aerospace Coatings, Sassenheim, The Netherlands.
- ANAC (2006), *Aerodur Finish C 21/100 Technical Data September 2006*, 30-02, Akzo Nobel Aerospace Coatings BV, Sassenheim, The Netherlands.
- Annis, C. (2008), *Generalized Linear Models on a P/C Spreadsheet*, available at: <http://www.statisticalengineering.com/glm.htm> (accessed 02 July 2009).
- Armstrong, K. B., Bevan, L. G. and Cole, W. F. (2005), *Care and repair of advanced composites*. 2nd ed. ed, SAE International, Warrendale, Pa.
- Asada, H., Sotozaki, T., Endoh, S. and Tomita, T. (1998), "Practical Evaluation of Crack Detection Capability for Visual Inspection in Japan", *Papers presented at the RTO AVT Workshop on "Airframe Inspection Reliability under Field/ Depot Conditions"*, Brussels, Belgium, May 13-14 1998 and published in *RTO MP-10*, pp. 15-1.

- Berens, A. P. and Hovey, P. W. (1982), "Characterization of NDE reliability", *Review of progress in quantitative nondestructive evaluation. Volume 1 - Proceedings of the Eighth U.S. Air Force/Defense Advanced Research Projects Agency Symposium on Quantitative Nondestructive Evaluation, Boulder, CO; United States; 2-7 Aug. 1981*, New York, Plenum Press.
- Bode, M. D., Spencer, F. W. and Piotrowski, D. (2006), "Analytical Issues in Determining Probability of Detection", *9th Joint FAA/DoD/NASA Aging Aircraft Conference*, 6-9 March, Atlanta, GA.
- Boeing (2009), *Boeing Commercial Airplanes 757-200 Background*, available at: [http://www.boeing.com/commercial/757family/pf/pf\\_200back.html](http://www.boeing.com/commercial/757family/pf/pf_200back.html) (accessed 16 June 2009).
- Boeing (2009), *Boeing Commercial Airplanes 777 Background*, available at: <http://www.boeing.com/commercial/777family/background.html> (accessed 6 May 2009).
- Boeing (2009), *Boeing Commercial Airplanes 787 Dreamliner Background*, available at: <http://www.boeing.com/commercial/787family/background.html> (accessed 16 June 2009).
- Boeing (2009), *Boeing Integrated Defense Systems, Commercial Products, MAUS V System Overview*, available at: <http://www.boeing.com/defense-space/support/maintenance/commercial/maus.html> (accessed 16 June 2009).
- Boeing (2008), *Boeing 787 Dreamliner Structure Test a Success (Rome, July 02)*, available at: [http://www.boeing.com/commercial/787family/news/2008/q3/080702b\\_nr.html](http://www.boeing.com/commercial/787family/news/2008/q3/080702b_nr.html) (accessed 16 June 2009).
- Boeing (2008), *Boeing Completes Destructive Testing on 787 Dreamliner Wing Box (Seattle, November 15)*, available at: [http://www.boeing.com/commercial/787family/news/2008/q4/081115a\\_nr.html](http://www.boeing.com/commercial/787family/news/2008/q4/081115a_nr.html) (accessed 16 June 2009).
- Boeing (2007), *Airplane Characteristics for Airport Planning, Revision A September 2007 (Preliminary)*, D6-58333, Boeing Commercial Airplanes, Seattle, Washington.
- Boeing (2007), *Final Assembly Begins on First Boeing 787 Dreamliner (Everett, May 21)*, available at: [http://www.boeing.com/commercial/787family/news/2007/q2/070521c\\_nr.html](http://www.boeing.com/commercial/787family/news/2007/q2/070521c_nr.html) (accessed 16 June 2009).
- Boeing (2005), *Boeing Completes First 7E7 Composite Fuselage Section (Seattle, January 11)*, available at: [http://www.boeing.com/commercial/787family/news/2005/q1/nr\\_050111g.html](http://www.boeing.com/commercial/787family/news/2005/q1/nr_050111g.html) (accessed 16 June 2009).
- Boeing (1988), *Advanced Composite Compression Tests, Boeing Specification Support Standard*, BSS 7260 Rev. C, The Boeing Company, Seattle, WA.
- Bopp (2006), *Metal Wire Cloth - Data Sheet/ Certificate for phosphor bronze mesh batch No.223118*, G. Bopp & Co. AG, Zürich, CH.

- Boulic. (Cranfield University), (2007), *Quantitative Morphology of Impact Damage to Composite Aircraft Structures* (unpublished report), Polytech'Orléans, France.
- Brombach, J., Hütte, T. and Strasser, H. (2006), "Surface-specific lighting scenarios enhancing the perceptibility of 3-dimensional flaws", *Occupational Ergonomics*, vol. 6, no. 2, pp. 75-83.
- Brookes, R. E. (2004), *Surface and sub-surface damage in plain weave carbon epoxy laminates due to low velocity impacts* (unpublished M.Sc. thesis), Cranfield University, United Kingdom.
- Brosius, D. (2007), "Boeing 787 Update", *High Performance Composites*, vol. 2007, no. May, pp. 56-59.
- Bruce, D. A. (1998), "NDT Reliability Estimation From Small Samples and In-Service Experience", *Papers presented at the RTO AVT Workshop on "Airframe Inspection Reliability under Field/ Depot Conditions"*, Brussels, Belgium, May 13-14 1998 and published in *RTO MP-10*, pp. 3-1.
- Bullock, M., Forsyth, D. and Fahr, A. (1994), *Statistical Functions and Computational Procedures for the POD Analysis of Hit/Miss NDI Data*, LTR-ST-1964, Institute for Aerospace Research, National Research Council Canada, Ottawa, Ontario.
- Bunsell, A. R. and Renard, J. (2005), *Fundamentals of fibre reinforced composite materials*, Institute of Physics Publishing, Bristol & Philadelphia.
- CAA (2005), *CAP 562: Civil Aircraft Airworthiness Information and Procedures, Issue 2, Amendment 1, 2005*, CAP 562, Civil Aviation Authority, Safety Regulation Group, United Kingdom.
- CAA (2003), *CAP 716: Aviation Maintenance Human Factors (EASA Part-145)*, CAP 716, Civil Aviation Authority, Safety Regulation Group, United Kingdom.
- Campbell, F. C. (2004), *Manufacturing processes for advanced composites*, Elsevier, New York.
- CMH-17 (2009), "Polymer Matrix Composites Forum", *CMH-17 Composites Materials Handbook, Coordination Meeting*, 4th March 2009, Salt Lake City, UT.
- Colquhoun, W. P. (1964), "Recent research in the psychology of inspection", *Journal of Textile Institute and Industry*, vol. 2, pp. 252-255.
- Composites World (2009), *New boat uses Zyvex carbon nanotube-enhanced prepreg*, 12th May 2009, available at: <http://www.compositesworld.com/news/new-boat-uses-zyvex-carbon-nanotube-enhanced-prepreg.aspx> (accessed 14/05/2009).
- Cuffaro, D. (2006), *Process, Materials and Measurements*, Rockport Publishers, Inc., Gloucester, Mass.
- Davies, G. A. O., Zhang, X. and Edlund, A. (1994), "Predicting damage in composite aircraft structures due to low velocity impact", *Aerotech 1994, Structures & Materials Seminar*, January 1994, Birmingham, UK.



- Davies, G. A. O. and Zhang, X. (1995), "Impact damage prediction in carbon composite structures", *International Journal of Impact Engineering*, vol. 16, no. 1, pp. 149-170.
- de Boer, J. B. (1977), "Performance and comfort in the presence of veiling reflections", *Lighting Research and Technology*, vol. 9, no. 4, pp. 169-176.
- Dekoker, N. and Frier, J. P. (1969), "Visibility of specular and semispecular tasks in sheet metal surfaces", *Illuminating Engineering*, vol. 64, pp. 167-175.
- Degussa (2006), *Plexiglas GS Product Description November 2006*, Degussa Methacrylates, Röhm GmbH, Darmstadt, Germany.
- DIN (1996), *Aerospace series - Fibre reinforced plastics - Test method; determination of the compression strength after impact*, DIN EN 6038, Deutsches Institut für Normung e. V., Berlin, Germany.
- Donckels, Y., Matthews, F. L. and Foreman, A. D. (2000), "Impact dent depth relaxation in polymer matrix composites", *ECCM9, Composites from Fundamentals to Exploitation*, 4-7 June 2000, Brighton, UK.
- Drury, C. G. (2000), "Human factors and quality: Integration and new directions", *Human Factors and Ergonomics in Manufacturing*, vol. 10, no. 1, pp. 45-59.
- Drury, C. G. (1993), "Exploring search strategies in aircraft inspection", *Visual Search*, vol. 2, pp. 101-112.
- Drury, C. G. (1989), "The Information Environment in Inspection", *Second FAA Meeting on Human Factors Issues in Aircraft Maintenance and Inspection, 13-14 December 1989*, Alexandria, Virginia.
- Drury, C. G. and Lock, M. W. B. (1995), "Reliability in Aircraft Inspection: UK and USA Perspectives", *DOT/FAA/AM-95/14 Human Factors in Aviation Maintenance - Phase 4, Progress Report (DTIC: ADA294756)*, pp. 147-161.
- Drury, C. G., Maheswar, G., Das, A. and Helander, M. G. (2001), "Improving visual inspection using binocular rivalry", *International Journal of Production Research*, vol. 39, no. 10, pp. 2143-2153.
- dti (2006), *Hybridmat 3: Advances in the Manufacture of Advanced Structural Composites in Aerospace : a Mission to the USA (Global Watch Mission report)*, Department of Trade and Industry, UK.
- Dupont, G. (1997), "The Dirty Dozen Errors in Maintenance", *Human Factors Issues in Aviation Maintenance and Inspection*, March 12-13, San Diego, CA, FAA.
- EASA (2008), *Certification Specifications for Large Aeroplanes, Amendment 5, September 2008*, CS-25, European Aviation Safety Agency, Koeln, Germany.
- Erhart, D., Ostrom, L. T. and Wilhelmsen, C. A. (2004), "Visual Detectability of Dents on a Composite Aircraft Inspection Specimen: An Initial Study", *International Journal of Applied Aviation Studies*, vol. 4, no. 2, pp. 111-122.

- FAA (1984), *Advisory Circular 20-107A Composite Aircraft Structure*, AC20-107A, U.S. Department of Transportation, Federal Aviation Administration.
- Fahr, A., Forsyth, D. and Bullock, M. (1993), *A comparison of Probability Of Detection (POD) data determined using different statistical methods*, LTR-ST-1947, Institute for Aerospace Research, National Research Council Canada, Ottawa, Ontario.
- Faulkner, T. W. and Murphy, T. J. (1973), "Lighting for difficult visual tasks", *Human factors*, vol. 15, no. 2, pp. 149-162.
- Forsyth, D. S. and Fahr, A. (1998), "An Evaluation of Probability of Detection Statistics", *Papers presented at the RTO AVT Workshop on "Airframe Inspection Reliability under Field/ Depot Conditions"*, Brussels, Belgium, May 13-14 1998 and published in *RTO MP-10*, pp. 10-1.
- Forsyth, D. S., Gould, R. W. and Komorowski, J. P. (1998), "Double pass retroreflection versus visual inspection of impact damage in composites", *Papers presented at the RTO AVT Workshop on "Airframe Inspection Reliability under Field/ Depot Conditions"*, Brussels, Belgium, May 13-14 1998 and published in *RTO MP-10*, pp. 18-1.
- Fualdes, C. (2006), "Composites at Airbus, Damage Tolerance Methodology", FAA Workshop for Composite Damage Tolerance and Maintenance, July 19 - 21, 2006, Chicago, IL.
- Gallwey, T. J. and Drury, C. G. (1986), "Task complexity in visual inspection", *Human factors*, vol. 28, no. 5, pp. 595-606.
- Gant, S. K. (2007), "Visual Assessment of Impact Damage on Painted Composite Aircraft Structures", *International SAMPE symposium and exhibition proceedings*, June 3-7, Baltimore, MD.
- Gao, S. and Kim, J. (1999), "Scanning acoustic microscopy as a tool for quantitative characterisation of damage in CFRPs", *Composites Science and Technology*, vol. 59, no. 3, pp. 345-354.
- Gardiner, G. (2006), "Lightning Strike Protection for Composite Structures", *High Performance Composites July 2006*, [Online], pp. 11/05/09 available at: <http://www.compositesworld.com/articles/lightning-strike-protection-for-composite-structures.aspx>.
- Georgiou, G. A. (2007), "PoD Curves, their derivation, applications and limitations", *INSIGHT - Non-Destructive Testing and Condition Monitoring*, vol. 49, no. 7, pp. 409-414.
- Georgiou, G. A. (2006), *Probability of Detection (PoD) curves - Derivation, applications and limitations*, Research Report 454, Health and Safety Executive, UK.
- Gibson, J. J. (1979), *The ecological approach to visual perception*, Houghton Mifflin, Dallas ; London.
- Gibson, J. J. (1950b), "The perception of visual surfaces", *American Journal of Psychology*, vol. 63, no. 3, pp. 367-384.

- Gibson, J. J. (1950a), *The Perception of the Visual World*, Riverside Press, Cambridge, Mass.
- Gramopadhye, A. K., Bhagwat, S., Kimbler, D. and Greenstein, J. (1998), "The use of advanced technology for visual inspection training", *Applied Ergonomics*, vol. 29, no. 5, pp. 361-375.
- Gramopadhye, A. K., Drury, C. G. and Prabhu, P. V. (1997), "Training strategies for visual inspection", *Human Factors and Ergonomics in Manufacturing*, vol. 7, no. 3, pp. 171-196.
- Gros, X. E., de Smet, M. A. and Takahashi, K. (1998), "On the efficiency of current NDT methods for impact damage detection and quantification in thermoplastic toughened CFRP materials", *International Conference on Advanced Composites (ICAC 98)*, 15-18 Dec. 1998, Hurgada, Egypt, Auburn University, Auburn, AL.
- Guseva, O., Brunner, S. and Richner, P. (2003), "Service life prediction for aircraft coatings", *Polymer Degradation and Stability*, vol. 82, no. 1, pp. 1-13.
- Hagemaijer, D. (1998), "Factors Influencing Eddy Current PoD in the Field Environment", *Papers presented at the RTO AVT Workshop on "Airframe Inspection Reliability under Field/ Depot Conditions"*, Brussels, Belgium, May 13-14 1998 and published in *RTO MP-10*, pp. 2-1.
- Halpin, J. C. (1994), "The evolution of design and material criteria for polymeric structural materials", *Composite Structures*, vol. 27, no. 1-2, pp. 3-6.
- Harris, B. (ed.) (2003), *Fatigue in composites: science and technology of the fatigue response of fibre-reinforced plastics*, CRC Press, Boca Raton, Florida.
- Harris, C. E. and Shuart, M. J. (2001), *An Assessment of the State-of-the-Art in the Design and Manufacturing of Large Composite Structures for Aerospace Vehicles*, NASA Langley Research Center, USA.
- Hexcel (2003), *HexPly8552 Product Data, Publication FTA 072a, May 2003*, Hexcel Composites, Cambridge, UK.
- Hounslow, L. E. (2000), *The influence of Z-pinning on low velocity impact performance of laminated carbon composites* (unpublished M.Sc. thesis), Cranfield University, United Kingdom.
- Hovey, P. W., Sproat, W. H. and Schattle, P. (1989), "The Test Plan for the Next Air Force NDI Capability and Reliability Assessment Program", in Thompson, D. O. and Chimenti, D. E. (eds.) *Review of Quantitative Nondestructive Evaluation*, Vol. 8B ed, Plenum Press, pp. 2213-2220.
- Hu, N., Zemba, Y., Okabe, T., Yan, C., Fukunaga, H. and Elmarakbi, A. M. (2008), "A new cohesive model for simulating delamination propagation in composite laminates under transverse loads", *Mechanics of Materials*, vol. 40, no. 11, pp. 920-935.
- Ilciewicz, L. (2009), "FAA Composite Safety & Certification Initiatives", *CMH-17 Composite Materials Handbook PMC Coordination Meeting*, 2-5 March 2009, Salt Lake City, Utah.

- Imielinska, K., Castaings, M., Wojtyra, R., Haras, J., Le Clezio, E. and Hosten, B. (2004), "Air-coupled ultrasonic C-scan technique in impact response testing of carbon fibre and hybrid: glass, carbon and Kevlar/epoxy composites", *Journal of Materials Processing Technology*, vol. 157-158, pp. 513-522.
- Ishibashi, S., (2006), *Use of Toray carbon fibre products in aerospace applications; Telephone communication with S Ishibashi, Technical Manager of SOFICAR (Toray/Arkema), January 2006*, Soficar, France.
- Kalpajian, S. (1995), *Manufacturing Engineering and Technology*, 3rd ed, Addison-Wesley, Reading, Mass.; Wokingham.
- Kim, H. (2007), "Blunt Impact Formation on Composite Aircraft Structures", *Commercial Aircraft Composite Repair Committee (CACRC) Meeting*, 12-16 November 2007, Wichita, Kansas.
- Kingdom, F. A. A. (2008), "Perceiving light versus material", *Vision research*, vol. 48, no. 20, pp. 2090-2105.
- Kolesnikov, B. and Herbeck, L. (2004), "Carbon Fiber Composite Airplane Fuselage: Concept and Analysis", *Merging the Efforts: Russia in European Research Programs on Aeronautics*, 11-12 May 2004, Berlin, Germany, German Aerospace Center (DLR) <http://elib.dlr.de/49781>.
- Komorowski, J. K., Gould, R. W. and Marincak, A. (1993), "Study of the effect of time and load on impact visibility", *2nd Canadian International Composites Conference and Exhibition (CANCOM 93)*, September 1993, Ottawa, Ontario, Canada, Canadian Association for Composite Structures and Materials, Montréal, pp. 441-446.
- Krutop, B. N. E. (2007), *Effect of impact damage and subsequent fatigue damage development in carbon-fibre polymer composites for aircraft* (unpublished M.Sc. thesis), Cranfield University, United Kingdom.
- Latorella, K. A., Gramopadhye, A. K., Prabhu, P. V., Drury, C. G., Smith, M. A. and Shanahan, D. E. (1992), "Computer-simulated aircraft inspection tasks for off-line experimentation", *Proceedings of the Human Factors Society 36th Annual Meeting. Part 2 (f 2)*, Vol. 1, 12 October 1992 through 16 October 1992, Atlanta, GA, USA, Publ by Human Factors Soc Inc, Santa Monica, CA, United States, pp. 92.
- Lewis, W. H., Sproat, W. H., Dodd, B. D. and Hamilton, J. M. (1978), *Reliability of Nondestructive Inspections, Final Report, SA-ALC/MME 76-6-38-1*, Lockheed-Georgia Company, Marietta, GA.
- Lippincott, H. W. and Stark, H. (1982), "Optical-digital detection of dents and scratches on specular metal surfaces.", *Applied Optics*, vol. 21, no. 16, pp. 2875-2881.
- Lloyd, C. J. (1998), "Towards the Development of More Effective Surface Inspection Methods", *Automotive Finishing '98*, June 9-11, 1998, Detroit, Michigan, Society of Manufacturing Engineers, Dearborn, MI.
- Lloyd, C. and He, Y. (1998), "An Objective Measure of Severity for Small Topographical Defects in Automotive Paint (SAE 982316)", *International Body Engineering Conference & Exposition September 1998*, Detroit, Michigan, USA.

- Lock, M. W. B. (1998), "The Effect of Aircraft Maintenance on Human Factors", *Papers presented at the RTO AVT Workshop on "Airframe Inspection Reliability under Field/ Depot Conditions"*, Brussels, Belgium, May 13-14 1998 and published in RTO MP-10, pp. 14-1.
- Lopes, C. S., Seresta, O., Coquet, Y., Gürdal, Z., Camanho, P. P. and Thuis, B. (2009), "Low-velocity impact damage on dispersed stacking sequence laminates. Part I: Experiments", *Composites Science and Technology*, vol. 69, no. 7-8, pp. 926-936.
- Mallet, L., Lee, B. C., Staszewski, W. J. and Scarpa, F. (2004), "Structural health monitoring using scanning laser vibrometry: II. Lamb waves for damage detection", *Smart Materials and Structures*, vol. 13, no. 2, pp. 261-269.
- Matthews, F. L. and Rawlings, R. D. (1994), *Composite materials : engineering and science*, Chapman and Hall, London.
- Megaw, E. D. (1979), "Factors affecting visual inspection accuracy", *Applied Ergonomics*, vol. 10, no. 1, pp. 27-32.
- Megaw, E. D. and Richardson, J. (1979), "Eye movements and industrial inspection", *Applied Ergonomics*, vol. 10, no. 3, pp. 145-154.
- Mills, A. (2006), "Developments in Resin Infusion Materials and Processes; Structural Unitisation and Component Integration Techniques", in *Hybridmat 3: Advances in the Manufacture of Advanced Structural Composites in Aerospace*, Department of Trade and Industry, London, UK, pp. 18-20.
- Mitrevski, T., Marshall, I. H. and Thomson, R. (2006), "The influence of impactor shape on the damage to composite laminates", *Composite Structures*, vol. 76, no. 1-2, pp. 116-122.
- Mitrevski, T., Marshall, I. H., Thomson, R. S. and Jones, R. (2006), "Low-velocity impacts on preloaded GFRP specimens with various impactor shapes", *Composite Structures*, vol. 76, no. 3, pp. 209-217.
- Mitrovic, M., Hahn, H. T., Carman, G. P. and Shyprykevich, P. (1999), "Effect of loading parameters on the fatigue behavior of impact damaged composite laminates", *Composites Science and Technology*, vol. 59, no. 14, pp. 2059-2078.
- Mullis, R. T. (1998), "C-141 Spanwise Splice Advanced NDI Method (Probability of Detection Experiment Results)", *Papers presented at the RTO AVT Workshop on "Airframe Inspection Reliability under Field/ Depot Conditions"*, Brussels, Belgium, May 13-14 1998 and published in RTO MP-10, pp. 19-1.
- Murgatroyd, R. A., Worrall, G. M., Waites, C., AEA Technology and Civil Aviation Authority (1995), *A study of the human factors influencing the reliability of aircraft inspection*, Civil Aviation Authority, London.
- Norman, J. F., Todd, J. T., Norman, H. F., Clayton, A. M. and McBride, T. R. (2006), "Visual discrimination of local surface structure: Slant, tilt, and curvedness", *Vision research*, vol. 46, no. 6-7, pp. 1057-1069.

- Norman, J. F., Todd, J. T. and Orban, G. A. (2004), "Perception of three-dimensional shape from specular highlights, deformations of shading, and other types of visual information", *Psychological Science*, vol. 15, no. 8, pp. 565-570.
- Norman, J. F., Todd, J. T. and Phillips, F. (1995), "The perception of surface orientation from multiple sources of optical information.", *Perception and Psychophysics*, vol. 57, no. 5, pp. 629-636.
- Papanicolaou, G. C. and Stavropoulos, C. D. (1995), "New approach for residual compressive strength prediction of impacted CFRP laminates", *Composites*, vol. 26, no. 7, pp. 517-523.
- PRC-DeSoto (2003), *Desothane HS polyurethane topcoats/ CA8000 Series, Technical Data, July 2003*, PRC-DeSoto International, Glendale, California.
- Psymouli, A., Harris, D. and Irving, P. (2005), "The Inspection of Composite Aircraft Structures: A Signal Detection Approach", *Human Factors and Aerospace Safety*, vol. 5, no. 2, pp. 91-108.
- RAF, (2006), *Personal communication - Visit/ discussions with Repair Management Team, Royal Air Force (RAF) Cottesmore, Oakham, Rutland, 2nd May 2006*.
- Raju, I. S. (2006), "NASA Langley Damage Tolerance Experiences", *FAA Symposium on Composite Damage Tolerance and Maintenance*, July 19-21 2006, Chicago.
- Roach, D. (2007), "Improving In-Service Inspection of Composite Structures", *Commercial Aircraft Composite Repair Committee (CACRC) Meeting*, 12-16 November 2007, Wichita, Kansas.
- Robinson, P. and Davies, G. A. O. (1992), "Impactor mass and specimen geometry effects in low velocity impact of laminated composites", *International Journal of Impact Engineering*, vol. 12, no. 2, pp. 189-207.
- Robois, S. (2005), "Composites at Airbus, In-Service Experience", *Composites and metallics in partnership: In service experience, Proceedings of one-day conference, 12th October 2005*, Royal Aeronautical Society, London, UK.
- Rouchon, J. (1990), "Certification of Large Aircraft Composite Structures, Recent Progress and New Trends in Compliance Philosophy", *17th International Council of the Aeronautical Sciences (ICAS)*, Stockholm, Sweden.
- Rouchon, J. (2009), "Fatigue and Damage Tolerance Evaluation of Structures: The Composite Materials Response, 22nd Plantema Memorial Lecture", *25th Symposium, International Committee on Aeronautical Fatigue (ICAF)*, 27 May 2009, Rotterdam, Netherlands, National Aerospace Laboratory NLR, Amsterdam, Netherlands.
- Rouchon, J. (2010) *personal communication at Cranfield University on 12<sup>th</sup> January 2010*.
- RTO (1998), *Airframe Inspection Reliability under Field/Depot Conditions*, RTO MP-10, Research and Technology Organization, North Atlantic Treaty Organization, F-92201 Neuilly-sur-Seine Cedex, France.

- Rummel, W. D. (1984), "Human factors considerations in the assessment of nondestructive evaluation (NDE) reliability", *Review of progress in quantitative nondestructive evaluation, Proceedings of the Tenth Annual Review*, Vol. 3A, 7-12 Aug. 1983, Santa Cruz, CA, Plenum Press, New York, pp. 44.
- Rummel, W. D. and Matzkanin, G. A. (1997), *Nondestructive Evaluation (NDE) Capabilities Databook, Third Edition*, NTIAC: DB-97-02, Nondestructive Testing Information Analysis Center (NTIAC), TRI/Austin, Inc., 415 Crystal Creek Drive, Austin, TX 78746-4725.
- Sadasivan, S., Vembar, D., Washburn, C. and Gramopadhye, A. K. (2007), "Evaluation of interaction devices for projector based virtual reality aircraft inspection training environments", *2nd International Conference on Virtual Reality, ICVR 2007*, Vol. 4563 LNCS, 22 July 2007 through 27 July 2007, Beijing, pp. 533.
- Sakata, H., Tsutsui, K. and Taira, M. (2003), "Representation of the 3D world in art and in the brain", *International Congress Series*, vol. 1250, pp. 15-35.
- Schoeppner, G. A. and Abrate, S. (2000), "Delamination threshold loads for low velocity impact on composite laminates", *Composites Part A: Applied Science and Manufacturing*, vol. 31, no. 9, pp. 903-915.
- Shyr, T. and Pan, Y. (2003), "Impact resistance and damage characteristics of composite laminates", *Composite Structures*, vol. 62, no. 2, pp. 193-203.
- Singh, R. (2000), *Three Decades of NDI Reliability Assessment*, Karta-3510-99-01, Karta Technologies Inc., San Antonio, TX, USA.
- Sohn, M. S., Hu, X. Z., Kim, J. K. and Walker, L. (2000), "Impact damage characterisation of carbon fibre/epoxy composites with multi-layer reinforcement", *Composites Part B: Engineering*, vol. 31, no. 8, pp. 681-691.
- SolidWorks (2000), *Solid Works 2000 Computer Aided Design software*, Solid Works Corporation.
- Spencer, F. W. (1998), *Identifying Sources of Variation for Reliability Analysis of Field Inspections*. SAND-98-0980C CONF-980552, US Department of Defense, Washington, DC.
- Spencer, F. W. (1996a), "Visual inspection reliability of transport aircraft", *Proceedings of SPIE - The International Society for Optical Engineering*, vol. 2945, pp. 160-171.
- Spencer, F. W. (1996b), *Visual Inspection Research Project Report on Benchmark Inspections (Final Report)*, AD-A321199; DOT/FAA/AR-96/65; NIPS-97-17825.
- Spencer, F. W., Borgonovi, G., Roach, D., Schurman, D. L., SMITH, R. O. N. and Sandia National Labs., Albuquerque, NM. (1993), *Reliability assessment at airline inspection facilities. Volume 1: A generic protocol for inspection reliability experiments (Final Report)*, DOT/FAA/CT-92/12-VOL-1.
- Staszewski, W. J. (2009), "Silence of the lamb-wave", *Aerospace Testing International March 2009*, pp. 76-77.

- Staszewski, W. J., Boller, C. and Tomlinson, G. R. (eds.) (2004), *Health Monitoring of Aerospace Structures - Smart Sensor Technologies and Signal Processing*, John Wiley & Sons, Ltd, Chichester, UK.
- Statsoft Inc. (2008) *Statistica 8.0 statistical analysis computer software*, Statsoft Inc, Tulsa, OK.
- Todd, J. T. (2004), "The visual perception of 3D shape", *Trends in cognitive sciences*, vol. 8, no. 3, pp. 115-121.
- Todd, J. T., Koenderink, J. J., Van Doorn, A. J. and Kappers, A. M. (1996), "Effects of Changing Viewing Conditions on the Perceived Structure of Smoothly Curved Surfaces", *Journal of Experimental Psychology: Human Perception and Performance*, vol. 22, no. 3, pp. 695-706.
- Toray (2001), *3631/ T800H Technical Data Sheet May 2001*, Toray Composites America, Inc., USA.
- Transport Canada (2004), *Advisory Circular 500-009 Composite Aircraft Structure*, 5009-6-500, Transport Canada.
- Tsutsui, K., Taira, M. and Sakata, H. (2005), "Neural mechanisms of three-dimensional vision", *Neuroscience research*, vol. 51, no. 3, pp. 221-229.
- US DoD (2007), *Nondestructive Evaluation System Reliability Assessment, United States Department of Defense Handbook, Latest Revision*, MIL-HDBK-1823, United States Department of Defence, Wright-Patterson AFB, OH.
- US DoD (2002), *Composite Materials Handbook, Volume 1. Polymer Matrix Composites, Guidelines for Characterisation of Structural Materials*, MIL-HDBK-17-1F, United States Department of Defence.
- US DoD (2002), *Composite Materials Handbook, Volume 3. Polymer Matrix Composites, Materials Usage, Design & Analysis*, MIL-HDBK-17-3F, United States Department of Defence.
- Volker, A. W. F., Dijkstra, F. H., Terpstra, S., Heerings, H. A. M. and Lont, M. A. (2004), "Modeling of NDE Reliability: Development of a POD-Generator", *16th World Conference on Nondestructive Testing*, Vol. Vol. 9, No. 11, Aug 30 - Sep 3 2004, Montreal, Canada, Canadian Institute for NDE, Hamilton, Ontario.
- Vora, J., Nair, S., Gramopadhye, A. K., Duchowski, A. T., Melloy, B. J. and Kanki, B. (2002), "Using virtual reality technology for aircraft visual inspection training: Presence and comparison studies", *Applied Ergonomics*, vol. 33, no. 6, pp. 559-570.
- Waite, S. (2009), "EASA Perspectives on Safe Composite Damage Tolerance and Maintenance Practices", *Commercial Aircraft Composite Repair Committee (CACRC) Meeting and Workshop for Composite Damage Tolerance & Maintenance*, 1-5 June 2009, Tokyo, Japan.
- Webborn, C. (2006), "Lower Cost Manufacturing in Composites", in *Hybridmat 3: Advances in the Manufacture of Advanced Structural Composites in Aerospace*, Department of Trade and Industry, London, UK, pp. 33-38.



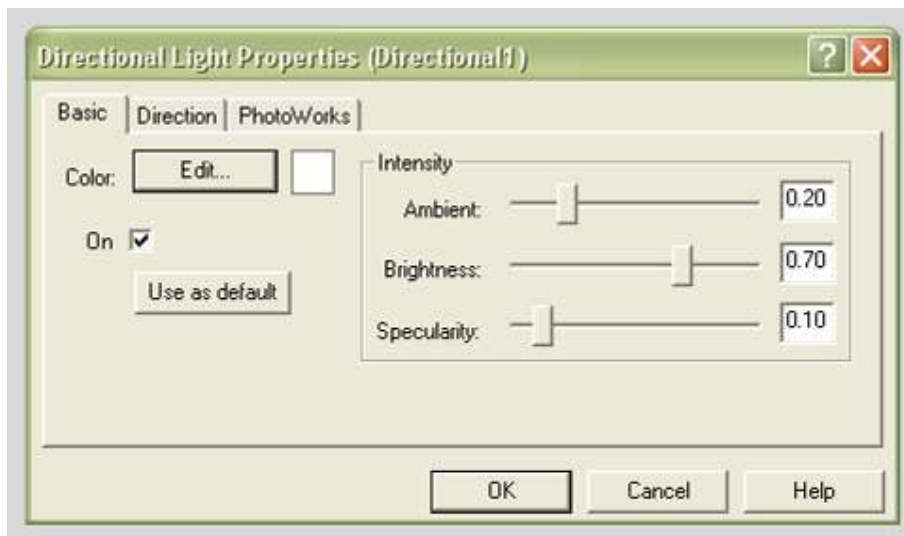
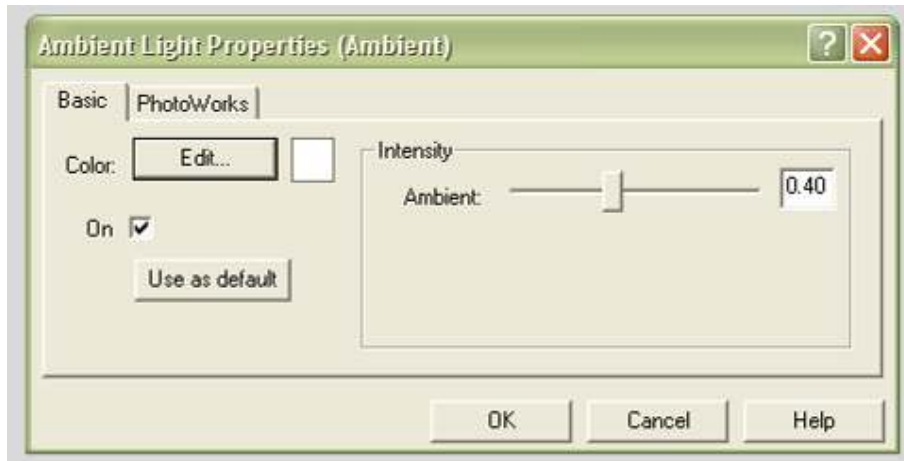
- Welch, J. M. (2007), "Repair, Design, Test and Process Considerations for Lightning Strikes", *CACRC/ MIL-HDBK-17 Conference*, May 7-11, 2007, Amsterdam, Netherlands.
- Wexler, M. and Van Boxtel, J. J. A. (2005), "Depth perception by the active observer", *Trends in cognitive sciences*, vol. 9, no. 9, pp. 431-438.
- Wickens, C.D. (2000), *Engineering psychology and human performance*, 3<sup>rd</sup> Ed, Prentice-Hall, New York.
- Xiao, B. and Brainard, D. H. (2008), "Surface gloss and color perception of 3D objects", *Visual neuroscience*, vol. 25, no. 3, pp. 371-385.
- Xiao, B. and Brainard, D. H. (2006), "Color perception of 3D objects: Constancy with respect to variation of surface gloss", pp. 63.

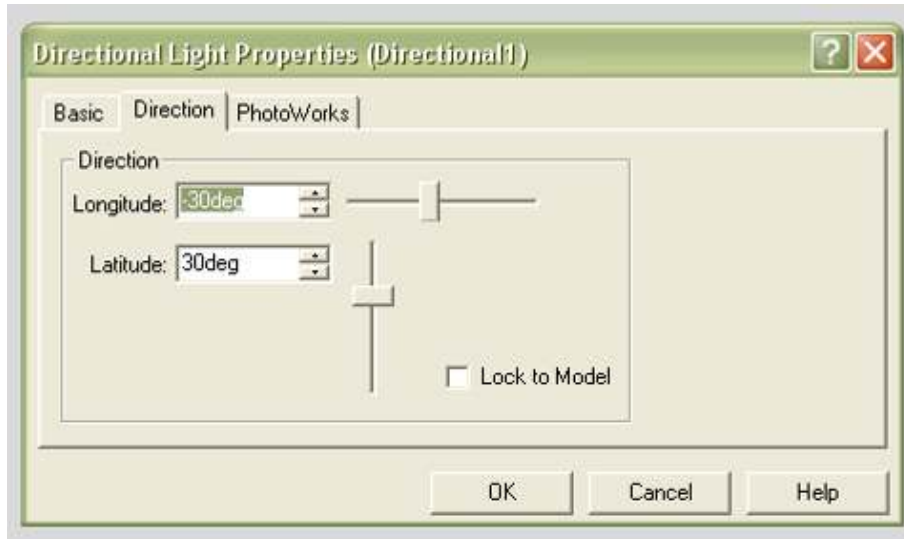
## *Appendix A*

### *CAD system rendering settings for virtual specimens*

#### *Lighting settings*

The following settings were used to define the ambient and directional light parameters for the virtual specimens in SolidWorks 2000.





***Materials settings***

The following materials editor settings were used for the PhotoWorks rendering application in the SolidWorks 2000 CAD Program to produce the virtual specimens:

Primary colour settings for material editor			
Hue:	160	Red:	242
Saturation:	0	Green:	242
Luminosity:	228	Blue:	242

Reflectance settings for material editor	
Ambient	1
Diffuse	1
Specular	0.8
Transparency	0
Specular Colour	Hue: 160, Sat: 0, Lum: 240 Red: 255, Green: 255, Blue: 255

## Appendix B

### Specimen & Flaw specifications for series 1 visual inspection trials

#### Trial 1 specimen/ flaw characteristics

Panel Number/ Flaw Details	Panel Number/ Flaw Details	Panel Number/ Flaw Details	Panel Number/ Flaw Details
1 UNFLAWED	31 UNFLAWED	61 UNFLAWED	91 UNFLAWED
2 UNFLAWED	32 Ø22 X = 527mm, Y = 524mm	62 UNFLAWED	92 UNFLAWED
3 UNFLAWED	33 Ø9 X = 671mm, Y = 385mm	63 UNFLAWED	93 UNFLAWED
4 UNFLAWED	34 UNFLAWED	64 UNFLAWED	94 UNFLAWED
5 UNFLAWED	35 Ø14 X = 659mm, Y = 550mm	65 Ø5 X = 540mm, Y = 240mm	95 UNFLAWED
6 UNFLAWED	36 Ø28 X = 186mm, Y = 259mm	66 UNFLAWED	96 UNFLAWED
7 UNFLAWED	37 UNFLAWED	67 X = 437mm, Y = 561mm Ø27	97 Ø8 X = 321mm, Y = 254mm
8 UNFLAWED	38 Ø18mm X = 368mm, Y = 360mm	68 UNFLAWED	98 UNFLAWED
9 UNFLAWED	39 UNFLAWED	69 UNFLAWED	99 Ø4 X = 315mm, Y = 134mm
10 Ø26mm X = 649mm, Y = 85mm	40 Ø30 X = 74mm, Y = 315mm	70 UNFLAWED	100 UNFLAWED
11 Ø8mm X = 142mm, Y = 533mm	41 UNFLAWED	71 UNFLAWED	101 UNFLAWED
12 UNFLAWED	42 UNFLAWED	72 UNFLAWED	102 UNFLAWED
13 UNFLAWED	43 UNFLAWED	73 Ø20 X = 677mm, Y = 698mm	103 UNFLAWED
14 UNFLAWED	44 UNFLAWED	74 UNFLAWED	104 UNFLAWED
15 UNFLAWED	45 UNFLAWED	75 Ø16 X = 578mm, Y = 526mm	105 UNFLAWED
16 UNFLAWED	46 UNFLAWED	76 Ø23 X = 640mm, Y = 374mm	106 UNFLAWED
17 UNFLAWED	47 UNFLAWED	77 Ø17 X = 5mm, Y = 392mm	107 Ø12 X = 339mm, Y = 454mm
18 UNFLAWED	48 Ø19 X = 370mm, Y = 341mm	78 UNFLAWED	108 Ø13 X = 580mm, Y = 425mm
19 UNFLAWED	49 UNFLAWED	79 UNFLAWED	109 UNFLAWED
20 UNFLAWED	50 UNFLAWED	80 UNFLAWED	110 Ø10 X = 703mm, Y = 94mm
21 UNFLAWED	51 Ø29 X = 305mm, Y = 665mm	81 UNFLAWED	111 Ø25 X = 120mm, Y = 664mm
22 UNFLAWED	52 UNFLAWED	82 UNFLAWED	112 UNFLAWED
23 Ø21 X = 165mm, Y = 233mm	53 UNFLAWED	83 Ø7 X = 361mm, Y = 631mm	113 UNFLAWED
24 UNFLAWED	54 Ø3 X = 535mm, Y = 100mm	84 Ø2 X = 567mm, Y = 412mm	114 UNFLAWED
25 UNFLAWED	55 UNFLAWED	85 UNFLAWED	115 UNFLAWED
26 UNFLAWED	56 UNFLAWED	86 UNFLAWED	116 UNFLAWED
27 Ø24 X = 547mm, Y = 537mm	57 UNFLAWED	87 Ø1 X = 210mm, Y = 456mm	117 UNFLAWED
28 UNFLAWED	58 UNFLAWED	88 Ø15 X = 645mm, Y = 529mm	118 UNFLAWED
29 UNFLAWED	59 UNFLAWED	89 UNFLAWED	119 UNFLAWED
30 Ø11 X = 375mm, Y = 486mm	60 UNFLAWED	90 UNFLAWED	120 UNFLAWED

### Trial 2 Specimen/ flaw characteristics

Panel Numbers & Flaw sizes:		Ø## = Flaw Width			#.## d = Flaw Depth										
1	Unflaw ed	21	Ø12mm 0.2mm d	41	Unflaw ed	61	Unflaw ed	81	Unflaw ed	101	Unflaw ed	121	Unflaw ed	141	Ø12mm 0.9mm d
2	Unflaw ed	22	Unflaw ed	42	Unflaw ed	62	Unflaw ed	82	Ø4.5mm 1.5mm d	102	Unflaw ed	122	Unflaw ed	142	Ø4.5mm 0.1mm d
3	Unflaw ed	23	Unflaw ed	43	Unflaw ed	63	Unflaw ed	83	Unflaw ed	103	Ø12mm 0.4mm d	123	Unflaw ed	143	Unflaw ed
4	Ø6.5mm 0.4mm d	24	Unflaw ed	44	Ø6.5mm 0.3mm d	64	Unflaw ed	84	Unflaw ed	104	Ø4.5mm 1.2mm d	124	Unflaw ed	144	Unflaw ed
5	Unflaw ed	25	Unflaw ed	45	Unflaw ed	65	Unflaw ed	85	Unflaw ed	105	Ø4.5mm 0.2mm d	125	Ø4.5mm 0.4mm d	145	Ø6.5mm 0.5mm d
6	Unflaw ed	26	Unflaw ed	46	Unflaw ed	66	Unflaw ed	86	Unflaw ed	106	Ø4.5mm 0.6mm d	126	Unflaw ed	146	Unflaw ed
7	Unflaw ed	27	Ø4.5mm 0.3mm d	47	Unflaw ed	67	Unflaw ed	87	Unflaw ed	107	Unflaw ed	127	Ø12mm 0.8mm d	147	Unflaw ed
8	Unflaw ed	28	Unflaw ed	48	Unflaw ed	68	Unflaw ed	88	Ø12mm 0.7mm d	108	Unflaw ed	128	Ø4.5mm 0.5mm d	148	Unflaw ed
9	Unflaw ed	29	Unflaw ed	49	Unflaw ed	69	Ø4.5mm 1.1mm d	89	Unflaw ed	109	Unflaw ed	129	Unflaw ed	149	Ø4.5mm 1.0mm d
10	Unflaw ed	30	Unflaw ed	50	Unflaw ed	70	Unflaw ed	90	Unflaw ed	110	Unflaw ed	130	Unflaw ed	150	Unflaw ed
11	Unflaw ed	31	Unflaw ed	51	Unflaw ed	71	Unflaw ed	91	Ø4.5mm 0.8mm d	111	Unflaw ed	131	Unflaw ed	151	Unflaw ed
12	Unflaw ed	32	Ø12mm 1.0mm d	52	Ø6.5mm 1.2mm d	72	Unflaw ed	92	Ø6.5mm 1.3mm d	112	Unflaw ed	132	Unflaw ed	152	Unflaw ed
13	Ø6.5mm 0.2mm d	33	Unflaw ed	53	Unflaw ed	73	Unflaw ed	93	Unflaw ed	113	Unflaw ed	133	Unflaw ed	153	Unflaw ed
14	Unflaw ed	34	Unflaw ed	54	Ø12mm 0.1mm d	74	Ø6.5mm 1.1mm d	94	Unflaw ed	114	Unflaw ed	134	Unflaw ed	154	Ø6.5mm 0.7mm d
15	Unflaw ed	35	Ø4.5mm 1.3mm d	55	Ø6.5mm 0.9mm d	75	Unflaw ed	95	Unflaw ed	115	Unflaw ed	135	Ø6.5mm 0.6mm d	155	Unflaw ed
16	Unflaw ed	36	Unflaw ed	56	Ø12mm 0.3mm d	76	Unflaw ed	96	Unflaw ed	116	Unflaw ed	136	Ø4.5mm 0.7mm d	156	Unflaw ed
17	Unflaw ed	37	Unflaw ed	57	Unflaw ed	77	Unflaw ed	97	Unflaw ed	117	Unflaw ed	137	Ø4.5mm 1.4mm d		
18	Unflaw ed	38	Unflaw ed	58	Ø6.5mm 0.1mm d	78	Unflaw ed	98	Unflaw ed	118	Ø12mm 1.1mm d	138	Unflaw ed		
19	Unflaw ed	39	Unflaw ed	59	Ø12mm 0.5mm d	79	Unflaw ed	99	Unflaw ed	119	Ø6.5mm 0.8mm d	139	Unflaw ed		
20	Ø12mm 0.6mm d	40	Unflaw ed	60	Ø4.5mm 0.9mm d	80	Ø6.5mm 1.0mm d	100	Unflaw ed	120	Unflaw ed	140	Unflaw ed		

X/Y Panel location coordinates; All in mm				
Flaw Width	Flaw Depth	X Coordinate	Y Coordinate	Internal Flaw Radius
Ø4.5mm	0.1	38	93	25.363
	0.2	686	294	12.756
	0.3	152	469	8.588
	0.4	13	4	6.528
	0.5	677	502	5.313
	0.6	64	428	4.519
	0.7	303	426	3.996
	0.8	600	226	3.564
	0.9	8	548	3.263
	1	104	616	3.031
	1.1	436	394	2.851
	1.2	693	94	2.709
	1.3	161	123	2.597
	1.4	299	477	2.508
	1.5	33	492	2.438
Ø6.5mm	0.1	619	302	52.863
	0.2	26	439	26.506
	0.3	485	305	17.754
	0.4	607	624	13.403
	0.5	91	3	10.813
	0.6	674	602	9.102
	0.7	362	604	7.895
	0.8	253	645	7.002
	0.9	29	643	6.318
	1	289	274	5.781
	1.1	43	381	5.351
	1.2	699	79	5.001
	1.3	277	455	4.713
Ø12mm	0.1	703	547	180.05
	0.2	472	262	90.1
	0.3	654	397	60.15
	0.4	147	142	45.2
	0.5	240	644	36.25
	0.6	10	325	30.3
	0.7	60	387	26.064
	0.8	356	333	22.9
	0.9	174	681	20.45
	1	281	286	18.5
	1.1	432	381	16.914

### Trial 3 specimen/ flaw characteristics

Panel Numbers & Flaw sizes:		Ø## = Flaw Width		#.## d = Flaw Depth											
1	Unflaw ed	21	Unflaw ed	41	Unflaw ed	61	Unflaw ed	81	Ø4.5mm 0.4mm d	101	Unflaw ed	121	Unflaw ed	141	Ø4.5mm 0.1mm d
2	Unflaw ed	22	Unflaw ed	42	Unflaw ed	62	Ø12mm 0.3mm d	82	Unflaw ed	102	Unflaw ed	122	Unflaw ed	142	Unflaw ed
3	Unflaw ed	23	Unflaw ed	43	Unflaw ed	63	Ø6.5mm 1.0mm d	83	Ø6.5mm 0.1mm d	103	Ø6.5mm 0.2mm d	123	Unflaw ed	143	Unflaw ed
4	Unflaw ed	24	Ø12mm 1.1mm d	44	Unflaw ed	64	Ø6.5mm 0.4mm d	84	Unflaw ed	104	Unflaw ed	124	Unflaw ed	144	Unflaw ed
5	Unflaw ed	25	Unflaw ed	45	Unflaw ed	65	Unflaw ed	85	Ø12mm 0.6mm d	105	Unflaw ed	125	Unflaw ed	145	Unflaw ed
6	Unflaw ed	26	Unflaw ed	46	Unflaw ed	66	Unflaw ed	86	Unflaw ed	106	Unflaw ed	126	Unflaw ed	146	Ø12mm 0.2mm d
7	Unflaw ed	27	Unflaw ed	47	Unflaw ed	67	Unflaw ed	87	Unflaw ed	107	Unflaw ed	127	Ø4.5mm 0.9mm d	147	Unflaw ed
8	Unflaw ed	28	Ø6.5mm 0.7mm d	48	Unflaw ed	68	Ø12mm 1.0mm d	88	Unflaw ed	108	Unflaw ed	128	Ø4.5mm 0.6mm d	148	Ø4.5mm 1.0mm d
9	Ø4.5mm 1.2mm d	29	Unflaw ed	49	Unflaw ed	69	Unflaw ed	89	Unflaw ed	109	Unflaw ed	129	Unflaw ed	149	Unflaw ed
10	Unflaw ed	30	Unflaw ed	50	Ø12mm 0.8mm d	70	Unflaw ed	90	Unflaw ed	110	Ø6.5mm 0.6mm d	130	Unflaw ed	150	Ø4.5mm 0.2mm d
11	Unflaw ed	31	Ø12mm 0.4mm d	51	Unflaw ed	71	Ø6.5mm 0.5mm d	91	Unflaw ed	111	Unflaw ed	131	Ø4.5mm 1.5mm d	151	Unflaw ed
12	Unflaw ed	32	Unflaw ed	52	Unflaw ed	72	Ø6.5mm 0.8mm d	92	Unflaw ed	112	Ø4.5mm 1.3mm d	132	Ø12mm 0.5mm d	152	Unflaw ed
13	Unflaw ed	33	Unflaw ed	53	Unflaw ed	73	Ø6.5mm 1.1mm d	93	Unflaw ed	113	Unflaw ed	133	Unflaw ed	153	Unflaw ed
14	Unflaw ed	34	Unflaw ed	54	Unflaw ed	74	Unflaw ed	94	Unflaw ed	114	Unflaw ed	134	Unflaw ed	154	Unflaw ed
15	Unflaw ed	35	Unflaw ed	55	Unflaw ed	75	Unflaw ed	95	Unflaw ed	115	Ø12mm 0.9mm d	135	Unflaw ed	155	Unflaw ed
16	Ø6.5mm 0.9mm d	36	Unflaw ed	56	Ø12mm 0.1mm d	76	Unflaw ed	96	Unflaw ed	116	Ø4.5mm 0.8mm d	136	Unflaw ed	156	Unflaw ed
17	Unflaw ed	37	Unflaw ed	57	Ø6.5mm 1.3mm d	77	Ø6.5mm 1.2mm d	97	Unflaw ed	117	Ø4.5mm 0.7mm d	137	Unflaw ed		
18	Unflaw ed	38	Unflaw ed	58	Unflaw ed	78	Ø4.5mm 1.4mm d	98	Ø4.5mm 1.1mm d	118	Unflaw ed	138	Unflaw ed		
19	Unflaw ed	39	Ø4.5mm 0.5mm d	59	Unflaw ed	79	Ø4.5mm 0.3mm d	99	Unflaw ed	119	Unflaw ed	139	Unflaw ed		
20	Unflaw ed	40	Ø12mm 0.7mm d	60	Unflaw ed	80	Unflaw ed	100	Unflaw ed	120	Unflaw ed	140	Ø6.5mm 0.3mm d		

Flaw details & X/Y Panel location coordinates; all in mm					
Flaw Width	Flaw Depth	X Coordinate	Y Coordinate	Internal Flaw Radius	Edge Blend Radius
Ø4.5mm	0.1	454	315	25.363	12.682
	0.2	13	107	12.756	6.378
	0.3	339	63	8.588	4.294
	0.4	665	425	6.528	3.264
	0.5	253	194	5.313	2.657
	0.6	400	563	4.519	2.260
	0.7	608	70	3.996	1.998
	0.8	607	433	3.564	1.782
	0.9	522	262	3.263	1.632
	1	210	546	3.031	1.516
	1.1	32	174	2.851	1.426
	1.2	247	30	2.709	1.355
	1.3	374	563	2.597	1.299
	1.4	446	175	2.508	1.254
	1.5	275	218	2.438	1.219
Ø6.5mm	0.1	235	446	52.863	26.432
	0.2	81	361	26.506	13.253
	0.3	546	227	17.754	8.877
	0.4	294	113	13.403	6.702
	0.5	45	15	10.813	5.407
	0.6	468	299	9.102	4.551
	0.7	95	167	7.895	3.948
	0.8	201	530	7.002	3.501
	0.9	183	52	6.318	3.159
	1	186	72	5.781	2.891
	1.1	683	183	5.351	2.676
	1.2	625	269	5.001	2.501
	1.3	510	446	4.713	2.357
Ø12mm	0.1	360	275	180.05	90.025
	0.2	245	366	90.1	45.050
	0.3	389	369	60.15	30.075
	0.4	426	640	45.2	22.600
	0.5	33	296	36.25	18.125
	0.6	175	270	30.3	15.150
	0.7	513	456	26.064	13.032
	0.8	664	410	22.9	11.450
	0.9	124	342	20.45	10.225
	1	246	65	18.5	9.250
	1.1	371	228	16.914	8.457



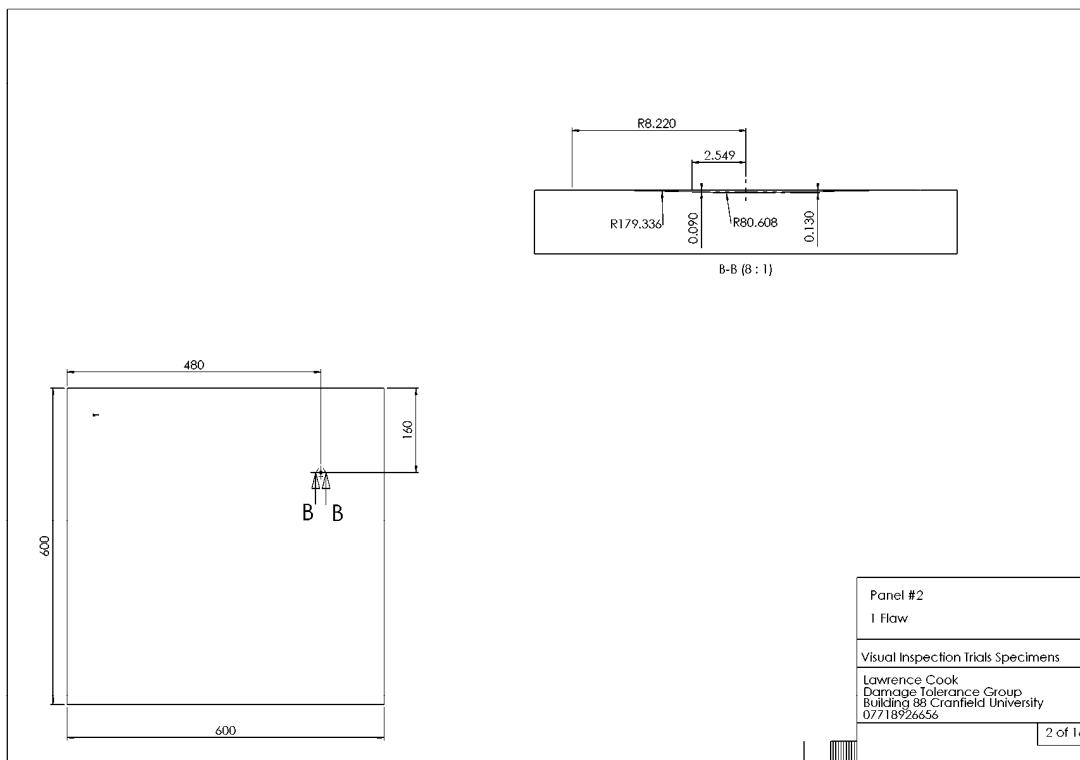
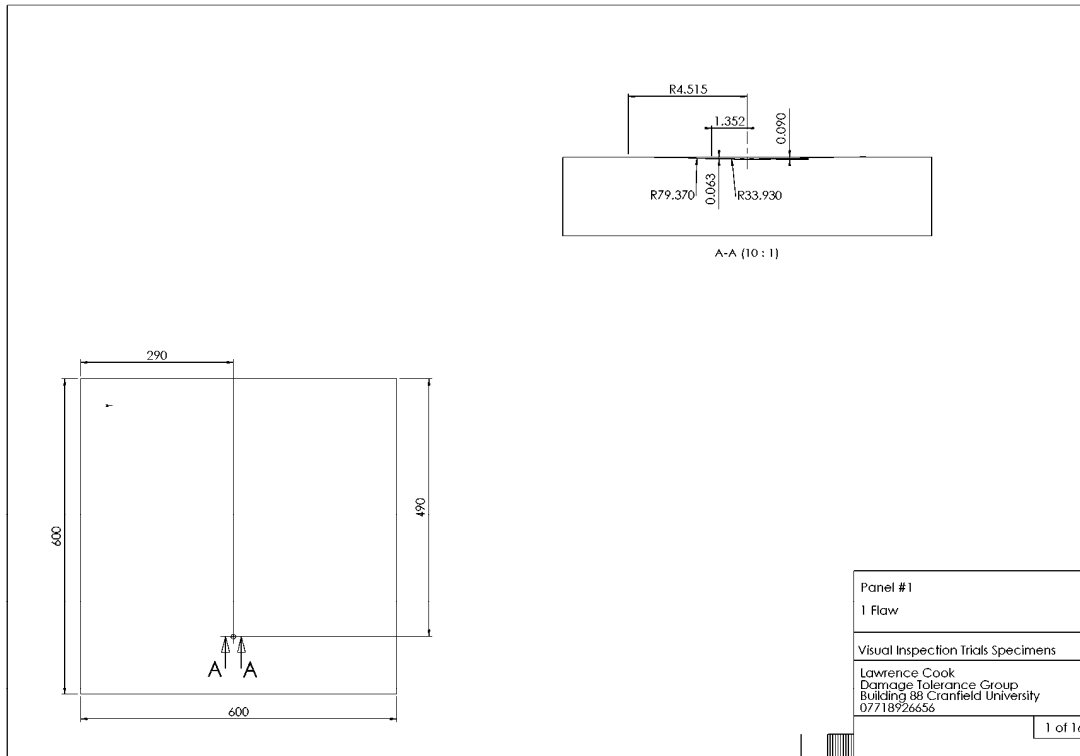
### Trial 4 specimen/ flaw characteristics

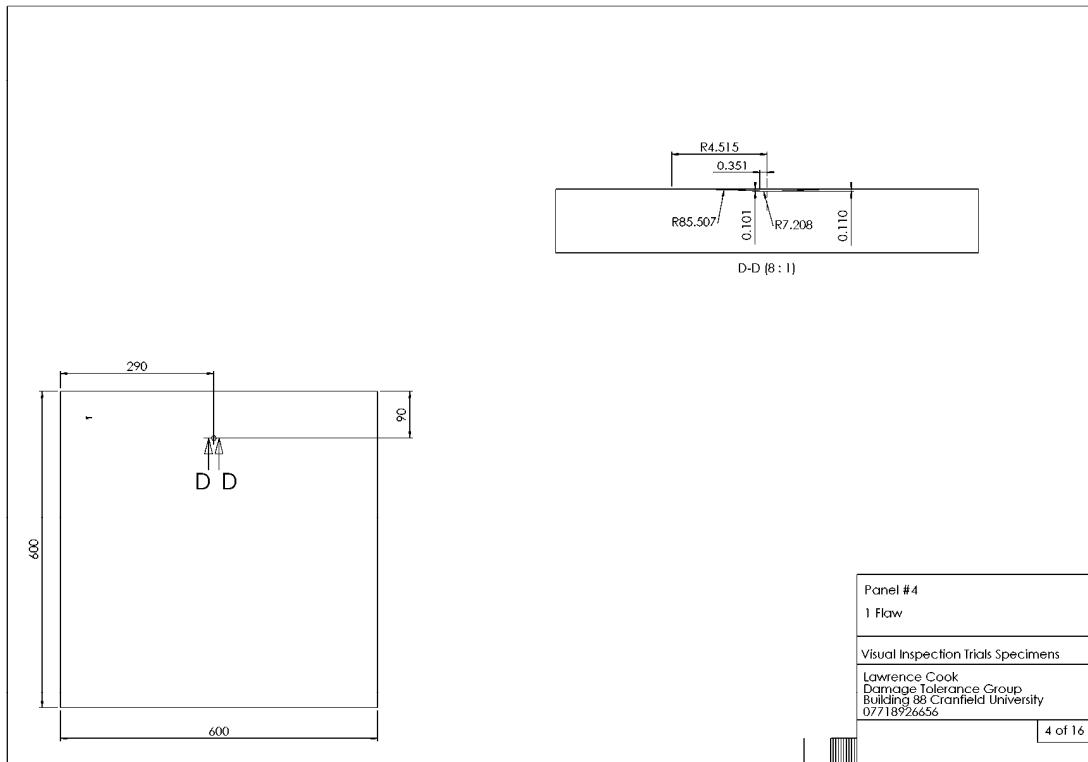
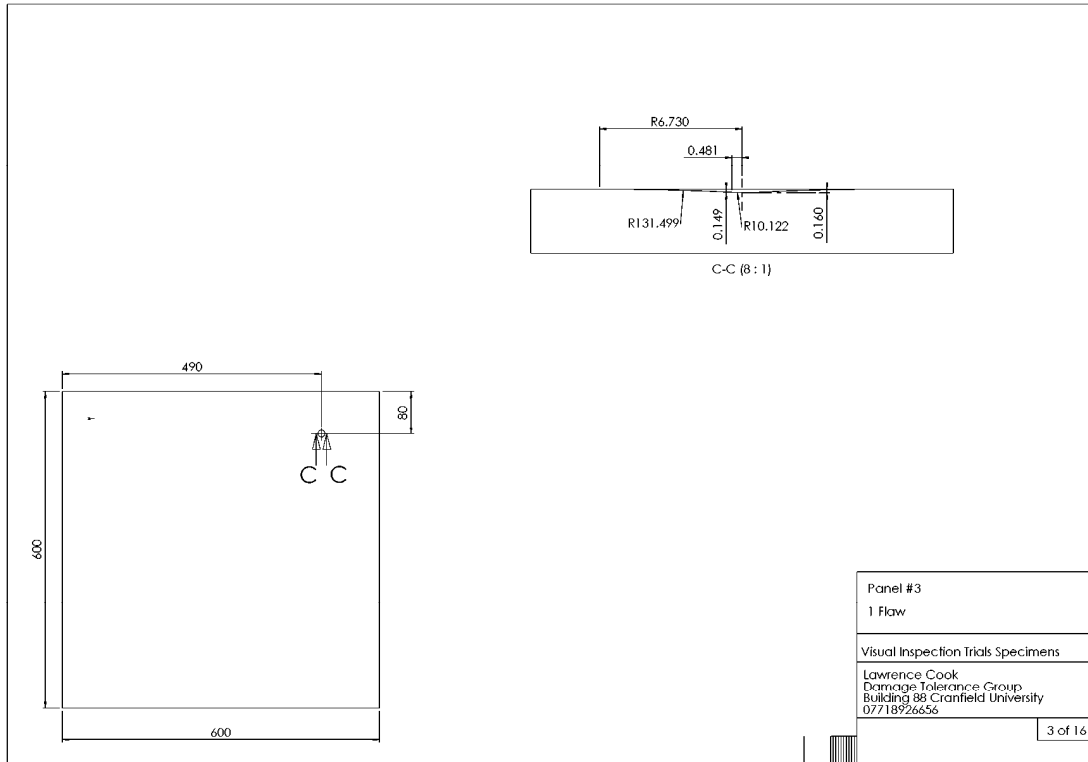
Panel Numbers & Flaw sizes:		Ø## = Flaw Width		#.## d = Flaw Depth											
1	Unfaw ed	23	Unfaw ed	45	Ø16mm HARD EDGED	67	Unfaw ed	89	Unfaw ed	111	Unfaw ed	133	Unfaw ed	155	Unfaw ed
2	Unfaw ed	24	Unfaw ed	46	Ø10mm HARD EDGED	68	Unfaw ed	90	Ø22mm HARD EDGED	112	Unfaw ed	134	Ø28mm BLENDED EDGE	156	Unfaw ed
3	Unfaw ed	25	Unfaw ed	47	Unfaw ed	69	Ø10mm BLENDED EDGE	91	Unfaw ed	113	Unfaw ed	135	Unfaw ed	157	Ø16mm BLENDED EDGE
4	Unfaw ed	26	Unfaw ed	48	Unfaw ed	70	Unfaw ed	92	Ø14mm HARD EDGED	114	Unfaw ed	136	Unfaw ed	158	Unfaw ed
5	Unfaw ed	27	Unfaw ed	49	Unfaw ed	71	Unfaw ed	93	Unfaw ed	115	Ø24mm HARD EDGED	137	Unfaw ed	159	Ø5mm BLENDED EDGE
6	Ø5mm HARD EDGED	28	Ø7mm BLENDED EDGE	50	Ø18mm BLENDED EDGE	72	Unfaw ed	94	Unfaw ed	116	Unfaw ed	138	Unfaw ed	160	Unfaw ed
7	Unfaw ed	29	Unfaw ed	51	Unfaw ed	73	Ø9mm HARD EDGED	95	Unfaw ed	117	Unfaw ed	139	Ø30mm BLENDED EDGE	161	Ø7mm HARD EDGED
8	Unfaw ed	30	Ø20mm HARD EDGED	52	Unfaw ed	74	Unfaw ed	96	Ø3mm BLENDED EDGE	118	Unfaw ed	140	Unfaw ed	162	Unfaw ed
9	Ø26mm HARD EDGED	31	Unfaw ed	53	Ø30mm HARD EDGED	75	Unfaw ed	97	Ø14mm BLENDED EDGE	119	Ø16mm HARD EDGED	141	Unfaw ed	163	Ø28mm HARD EDGED
10	Unfaw ed	32	Ø10mm HARD EDGED	54	Unfaw ed	76	Ø9mm BLENDED EDGE	98	Unfaw ed	120	Unfaw ed	142	Ø10mm BLENDED EDGE	164	Unfaw ed
11	Unfaw ed	33	Unfaw ed	55	Ø30mm BLENDED EDGE	77	Unfaw ed	99	Unfaw ed	121	Unfaw ed	143	Ø4mm HARD EDGED	165	Ø4mm BLENDED EDGE
12	Unfaw ed	34	Ø6mm BLENDED EDGE	56	Unfaw ed	78	Unfaw ed	100	Unfaw ed	122	Unfaw ed	144	Unfaw ed	166	Unfaw ed
13	Unfaw ed	35	Unfaw ed	57	Unfaw ed	79	Unfaw ed	101	Unfaw ed	123	Ø24mm BLENDED EDGE	145	Unfaw ed	167	Unfaw ed
14	Unfaw ed	36	Unfaw ed	58	Unfaw ed	80	Unfaw ed	102	Ø30mm HARD EDGED	124	Unfaw ed	146	Unfaw ed	168	Ø8mm BLENDED EDGE
15	Unfaw ed	37	Unfaw ed	59	Unfaw ed	81	Unfaw ed	103	Ø12mm BLENDED EDGE	125	Unfaw ed	147	Unfaw ed	169	Unfaw ed
16	Unfaw ed	38	Unfaw ed	60	Unfaw ed	82	Unfaw ed	104	Unfaw ed	126	Unfaw ed	148	Ø8mm HARD EDGED	170	Unfaw ed
17	Unfaw ed	39	Unfaw ed	61	Ø5mm BLENDED EDGE	83	Unfaw ed	105	Unfaw ed	127	Unfaw ed	149	Unfaw ed	171	Unfaw ed
18	Ø26mm BLENDED EDGE	40	Ø16mm BLENDED EDGE	62	Unfaw ed	84	Unfaw ed	106	Unfaw ed	128	Unfaw ed	150	Unfaw ed	172	Unfaw ed
19	Unfaw ed	41	Unfaw ed	63	Unfaw ed	85	Unfaw ed	107	Unfaw ed	129	Unfaw ed	151	Ø20mm BLENDED EDGE	173	Unfaw ed
20	Unfaw ed	42	Unfaw ed	64	Unfaw ed	86	Ø6mm HARD EDGED	108	Unfaw ed	130	Ø5mm HARD EDGED	152	Unfaw ed	174	Unfaw ed
21	Unfaw ed	43	Ø12mm HARD EDGED	65	Unfaw ed	87	Unfaw ed	109	Ø3mm HARD EDGED	131	Unfaw ed	153	Unfaw ed	175	Unfaw ed
22	Unfaw ed	44	Unfaw ed	66	Ø18mm HARD EDGED	88	Unfaw ed	110	Unfaw ed	132	Unfaw ed	154	Unfaw ed	176	Ø22mm BLENDED EDGE

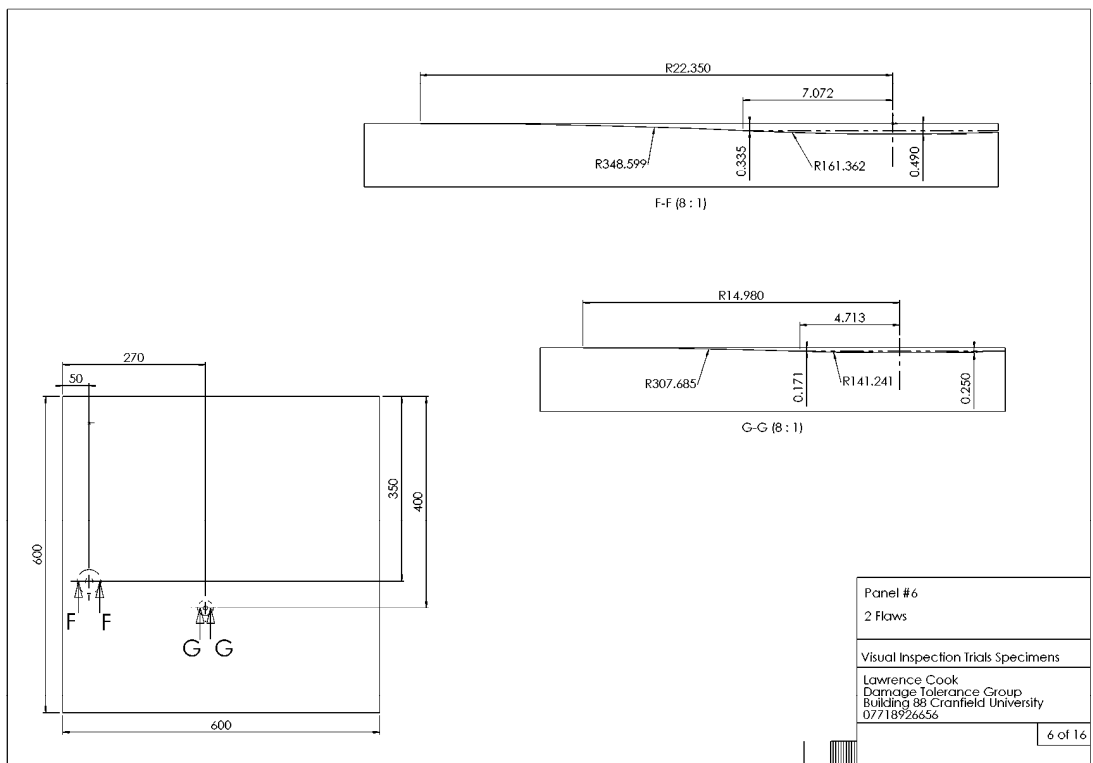
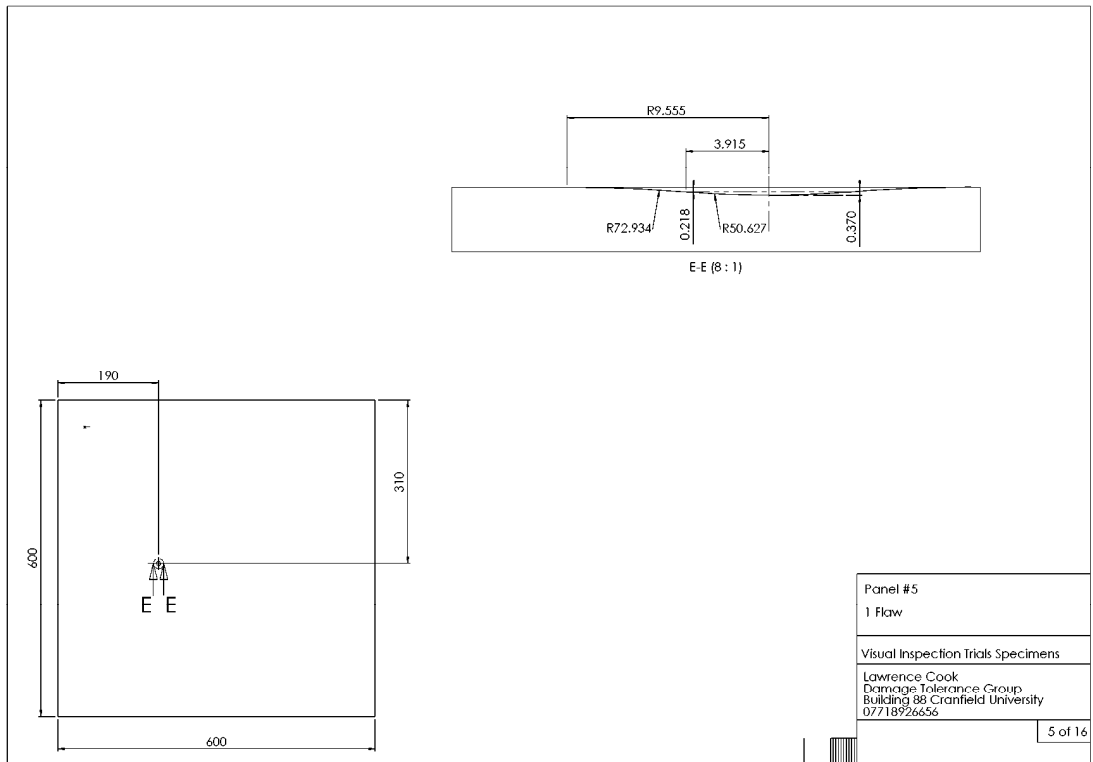
Flaw details & X/Y Panel location coordinates; all in mm						
Flaw Depth	Flaw Width	Edge Type	X Coordinate	Y Coordinate	Internal Flaw Radius	Edge Blend Radius
0.15	3	Blended Edge	410	138	7.575	7.575
	3	Hard Edge	643	60	7.575	~
	4	Blended Edge	695	143	13.408	13.408
	4	Hard Edge	333	204	13.408	~
	5	Blended Edge	286	501	20.908	20.908
	5	Blended Edge	11	543	20.908	20.908
	5	Hard Edge	626	72	20.908	~
	5	Hard Edge	236	480	20.908	~
	6	Blended Edge	546	375	30.075	30.075
	6	Hard Edge	183	694	30.075	~
	7	Blended Edge	91	318	40.908	40.908
	7	Hard Edge	339	379	40.908	~
	8	Blended Edge	177	116	53.408	53.408
	8	Hard Edge	701	184	53.408	~
	9	Blended Edge	143	363	67.575	67.575
	9	Hard Edge	380	310	67.575	~
	10	Blended Edge	298	66	83.408	83.408
	10	Blended Edge	570	594	83.408	83.408
	10	Hard Edge	46	270	83.408	~
	10	Hard Edge	522	446	83.408	~
	12	Blended Edge	71	519	120.075	120.075
	12	Hard Edge	16	646	120.075	~
	14	Blended Edge	635	140	163.408	163.408
	14	Hard Edge	642	303	163.408	~
	16	Blended Edge	616	485	213.408	213.408
	16	Blended Edge	522	663	213.408	213.408
	16	Hard Edge	84	325	213.408	~
	16	Hard Edge	15	489	213.408	~
	18	Blended Edge	261	115	270.075	270.075
	18	Hard Edge	337	138	270.075	~
	20	Blended Edge	497	65	333.408	333.408
	20	Hard Edge	422	635	333.408	~
	22	Blended Edge	453	21	403.408	403.408
	22	Hard Edge	343	525	403.408	~
	24	Blended Edge	150	92	480.075	480.075
	24	Hard Edge	69	213	480.075	~
	26	Blended Edge	386	522	563.408	563.408
	26	Hard Edge	404	318	563.408	~
	28	Blended Edge	351	348	653.408	653.408
	28	Hard Edge	679	687	653.408	~
30	Blended Edge	486	113	750.075	750.075	
30	Blended Edge	576	300	750.075	750.075	
30	Hard Edge	423	124	750.075	~	
30	Hard Edge	428	168	750.075	~	

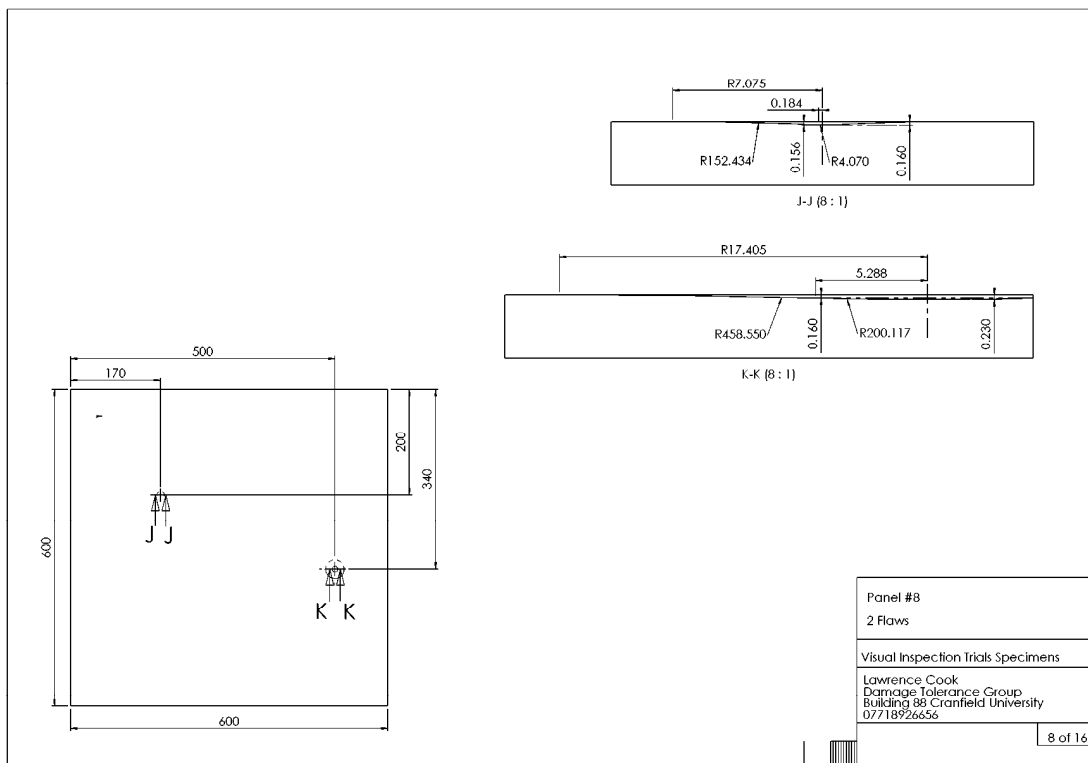
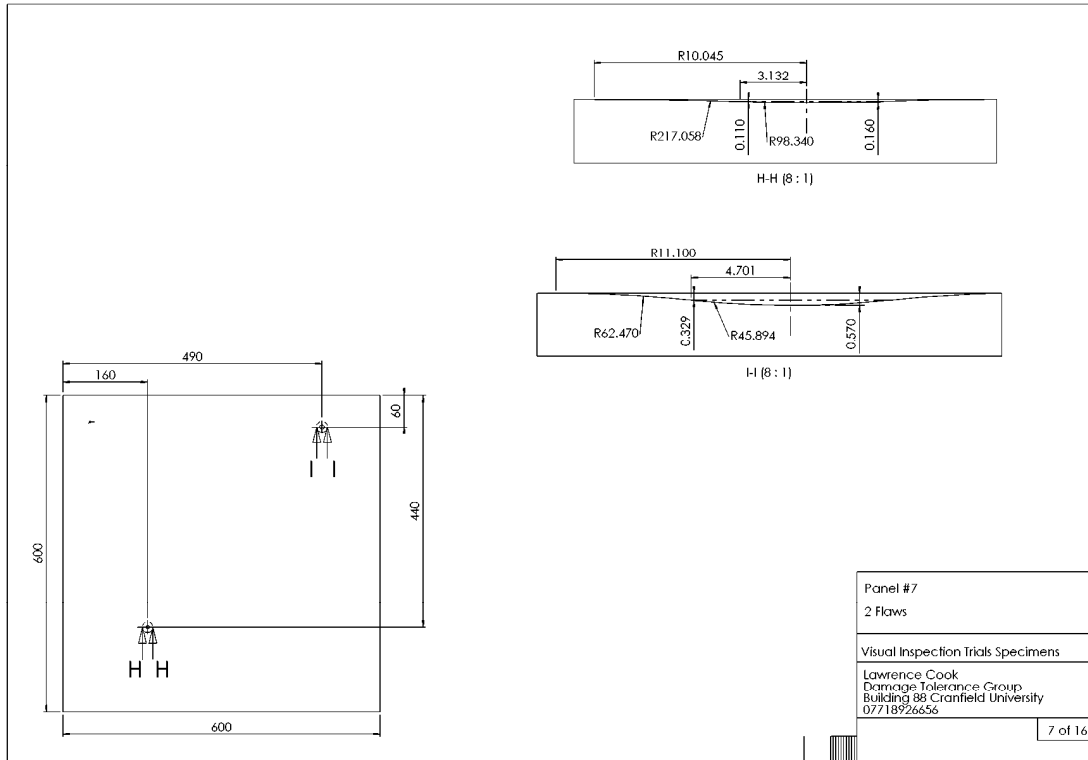
# Appendix C

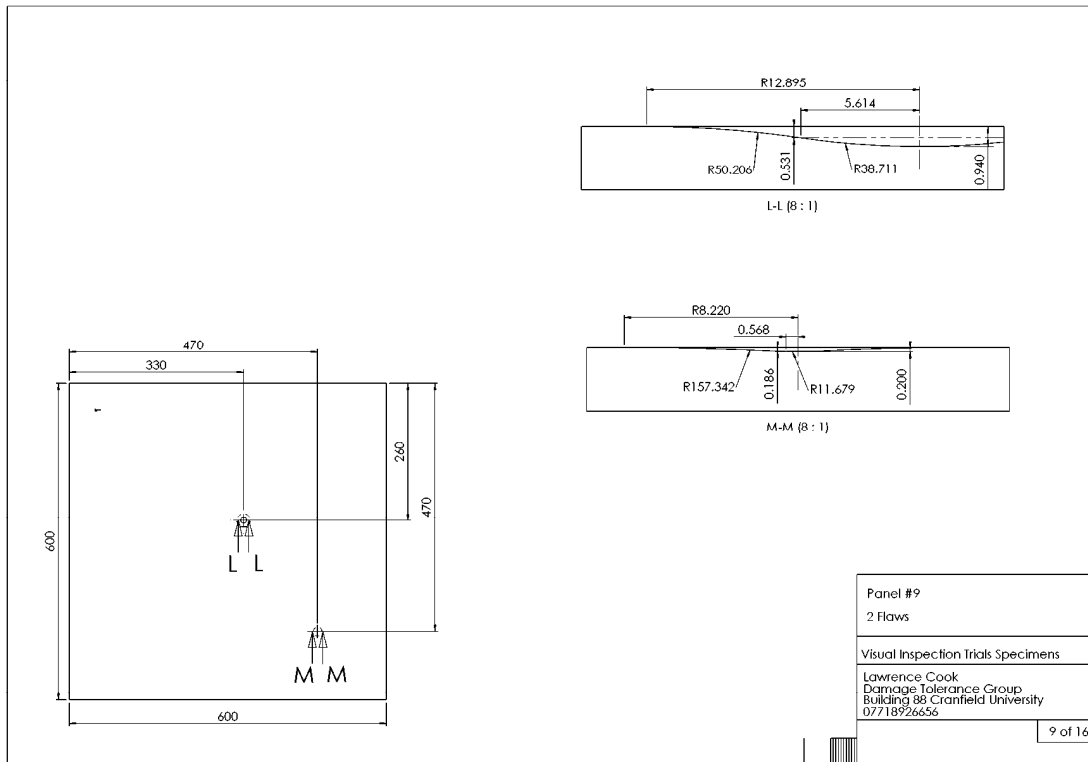
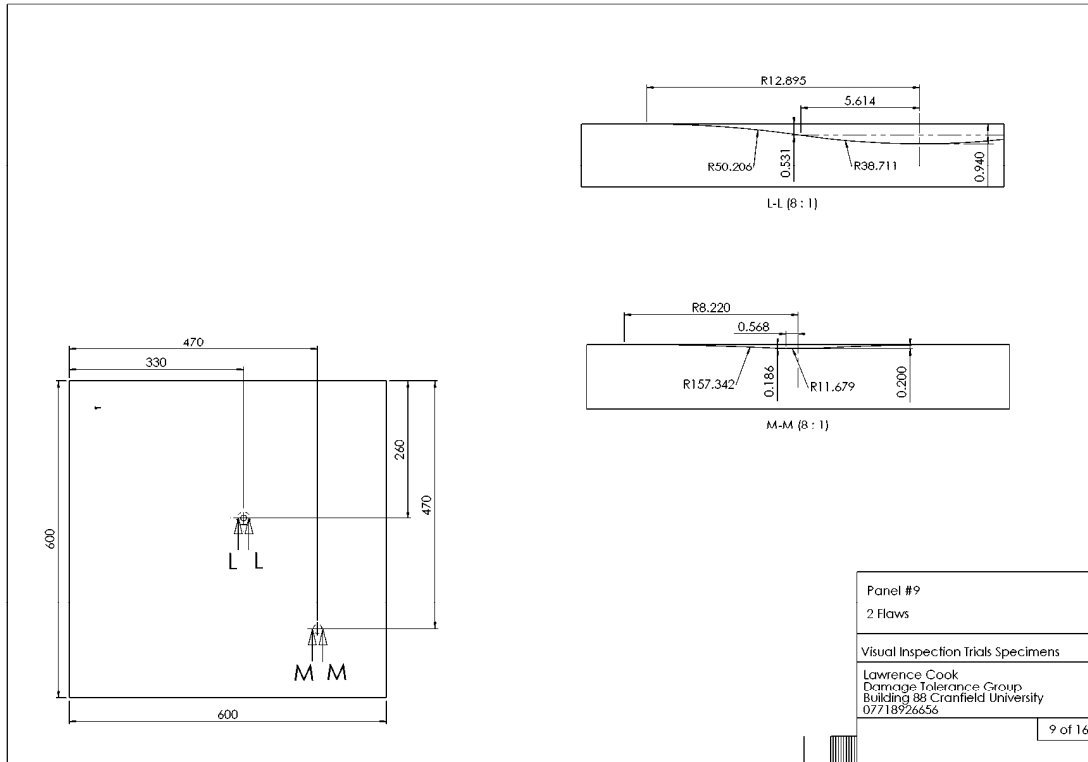
## Drawings of specimen panels for series 2 visual inspection trials

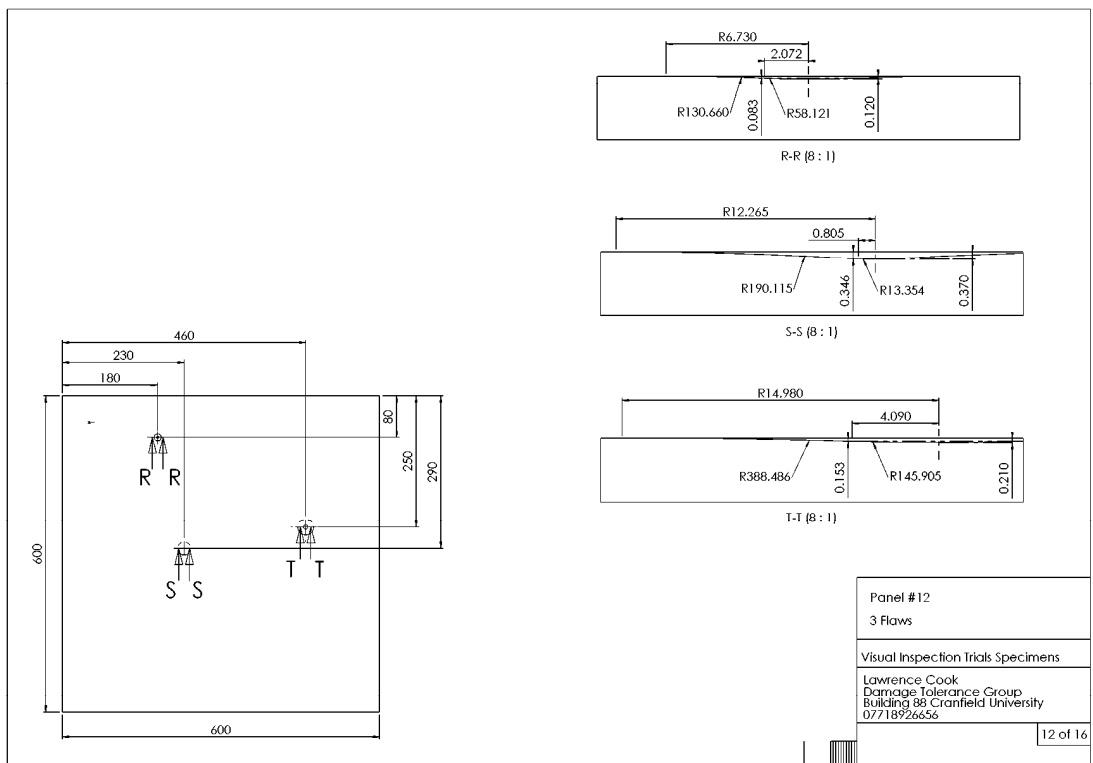
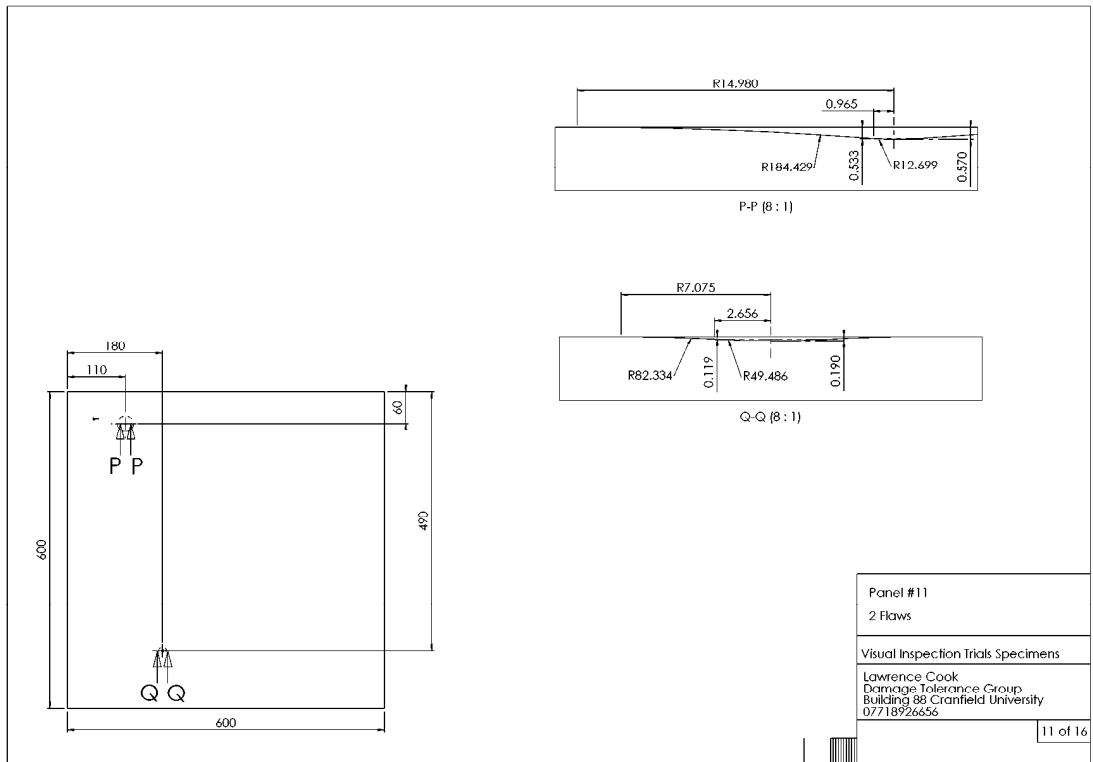




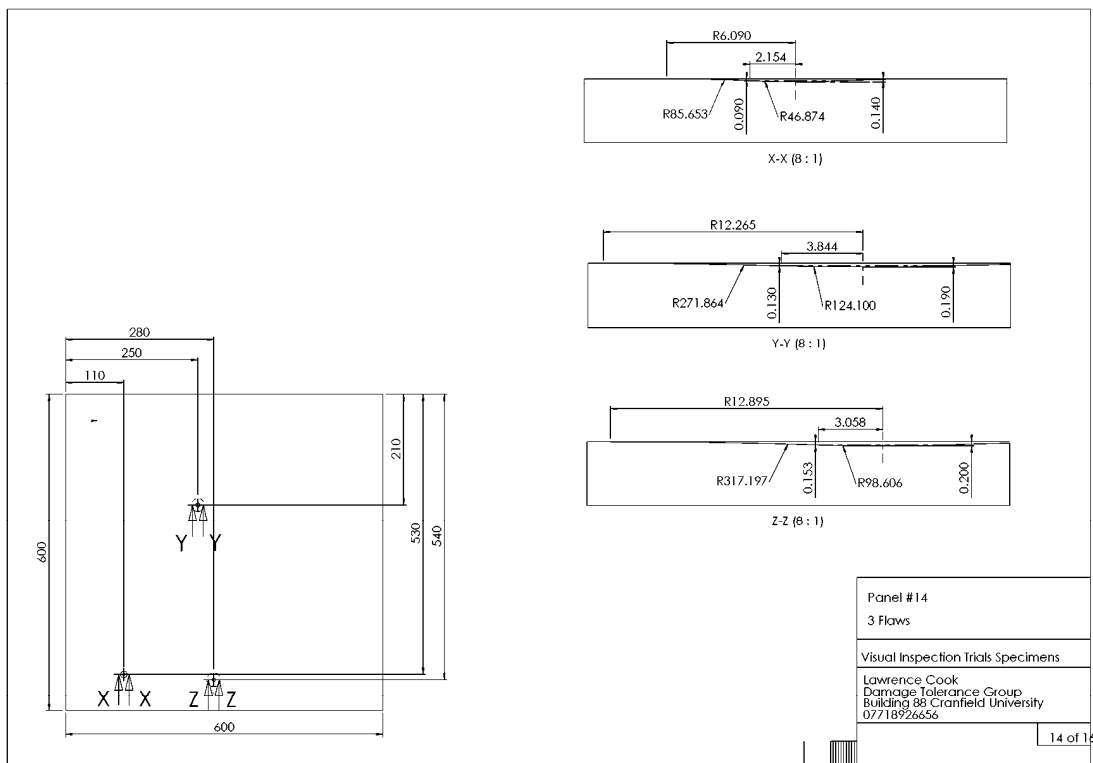
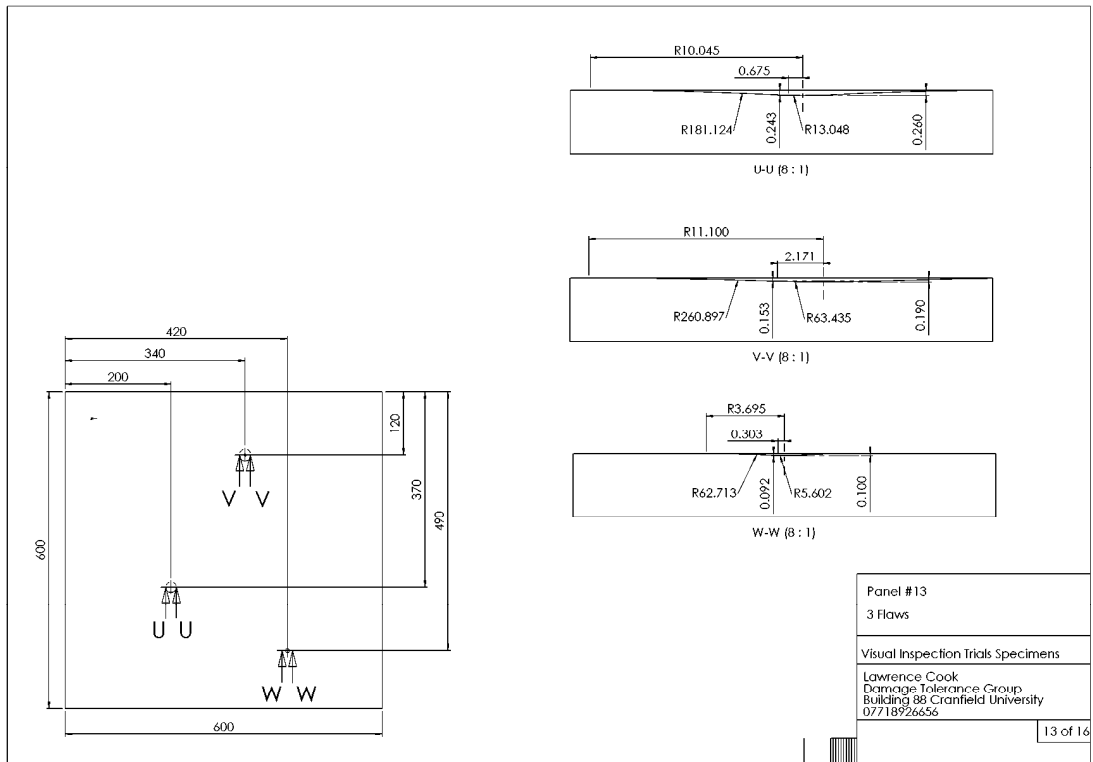


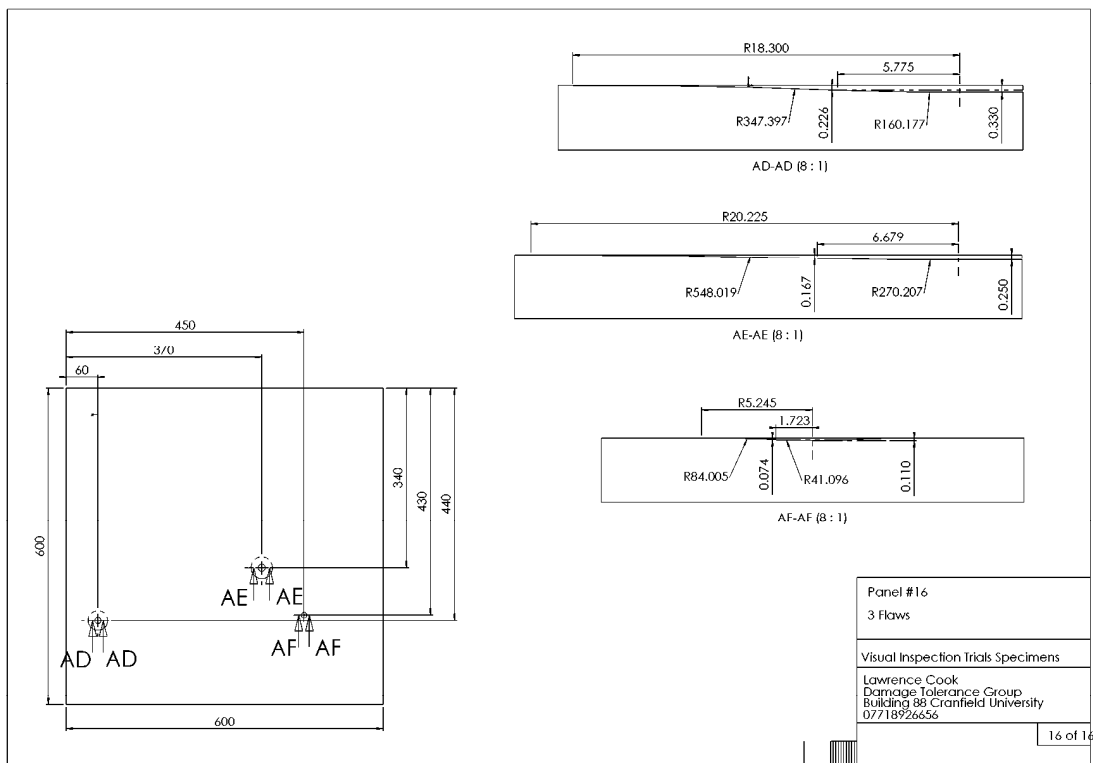
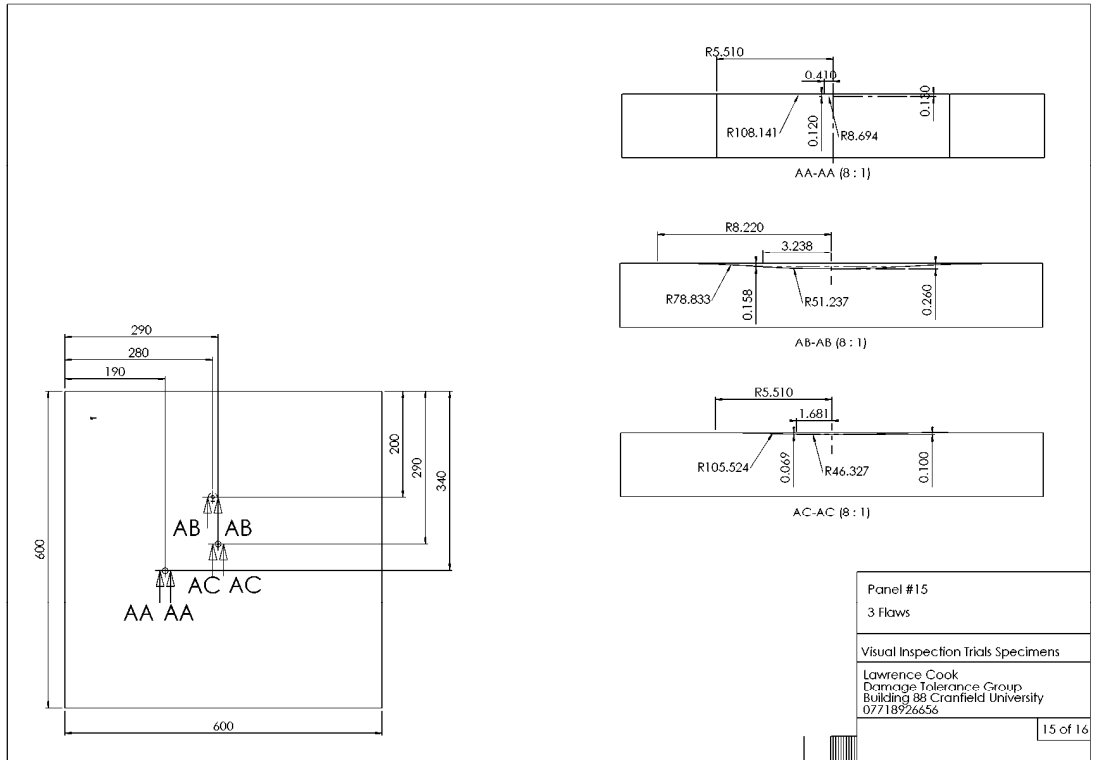








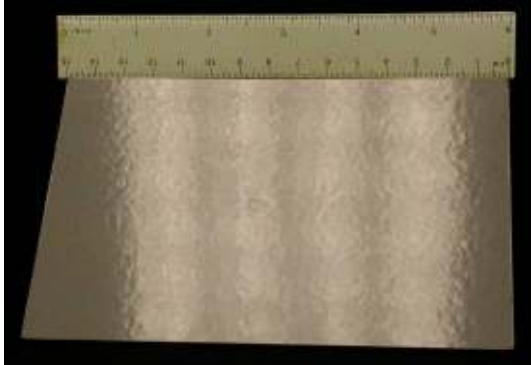




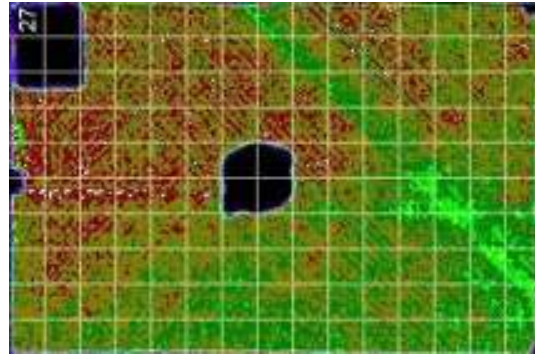
## ***Appendix D***

### ***Examples of impact damage to AS4/8552 CFRP Coupons***

The impact damage to coupons of 17ply and 33ply AS4/8552 CFRP laminates are presented in this appendix in the form of photographs of the damage and corresponding C-Scan images fitted with a 10 mm x 10 mm grid. Where available, corresponding photographs from metallographic sectioning of the impact damage sites from Boulic 2007 are also provided.



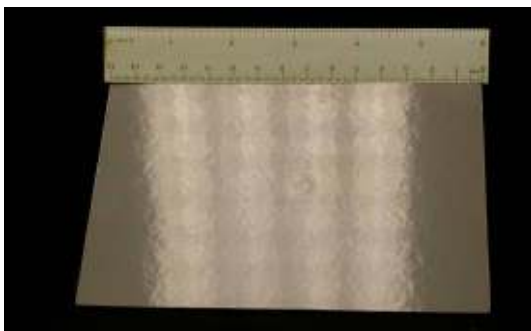
Photograph of impact damage coupon #27  
(17ply + mesh painted, Ø20mm/5J)



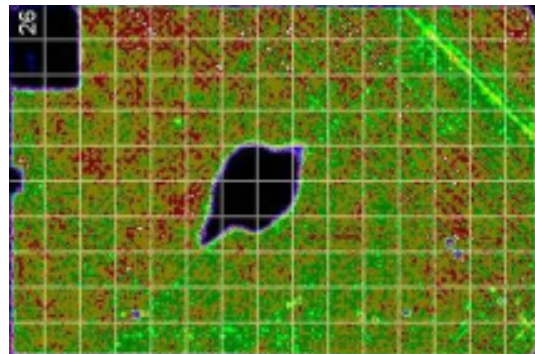
C-Scan of impact damage coupon #27



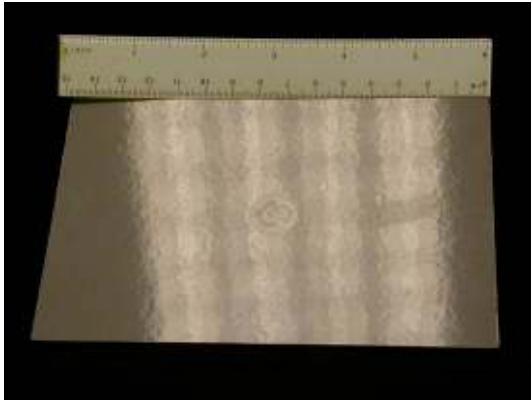
Metallographic section image of Ø20mm/5J impact (from Boulic, 2007)



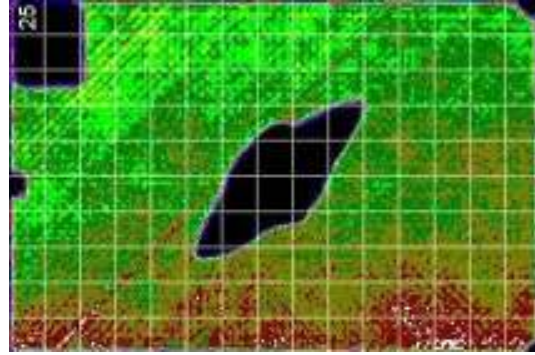
Photograph of impact damage coupon #26  
(17ply + mesh painted, Ø20mm/10J)



C-Scan of impact damage coupon #26



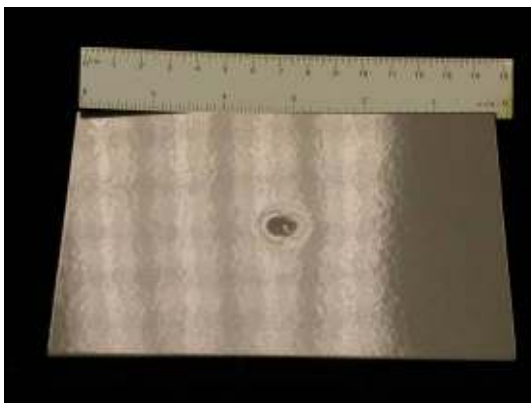
Photograph of impact damage coupon #25  
(17ply + mesh painted, Ø20mm/15J)



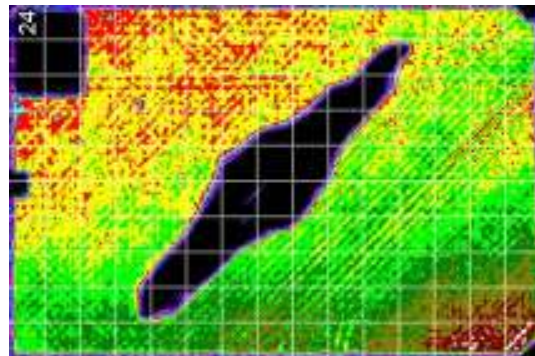
C-Scan of impact damage coupon #25



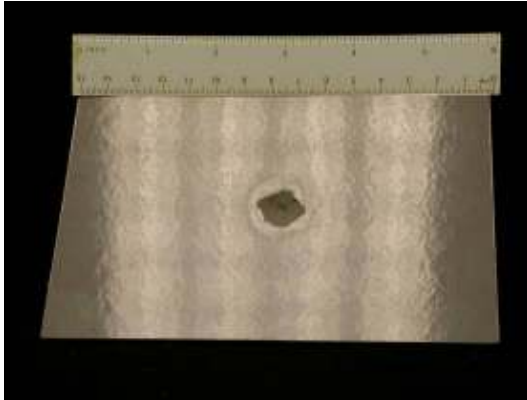
Metallographic section image of Ø20mm/15J impact (from Boulic, 2007)



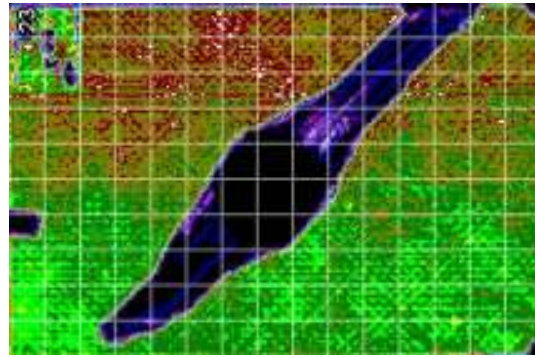
Photograph of impact damage coupon #24  
(17ply + mesh painted, Ø20mm/20J)



C-Scan of impact damage coupon #24



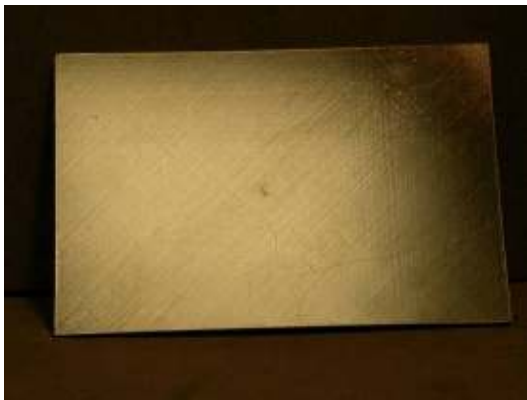
Photograph of impact damage coupon #23  
(17ply + mesh painted, Ø20mm/30J)



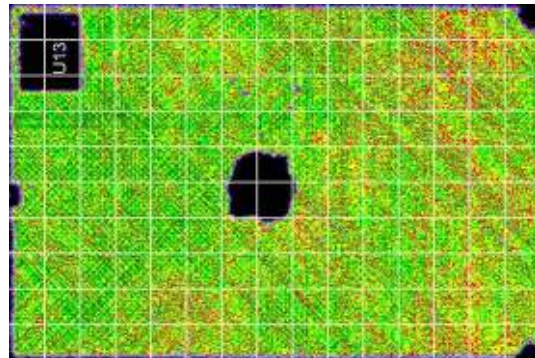
C-Scan of impact damage coupon #23



Metallographic section image of Ø20mm/30J impact (from Boulic, 2007)



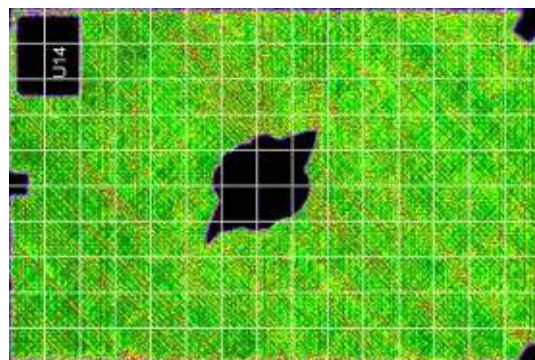
Photograph of impact damage coupon #U13  
(17ply unpainted, Ø20mm/5J)



C-Scan of impact damage coupon #U13

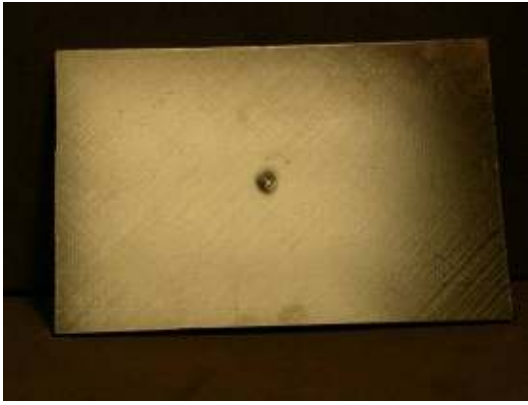


Photograph of impact damage coupon #U14  
(17ply unpainted, Ø20mm/10J)

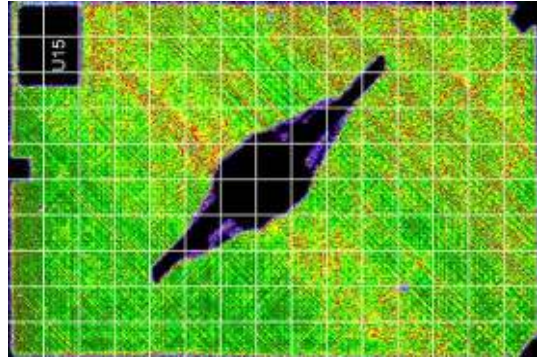


C-Scan of impact damage coupon #U14

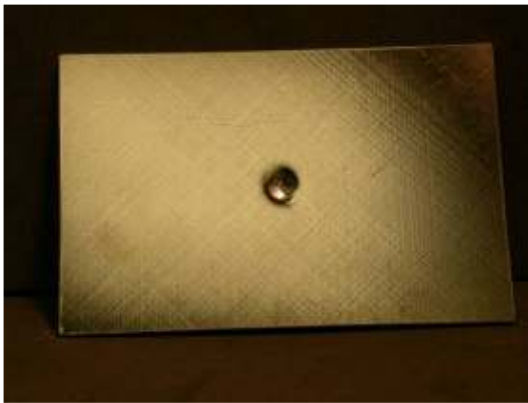




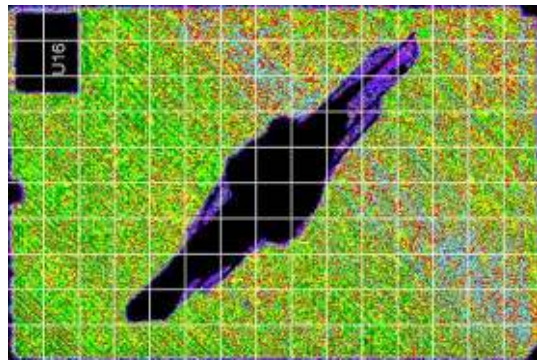
Photograph of impact damage coupon #U15  
(17ply unpainted, Ø20mm/15J)



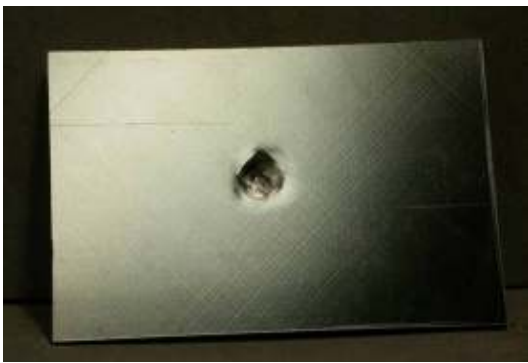
C-Scan of impact damage coupon #U15



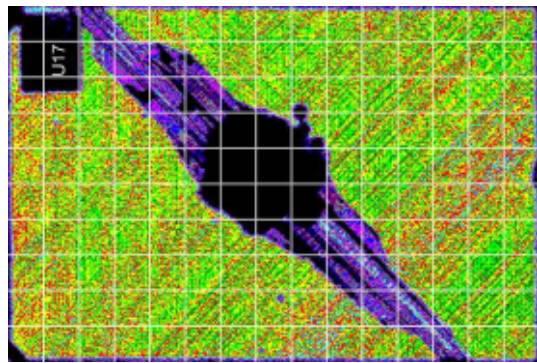
Photograph of impact damage coupon #U16  
(17ply unpainted, Ø20mm/20J)



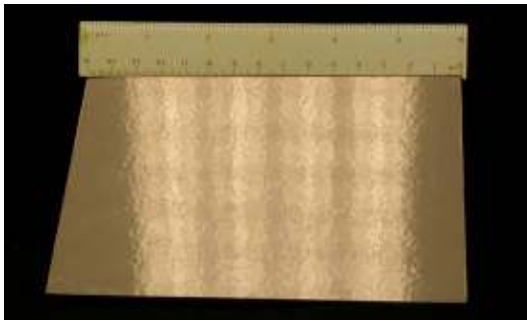
C-Scan of impact damage coupon #U16



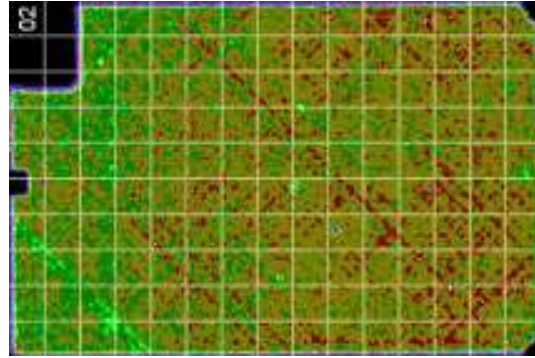
Photograph of impact damage coupon #U17  
(17ply unpainted, Ø20mm/30J)



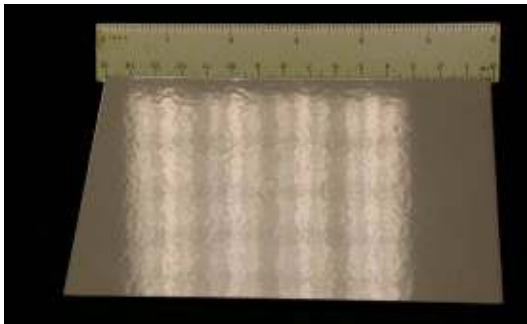
C-Scan of impact damage coupon #U17



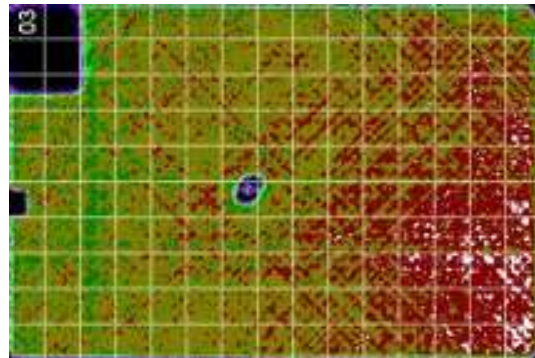
Photograph of impact damage coupon #2  
(33ply + mesh painted, Ø20mm/5J)



C-Scan of impact damage coupon #2



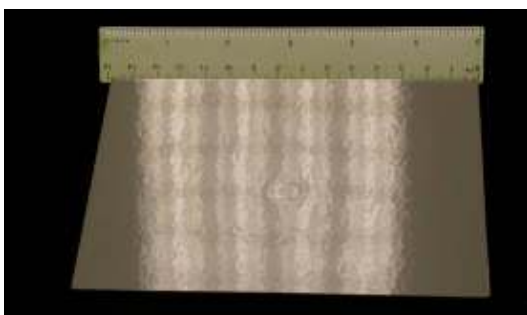
Photograph of impact damage coupon #3  
(33ply + mesh painted, Ø20mm/10J)



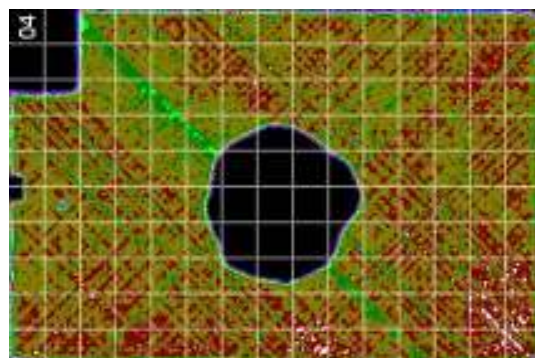
C-Scan of impact damage coupon #3



Metallographic section image of Ø20mm/10J impact (from Boulic, 2007)

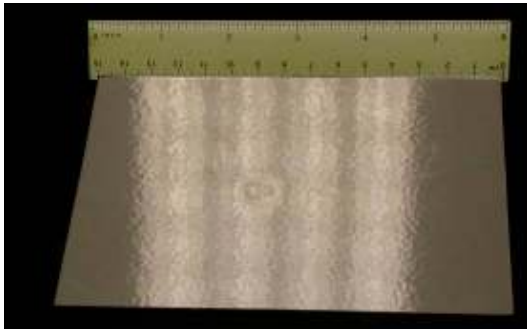


Photograph of impact damage coupon #4  
(33ply + mesh painted, Ø20mm/15J)

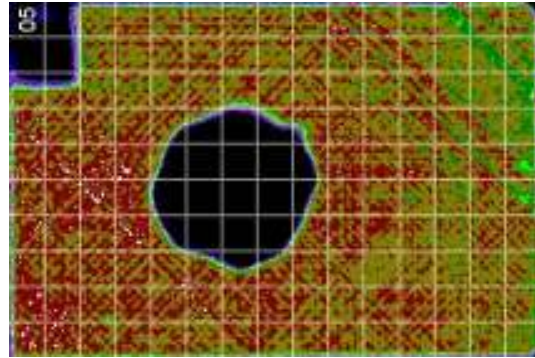


C-Scan of impact damage coupon #4





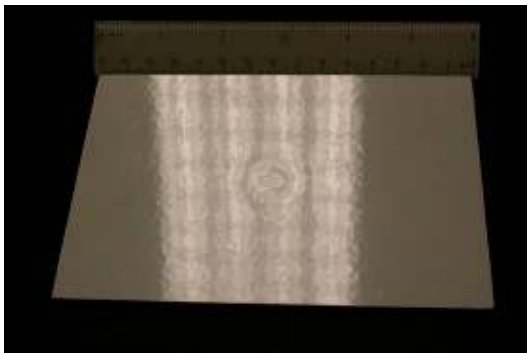
Photograph of impact damage coupon #5  
(33ply + mesh painted, Ø20mm/20J)



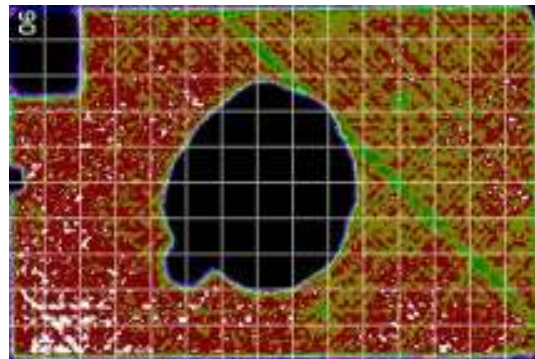
C-Scan of impact damage coupon #5



Metallographic section image of Ø20mm/20J impact (from Boulic, 2007)

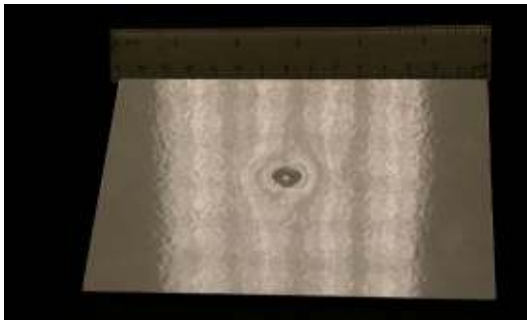


Photograph of impact damage coupon #6  
(33ply + mesh painted, Ø20mm/30J)

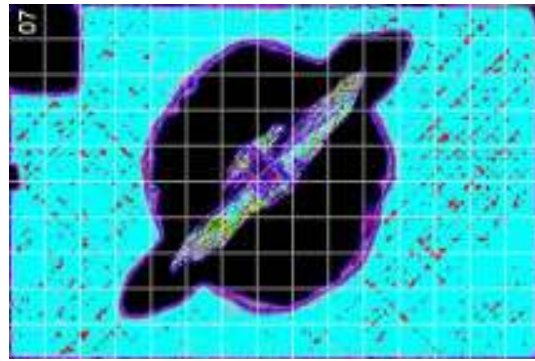


C-Scan of impact damage coupon #6





Photograph of impact damage coupon #7  
(33ply + mesh painted, Ø20mm/50J)



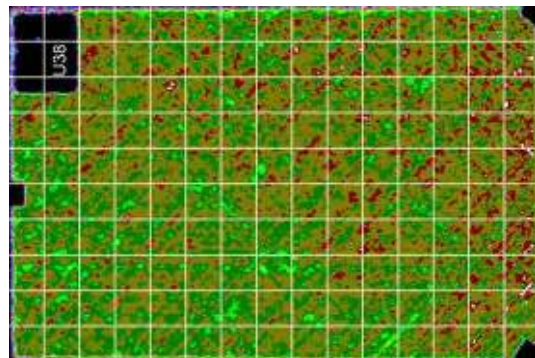
C-Scan of impact damage coupon #7



Metallographic section image of Ø20mm/50J impact (from Boulic, 2007)



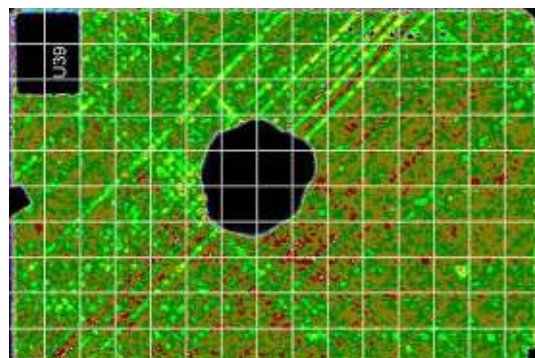
Photograph of impact damage coupon #U38  
(33ply unpainted, Ø20mm/5J)



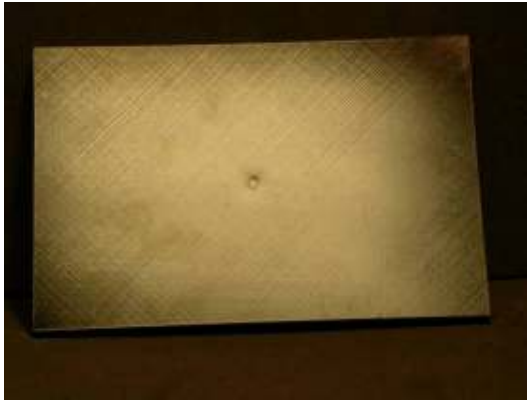
C-Scan of impact damage coupon #U38



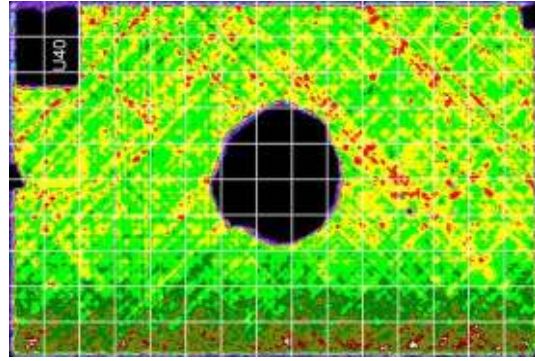
Photograph of impact damage coupon #U39  
(33ply unpainted, Ø20mm/10J)



C-Scan of impact damage coupon #U39



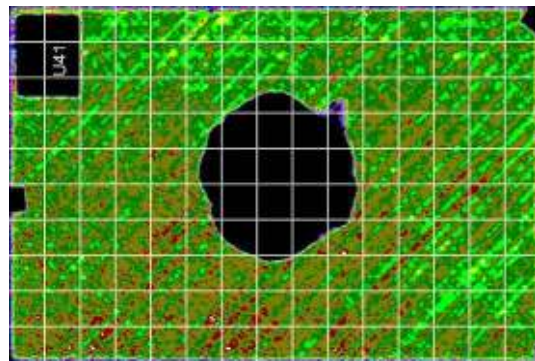
Photograph of impact damage coupon #U40  
(33ply unpainted, Ø20mm/15J)



C-Scan of impact damage coupon #U40



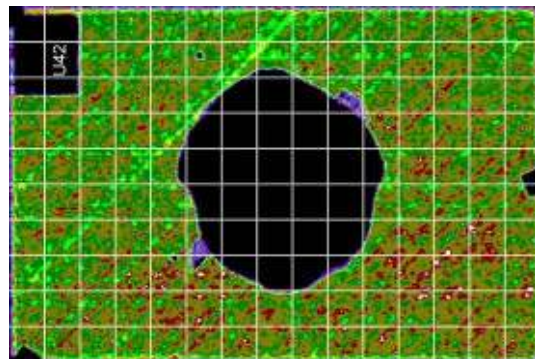
Photograph of impact damage coupon #U41  
(33ply unpainted, Ø20mm/20J)



C-Scan of impact damage coupon #U41



Photograph of impact damage coupon #U42  
(33ply unpainted, Ø20mm/30J)

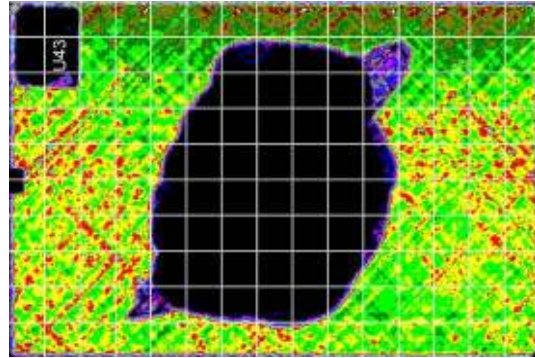


C-Scan of impact damage coupon #U42

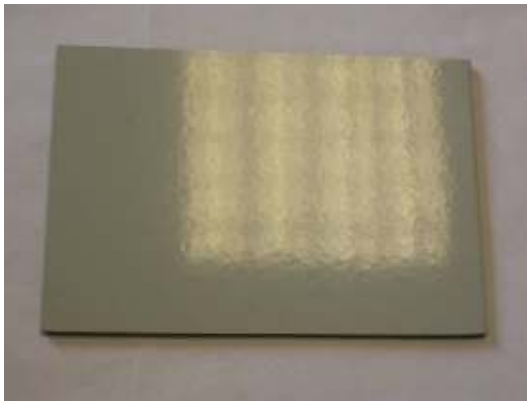




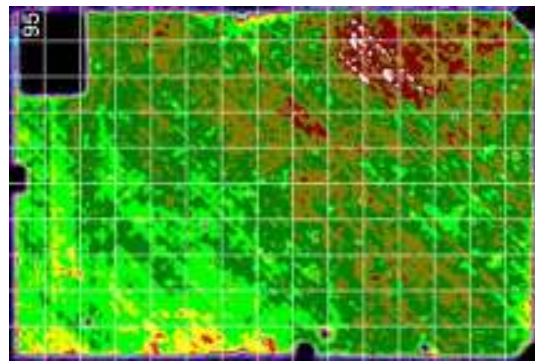
Photograph of impact damage coupon #U43  
(33ply unpainted, Ø20mm/50J)



C-Scan of impact damage coupon #U43



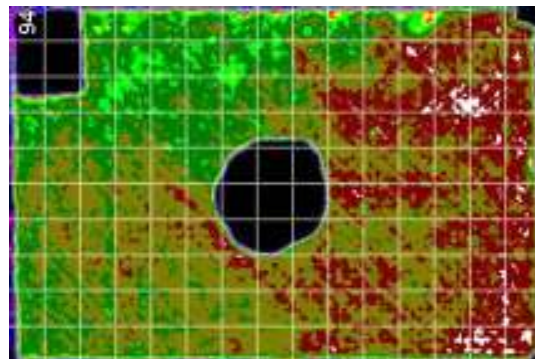
Photograph of impact damage coupon #95  
(17ply + mesh painted, Ø87mm/5J)



C-Scan of impact damage coupon #95



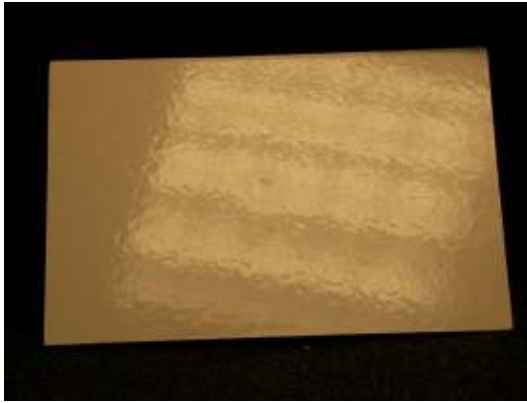
Photograph of impact damage coupon #94  
(17ply + mesh painted, Ø87mm/10J)



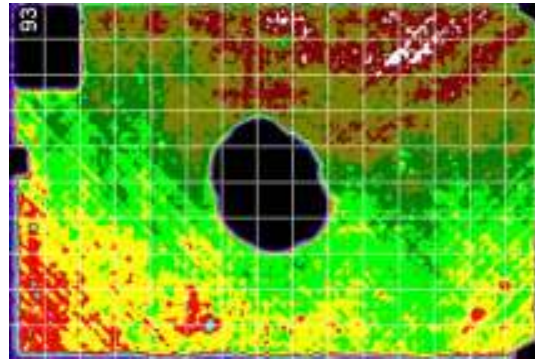
C-Scan of impact damage coupon #94



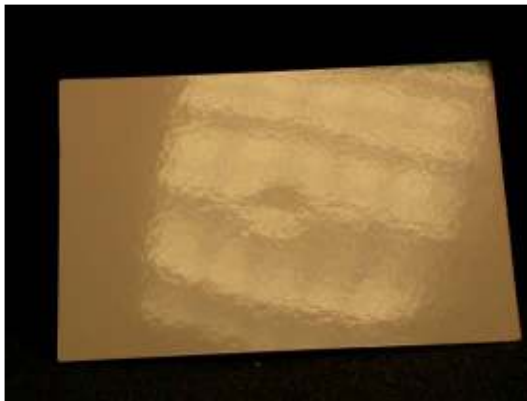
Metallographic section image of Ø87mm/10J impact (from Boulic, 2007)



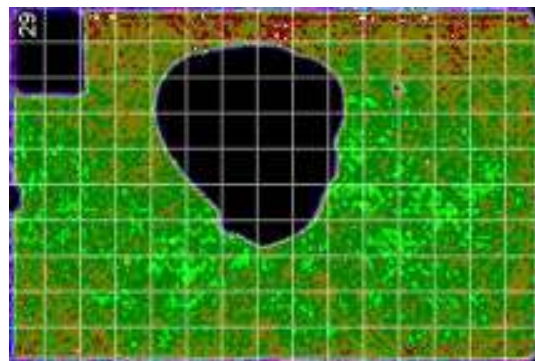
Photograph of impact damage coupon #93  
(17ply + mesh painted, Ø87mm/15J)



C-Scan of impact damage coupon #93



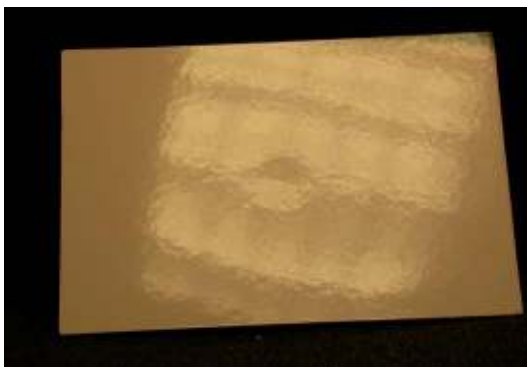
Photograph of impact damage coupon #29  
(17ply + mesh painted, Ø87mm/20J)



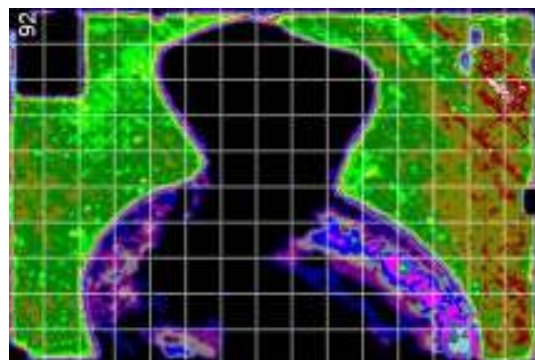
C-Scan of impact damage coupon #29



Metallographic section image of Ø87mm/20J impact (from Boulic, 2007)



Photograph of impact damage coupon #92  
(17ply + mesh painted, Ø87mm/30J)

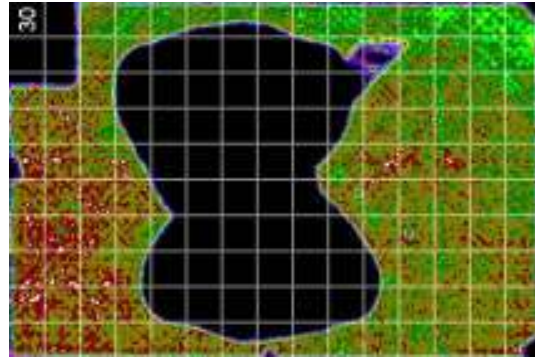


C-Scan of impact damage coupon #92





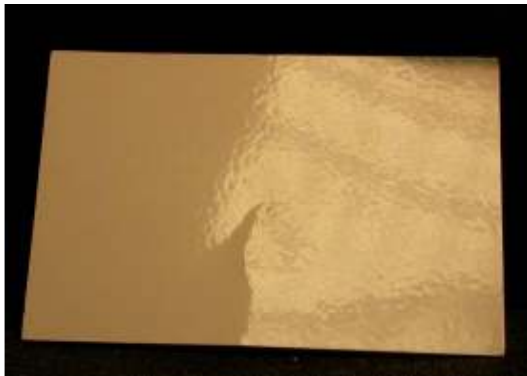
Photograph of impact damage coupon #30  
(17ply + mesh painted, Ø87mm/40J)



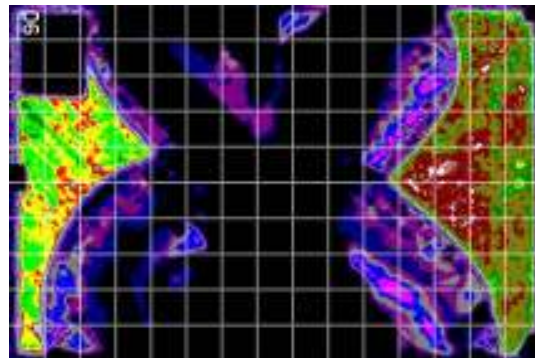
C-Scan of impact damage coupon #30



Metallographic section image of Ø87mm/40J impact (from Boulic, 2007)



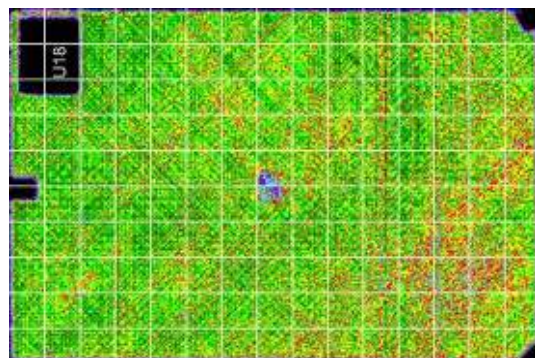
Photograph of impact damage coupon #90  
(17ply + mesh painted, Ø87mm/50J)



C-Scan of impact damage coupon #90



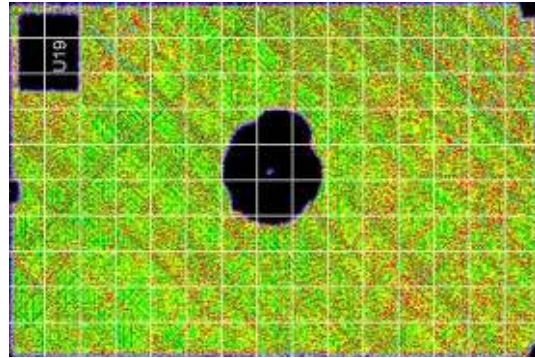
Photograph of impact damage coupon #U18  
(17ply unpainted, Ø87mm/5J)



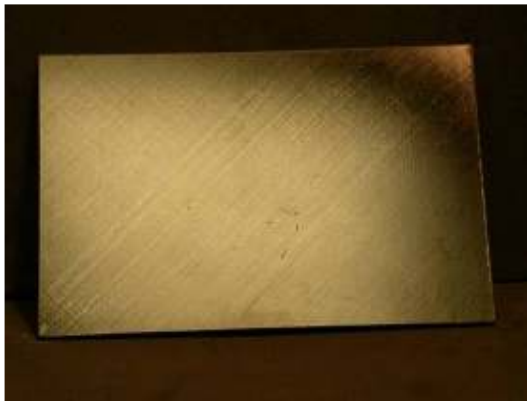
C-Scan of impact damage coupon #U18



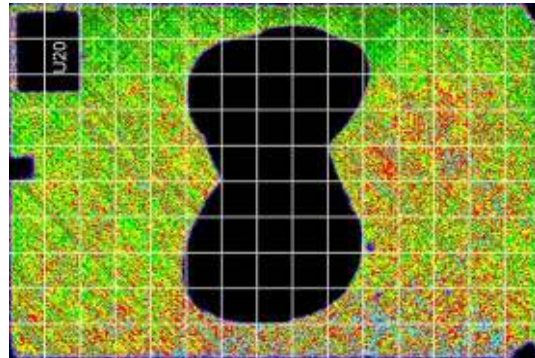
Photograph of impact damage coupon # U19  
(17ply unpainted, Ø87mm/10J)



C-Scan of impact damage coupon #U19



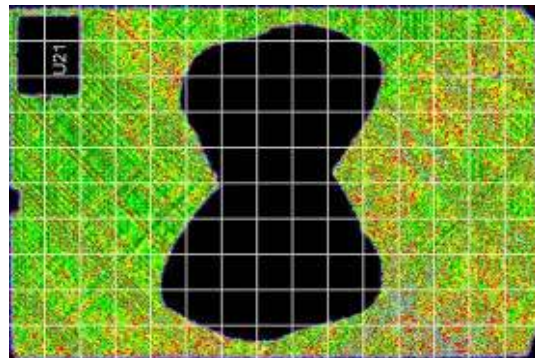
Photograph of impact damage coupon # U20  
(17ply unpainted, Ø87mm/15J)



C-Scan of impact damage coupon #U20



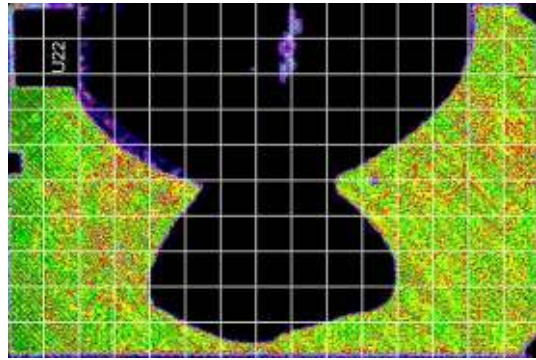
Photograph of impact damage coupon # U21  
(17ply unpainted, Ø87mm/20J)



C-Scan of impact damage coupon #U21



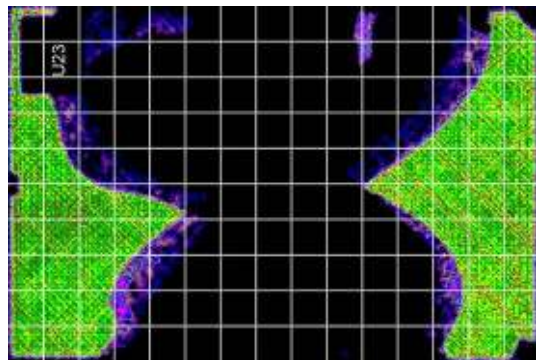
Photograph of impact damage coupon # U22  
(17ply unpainted, Ø87mm/30J)



C-Scan of impact damage coupon #U22



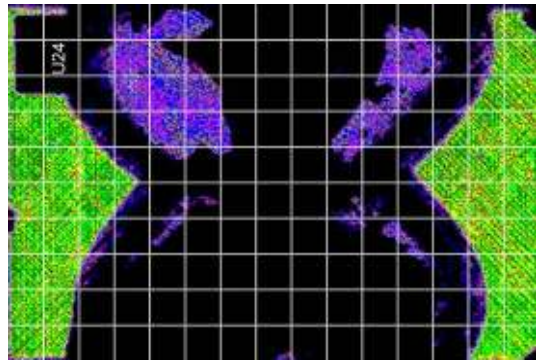
Photograph of impact damage coupon # U23  
(17ply unpainted, Ø87mm/40J)



C-Scan of impact damage coupon #U23

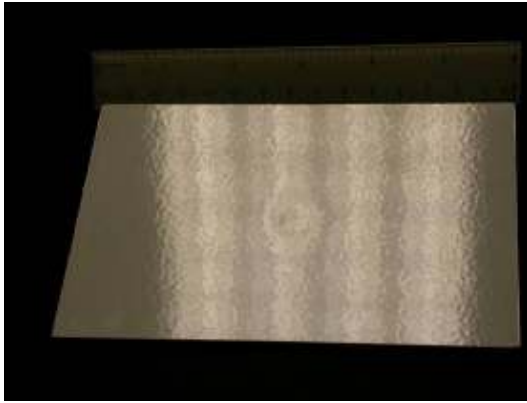


Photograph of impact damage coupon # U24  
(17ply unpainted, Ø87mm/50J)

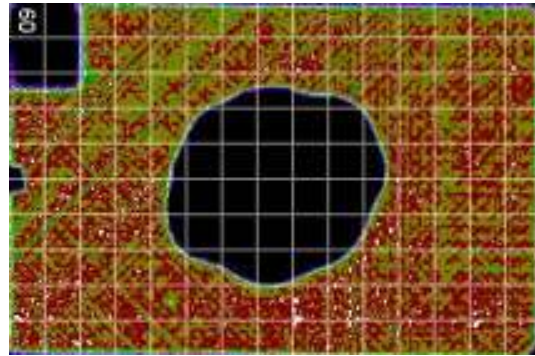


C-Scan of impact damage coupon #U24





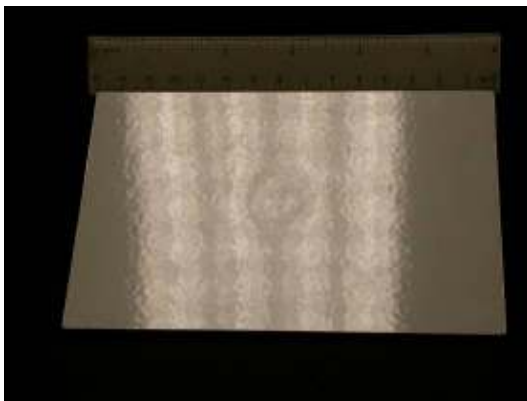
Photograph of impact damage coupon #9  
(33ply + mesh painted, Ø87mm/20J)



C-Scan of impact damage coupon #9



Metallographic section image of Ø87mm/20J impact (from Boulic, 2007)

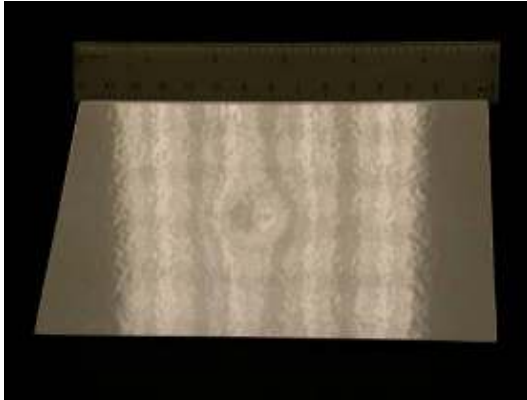


Photograph of impact damage coupon #8  
(33ply + mesh painted, Ø87mm/30J)

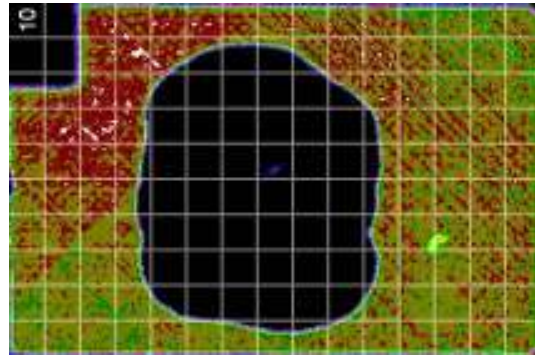
Not available

C-Scan of impact damage coupon #8





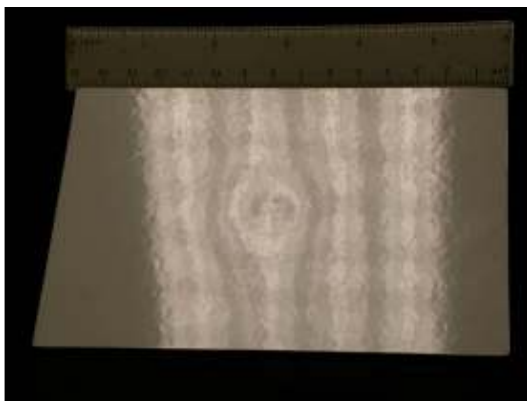
Photograph of impact damage coupon #10  
(33ply + mesh painted, Ø87mm/40J)



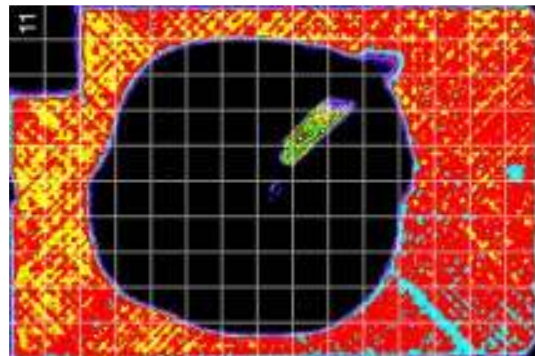
C-Scan of impact damage coupon #10



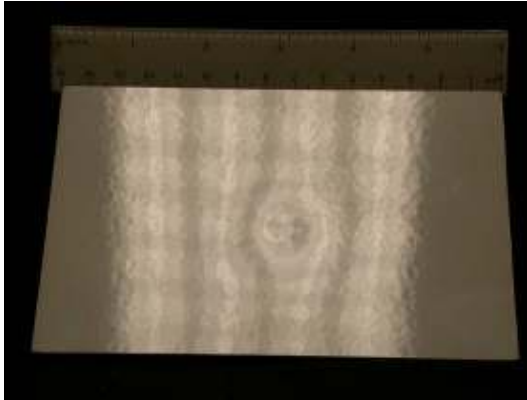
Metallographic section image of Ø87mm/40J impact (from Boulic, 2007)



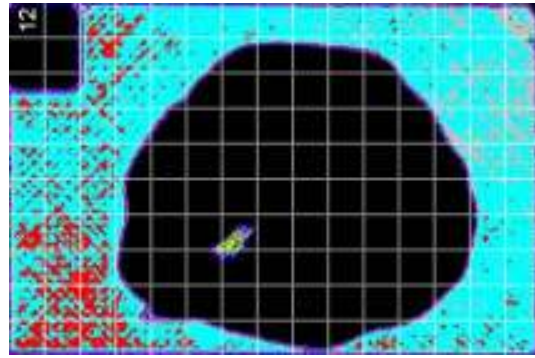
Photograph of impact damage coupon #11  
(33ply + mesh painted, Ø87mm/50J)



C-Scan of impact damage coupon #11



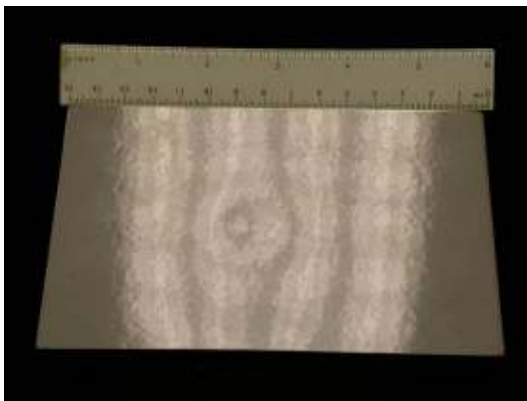
Photograph of impact damage coupon #12  
(33ply + mesh painted, Ø87mm/60J)



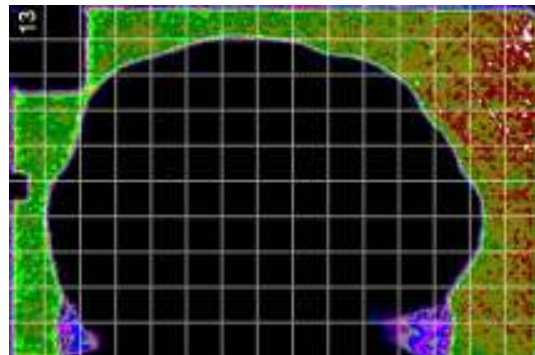
C-Scan of impact damage coupon #12



Metallographic section image of Ø87mm/60J impact (from Boulic, 2007)



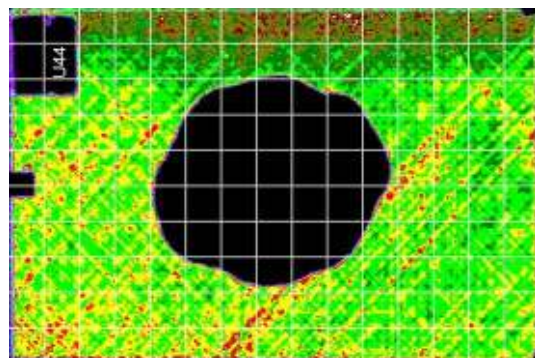
Photograph of impact damage coupon #13  
(33ply + mesh painted, Ø87mm/70J)



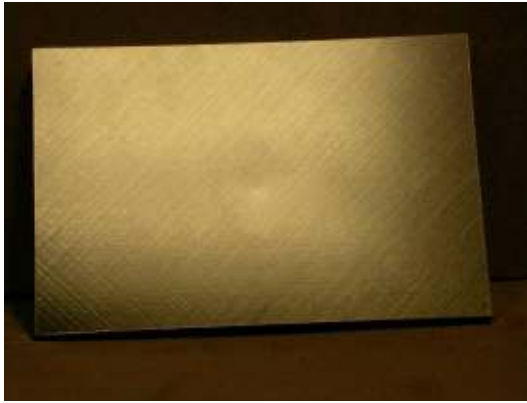
C-Scan of impact damage coupon #13



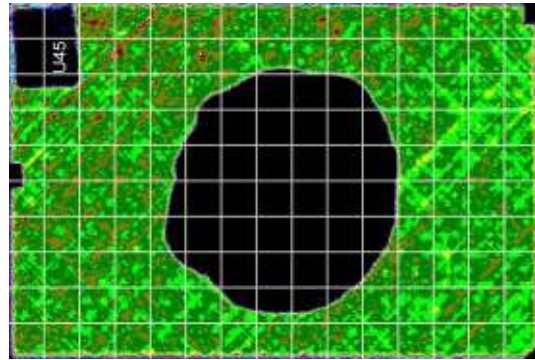
Photograph of impact damage coupon #U44  
(33ply unpainted, Ø87mm/20J)



C-Scan of impact damage coupon #U44



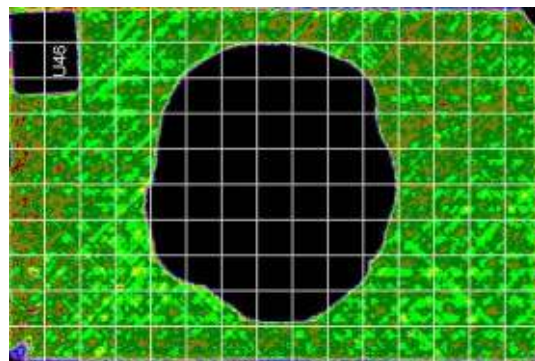
Photograph of impact damage coupon #U45  
(33ply unpainted, Ø87mm/30J)



C-Scan of impact damage coupon #U45



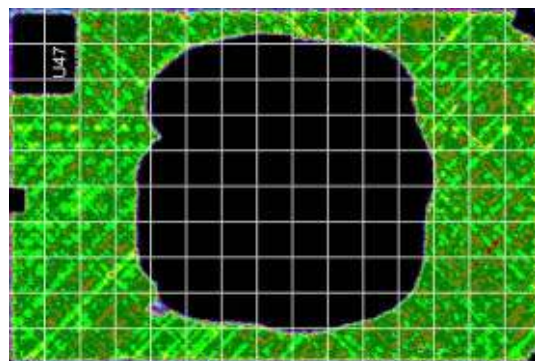
Photograph of impact damage coupon #U46  
(33ply unpainted, Ø87mm/40J)



C-Scan of impact damage coupon #U46

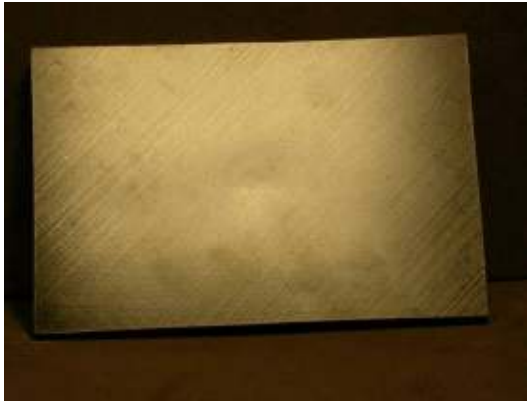


Photograph of impact damage coupon #U47  
(33ply unpainted, Ø87mm/50J)

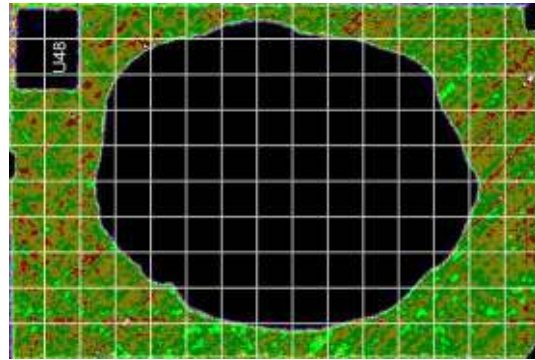


C-Scan of impact damage coupon #U47





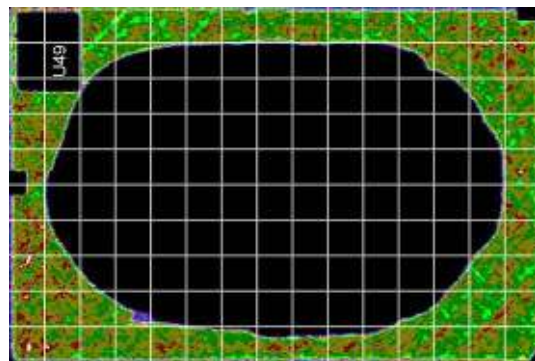
Photograph of impact damage coupon #U48  
(33ply unpainted, Ø87mm/60J)



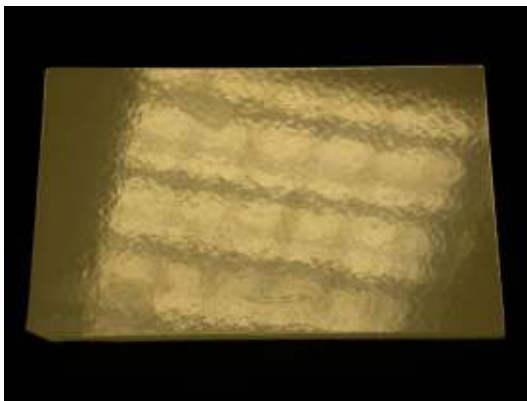
C-Scan of impact damage coupon #U48



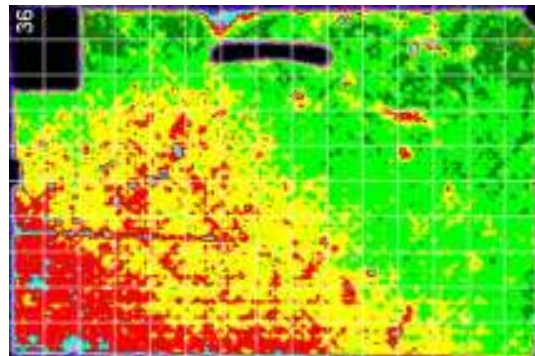
Photograph of impact damage coupon #U49  
(33ply unpainted, Ø87mm/70J)



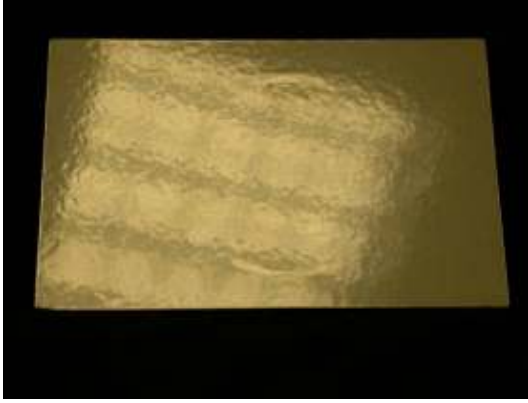
C-Scan of impact damage coupon #U49



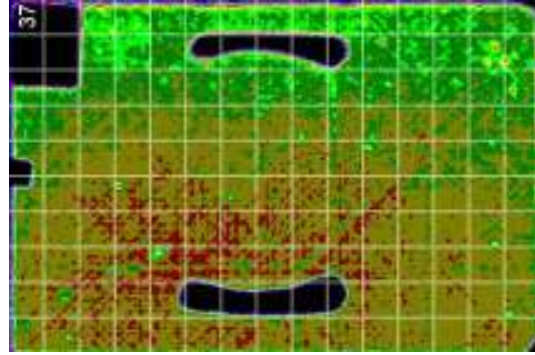
Photograph of impact damage coupon #36  
(17ply + mesh painted, Ø70mm cylinder/10J)



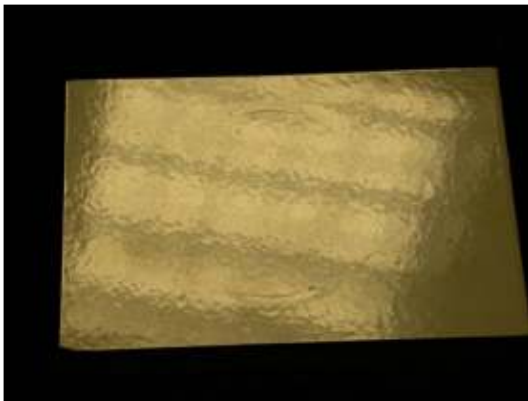
C-Scan of impact damage coupon #36



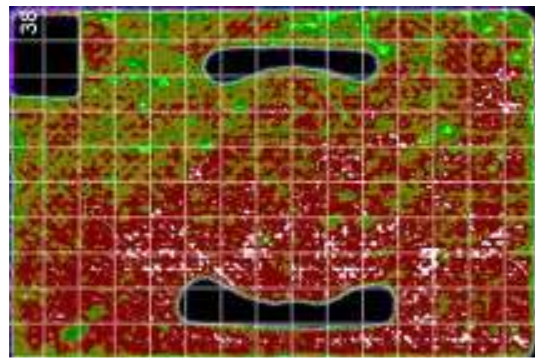
Photograph of impact damage coupon #37  
(17ply + mesh painted, Ø70mm cylinder/15J)



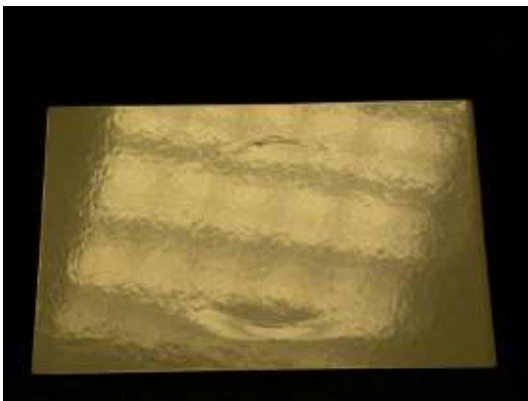
C-Scan of impact damage coupon #37



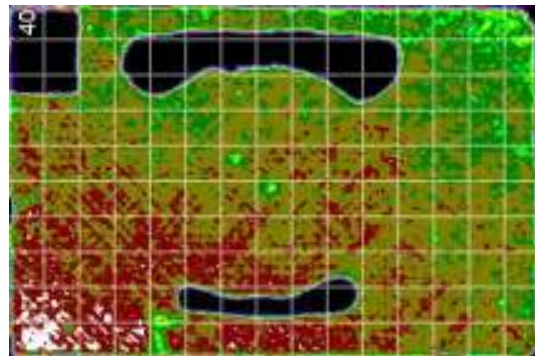
Photograph of impact damage coupon #38  
(17ply + mesh painted, Ø70mm cylinder/20J)



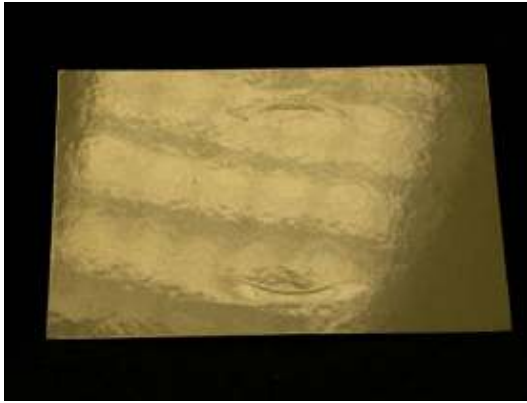
C-Scan of impact damage coupon #38



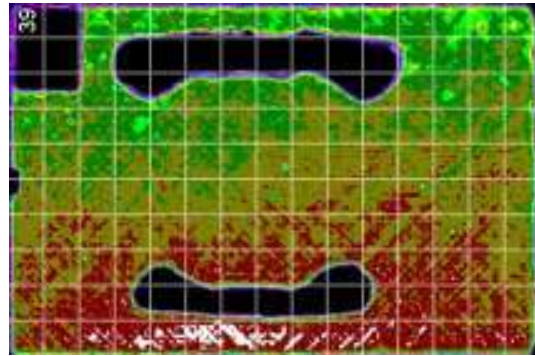
Photograph of impact damage coupon #40  
(17ply + mesh painted, Ø70mm cylinder/30J)



C-Scan of impact damage coupon #40



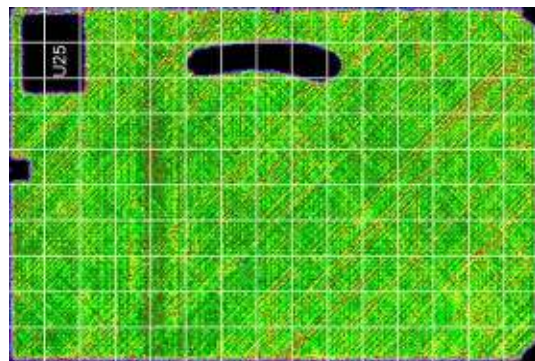
Photograph of impact damage coupon #39  
(17ply + mesh painted, Ø70mm cylinder/40J)



C-Scan of impact damage coupon #39



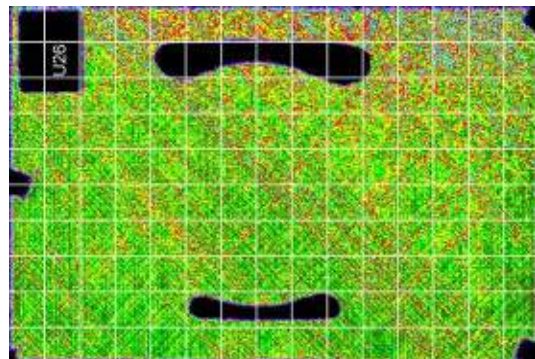
Photograph of impact damage coupon #U25  
(17ply unpainted, Ø70mm cylinder/10J)



C-Scan of impact damage coupon #U25



Photograph of impact damage coupon #U26  
(17ply unpainted, Ø70mm cylinder/15J)

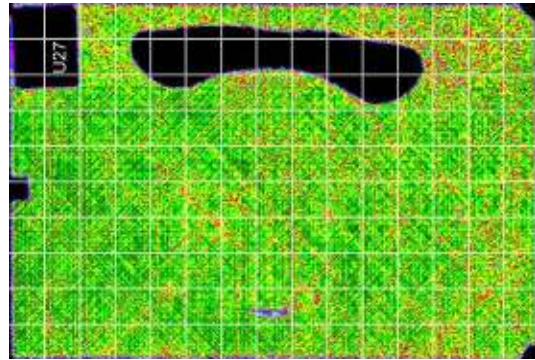


C-Scan of impact damage coupon #U26





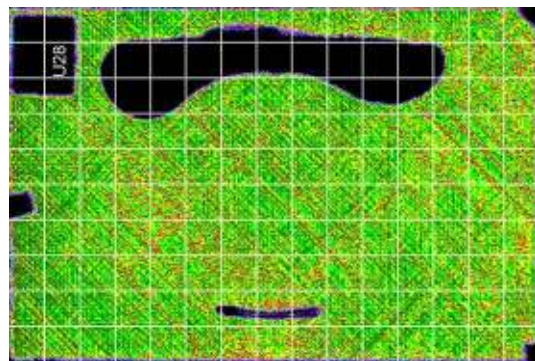
Photograph of impact damage coupon #U27  
(17ply unpainted, Ø70mm cylinder/20J)



C-Scan of impact damage coupon #U27



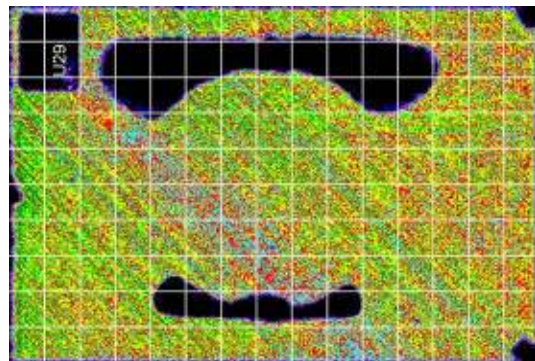
Photograph of impact damage coupon #U28  
(17ply unpainted, Ø70mm cylinder/30J)



C-Scan of impact damage coupon #U28

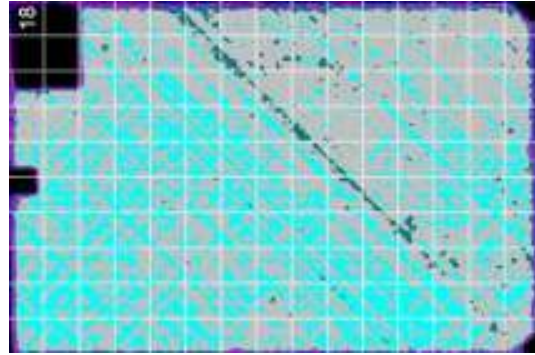


Photograph of impact damage coupon #U29  
(17ply unpainted, Ø70mm cylinder/40J)



C-Scan of impact damage coupon #U29

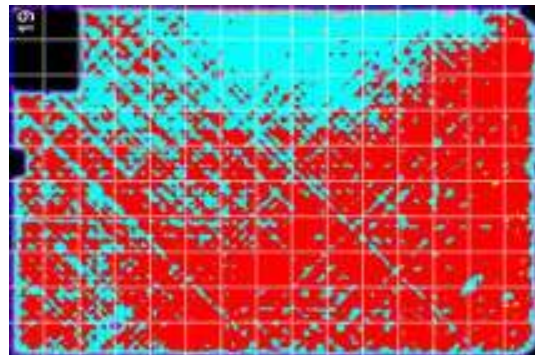
Not available



Photograph of impact damage coupon #18  
(33ply + mesh painted, Ø70mm cylinder/10J)

C-Scan of impact damage coupon #18

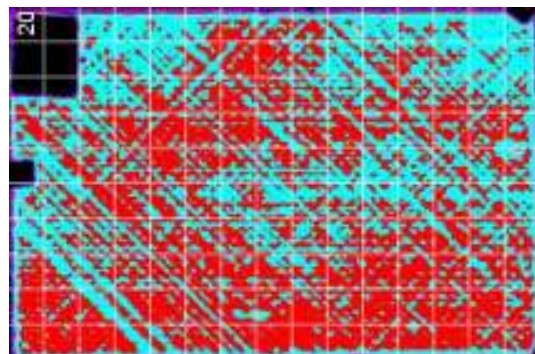
Not available



Photograph of impact damage coupon #19  
(33ply + mesh painted, Ø70mm cylinder/20J)

C-Scan of impact damage coupon #19

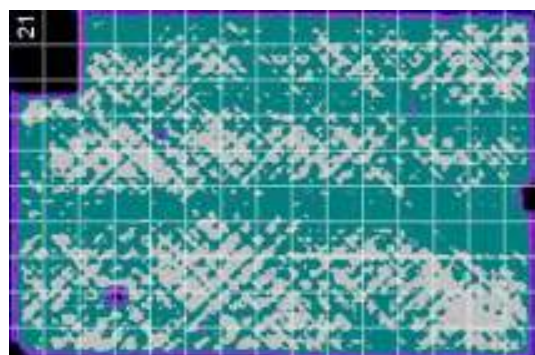
Not available



Photograph of impact damage coupon #20  
(33ply + mesh painted, Ø70mm cylinder/30J)

C-Scan of impact damage coupon #20

Not available

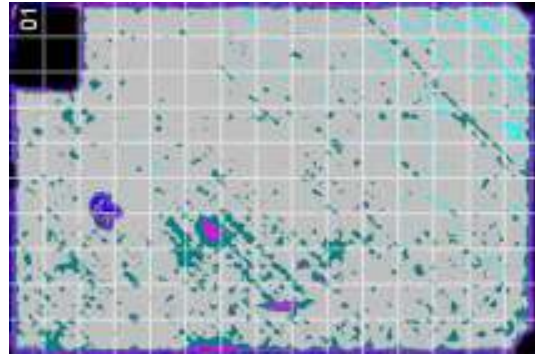


Photograph of impact damage coupon #21  
(33ply + mesh painted, Ø70mm cylinder/40J)

C-Scan of impact damage coupon #21



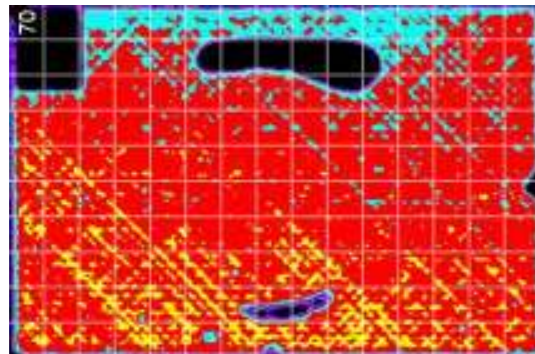
Not available



C-Scan of impact damage coupon #1

Photograph of impact damage coupon #1  
(33ply + mesh painted, Ø70mm cylinder/50J)

Not available

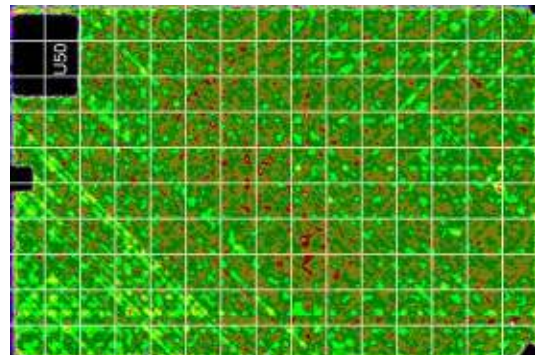


C-Scan of impact damage coupon #70

Photograph of impact damage coupon #70  
(33ply + mesh painted, Ø70mm cylinder/60J)



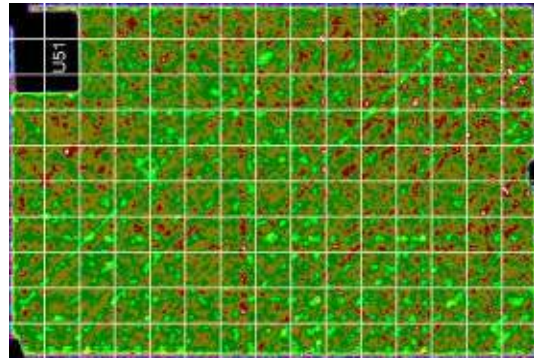
Photograph of impact damage coupon #U50  
(33ply unpainted, Ø70mm cylinder/10J)



C-Scan of impact damage coupon #U50



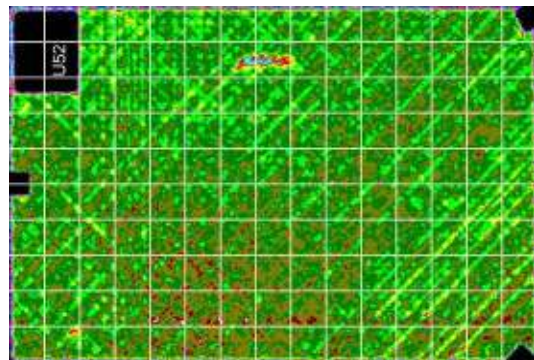
Photograph of impact damage coupon #U51  
(33ply unpainted, Ø70mm cylinder/20J)



C-Scan of impact damage coupon #U51



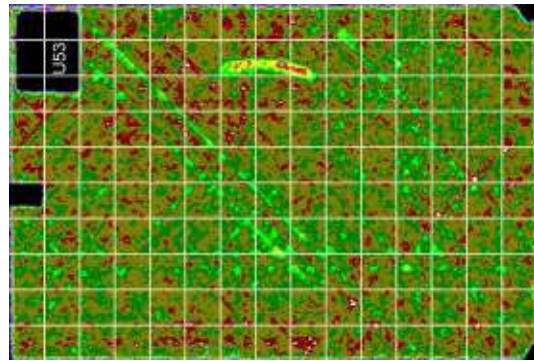
Photograph of impact damage coupon #U52  
(33ply unpainted, Ø70mm cylinder/30J)



C-Scan of impact damage coupon #U52



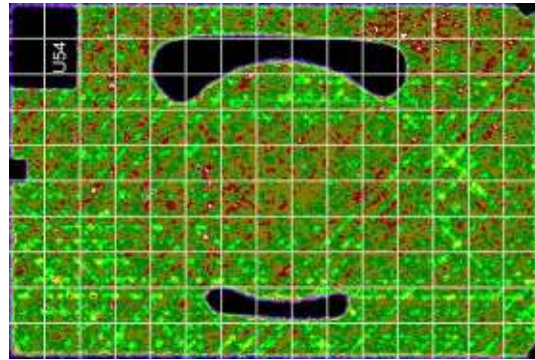
Photograph of impact damage coupon #U53  
(33ply unpainted, Ø70mm cylinder/40J)



C-Scan of impact damage coupon #U53



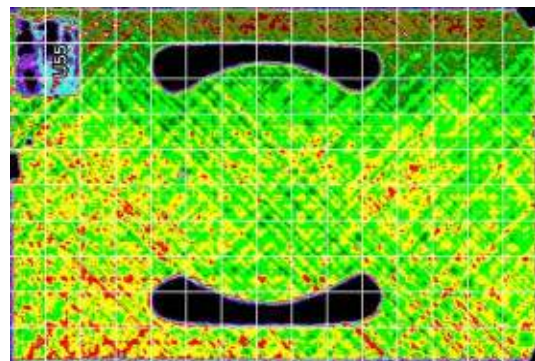
Photograph of impact damage coupon #U54  
(33ply unpainted, Ø70mm cylinder/50J)



C-Scan of impact damage coupon #U54



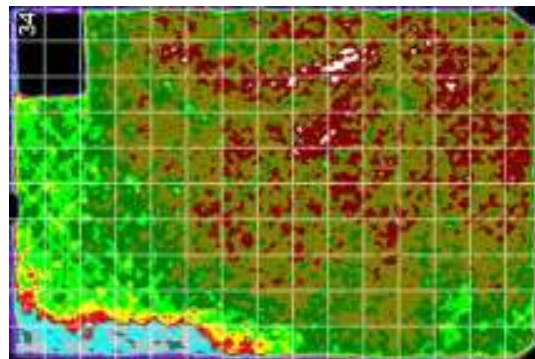
Photograph of impact damage coupon #U55  
(33ply unpainted, Ø70mm cylinder/60J)



C-Scan of impact damage coupon #U55

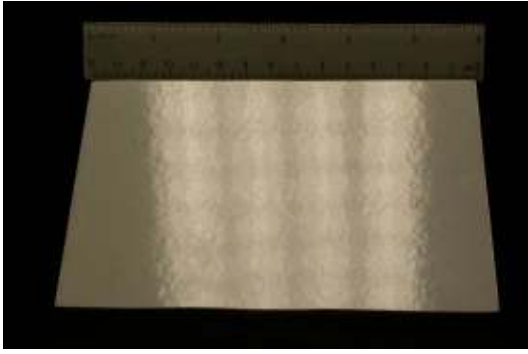


Photograph of impact damage coupon #34  
(17ply + mesh painted, tool shape/5J)

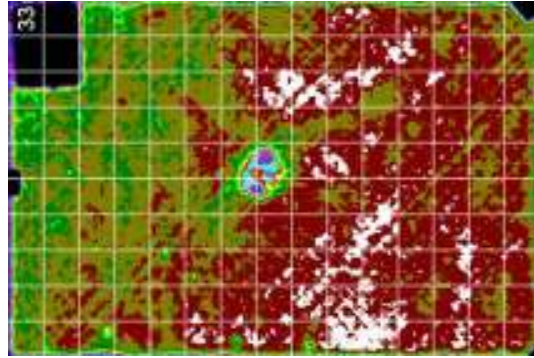


C-Scan of impact damage coupon #34

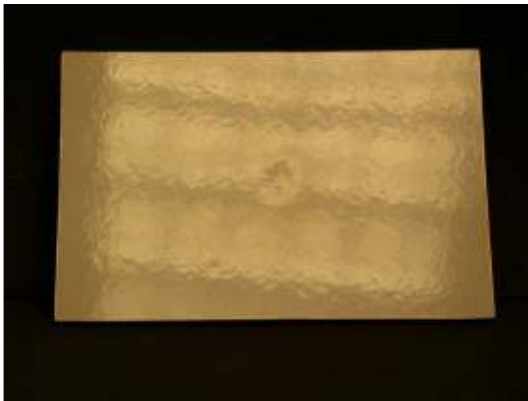




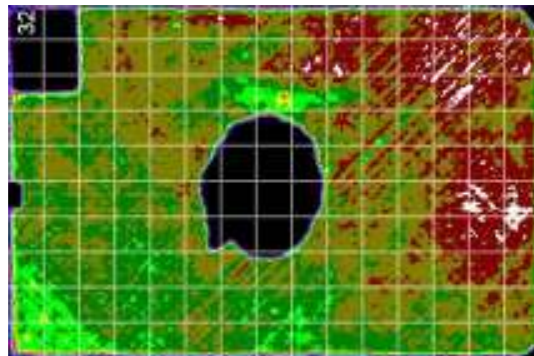
Photograph of impact damage coupon #33  
(17ply + mesh painted, tool shape/10J)



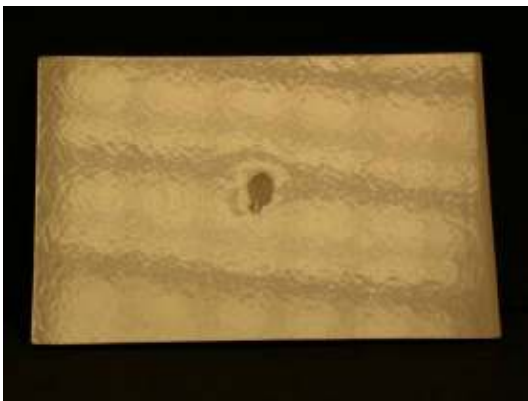
C-Scan of impact damage coupon #33



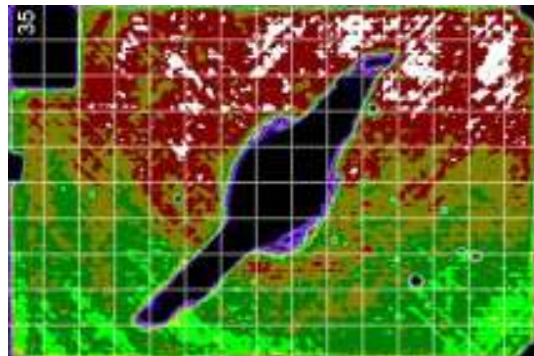
Photograph of impact damage coupon #32  
(17ply + mesh painted, tool shape/15J)



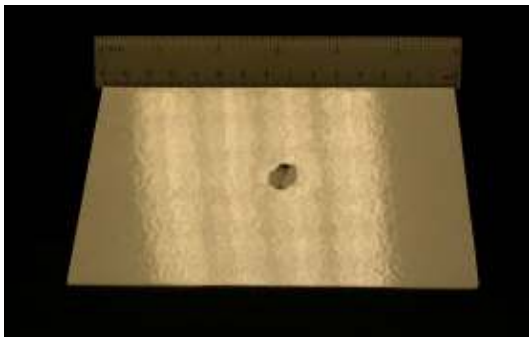
C-Scan of impact damage coupon #32



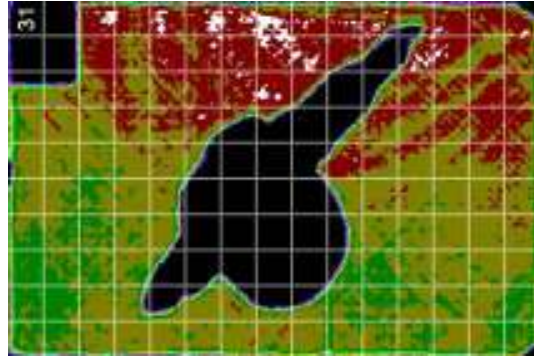
Photograph of impact damage coupon #35  
(17ply + mesh painted, tool shape/17.5J)



C-Scan of impact damage coupon #35



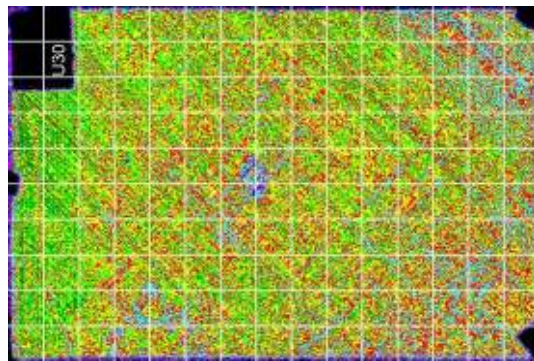
Photograph of impact damage coupon #31  
(17ply + mesh painted, tool shape/20J)



C-Scan of impact damage coupon #31



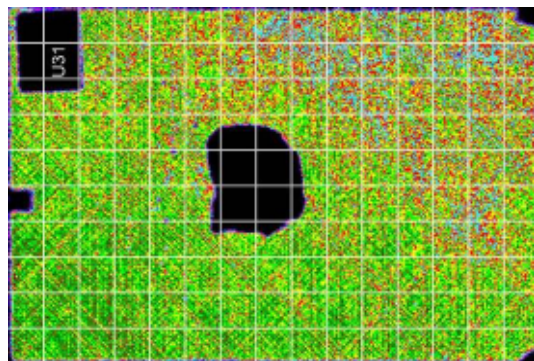
Photograph of impact damage coupon #U30  
(17ply unpainted, tool shape/5J)



C-Scan of impact damage coupon #U30



Photograph of impact damage coupon #U31  
(17ply unpainted, tool shape/10J)

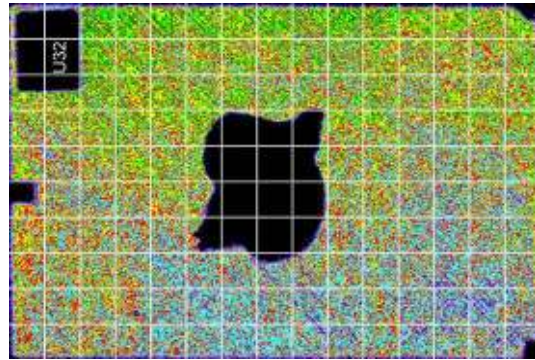


C-Scan of impact damage coupon #U31





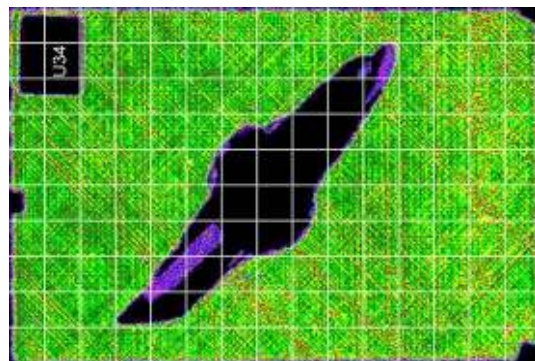
Photograph of impact damage coupon #U32  
(17ply unpainted, tool shape/15J)



C-Scan of impact damage coupon #U32



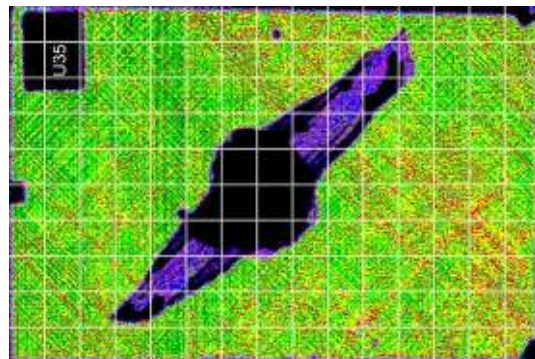
Photograph of impact damage coupon #U34  
(17ply unpainted, tool shape/17.5J)



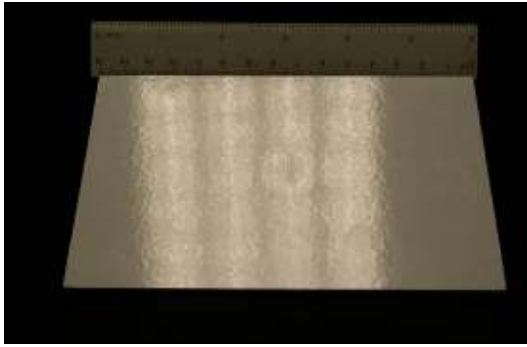
C-Scan of impact damage coupon #U34



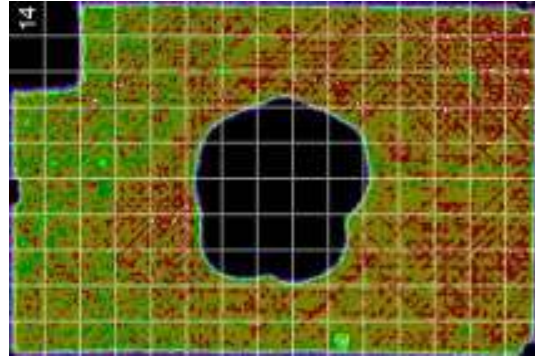
Photograph of impact damage coupon #U35  
(17ply unpainted, tool shape/20J)



C-Scan of impact damage coupon #U35

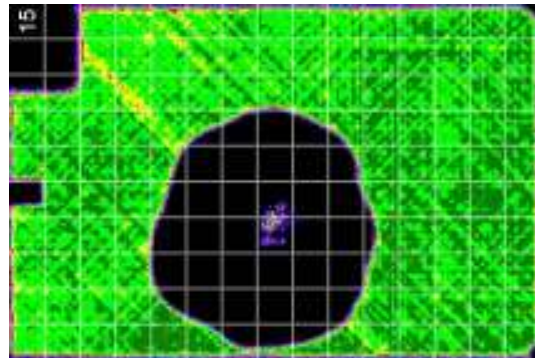


Photograph of impact damage coupon #14  
(33ply + mesh painted, tool shape/20J)



C-Scan of impact damage coupon #14

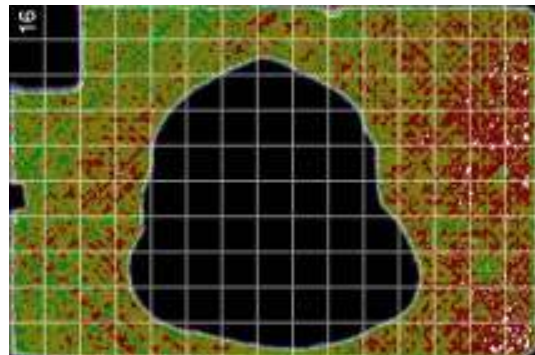
Not available



C-Scan of impact damage coupon #15

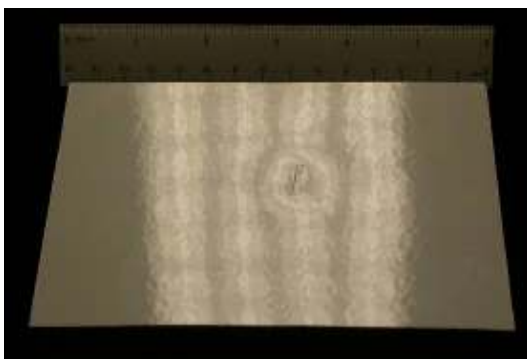
Photograph of impact damage coupon #15  
(33ply + mesh painted, tool shape/30J)

Not available

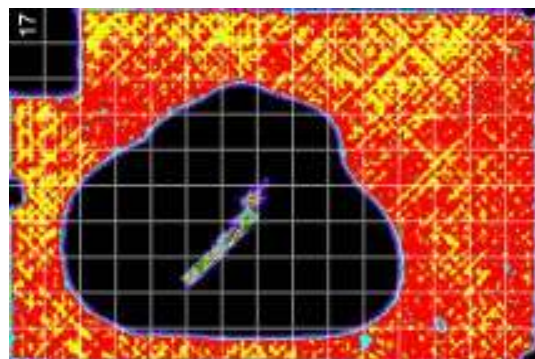


C-Scan of impact damage coupon #16

Photograph of impact damage coupon #16  
(33ply + mesh painted, tool shape/40J)



Photograph of impact damage coupon #17  
(33ply + mesh painted, tool shape/50J)

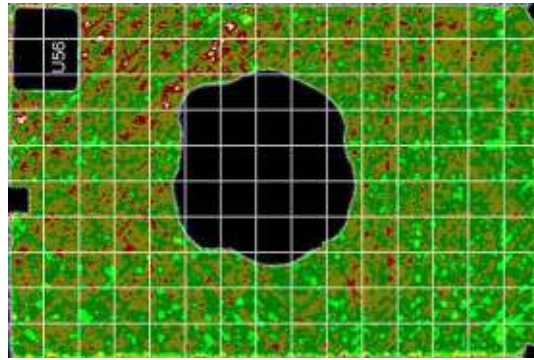


C-Scan of impact damage coupon #17





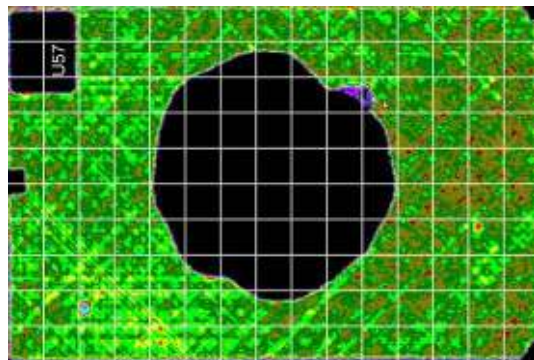
Photograph of impact damage coupon #U56  
(33ply unpainted, tool shape/20J)



C-Scan of impact damage coupon #U56



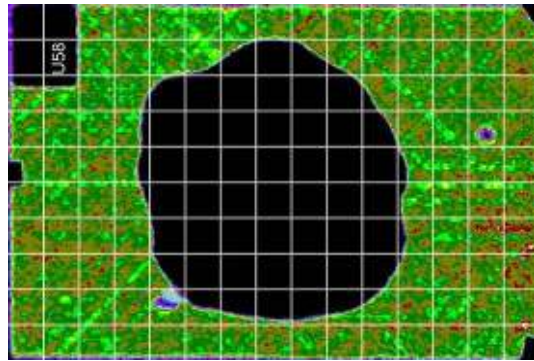
Photograph of impact damage coupon #U57  
(33ply unpainted, tool shape/30J)



C-Scan of impact damage coupon #U57



Photograph of impact damage coupon #U58  
(33ply unpainted, tool shape/40J)

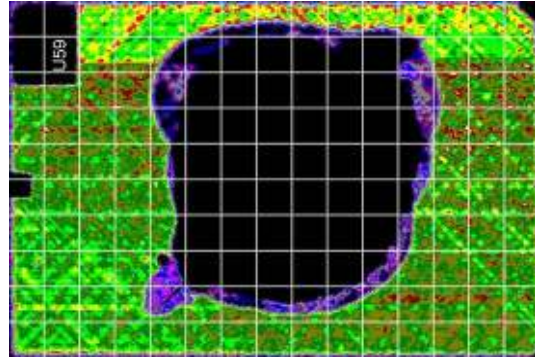


C-Scan of impact damage coupon #U58





Photograph of impact damage coupon #U59  
(33ply unpainted, tool shape/50J)



C-Scan of impact damage coupon #U59

### ***References***

Boulic. (Cranfield University), (2007), *Quantitative Morphology of Impact Damage to Composite Aircraft Structures* (unpublished report), Polytech'Orléans, France.

## Appendix E

### Hit/Miss results data from Trial 1

Flaw Size (a)	Participant Number:							Total Detections for Flaw Size (a)
	1	2	3	4	5	6	7	
1	0	0	0	0	0	0	0	0
2	0	0	0	0	0	0	0	0
3	0	0	0	0	0	0	0	0
4	0	0	0	0	0	0	0	0
5	0	0	1	1	1	1	1	5
6	1	1	1	1	1	1	1	7
7	1	0	1	1	1	1	1	6
8	1	1	1	1	1	1	1	7
9	1	0	1	1	1	1	1	6
10	1	1	1	1	1	1	1	7
11	1	0	1	1	1	1	1	6
12	1	1	1	1	1	1	1	7
13	1	0	1	1	1	1	1	6
14	1	1	1	1	1	1	1	7
15	1	1	1	1	1	1	1	7
16	1	0	1	1	1	1	1	6
17	1	1	1	1	1	1	1	7
18	1	1	1	1	1	1	1	7
19	1	1	1	1	1	1	1	7
20	1	0	1	1	1	1	1	6
21	1	1	1	1	1	1	1	7
22	1	1	1	1	1	1	1	7
23	1	1	1	1	1	1	1	7
24	1	0	1	1	1	1	1	6
25	1	0	1	1	1	1	1	6
26	1	1	1	1	1	1	1	7
27	1	1	1	1	1	1	1	7
28	1	1	1	1	1	1	1	7
29	1	1	1	1	1	1	1	7
30	1	0	1	1	1	1	1	6
Total No of Flaws Detected (per Inspector)	25	16	26	26	26	26	26	

*Hit/Miss results data from Trial 2*

Flaw Size (a)	Participant Number:															Total Detections for Flaw Size (a)	
	1	2	3	4	5	6	7	8	9	10	11	12	13	14	15		
Ø4.5mm	0.1mm d	0	0	0	0	1	0	1	0	0	0	0	0	0	0	0	2
	0.2mm d	0	0	1	1	1	1	0	0	1	0	1	1	1	1	0	9
	0.3mm d	1	1	1	1	1	1	1	1	1	1	1	1	1	1	1	15
	0.4mm d	1	0	1	1	1	1	0	1	1	1	1	1	0	1	0	11
	0.5mm d	1	1	1	1	1	1	0	1	1	1	1	1	1	1	1	14
	0.6mm d	1	1	1	1	1	1	1	1	1	1	1	1	1	1	1	15
	0.7mm d	1	1	1	1	1	1	1	1	1	1	1	1	1	1	1	15
	0.8mm d	1	1	1	1	1	1	1	1	1	1	1	1	1	1	1	15
	0.9mm d	1	1	1	1	1	1	1	1	1	1	1	1	1	1	1	15
	1.0mm d	1	1	1	1	1	1	1	1	1	1	1	1	1	1	1	15
	1.1mm d	1	1	1	1	1	1	1	1	1	1	1	1	1	1	1	15
	1.2mm d	1	1	1	1	1	1	1	1	1	1	1	1	1	1	1	15
	1.3mm d	1	1	1	1	1	1	1	1	1	1	1	1	1	1	1	15
	1.4mm d	1	1	1	1	1	1	1	1	1	1	1	1	1	1	1	15
	1.5mm d	1	1	1	1	1	1	1	1	1	1	1	1	1	1	1	15
Ø6.5mm	0.1mm d	0	0	0	1	0	1	0	0	0	1	0	1	1	0	0	5
	0.2mm d	1	1	1	1	1	1	1	1	1	1	0	1	1	1	1	14
	0.3mm d	1	1	1	1	1	1	1	1	1	1	1	1	1	1	1	15
	0.4mm d	1	1	1	1	1	1	1	0	1	1	1	1	1	1	1	14
	0.5mm d	1	1	1	1	1	1	1	1	1	1	1	1	1	1	1	15
	0.6mm d	1	1	1	1	1	1	1	1	1	1	1	1	1	1	1	15
	0.7mm d	1	1	1	1	1	1	1	1	1	1	1	1	1	1	1	15
	0.8mm d	1	1	1	1	1	1	1	1	1	1	1	1	1	1	1	15
	0.9mm d	1	1	1	1	1	1	1	1	1	1	1	1	1	1	1	15
	1.0mm d	1	1	1	1	1	1	1	1	1	1	1	1	1	1	1	15
	1.1mm d	1	1	1	1	1	1	1	1	1	1	1	1	1	1	1	15
	1.2mm d	1	1	1	1	1	1	1	1	1	1	1	1	1	1	1	15
	1.3mm d	1	1	1	1	1	1	1	1	1	1	1	1	1	1	1	15
Ø12mm	0.1mm d	0	0	0	0	0	0	0	0	0	0	0	0	0	0	0	0
	0.2mm d	1	1	1	1	1	1	1	1	1	1	1	1	1	1	1	15
	0.3mm d	1	1	1	1	1	1	1	1	1	1	1	1	1	1	1	15
	0.4mm d	1	1	1	1	1	1	1	1	1	1	1	1	1	1	1	15
	0.5mm d	1	1	1	1	1	1	1	1	1	1	1	1	1	1	1	15
	0.6mm d	1	1	1	1	1	1	1	1	1	1	1	1	1	1	1	15
	0.7mm d	1	1	1	1	1	1	1	1	1	1	1	1	1	1	1	15
	0.8mm d	1	1	1	1	1	1	1	1	1	1	1	1	1	1	1	15
	0.9mm d	1	1	1	1	1	1	1	1	1	1	1	1	1	1	1	15
	1.0mm d	1	1	1	1	1	1	1	1	1	1	1	1	1	1	1	15
	1.1mm d	1	1	1	1	1	1	1	1	1	1	1	1	1	1	1	15
Total No of Flaws Detected (per Inspector)	35	34	36	37	37	37	34	34	36	36	35	37	36	36	34		
No of False Calls	0	0	0	0	0	3	2	0	0	0	0	1	0	2	0		

*Hit/Miss results data from Trial 3*

Flaw Size (a)	Participant Number:															Total Detections for Flaw Size (a)	
	1	2	3	4	5	6	7	8	9	10	11	12	13	14	15		
Ø4.5mm	0.1mm d	0	0	0	0	0	0	0	0	0	0	0	0	0	0	0	0
	0.2mm d	1	1	1	1	1	1	1	1	1	1	1	1	0	1	0	13
	0.3mm d	1	1	1	1	1	1	1	1	1	1	1	1	0	1	0	13
	0.4mm d	1	1	1	0	1	1	1	1	1	1	1	1	0	1	0	12
	0.5mm d	1	1	1	1	1	1	1	1	1	1	1	1	1	1	1	15
	0.6mm d	1	1	1	1	1	1	1	1	1	1	1	1	1	1	1	15
	0.7mm d	1	1	1	1	1	1	1	1	1	1	1	1	1	1	1	15
	0.8mm d	1	1	1	1	1	1	1	1	1	1	1	1	1	1	1	15
	0.9mm d	1	1	1	1	1	1	1	1	1	1	1	1	1	1	1	15
	1.0mm d	1	1	1	1	1	1	1	1	1	1	1	1	1	1	1	15
	1.1mm d	1	1	1	1	1	1	1	1	1	1	1	1	1	1	1	15
	1.2mm d	1	1	1	1	1	1	1	1	1	1	1	1	1	1	1	15
	1.3mm d	1	1	1	1	1	1	1	1	1	1	1	1	1	1	1	15
	1.4mm d	1	1	1	1	1	1	1	1	1	1	1	1	1	1	1	15
	1.5mm d	1	1	1	1	1	1	1	1	1	1	1	1	1	1	1	15
Ø6.5mm	0.1mm d	0	0	0	0	0	0	1	0	0	0	0	0	0	0	1	
	0.2mm d	1	1	1	1	1	1	1	1	1	1	1	1	1	1	15	
	0.3mm d	1	1	1	1	1	1	1	1	1	1	1	1	1	1	15	
	0.4mm d	1	1	1	1	1	1	1	1	1	1	1	1	1	1	15	
	0.5mm d	1	1	1	1	1	1	1	1	1	1	1	1	1	1	15	
	0.6mm d	1	1	1	1	1	1	1	1	1	1	1	1	1	1	15	
	0.7mm d	1	1	1	1	1	1	1	1	1	1	1	1	1	1	15	
	0.8mm d	1	1	1	1	1	1	1	1	1	1	1	1	1	1	15	
	0.9mm d	1	1	1	1	1	1	1	1	1	1	1	1	1	1	15	
	1.0mm d	1	1	1	1	1	1	1	1	1	1	1	1	1	1	15	
	1.1mm d	1	1	1	1	1	1	1	1	1	1	1	1	1	1	15	
	1.2mm d	1	1	1	1	1	1	1	1	1	1	1	1	1	1	15	
	1.3mm d	1	1	1	1	1	1	1	1	1	1	1	1	1	1	15	
Ø12mm	0.1mm d	1	0	0	1	0	0	0	1	0	0	0	0	0	0	3	
	0.2mm d	1	1	1	1	1	1	1	1	1	1	1	1	1	1	15	
	0.3mm d	1	1	1	1	1	1	1	1	1	1	1	1	1	1	15	
	0.4mm d	1	1	1	1	1	1	1	1	1	1	1	1	1	1	15	
	0.5mm d	1	1	1	1	1	1	1	1	1	1	1	1	1	1	15	
	0.6mm d	1	1	1	1	1	1	1	1	1	1	1	1	1	1	15	
	0.7mm d	1	1	1	1	1	1	1	1	1	1	1	1	1	1	15	
	0.8mm d	1	1	1	1	1	1	1	1	1	1	1	1	1	1	15	
	0.9mm d	1	1	1	1	1	1	1	1	1	1	1	1	1	1	15	
	1.0mm d	1	1	1	1	1	1	1	1	1	1	1	1	1	1	15	
	1.1mm d	1	1	1	1	1	1	1	1	1	1	1	1	1	1	15	
Total No of Flaws Detected (per Inspector)	37	36	36	36	36	36	37	37	36	36	36	36	33	36	33		
No of False Calls	0	0	0	1	0	0	0	1	0	0	0	0	2	0	0		

*Hit/Miss results data from Trial 4*

Flaw Diameter (mm)	Participant number:														Total Detections
	1	2	3	4	5	6	7	8	9	10	11	12	13	14	
03 BE	0	0	1	0	0	0	0	0	0	0	0	0	0	0	1
03 HE	0	0	0	0	0	1	1	0	0	0	0	0	0	0	2
04 BE	1	1	1	1	1	1	1	0	1	1	1	1	1	1	13
04 HE	1	1	1	1	0	0	1	1	0	1	1	0	0	0	8
05 BE (a)	1	1	1	1	0	1	1	0	1	1	1	1	0	1	11
05 BE(b)	0	0	0	1	1	1	0	1	0	1	0	1	0	1	7
05 HE(a)	0	0	1	0	0	1	1	0	1	1	1	1	1	1	9
05 HE(b)	1	1	1	1	1	1	1	1	1	1	1	1	1	1	14
06 BE	1	1	1	0	1	1	1	1	1	1	0	1	0	1	11
06 HE	1	1	0	1	1	0	1	0	1	1	1	1	1	1	11
07 BE	1	1	1	0	0	1	1	0	1	1	1	1	0	1	10
07 HE	1	1	1	1	1	1	1	0	1	1	1	1	1	0	12
08 BE	1	1	1	1	1	1	1	0	1	1	1	0	1	1	12
08 HE	0	0	1	0	0	1	0	1	0	0	0	1	1	0	5
09 BE	1	1	1	1	1	1	1	0	0	1	1	1	1	1	12
09 HE	1	1	1	1	1	1	1	0	0	1	1	1	1	1	12
10 BE (a)	1	0	1	1	0	1	1	1	1	1	1	1	1	1	12
10 BE (b)	1	1	1	1	0	1	0	1	1	1	1	1	1	1	12
10 HE (a)	1	1	1	0	1	1	1	1	1	1	1	1	1	1	13
10 HE (b)	1	1	1	1	1	1	1	0	0	1	1	1	1	1	12
12 BE	1	1	1	1	1	1	1	1	1	1	1	0	1	1	13
12 HE	1	1	0	1	1	1	1	1	1	1	1	0	1	1	12
14 BE	1	1	1	1	0	1	1	0	1	1	1	1	1	1	12
14 HE	1	1	1	1	0	1	0	1	1	1	1	0	1	1	11
16 BE (a)	1	1	1	1	1	1	1	0	1	1	1	0	1	1	12
16 BE (b)	1	0	0	0	1	0	0	1	0	0	0	1	1	1	6
16 HE (a)	1	1	1	1	1	1	1	1	1	1	1	1	1	1	14
16 HE (b)	1	1	0	1	1	1	0	0	0	1	1	0	0	1	8
18 BE	0	0	1	0	0	1	1	0	0	1	1	0	0	0	5
18 HE	1	0	1	1	1	1	1	0	1	1	1	0	1	1	11
20 BE	1	0	1	0	0	1	0	0	1	0	1	1	1	0	7
20 HE	0	1	1	1	1	1	1	1	0	1	1	1	0	1	11
22 BE	0	0	0	0	0	1	0	0	0	0	0	0	0	0	1
22 HE	1	1	1	1	0	1	1	1	0	1	1	1	1	1	12
24 BE	0	1	0	1	1	1	0	1	1	0	1	0	0	0	7
24 HE	0	1	1	1	1	1	1	0	1	1	1	1	0	1	11
26 BE	0	0	0	0	0	1	0	0	0	0	0	0	0	0	1
26 HE	0	0	1	1	0	1	0	0	1	1	1	1	0	1	8
28 BE	0	0	1	0	0	1	0	0	1	0	0	0	0	1	4
28 HE	0	0	0	1	0	0	0	0	0	0	0	0	0	0	1
30 BE (a)	0	0	0	0	0	0	0	0	0	0	0	0	0	0	0
30 BE (b)	0	0	0	0	0	0	0	0	0	0	0	0	0	1	1
30 HE (a)	0	0	0	1	0	1	1	0	1	0	0	0	1	1	6
30 HE (b)	1	0	1	1	1	0	0	1	1	1	0	1	1	0	9
Total Detections	27	25	31	29	22	36	27	17	26	31	30	25	25	31	
False Calls	0	1	1	1	0	1	0	3	0	1	1	1	0	1	

BE = Blended edge flaw HE = Hard edge flaw (a) & (b) used to denote flaws of same size

## ***Appendix F***

### ***POD curve & RIM calculations***

The data from the series 1 visual inspection trials were plotted using the following log-odds POD function, as given by *Berens & Hovey 1982* in *Bullock et al. 1994*.

$$P_i = \frac{\exp(\alpha + \beta \ln(a_i))}{1 + \exp(\alpha + \beta \ln(a_i))}$$

Where  $P_i$  is the probability of detection of flaw  $i$ ,  $a_i$  is the flaw size and  $\alpha$  &  $\beta$  are constant parameters.

In order to determine values for  $\alpha$  &  $\beta$ , the range interval method (RIM) was used (see *Bullock et al. 1994*). Regression plots were produced by calculating the following values for each flaw size interval:

$$Y_i = \ln\left(\frac{P_i}{1 - P_i}\right), X_i = \ln(a_i)$$

Where  $p_i$  is the proportion of flaws detected,  $a_i$  is the flaw size and  $i$  is the interval size.

The values of  $\alpha$  &  $\beta$  were derived by fitting the regression plot with a linear regression line constructed using the following equation (as per *Bullock et al. 1994*)

$$Y = \alpha + \beta X$$

### ***References***

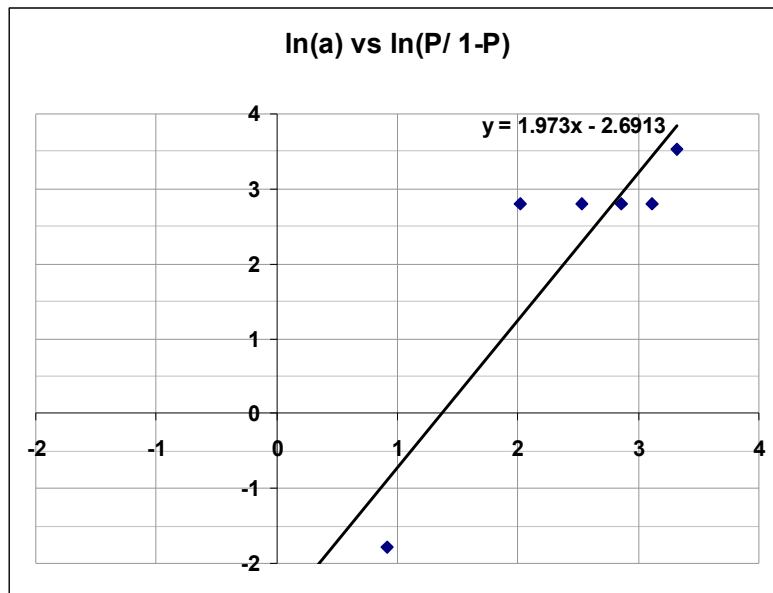
- Berens, A. P. and Hovey, P. W. (1982), "Characterization of NDE reliability", *Review of progress in quantitative nondestructive evaluation. Volume 1 - Proceedings of the Eighth U.S. Air Force/Defense Advanced Research Projects Agency Symposium on Quantitative Nondestructive Evaluation, Boulder, CO; United States; 2-7 Aug. 1981*, New York, Plenum Press,.
- Bullock, M., Forsyth, D. and Fahr, A. (1994), *Statistical Functions and Computational Procedures for the POD Analysis of Hit/Miss NDI Data*, LTR-ST-1964, Institute for Aerospace Research, National Research Council Canada, Ottawa, Ontario.

POD curve calculations for Trial 1

Regression plot values:

<b>Y = ln(P/1-P), X = ln(a) RIM values</b>						
Flaw Width Interval	Interval Value (a)	ln(a)	No. of flaws	No. Detected	P	ln(P/ 1-P)
1mm – 5mm	2.5	0.92	35	5	0.14	-1.79
5mm -10mm	7.5	2.01	35	33	0.94	2.80
10mm – 15mm	12.5	2.53	35	33	0.94	2.80
15mm – 20mm	17.5	2.86	35	33	0.94	2.80
20mm – 25mm	22.5	3.11	35	33	0.94	2.80
25mm – 30mm	27.5	3.31	35	34	0.97	3.53

Regression plot:



POD Function values

<b>Values for:</b>			
$P = \frac{\text{EXP}(A + B\ln(a))}{1 + \text{EXP}(A + B\ln(a))}$			
Interval Size (a)	P	Alpha (A) ( $\alpha$ )	Beta (B) ( $\beta$ )
2.5	0.29		
7.5	0.78		
12.5	0.91		
17.5	0.95		
22.5	0.97		
27.5	0.98		
30	0.98		

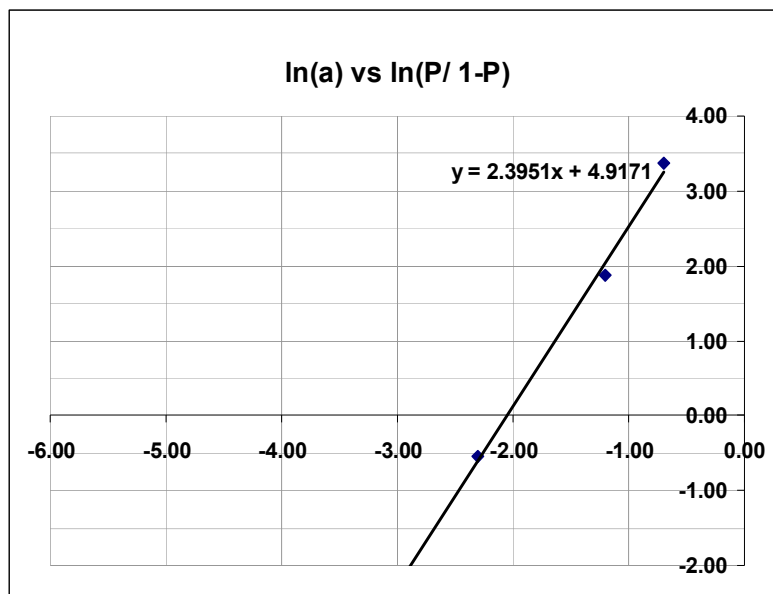
**POD curve calculations for Trial 2**

**Trial 2 – 4.5 mm wide flaws**

Regression plot values:

Y = ln(P/1-P), X = ln(a) RIM values						
Flaw Depth Interval	Interval Value (a)	ln(a)	No. of flaws	No. Detected	P	ln(P/ 1-P)
0mm - 0.2mm	0.1	-2.30	30	11	0.37	-0.55
0.2mm - 0.4mm	0.3	-1.20	30	26	0.87	1.87
0.4mm - 0.6mm	0.5	-0.69	30	29	0.97	3.37
0.6mm - 0.8mm	0.7	-0.36	30	30	1.00	N/A
0.8mm - 1.0mm	0.9	-0.11	30	30	1.00	N/A
1.0mm - 1.2mm	1.1	0.10	30	30	1.00	N/A
1.2mm - 1.4mm	1.3	0.26	30	30	1.00	N/A
1.4mm - 1.6mm	1.5	0.41	15	15	1.00	N/A

Regression plot:





POD Function values

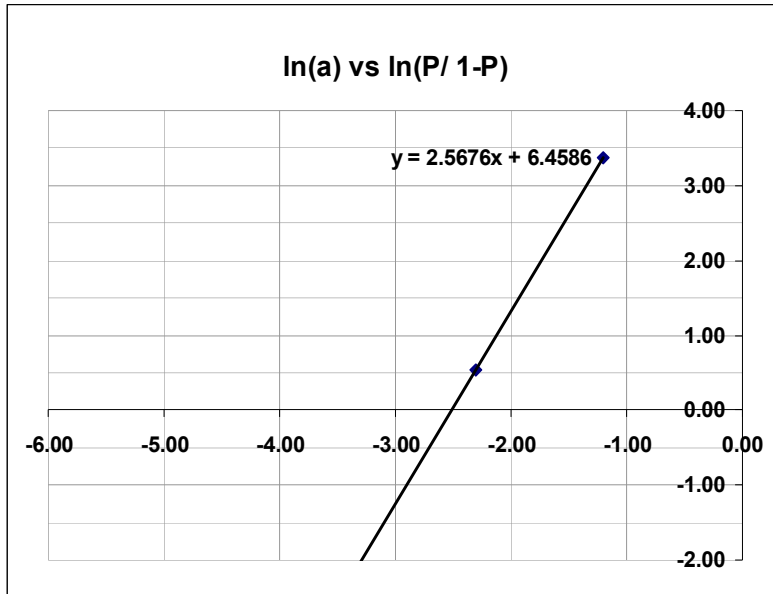
Values for:			
$P = \frac{\text{EXP}(A + B\ln(a))}{1 + \text{EXP}(A + B\ln(a))}$			
Interval Size (a)	P	Alpha (A) ( $\alpha$ )	Beta (B) ( $\beta$ )
0.1	0.35	4.9171	2.3951
0.3	0.88		
0.5	0.96		
0.7	0.98		
0.9	0.99		
1.1	0.99		
1.3	1.00		
1.5	1.00		

**Trial 2 – 6.5 mm wide flaws**

Regression plot values:

Y = ln(P/1-P), X = ln(a) RIM values						
Flaw Depth Interval	Interval Value (a)	ln(a)	No. of flaws	No. Detected	P	ln(P/ 1-P)
0mm - 0.2mm	0.1	-2.30	30	19	0.63	0.55
0.2mm - 0.4mm	0.3	-1.20	30	29	0.97	3.37
0.4mm - 0.6mm	0.5	-0.69	30	30	1.00	N/A
0.6mm - 0.8mm	0.7	-0.36	30	30	1.00	N/A
0.8mm - 1.0mm	0.9	-0.11	30	30	1.00	N/A
1.0mm - 1.2mm	1.1	0.10	30	30	1.00	N/A
1.2mm - 1.4mm	1.3	0.26	15	15	1.00	N/A

Regression plot:



POD Function values:

**Values for:**

$$P = \frac{\text{EXP}(A + B\ln(a))}{1 + \text{EXP}(A + B\ln(a))}$$

Interval Size (a)	P	Alpha (A) ( $\alpha$ )	Beta (B) ( $\beta$ )
0.1	0.63		
0.3	0.97		
0.5	0.99		
0.7	1.00		
0.9	1.00		
1.1	1.00		
1.3	1.00		

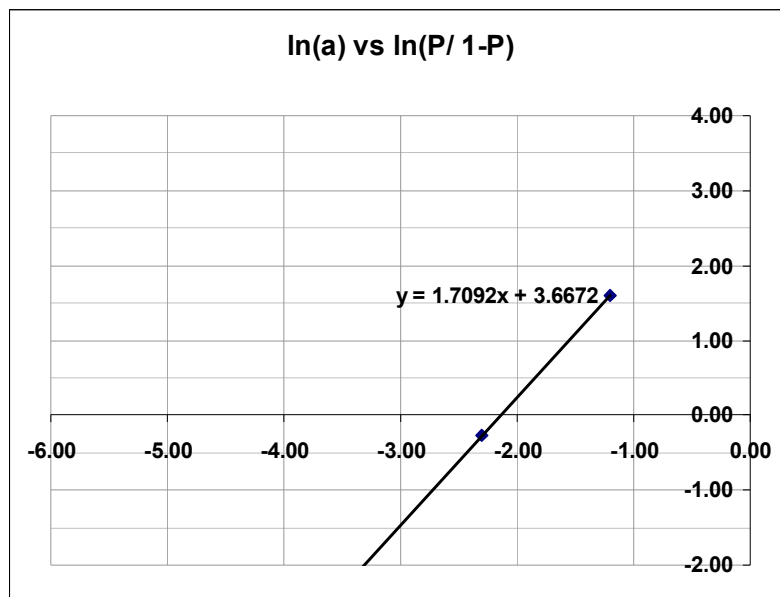
**POD curve calculations for Trial 3**

**Trial 3 – 4.5 mm wide flaws**

Regression plot values:

Y = ln(P/1-P), X = ln(a) RIM values						
Flaw Depth Interval	Interval Value (a)	ln(a)	No. of flaws	No. Detected	P	ln(P/ 1-P)
0mm - 0.2mm	0.1	-2.30	30	13	0.43	-0.27
0.2mm - 0.4mm	0.3	-1.20	30	25	0.83	1.61
0.4mm - 0.6mm	0.5	-0.69	30	30	1.00	N/A
0.6mm - 0.8mm	0.7	-0.36	30	30	1.00	N/A
0.8mm - 1.0mm	0.9	-0.11	30	30	1.00	N/A
1.0mm - 1.2mm	1.1	0.10	30	30	1.00	N/A
1.2mm - 1.4mm	1.3	0.26	30	30	1.00	N/A
1.4mm - 1.6mm	1.5	0.41	15	15	1.00	N/A

Regression plot:



POD Function values

<b>Values for:</b>			
$P = \frac{\text{EXP}(A + B \ln(a))}{1 + \text{EXP}(A + B \ln(a))}$			
Interval Size (a)	<b>P</b>	<b>Alpha (A) (<math>\alpha</math>)</b> 3.6672	<b>Beta (B) (<math>\beta</math>)</b> 1.7092
0.1	0.43		
0.3	0.83		
0.5	0.92		
0.7	0.96		
0.9	0.97		
1.1	0.98		
1.3	0.98		
1.5	0.99		

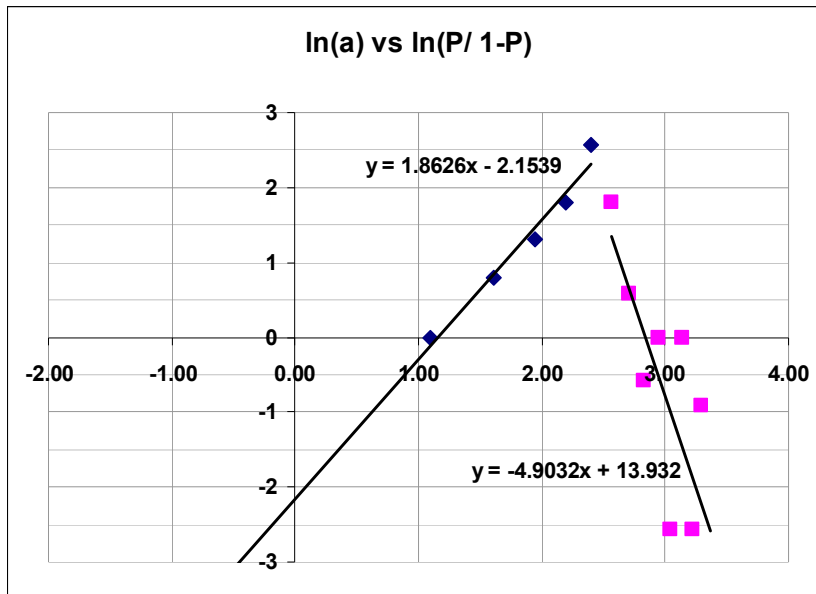
**POD curve calculations for Trial 4**

**Trial 4 – blended edge flaws**

Regression plot values:

<b>Y = ln(P/1-P), X = ln(a) RIM values</b>						
Flaw Depth Interval	Interval Value (a)	ln(a)	No. of flaws	No. Detected	P	ln(P/ 1-P)
2mm - 4mm	3	1.10	28	14	0.50	0
4mm - 6mm	5	1.61	42	29	0.69	0.80
6mm - 8mm	7	1.95	28	22	0.79	1.30
8mm - 10mm	9	2.20	42	36	0.86	1.79
10mm - 12mm	11	2.40	14	13	0.93	2.56
12mm - 14mm	13	2.56	14	12	0.86	1.79
14mm - 16mm	15	2.71	28	18	0.64	0.59
16mm - 18mm	17	2.83	14	5	0.36	-0.59
18mm - 20mm	19	2.94	14	7	0.50	0.00
20mm - 22mm	21	3.04	14	1	0.07	-2.56
22mm - 24mm	23	3.14	14	7	0.50	0.00
24mm - 26mm	25	3.22	14	1	0.07	-2.56
26mm - 28mm	27	3.30	14	4	0.29	-0.92
28mm - 30mm	29	3.37	28	1	0.04	-3.30

Regression plot:



POD Function values:

**Values for:**

$$P = \frac{\text{EXP}(A + B \ln(a))}{1 + \text{EXP}(A + B \ln(a))}$$

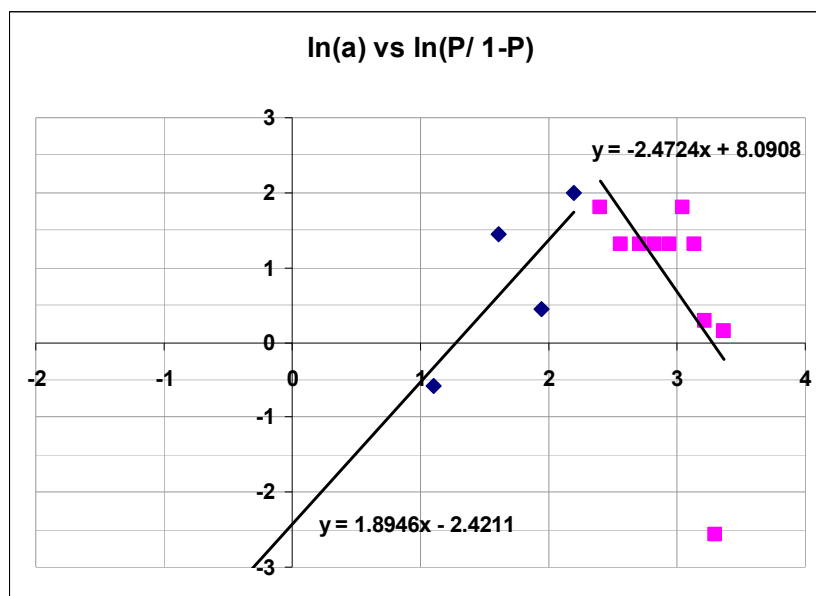
Interval Size (a)	P	Alpha (A) ( $\alpha$ )	Beta (B) ( $\beta$ )
3	0.47	-2.1539	1.8626
5	0.70		
7	0.81		
9	0.87		
11	0.91		
13	0.80	13.932	-4.9032
15	0.66		
17	0.51		
19	0.38		
21	0.27		
23	0.19		
25	0.14		
27	0.10		
29	0.07		

### Trial 4 – hard edge flaws

Regression plot values:

Y = ln(P/1-P), X = ln(a) RIM values						
Flaw Depth Interval	Interval Value (a)	ln(a)	No. of flaws	No. Detected	P	ln(P/ 1-P)
2mm - 4mm	3	1.10	28	10	0.36	-0.59
4mm - 6mm	5	1.61	42	34	0.81	1.45
6mm - 8mm	7	1.95	28	17	0.61	0.44
8mm - 10mm	9	2.20	42	37	0.88	2.00
10mm - 12mm	11	2.40	14	12	0.86	1.79
12mm - 14mm	13	2.56	14	11	0.79	1.30
14mm - 16mm	15	2.71	28	22	0.79	1.30
16mm - 18mm	17	2.83	14	11	0.79	1.30
18mm - 20mm	19	2.94	14	11	0.79	1.30
20mm - 22mm	21	3.04	14	12	0.86	1.79
22mm - 24mm	23	3.14	14	11	0.79	1.30
24mm - 26mm	25	3.22	14	8	0.57	0.29
26mm - 28mm	27	3.30	14	1	0.07	-2.56
28mm - 30mm	29	3.37	28	15	0.54	0.14

Regression plot:



POD Function values:

Values for:			
$P = \frac{\text{EXP}(A + B \ln(a))}{1 + \text{EXP}(A + B \ln(a))}$			
Interval Size (a)	P	Alpha (A) ( $\alpha$ )	Beta (B) ( $\beta$ )
3	0.42	-2.4211	1.8946
5	0.65		
7	0.78		
9	0.85		
11	0.90	8.0908	-2.4724
13	0.85		
15	0.80		
17	0.75		
19	0.69		
21	0.64		
23	0.58		
25	0.53		
27	0.49		
29	0.44		













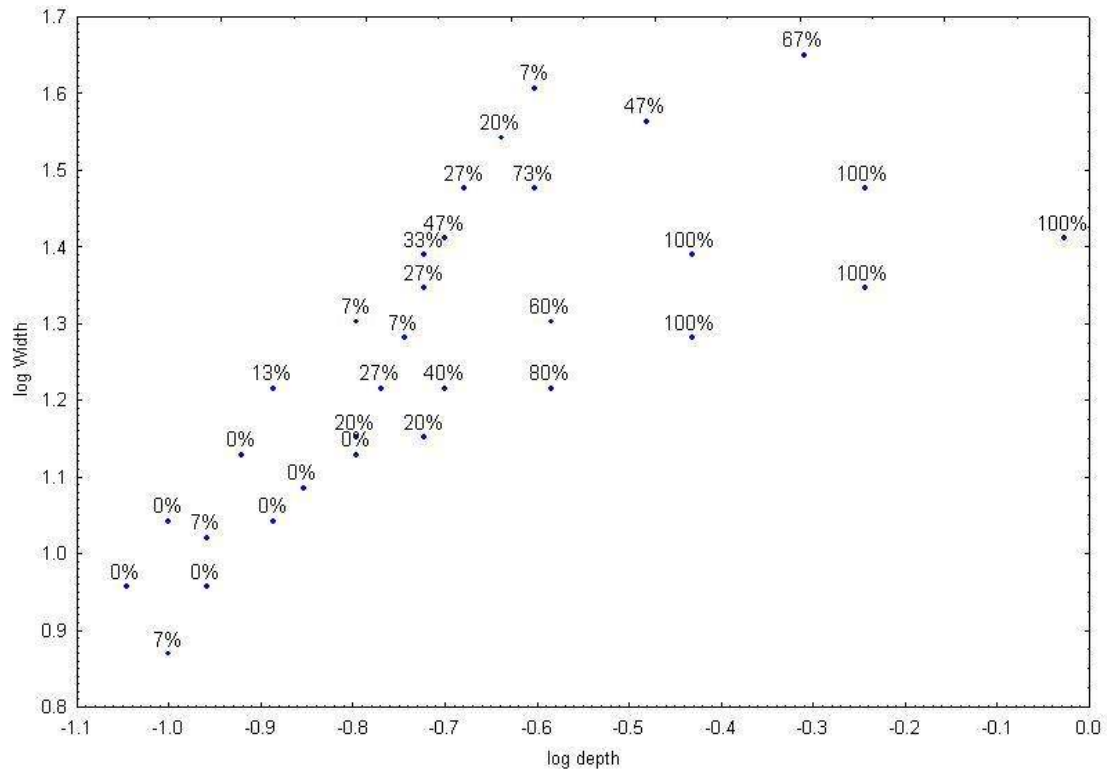




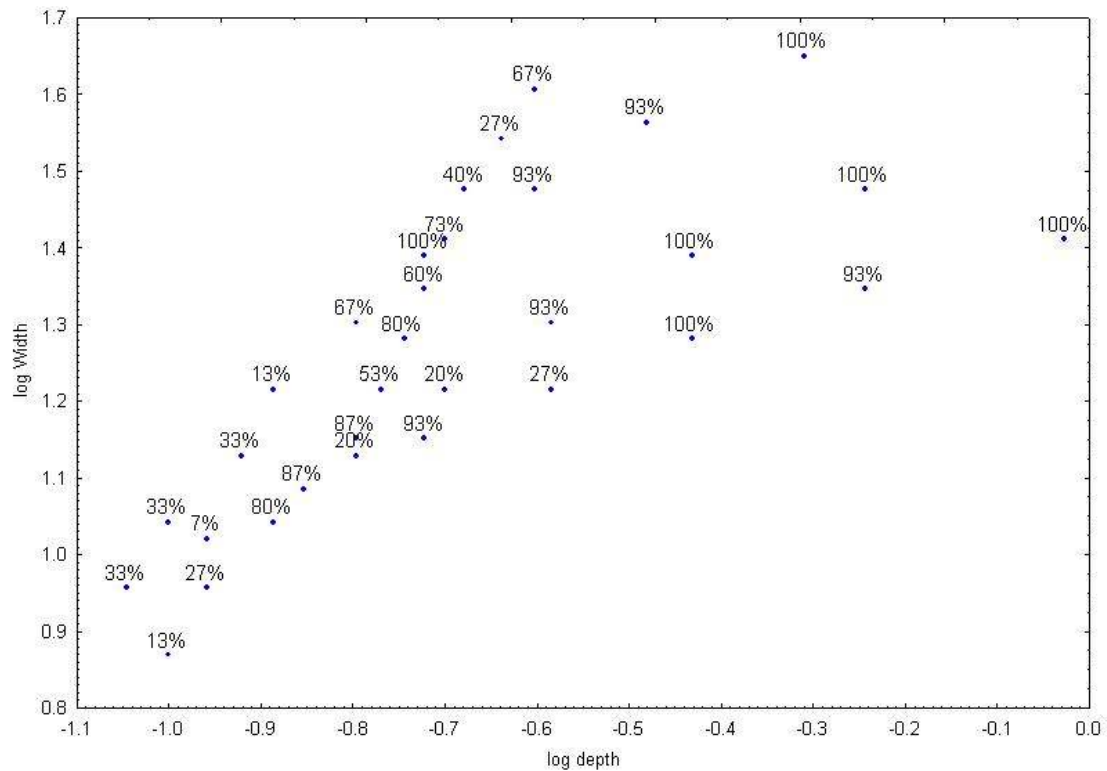


## Appendix H

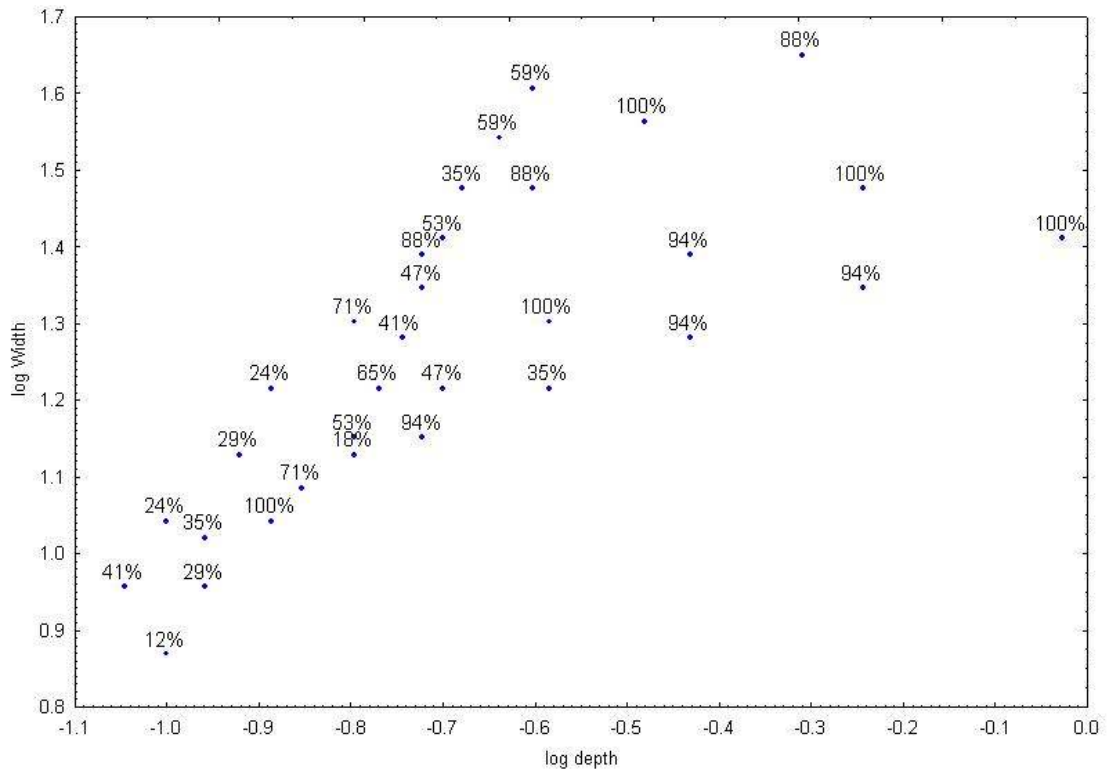
### Detection plots of results from series 2 visual inspection trials



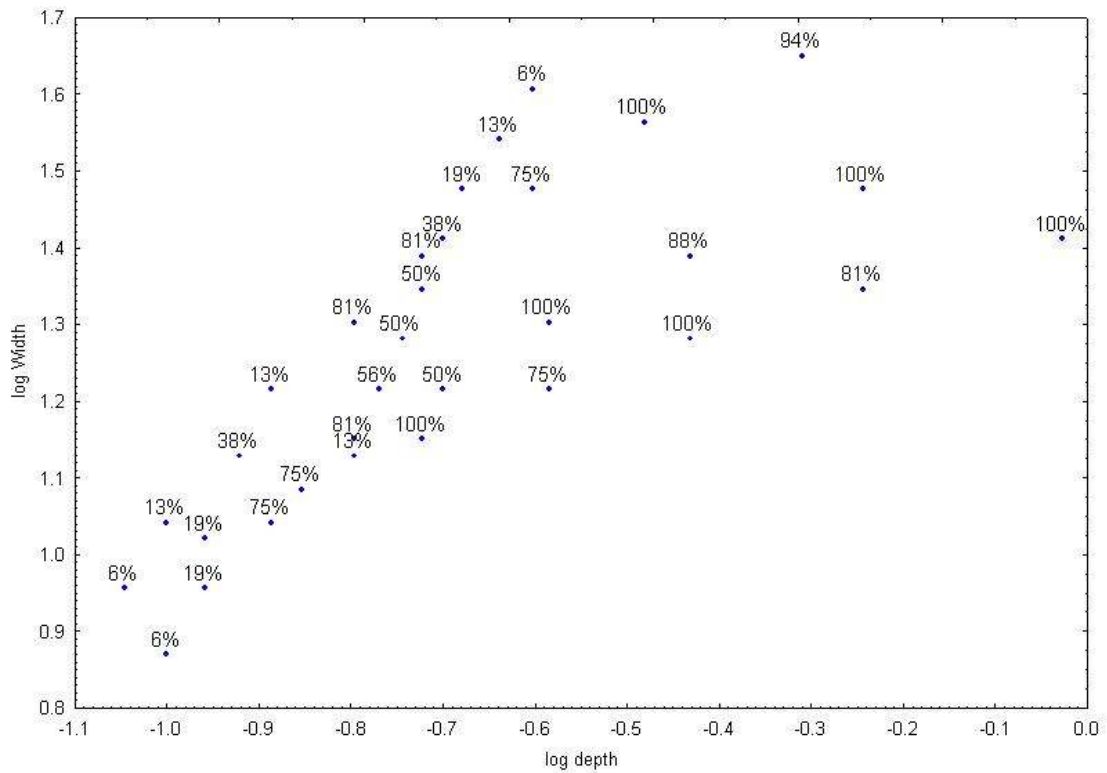
Original scatter plot of detection rates obtained with virtual specimens



Original scatter plot of detection rates obtained with gloss grey specimens

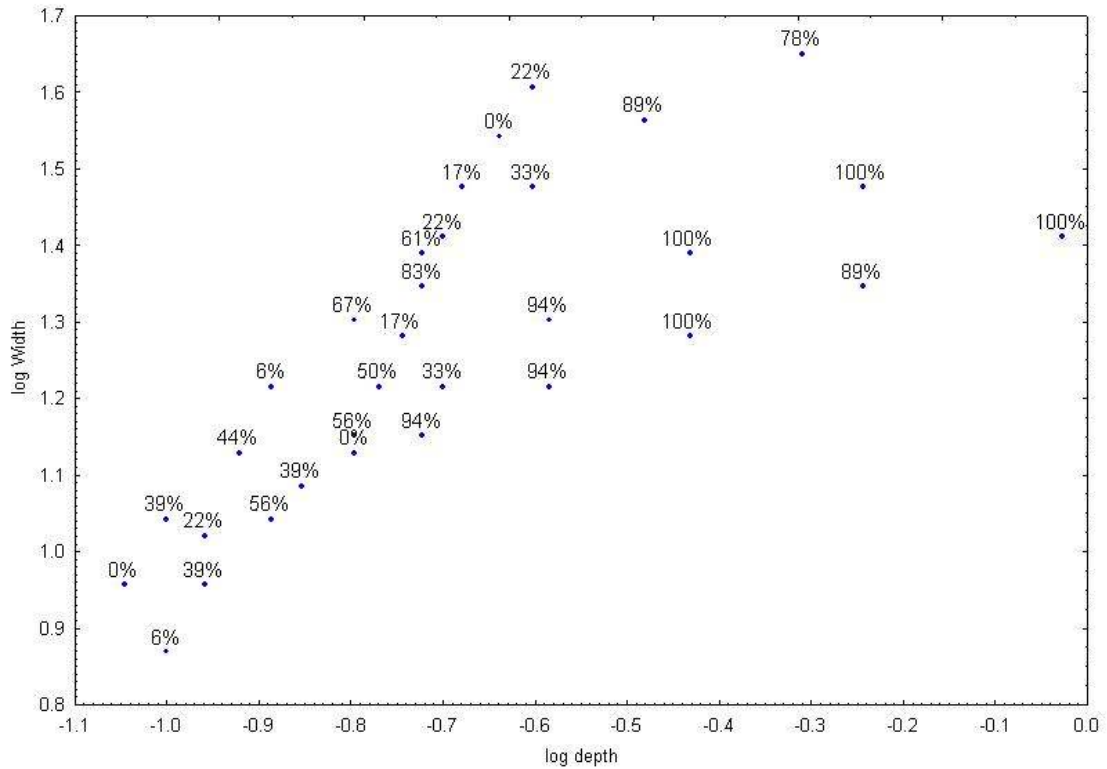


Original scatter plot of detection rates obtained with matt grey specimens

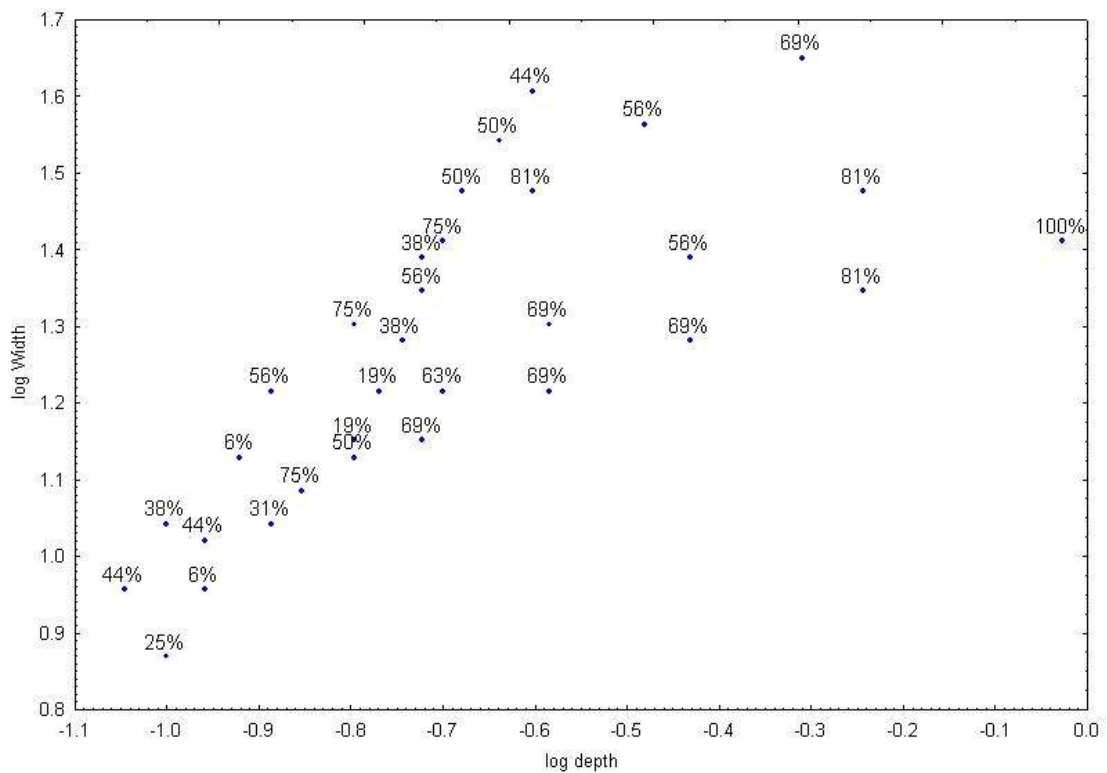


Original scatter plot of detection rates obtained with gloss white specimens

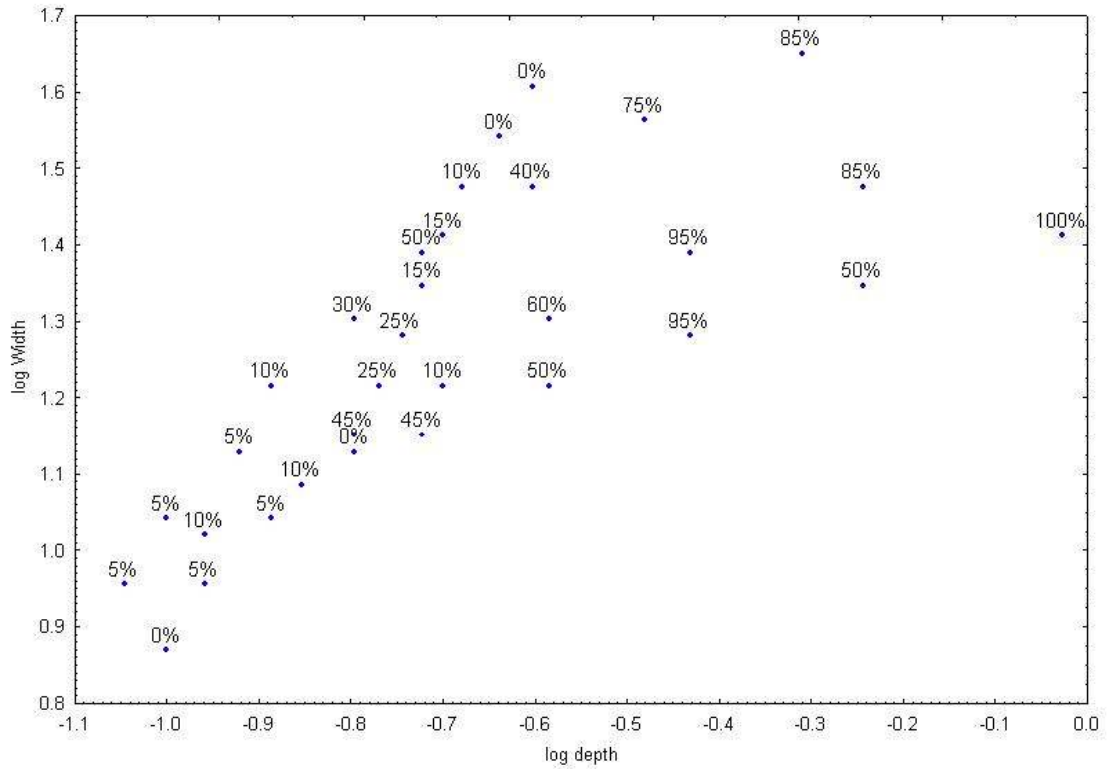




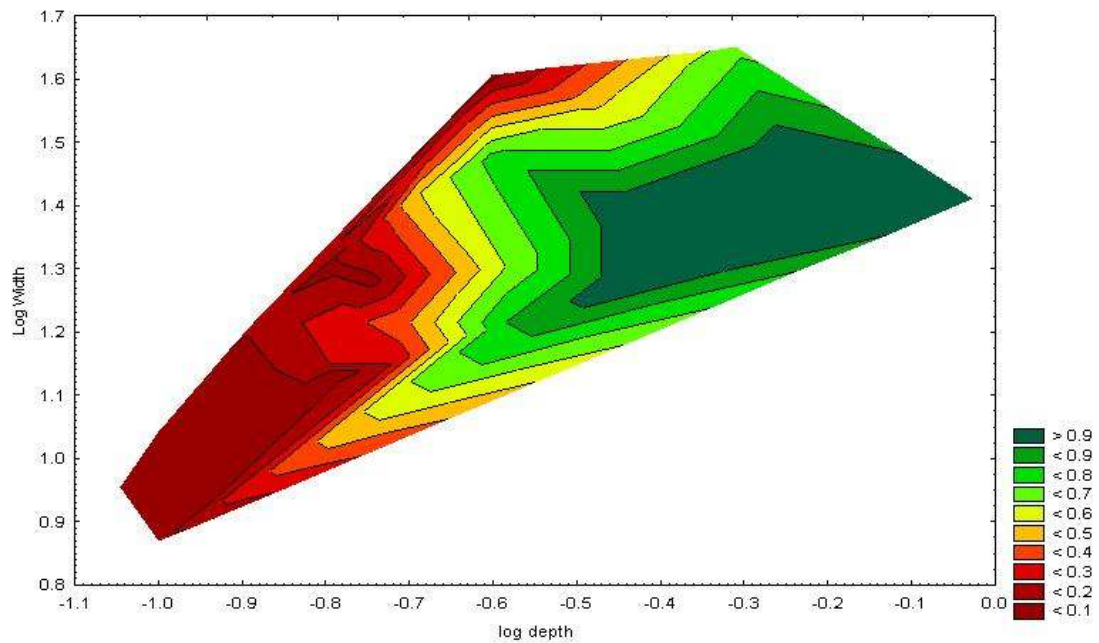
Original scatter plot of detection rates obtained with matt white specimens



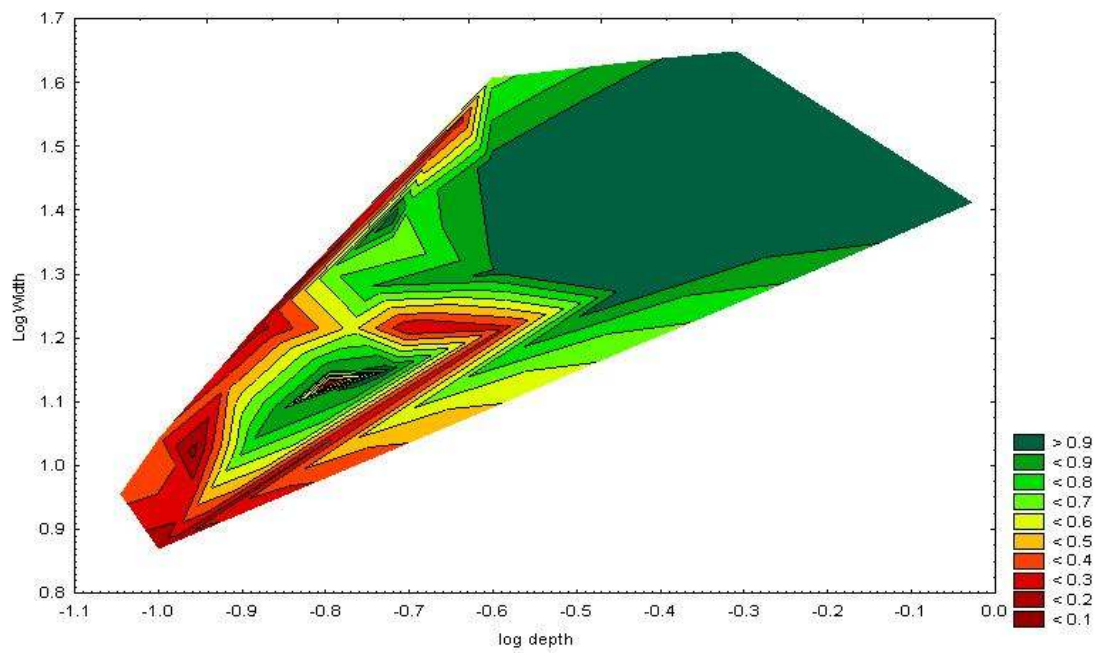
Original scatter plot of detection rates obtained with gloss blue specimens



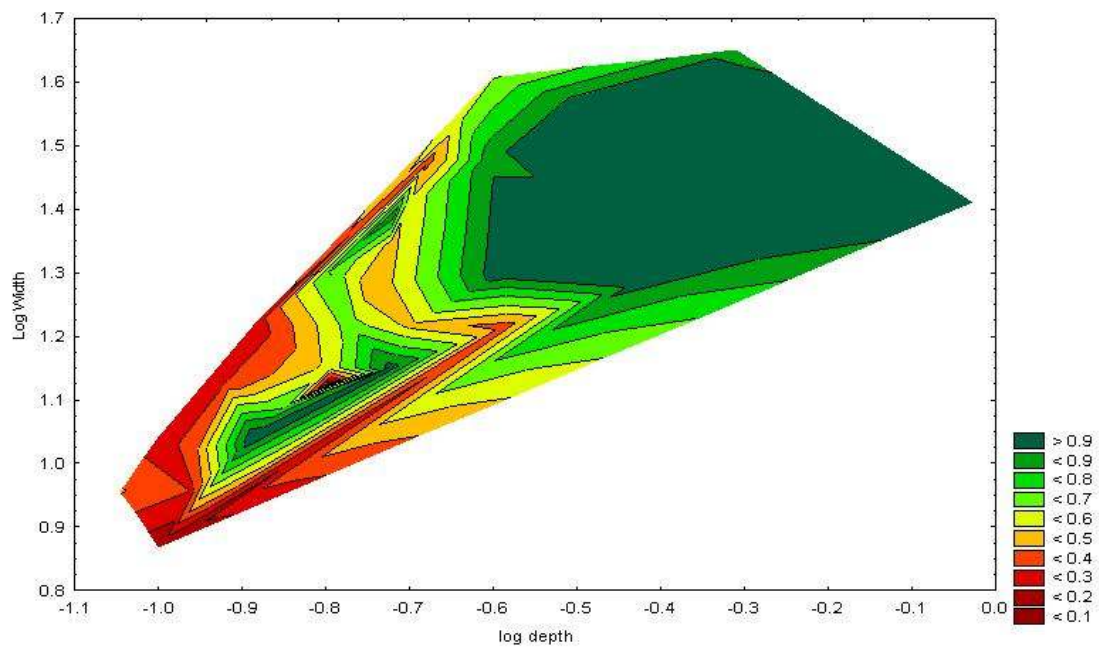
Original scatter plot of detection rates obtained with matt blue specimens



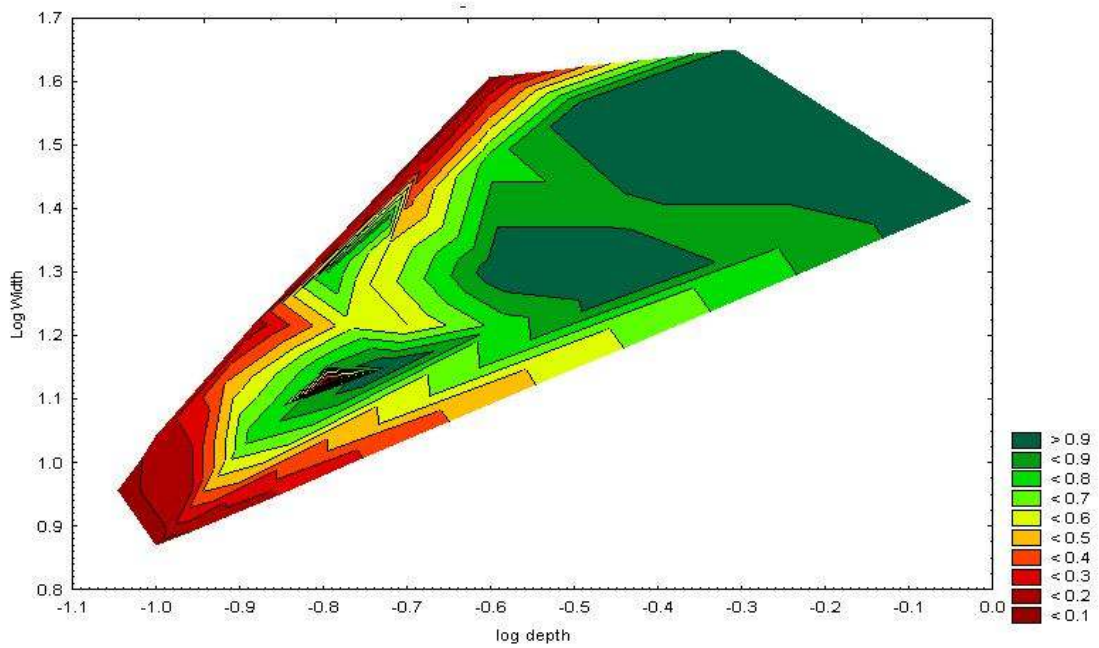
Original wafer plot of detection rates obtained with virtual specimens



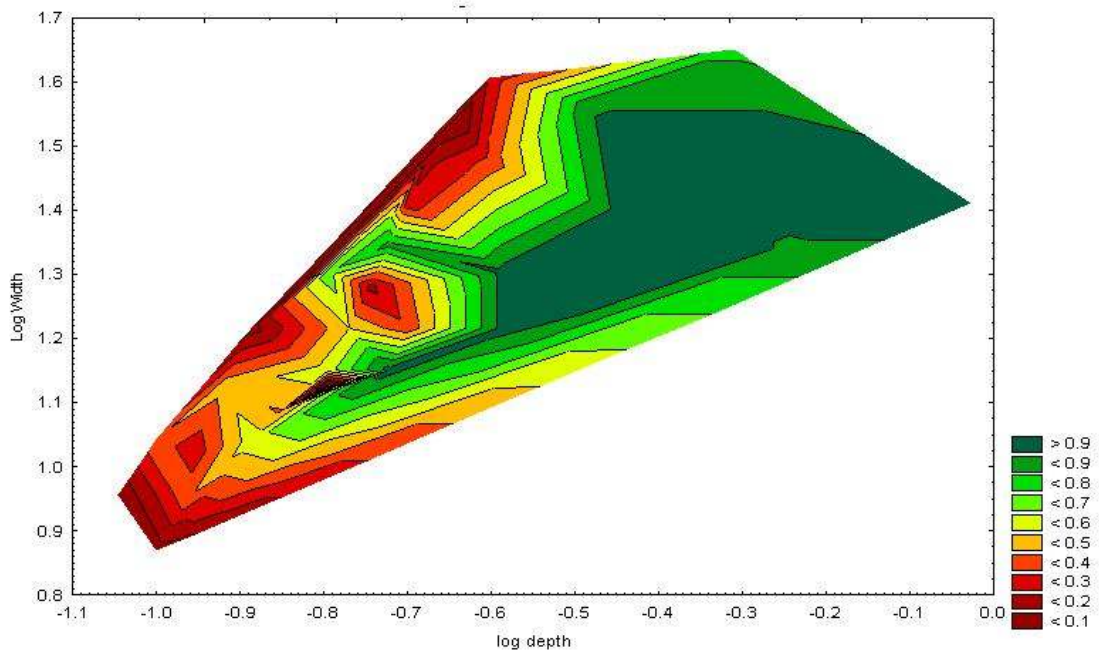
Original wafer plot of detection rates obtained with gloss grey specimens



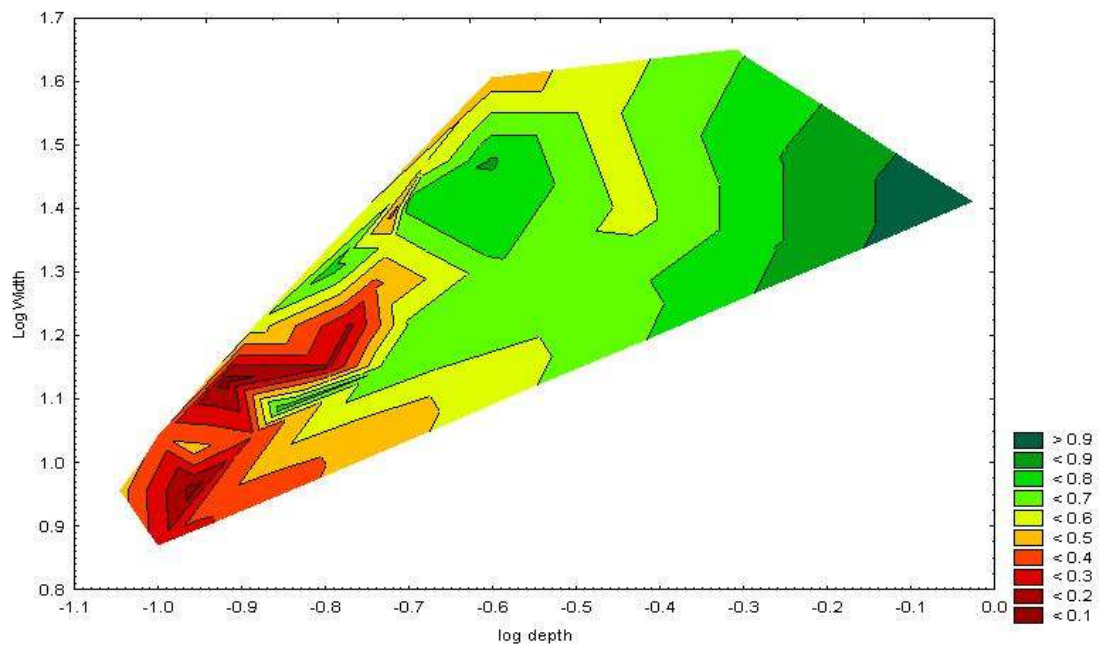
Original wafer plot of detection rates obtained with matt grey specimens



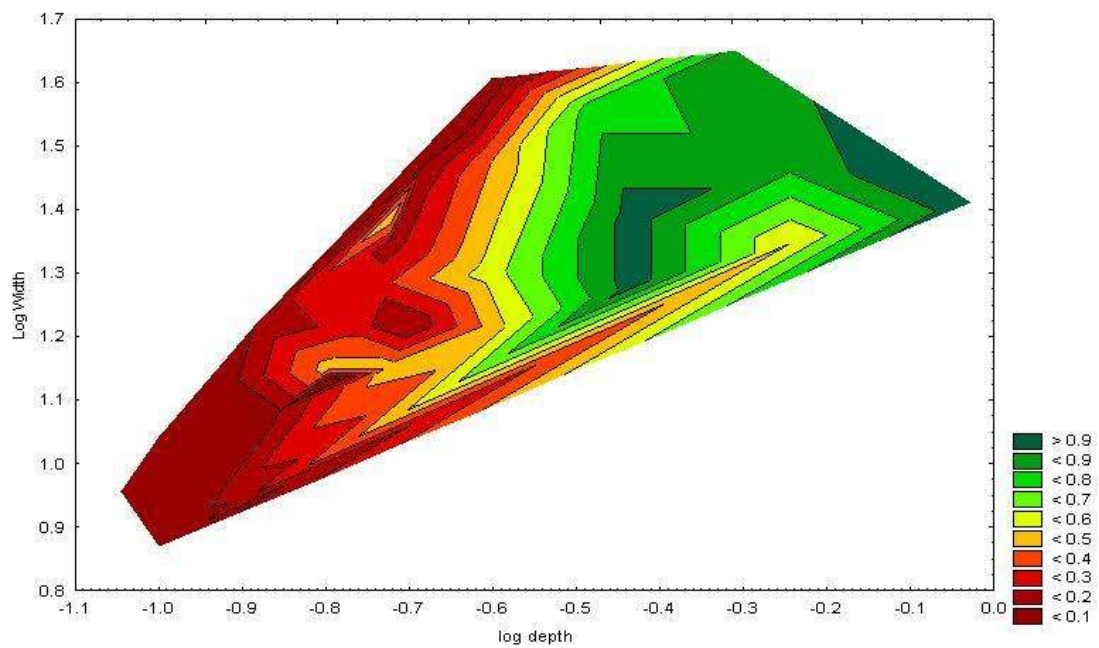
Original wafer plot of detection rates obtained with gloss white specimens



Original wafer plot of detection rates obtained with matt white specimens



Original wafer plot of detection rates obtained with gloss blue specimens



Original wafer plot of detection rates obtained with matt blue specimens